LOWER HYBRID EXPERIMENTS USING AN INTERDIGITAL LINE ANTENNA ON THE REVERSED FIELD PINCH

by

Michael C. Kaufman

A dissertation submitted in partial fulfillment of the

requirements for the degree of

Doctor of Philosophy

(Physics)

at the

UNIVERSITY OF WISCONSIN-MADISON

2009

Lower Hybrid Experiments Using an Interdigital Line Antenna on the Reversed Field Pinch

Michael C. Kaufman

Under the supervision of Professor Stewart C. Prager

At the University of Wisconsin-Madison

Abstract

Lower hybrid current drive has been offered as a means of improving confinement in the reversed field pinch by reducing tearing fluctuations. Modeling suggests that a slow wave launched at 800 MHz and an $n_\parallel$ of 7.8 will penetrate to the region of maximum magnetic stochasticity and significantly reduce core tearing mode activity.

The particular constraints of the Madison Symmetric Torus lead to the use of a novel interdigital-line traveling wave antenna structure rather than the traditional waveguide grill antenna. Several generations of this antenna type have been constructed and installed in MST. Scattering parameters have been measured and with the addition of external tuning, the antenna suffers from less than -15 dB of reflection in most plasma conditions. The latest generation antenna has achieved $\gtrsim 220$ kW of applied power. Measurements of the launch spectrum show a lower peak $n_\parallel$ than was designed. Subsequent modeling of the antenna geometry provides the reason and offers a method to compensate without fabricating another antenna.

The launch spectrum displays good directivity, and the antenna operates

well in a variety of plasma conditions. Coupling is compared to theory and simulation and shows good qualitative agreement, though lack of good edge density profiles limits the prospects for predictive capability. The use of a plasma limiter has been shown to reduce the dependence of coupling on the plasma density, and local gas puffing has been shown to maintain the amount of loading even in low density or high confinement plasmas.

A hard x-ray survey of rf in standard MST plasmas shows a toroidal asymmetry in the hard x-ray flux. Modeling indicates that this flux is consistent with electrons being accelerated to high energies in the near-field of the antenna. Analysis indicates that power losses to these electrons may be on the order of several percent of the input power.

Contents

List of Figures

List of Tables

Acknowledgements

Though this list is necessarily incomplete, I'd like to acknowledge a few kind souls without whom this work would not exist:

Stewart Prager for keeping me from slipping at times into despair.

Cary Forest for innumerable discussions on rf physics and especially for steering me off a few of my rather more speculative tangents.

Vladimir Mirnov for many discussions on wave physics and for helping me grind through V. E. Golant's coupling theory.

Mark Thomas for teaching me the basics and for having the memory of an elephant. That and the antenna design.

John Goetz, I could not have hoped for a better mentor.

Dave Burke my comrade in arms.

Harold Myers, I don't know how many students you inspired to pursue advanced degrees in chemistry or physics, but I am certainly one of them. You will be missed.

All those on the MST team, to keep the machine running, and for being available for consultations about any crazy idea I might have had at the time.

All my family and friends.

Michael Kaufman

Madison, Wisconsin

December, 2009

The known is finite, the unknown infinite; intellectually we stand on an islet in the midst of an illimitable ocean of inexplicability. Our business in every generation is to reclaim a little more land...

T. H. Huxley, 1887

Chapter 1

Introduction

1.1 The Motivation for RF in an RFP

Radio frequency waves have been an integral part of fusion research for decades. Rf waves have been used to drive mega-amps of current, have heated plasmas to many keV, or have simply been used as a non-perturbative diagnostic. Today the use of rf has become indispensable in producing and controlling high-quality plasmas on many of the large machines [1]. Despite its extensive use throughout the field, rf heating and/or current drive has only recently been employed on the reversed field pinch (RFP). The use of a novel antenna for launching lower hybrid waves into the RFP as well as the coupling to and interaction with the plasma will be the focus of this work.

The reversed field pinch is normally compared to the much more well known tokamak configuration. Both are toroidal devices, with generally helical magnetic field lines. The principal difference is that the RFP has a relatively weak toroidal field, where the

main confining field is the poloidal field generated by the large toroidal plasma current. This feature has made the RFP attractive as a reactor concept since it allows a high engineering beta (the ratio of plasma pressure to the square of the field strength at the coils), and it does not require the use of superconducting coils — a major cost driver [2].

A conventional reversed field pinch plasma is formed by applying a toroidal electric field in a weak toroidal field. After an initial unstable phase, the plasma relaxes into a minimum energy state where the parallel normalized current density ($\lambda \equiv J_\parallel/B$) is nearly flat [3]. The parallel component of the generalized Ohm's Law is:

$$E_\parallel + \langle \tilde{\mathbf{v}} \times \tilde{\mathbf{b}} \rangle_\parallel - \frac{1}{ne} \langle \tilde{\mathbf{j}} \times \tilde{\mathbf{b}} \rangle_\parallel + \cdots = \eta J_\parallel \tag{1.1}$$

where $E_\parallel$ is the parallel component of the inductive electric field, η is the resistivity, and $J_\parallel$ is the parallel current density. The $\langle \tilde{\mathbf{v}} \times \tilde{\mathbf{b}} \rangle$ term is the MHD dynamo and $\langle \tilde{\mathbf{j}} \times \tilde{\mathbf{b}} \rangle$ is the Hall dynamo term. A flat λ-profile requires substantial edge poloidal current not provided by $E_\parallel$, and it is the dynamo terms in (1.1) that provide that current and act to reverse the edge toroidal field [4]. These terms are self-generated by large amplitude magnetic fluctuations driven mostly by the current density gradient [5].

The reversal of the toroidal field gives a much different q profile ($q \equiv rB_z/RB_\theta$) than one would see in the tokamak. The q profile is a monotone decreasing function of minor radius with an on-axis value of about 0.2 (for MST) and passes through zero (the reversal surface) at the edge. A diagram of the RFP profile is shown in Figure 1.1.

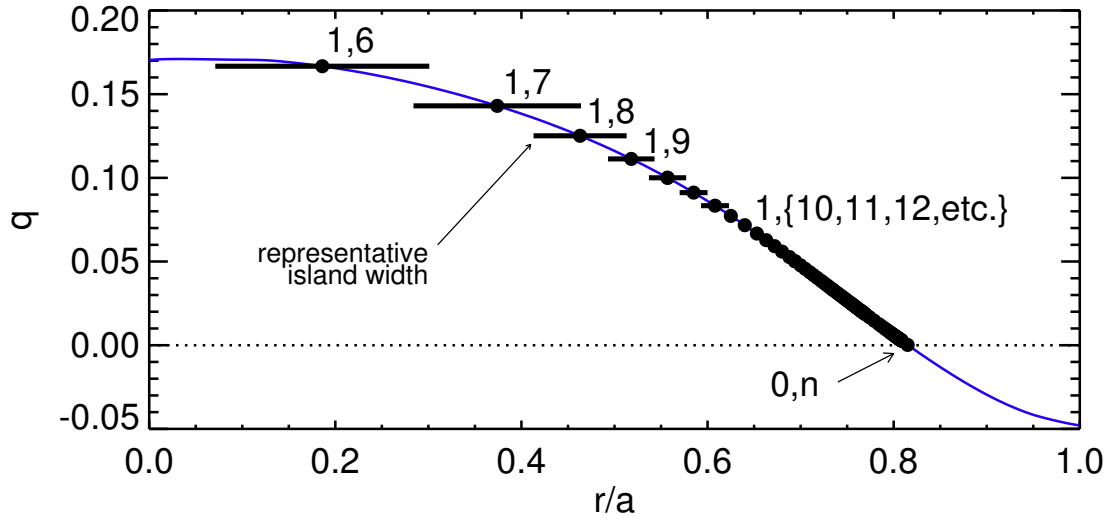

Figure 1.1: A typical reversed field pinch q profile and the locations of the (m, n) resonance surfaces inside the reversal surface. The lines show representative island widths at each resonance demonstrating the overlap. In this profile, the maximum q is below 0.2 so the $(1, 5)$ mode is not resonant.

The large magnetic fluctuations required to generate the dynamo (and the reversed field pinch) at the same time have a deleterious effect on the plasma confinement. The great majority of the fluctuating power is contained in modes with poloidal mode number $m = 1$ and toroidal mode numbers $n = 5 - 8$. Comparisons between MHD computations and experiment have established that these modes are core tearing fluctuations described by resistive MHD [6]. Despite the fact that the fluctuation level is around 1-2%, the closeness of the mode rational surfaces allows the magnetic islands from adjacent surfaces to overlap and creates large regions of magnetic stochasicity. This stochasticity allows rapid energy and particle transport and is a key issue for the RFP as a fusion reactor.

If the inductive electric field can be tailored so that the current density profile is sufficiently flat to maintain the RFP configuration, then the dynamo terms supplying the edge current are no longer needed. This can be accomplished by driving the toroidal field winding to induce an additional poloidal electric field E_θ [7]. This technique, known as pulsed poloidal (or parallel) current drive (PPCD) has been used successfully on the Madison Symmetric Torus and other devices to reduce transport and improve confinement by at least a factor of ten [8] and restore flux surfaces.

PPCD can be pictured as an auxiliary forcing term [9] which modifies the original applied ohmic electric field and acts to replace the dynamo terms in (1.1):

$$E_\parallel = E_{\parallel_{orig}} + \frac{F_a \hat{\mathbf{b}}}{ne} = \eta J_\parallel. \tag{1.2}$$

Figure 1.2a shows a Gaussian-shaped *ad hoc* force and the resulting flattened λ-profile. Figure 1.2b shows the results of the non-linear MHD code DEBS [10]. The core tearing mode fluctuations are reduced by several orders of magnitude in response to the change in the λ-profile.

While the forcing term in (1.2) is inductive when using PPCD, it need not be. Any mechanism that can drive current at the proper location at the edge may be used. It is here that using radio frequency waves to drive the current comes to mind since the *ad hoc* forcing term is reminiscent of rf-current drive profiles. PPCD is inherently transient and requires significantly altering the q profile. On the other hand, rf power can be made steady state, a distinct advantage for reactor scenarios, and it can be used under any plasma conditions in which the rf waves can couple and drive the appropriate

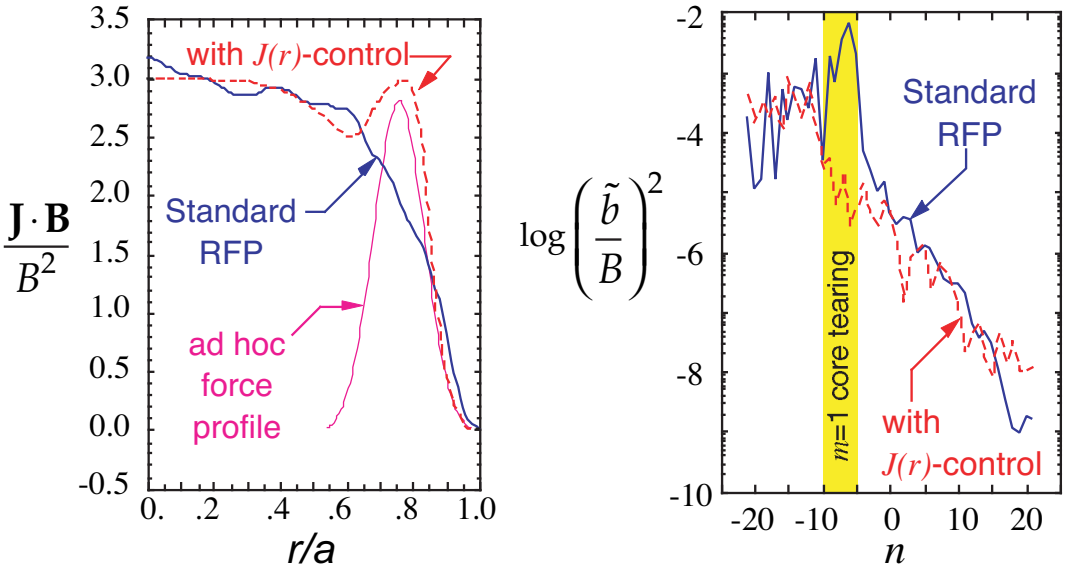

Figure 1.2: Profile and fluctuations with and without profile control. From [11,12]. (a) The parallel current profile for standard discharges and with the addition of an *ad hoc* force at the edge. (b) The axial mode spectrum for $m = 1$ tearing mode fluctuations from DEBS computation. The red dashed line is the reduction after profile modification.

amount of current. Additionally, because PPCD depends on the changing toroidal flux to improve confinement and rf does not, physics experiments that benefit from stable magnetic and current profiles will be possible using LHCD.

1.2 MST

The Madison Symmetric Torus (MST) is a reversed field pinch located on the campus of the University of Wisconsin-Madison [13]. A diagram of MST is shown in Figure 1.3. MST has a circular cross-section with a major radius of 1.5 m and a minor radius of 0.52 m. It has a close-fitting 5 cm thick conducting shell of aluminum which serves as the

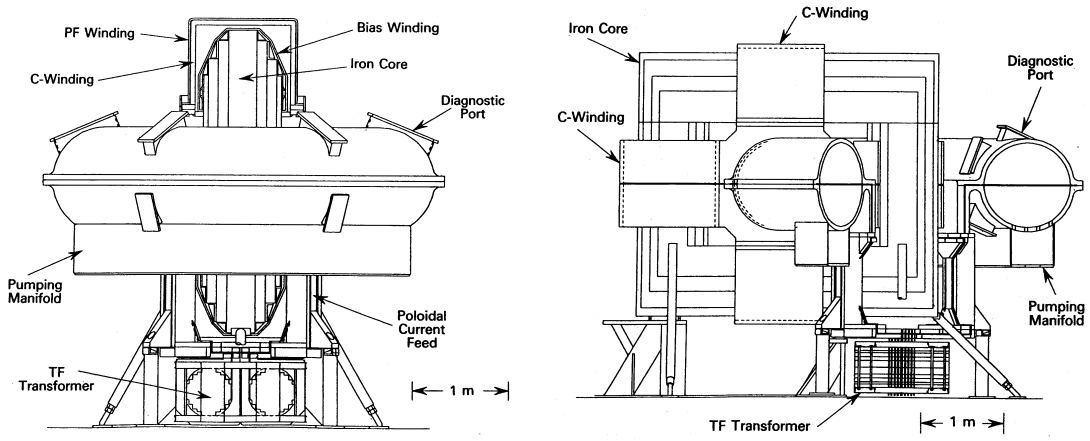

Figure 1.3: Diagram of Madison Symmetric Torus. From [13].

vacuum vessel as well as the toroidal field coil. It is the characteristics of the vacuum vessel that necessitates a non-standard antenna design for launching rf waves. The plasma is limited by toroidal graphite limiters on the inboard and outboard midplane that have a 1 cm radial extent.

Operating parameters for the machine are 200-600 kA toroidal current, with an average edge field of $\sim 1.5\,\mathrm{kG}$ with $3-4\,\mathrm{kG}$ in the core for 400 kA plasmas. Typical densities run $0.4-2\times10^{13}\,\mathrm{cm}^{-3}$ with deuterium as the standard operating gas. There are several standard operating scenarios for MST. Unless otherwise specified, rf power will be launched into 400 kA standard plasmas: the plasma flat-top will have an average plasma current $I_p = 400$ kA, the line-average density will be $1\times10^{13}\,\mathrm{cm}^{-3}$, the reversal parameter F will be -0.2, and the pinch parameter $\Theta \simeq 1.7$. Here F and Θ are defined

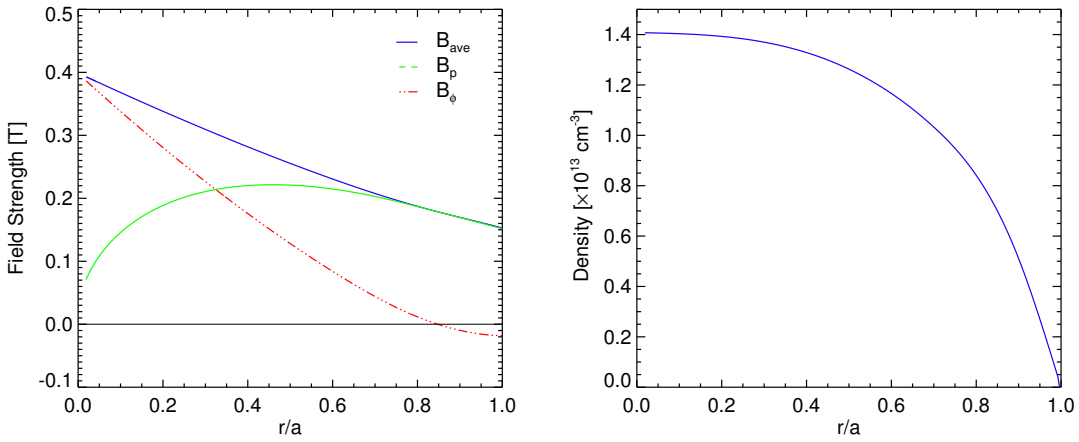

Figure 1.4: Equilibrium reconstructed profiles for a 400 kA standard MST plasma (a) Radial magnetic field profiles. (b) Radial density profile for a line-averaged density of $1 \times 10^{13}\,\mathrm{cm}^{-3}$.

as:

$$F = \frac{B_\phi\,(a)}{\langle B_\phi \rangle}, \qquad \Theta = \frac{B_\theta\,(a)}{\langle B_\phi \rangle} \tag{1.3}$$

where a is the minor radius of the machine and $\langle\rangle$ is the average over the poloidal cross-section. Electron temperatures range from about 40 eV at the edge to 300 eV in the core. Some typical profiles for this operating regime are shown in Figure 1.4.

The typical discharge is $\sim$80 ms in duration which includes about 30 ms of "flat-top" regime where plasma current, field equilibrium and density can be held relatively constant. Most rf-injection for our purposes takes place during the the flattop.

1.3 RF Current Drive

The use of waves to drive current in toroidal plasmas has been known as early as the 1950's. Energy and/or momentum can be transferred to particles from waves via the Landau resonance:

$$\omega - \mathbf{v} \cdot \mathbf{k} = 0 \tag{1.4}$$

where $\mathbf{v}$ is the particle velocity and ω and $\mathbf{k}$ are the wave frequency and wave number, or by the cyclotron resonance,

$$\omega - k_{\|} v_{\|} - n\Omega = 0, \tag{1.5}$$

with $\Omega \equiv qB/m$ the cyclotron frequency and n is an integer. Early suggestions for driving toroidal current in larger machines focused on transferring wave momentum to slow electrons — for example by Alfvén waves — as it is more efficient to add energy to slow rather than fast electrons [14]. Fisch [15] showed that using the lower-hybrid wave, driving fast electrons ($v_{\phi_{\|}} \gg v_{th}$, $v_{\phi} = \omega/k$) can be just as efficient since the collision frequency goes as $1/v_{\phi_{\|}}^3$, the power required to maintain the current is much less. In fact, because slow electrons suffer from trapping, much less current can be driven when the trapped fraction is high.

Despite this potential problem, several early studies [16,17] explored the possibility of using Alfvén waves to drive current in the reverse field pinch. Uchimoto *et al* [11] showed that lower hybrid waves are ideally suited to drive poloidal current in the outer region of the RFP. The use of this method will be a focus of this work.

Before going into the specifics of the rf launch and propagation, it may be useful to estimate the amount of power required to stabilize tearing modes and improve confinement using rf rather than PPCD. The 3D non-linear MHD simulation showed that to effect the changes in Figure 1.2a, 25% of the poloidal current should be driven by auxillary, i.e. rf, sources. For typical RFP equilibria, the poloidal current can be approximated by

$$I_\theta = \frac{3R}{a\Theta} I_\phi \tag{1.6}$$

where R/a is the aspect ratio. For an $I_\phi = 400$ kA plasma, it will be necessary to drive approximately 500 kA of current by rf to maintain an improved confinement mode.

To determine how much power is required to drive this current we need the current drive efficiency:

$$\eta = j_\parallel^{rf} / p^{rf} \tag{1.7}$$

where $j_\parallel^{rf}$ is the rf-driven current density, and p^{rf} is the deposited rf power density. A useful approximation can relate (1.7) to the total current and power. If we assume that the LHCD occurs in a cylindrical shell between r_1 and r_2, then we have:

$$I_\theta^{rf} / P = \frac{j_\parallel^{rf} 2\pi R \left(r_2 - r_1\right)}{p^{rf} 2\pi R \left(\pi r_2^2 - \pi r_1^2\right)} = \eta / \left(2\pi r_{av}\right) \tag{1.8}$$

where $r_{av} = \left(r_1 + r_2\right)/2$. The efficiency can also be written as:

$$\eta = 3.84 \times 10^{19} \frac{T_e}{n_e \ln \Lambda} \tilde{\eta}, \tag{1.9}$$

where $\ln \Lambda$ is the Coulomb logarithm, T_e and n_e are in units of keV and SI units, and

$\tilde{\eta}$ is a dimensionless quantity that depends on Z, the trapping ratio and the ratio of $v_{\phi_\parallel}/v_{th}$ and is plotted in Ehst [18].

Uchimoto estimates that a $\tilde{\eta} \simeq 10$ can be achieved for MST parameters with a resultant driven current of 0.5 A/W. Then we would expect to need approximately 1 MW of rf power for confinement improvement. In this calculation however, a Z of 1 was used. At the reversal surface, we might expect an effective Z of 3 or 4 to be a better estimate. This has the effect of reducing the efficiency. Using the analytic function given by Ehst for $Z = 3$, we have $\tilde{\eta}$ closer to 4. Using this value and the plasma parameters where the power absorption is maximum, we have $I_\theta^{rf}/P \simeq 0.24$ A/W. For $0.25I_\theta$, we require $\sim$2.1 MW, a significant increase in the deposited power.

This analysis does not treat the high radial diffusion in standard RFP plasmas which will reduce the initial efficiency of the injected power. To avoid this, it may be necessary to use PPCD to achieve an initial improved confinement state before applying rf power [19]. A better estimate of the driven current for a given input power can be made with a Fokker-Planck solver such as CQL3D [20]. While important to determine the true size of a full power rf system, this calculation is not a focus of this thesis. Instead, the emphasis will be on hardware limits of delivering the power.

1.4 Wave Propagation

The theory of lower hybrid wave propagation has been discussed by many authors, so only an overview with details pertinent to LHRF on MST will be treated here. Following the notation of Bonoli [21], we have for the wave equation in the geometric-

optics approximation:

$$\mathbf{n} \times \mathbf{n} \times \mathbf{E} + \boldsymbol{\epsilon} \cdot \mathbf{E} = 0, \tag{1.10}$$

where $\mathbf{E} \sim e^{i(\mathbf{k}\cdot\mathbf{x}-\omega t)}$, $\mathbf{n} = \mathbf{k}c/\omega$ is the index of refraction, and $\boldsymbol{\epsilon}$ is the cold plasma dielectric tensor:

$$\boldsymbol{\epsilon} = \begin{bmatrix} \epsilon_\perp & -i\epsilon_{xy} & 0 \\ i\epsilon_{xy} & \epsilon_\perp & 0 \\ 0 & 0 & \epsilon_{||} \end{bmatrix}. \tag{1.11}$$

We have defined the parallel and perpendicular directions with respect to a static background magnetic field B_0, and the matrix elements can be derived using the single particle equations of motion and Maxwell's Laws [22].

The lower hybrid range of frequencies is generally defined as $\Omega_{ci} \ll \omega \ll \Omega_{ce}$, where Ω_{cj} and $\omega_{pj} \equiv \sqrt{n_j e^2/m_j\epsilon_0}$ are the cyclotron and plasma frequencies respectively. Using this approximation, the matrix elements of (1.11) are:

$$\begin{aligned} \epsilon_\perp &= 1 + \omega_{pe}^2/\Omega_{ce}^2 - \omega_{pi}^2/\omega^2 \\ \epsilon_{||} &= 1 - \omega_{pe}^2/\omega^2 - \omega_{pi}^2/\omega^2 \\ \epsilon_{xy} &= \frac{\omega_{pe}^2}{\omega\Omega_{ce}}. \end{aligned} \tag{1.12}$$

From (1.10) and (1.11) we can form a dispersion relation $\mathbf{D}\cdot\mathbf{E} = 0$ whose non-trivial solution is

$$P_0 n_\perp^4 + P_2 n_\perp^2 + P_4 = 0, \tag{1.13}$$

where $n_\perp$ is the perpendicular component of the index of refraction and the coefficients

P_0, P_2, P_4 are:

$$\begin{aligned} P_0 &= \epsilon_{||}\left[\left(n_{||}^2-\epsilon_\perp\right)^2-\epsilon_{xy}^2\right] \\ P_2 &= \left(\epsilon_\perp+\epsilon_{||}\right)\left(n_{||}^2-\epsilon_\perp\right)+\epsilon_{xy}^2 \\ P_4 &= \epsilon_\perp. \end{aligned} \tag{1.14}$$

The expression (1.13) is quadratic in $n_\perp^2$ whose solutions are

$$n_\perp^2=\frac{-P_2\pm\sqrt{\Delta}}{2P_4},\quad \Delta=P_2^2-4P_0P_4. \tag{1.15}$$

For a fixed $n_{||}$, (1.15) completes the description for the wave propagation into a cold plasma and shows the two distinct branches for propagation: the "slow" and "fast" corresponding to the positive and negative signs respectively. The slow wave branch has a resonance condition ($n_\perp\to\infty$) at $P_4=\epsilon_\perp=0$, which defines the lower hybrid frequency,

$$\omega_{lh}=\frac{\omega_{pi}\Omega_{ce}}{\sqrt{\Omega_{ce}^2+\omega_{pe}^2}} \tag{1.16}$$

and a density, N_{LH}, at which the slow wave will cease to propagate. It is the slow wave branch that is generally associated with lower hybrid waves and is the branch that we will use to launch waves into MST plasmas.

Figure 1.5 shows solutions of (1.15) for different values of $n_\parallel$. If $n_\parallel$ is greater or equal to some critical value n_a as in the second and third panels of the Figure, then the slow wave can propagate from its cutoff at N_S all the way to the lower hybrid resonance. If however, $n_\parallel<n_a$, then the slow wave will mode convert to the fast branch

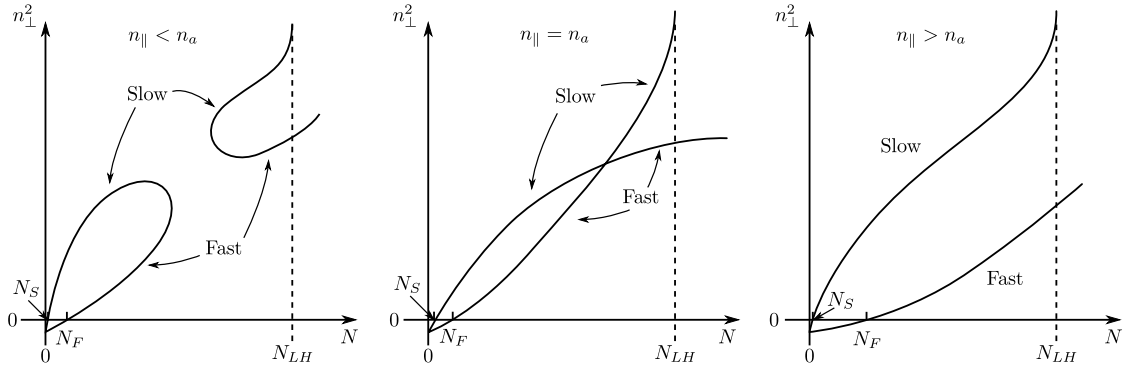

Figure 1.5: Slow and fast wave branches for different values of $n_\parallel$ relative to n_a. N_S and N_F are the slow and fast wave cutoffs. N_{LH} is the density corresponding to the lower hybrid resonance.

and propagate back out of the plasma. This accessibility condition n_a is defined by requiring $\Delta \geqslant 0$ for all densities in (1.15) so the two modes do not coalesce.

The fast wave branch does not suffer from the lower hybrid resonance, and so it may be useful in reactor scenarios as it can penetrate to arbitrarily high densities [23]. It has a distinct disadvantage relative to the slow wave, however: its cutoff N_F is at a higher density than N_S and so must tunnel farther before it begins to propagate. In MST this corresponds to ~ 5 cm into the plasma, making the fast wave unusable for launching waves.

The wave need not propagate to the lower hybrid resonance for heating or current drive. The launched waves must only reach a location where the density and/or temperature is high enough for efficient absorption (via Landau damping for example). As discussed above, the presence of the lower hybrid resonance may be detrimental for high density operation. Setting the pump frequency ω higher than ω_{lh} at the target location will avoid this density limit. For tokamak plasmas with strong magnetic

fields, this requires the wave frequency to be on the order of GHz for targets inside mid-radius. For MST, the fields are much lower and the target density is also quite low, so the minimum frequency required to avoid the density limit is also lower. As long as the frequency is higher than about 550 MHz, the lower hybrid resonance moves to densities that exceed the maximum that can be normally obtained in MST. Since the current drive scenario for MST requires deposition at $r/a \simeq 0.7$ and at a density of $0.7 \times 10^{13}\,\mathrm{cm}^{-3}$, the accessibility criterion is relaxed. We require only that we can propagate to that point before the wave mode converts to the fast wave.

Because rf sources from Princeton Plasma Physics Laboratory were made available to the project at no cost, 800 MHz was chosen as the operating frequency. This frequency is high enough to avoid the density limit discussed above, but for MST edge parameters of $B_0 = 1500$ G in D_2 gas, we require an $n_\parallel \simeq 11.2$ to reach the target absorption region at $\sim 0.7 \times 10^{13}\,\mathrm{cm}^{-3}$ before converting to the fast wave.

The accessibility calculation has not taken into account the magnetic field gradient or the toroidal geometry. The field increases as the density increases, which reduces the required $n_\parallel$. In a toroidal geometry, when launching from the inboard side, an upshift occurs in the parallel refraction which also enables the wave to access deeper regions of the plasma [24]. This allows a much lower launch $n_\parallel$ than expected from the slab model.

For a more accurate solution to the wave propagation, ray tracing can be used. GENRAY is a general ray tracing code for the calculation of wave propagation and absorption in a geometric optics approximation and accounts for realistic density and magnetic field profiles as well as a toroidal geometry [25]. For a inboard launch, Fig-

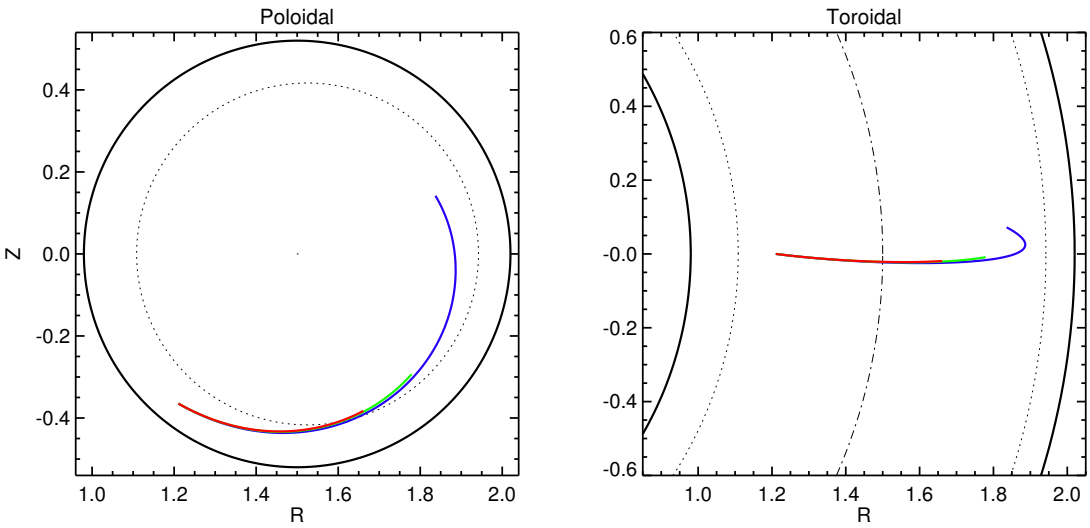

Figure 1.6: GENRAY ray-tracing of LH wave into 400 kA standard plasmas. Rays are launched in the co-current direction at $n_{\|}$ of 6, 8, and 10 (blue, green, red).

ures 1.6 and 1.7 show the poloidal and toroidal wave propagation for an $n_{\|}$ of 6, 8, and 10 and -6, -8 and -10. The wave is followed until 99% of the power has been absorbed. The ray tracing indicates that launching a wave with an $n_{\|} \simeq 7.8$ from the lower inboard side of the machine will propagate into a region just inside the reversal surface, where we require power deposition for fluctuation reduction.

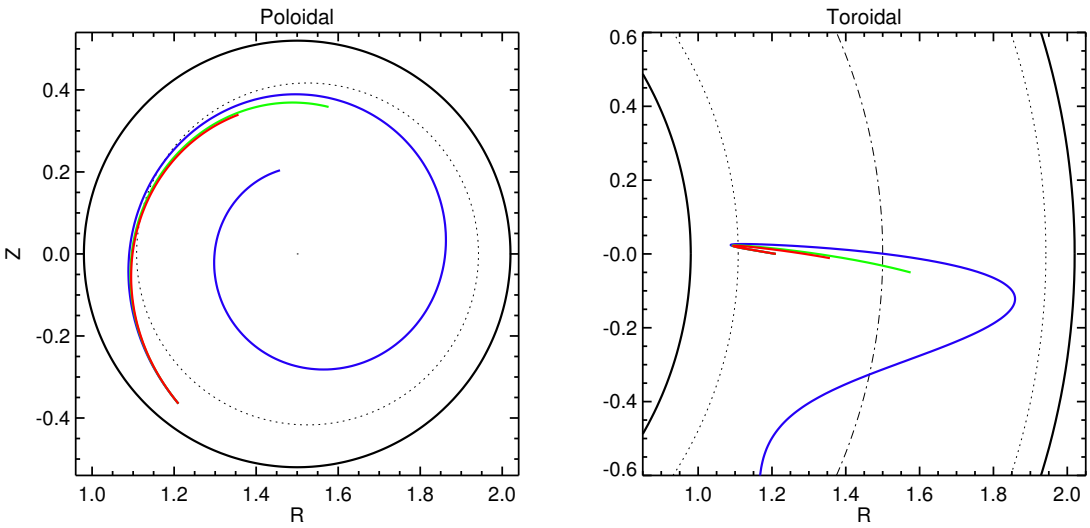

Figure 1.7: GENRAY ray-tracing of LH wave into 400 kA standard plasmas. Rays are launched in the counter-current direction at $n_{\|}$ of -6, -8, and -10 (blue, green, red).

1.5 Summary and Thesis Outline

Inductive current drive has been used to great success in MST, with PPCD increasing the energy confinement time by an order of magnitude. The use of lower hybrid current drive as a steady-state technique is a natural extension of the program. An efficiency calculation shows that 1-2 MW of rf power will be required to obtain PPCD-like conditions. Ray tracing shows that an antenna structure capable of launching a slow wave at 800 MHz and an $n_{\|} \simeq 7.8$ from the inboard side should allow for wave absorption in the desired location.

The lower hybrid project on MST has been initially tasked with determining the feasibility of using LHRF to drive enough current to improve confinement on par with the transient technique of PPCD. With an estimate of the required power necessary to

alter the current profile, the question turns to designing an antenna with the following properties: it must launch a wave with the correct polarization along the magnetic field, and it must have the required $n_{\|}$ spectrum. It must also have a a geometry which will satisfy the particular constraints of MST. Chapter 2 will show that an antenna based on an interdigital-line will fulfill these requirements and describes the constructed antenna with its diagnostics and transmission system. Additionally, the power handling of the antenna design will be tested as a step towards determining the full size of the rf system necessary for improved confinement.

No less important is characterizing the coupling of the interdigital-line antenna to the plasma. Without good coupling, the antenna will not efficiently transfer power to the plasma which increases the source power required for a current drive system. Chapter 3 gives an overview of plasma coupling theory for a traveling wave antenna and compares it to experiment and simulation. We show that the antenna is well loaded in a variety of plasma conditions with the plasma density the most influential parameter for antenna performance. The Chapter also discusses the use of an antenna limiter and local gas puffing to externally control antenna coupling.

A powerful non-pertubative technique to measure the effects of injected rf waves is the use of x-ray diagnostics. This work will make use of a set of hard x-ray detectors in an attempt to measure any rf-induced fast electrons associated with current drive. Chapter 4 will first describe the diagnostic and analysis method. While current drive at the present power level cannot be confirmed with the hard x-ray diagnostic, observations will be presented including a toroidal asymmetry in high energy x-ray production. This asymmetry can be best explained by an interaction of bulk electrons

with the near field of the antenna. Monte Carlo simulations will be performed to support this hypothesis, and an accounting will be done to confirm that the power loss to these fast electrons is not significant. The results are summarized and possible future work is described in Chapter 5.

Bibliography

[1] Porkolab, M. RF heating and current drive in magnetically confined plasma: a historical perspective. In P. M. Ryan and D. Rasmussen, editors, *Radio Frequency Power In Plasmas: 17th Topical Conference on Radio Frequency Power in Plasmas*, volume 933, pp. 3–12. AIP, 2007.

[2] Najmabadi, F., et al. The TITAN reversed field pinch fusion reactor study – the final report. Technical Report UCLA-PPG-1200, UCLA, 1990.

[3] Taylor, J. B. Relaxation of toroidal plasma and generation of reverse magnetic fields. *Phys. Rev. Lett.*, **33**(19):1139–1141, 1974.

[4] Anderson, J. K., et al. Dynamo-free plasma in the reversed-field pinch: Advances in understanding the reversed-field pinch improved confinement mode. *Physics of Plasmas*, **12**(056118), 2005.

[5] Chapman, B. E., et al. Modifications to the edge current profile with auxiliary edge current drive and improved confinement in a reversed-field pinch. *Physics of Plasmas*, **7**(9):3491–3494, 2000.

[6] Caramana, E. J., Nebel, R. A., and Schnack, D. D. Nonlinear, single-helicity magnetic reconnection in the reversed-field pinch. *Physics of Fluids*, **26**(5):1305–1319, 1983.

[7] Sarff, J. S., et al. Fluctuation and transport reduction in a reversed field pinch by inductive poloidal current drive. *Phys. Rev. Lett.*, **72**(23):3670–3673, 1994.

[8] Chapman, B. E., et al. Improved-confinement plasmas at high temperature and high beta in the MST RFP. *Nuclear Fusion*, **49**(10):104020 (10pp), 2009.

[9] Sovinec, C. and Prager, S. Magnetohydrodynamic effects of current profile control in reversed field pinches. *Nuclear Fusion*, **39**(6):777–790, 1999.

[10] Schnack, D. D., et al. Semi-implicit magnetohydrodynamic calculations. *Journal of Computational Physics*, **70**(2):330 – 354, 1987.

[11] Uchimoto, E., et al. Lower-hybrid poloidal current drive for fluctuation reduction in a reversed field pinch. *Physics of Plasmas*, **1**(11):3517–3519, 1994.

[12] Sarff, J. S. The RFP: plasma confinement with a reversed twist, 1997. Invited Tutorial, APS DPP Meeting.

[13] Dexter, R. N., et al. The Madison Symmetric Torus. *Fusion Technology*, **19**:131–139, 1991.

[14] Fisch, N. J. Theory of current drive in plasmas. *Reviews of Modern Physics*, **59**(1):175–234, 1987.

[15] Fisch, N. J. Confining a tokamak plasma with rf-driven currents. *Phys. Rev. Lett.*, **41**(13):873–876, 1978.

[16] Hasegawa, A., et al. Study of reversed field pinch with surface current. *Journal of the Physical Society of Japan*, **53**(4):1316–1325, 1984.

[17] Shiina, S., Kondoh, Y., and Ishii, H. Partial current drive by a fast magnetosonic wave in reversed field pinch plasma. *Nuclear Fusion*, **34**(11):1473–88, 1994.

[18] Ehst, D. A. and Karney, C. F. F. Approximate formula for radio-frequency current drive efficiency with magnetic trapping. *Nuclear Fusion*, **31**(10):1933–1938, 1991.

[19] Hokin, S., et al. Confinement improvement with RF poloidal current drive in the reversed field pinch. *Nuclear Fusion*, **34**(11), 1994.

[20] Harvey, R. W. and McCoy, M. G. The CQL3D Fokker-Planck code. Technical Report GA-A20978, General Atomics, 2005.

[21] Bonoli, P. Linear theory of lower hybrid heating. *IEEE Transactions on Plasma Science*, **12**(2):95–107, 1984.

[22] Swanson, D. G. *Plasma Waves*. IOP Publishing, 2nd edition, 2003.

[23] Pinsker, R. *Fast wave current drive experiments on the Princeton Large Torus*. Ph.D. thesis, Princeton University, 1988.

[24] Bonoli, P. T. and Ott, E. Toroidal and scattering effects on lower-hybrid wave propagation. *Phys. Fluids*, **25**(2):359–375, 1982.

[25] Smirnov, A. P. and Harvey, R. W. The GENRAY ray tracing code. Technical Report CompX-2000-01, Ver. 2, CompX, 2003.

Chapter 2

The Lower Hybrid System on MST

The lower hybrid system on MST is comprised of all the hardware necessary for generating, transmitting, and launching lower hybrid waves. The unique constraints of MST neccesitate a novel antenna design and will be the focus of this chapter. We will begin with an in-depth look at the MST lower hybrid antenna, including its design considerations, theory of operation and modeling. Next in the discussion will be the backend power generation and transmission system. The diagnostics pertaining to the operation of the antenna circuit are in this chapter while plasma diagnostics are dealt with later. Lastly, measurements of the system without plasma are presented.

2.1 Antenna

The choice of design for the lower hybrid antenna is driven almost entirely by constraints. As described in §1.4, we must first and foremost have an antenna that can

launch a slow wave at high enough $n_{\|}$ to avoid an accessibility cutoff and an appropriate frequency for absorption in the target region. These two constraints alone will force a geometry of a size necessary to support a given wavelength and propagation constant. Finally, while not a technical constraint, the laboratory was given the opportunity to obtain rf sources in the UHF (pretuned to 800 MHz) at no cost.

The constraints posed by MST's vacuum vessel are just as onerous. MST uses a conducting shell for plasma stabilization so a porthole large enough to accommodate the now-standard grill antenna [1] would cause unacceptably large field perturbations [2]. Second, the conducting shell is close-fitting to the plasma, so the radial extent of the antenna must be small so as not to perturb the plasma and act as a limiter. This extent is around 2 cm on the inboard side of the machine and less still on the outboard side. Additionally, while the machine vacuum vessel is a clamshell and can be disassembled for easier interior access [3], the time penalty for disassembly is too high for demonstrating the antenna concept. Because of this and the porthole constraints, the transverse dimensions of the antenna must be small enough to fit through the largest porthole on MST — 11.43 cm in diameter.

These restrictions, taken together, lead to the choice of an interdigital-line traveling wave antenna. This particular antenna design is novel for plasma applications, but it has forebears. The stripline antenna [4] or Yagi-Uda array antenna [5] which begat the modern ICRF strap antennas similarly use conductors phased to set up the desired propagation constant. With these, however, each conductor is fed by its own power generator. True traveling wave antennas such as the combline [6,7] and fishbone antennas [8] are much closer cousins to the interdigital-line concept, though these an-

tennas launch fast waves rather than slow waves and at much lower frequencies. The remainder of the section will describe how an interdigital line operates as well as how an antenna utilizing an interdigital line can satisfy the constraints imposed by MST.

2.1.1 The Interdigital Line

The interdigital circuit was developed in the 1950's as an alternative to helix structures in traveling-wave amplifiers [9]. In its most basic sense the combline or interdigital-line structure uses a set of parallel resonators that are capacitively and/or inductively coupled to propagate a wave down the structure. The combline has all its resonators grounded on one end and open on the other while the interdigital line's resonators are interlaced with each end alternately grounded or open-circuited. It can be thought of as a pair of comblines that are interleaved. A section of the circuit is shown in Figure 2.1.

The line can be situated over a groundplane or alternatively between a set of grounded planes so as to change the impedance of the circuit and for structural integrity. The MST antenna has a pair of grounded planes with an aperture cut in the plasma-facing plane so that the fields on the structure can couple to the plasma. The length and spacing of the conductors determines what operating frequency the structure can support and defines a dispersion relation. This dispersion relation stipulates the phase advance and thus the propagation constant of the traveling wave.

To elucidate the theory of the antenna, we start with an idealized interdigital line. We ignore the ends of the resonators for the moment and imagine those parallel conductors — which we will also call rods or "fingers" — as semi-infinite in the y-direction.

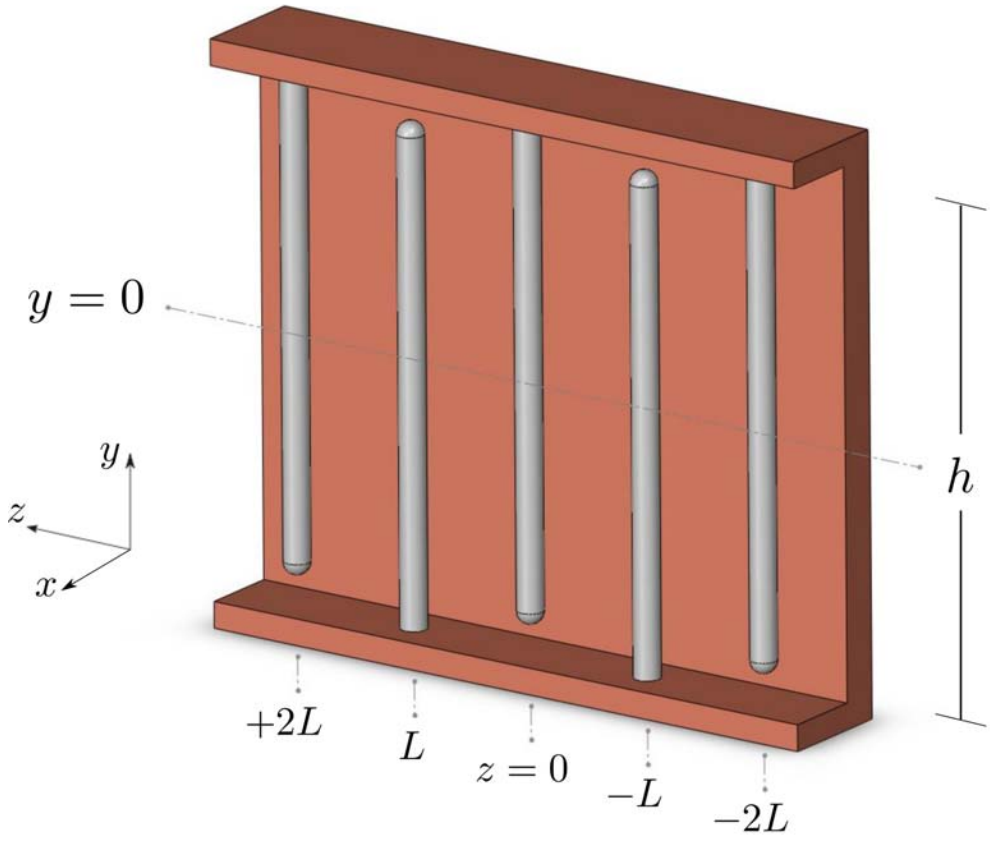

Figure 2.1: Schematic of an interdigital line shown here without a grounded frontplane. Rods are L apart and h long.

Taking a single rod and the groundplane, we have a pair of conductors whose cross-section is uniform. A wave traveling in the y-direction with no field components in that direction satisfies Maxwell's equations and can be classified as a TEM mode. (Since the resonators are not of infinite length, these are actually quasi-TEM modes since y-components become non-zero at the ends, but this can be neglected for the time

being.) With $E_y = H_y = 0$, the wave satisfies the transverse Laplace equation:

$$\nabla_t^2 \varphi(x, z) = 0 \tag{2.1}$$

where $\nabla_t^2 = \partial^2/\partial x^2 + \partial^2/\partial z^2$ and $\varphi(x, z)$ is the potential at a point (x, z) with respect to the ground plane.

Given a mode of a single frequency ω and a propagation constant $\beta = k = 2\pi/\lambda$, we have two waves for this mode, traveling at the speed of light, one traveling in the $+y$ direction and one traveling in the $-y$ direction. The potential in three dimensions can be written as

$$\varphi(x, y, z, t) = F(x, z)\left(Ae^{-i\beta y} + Be^{i\beta y}\right)e^{-i\omega t} \tag{2.2}$$

where $\nabla_t^2 F = 0$. For the remainder of the section, we will look at only the variation of the waves in the y direction, and the common factor $e^{-i\omega t}$ will be suppressed.

Bringing the ends of the rods back into the picture, we have each rod in the line alternatively shorted on one end and open-circuited on the other. Designating $V_m(y)$ and $I_m(y)$ as the voltage and current on the m'th rod, this description corresponds to the set of boundary conditions:

$$V_{2n}\left(\frac{h}{2}\right) = V_{2n+1}\left(-\frac{h}{2}\right) = 0 \tag{2.3}$$

and

$$I_{2n}\left(-\frac{h}{2}\right) = I_{2n+1}\left(\frac{h}{2}\right) = 0 \tag{2.4}$$

where $n \in \mathbb{Z}$.

If we have a wave propagating along the structure transverse to the conductors (in the z-direction), and the periodicity of the boundary conditions is N (the boundary conditions are repeated every N'th rod), then N modes are required to satisfy the constraints [10], and follows from Floquet's theorem [11, 12]. For each of these modes ν, the rod-to-rod phase advance is

$$\theta_\nu = \theta + 2\pi\nu/N, \qquad \nu = 0, 1, 2, \ldots, N-1 \tag{2.5}$$

where θ will be determined by a dispersion relation which we will derive. For the case of the interdigital line, the periodicity is $N = 2$ since a "unit cell" contains a pair of resonators. Applying (2.5), we need two different wave modes: one that propagates as $e^{-im\theta}$ and the other as $e^{-im(\theta+\pi)}$ where $z = mL$, $m \in \mathbb{Z}$.

The voltage on the m'th rod can be written as

$$\begin{aligned} V_m(y) = &\left(A_1 \cos\beta y + A_2 \sin\beta y\right) e^{-im(\theta+\pi)} \\ &+ \left(A_3 \cos\beta y + A_4 \sin\beta y\right) e^{-im\theta} \end{aligned} \tag{2.6}$$

and since the current is related to the voltage by the characteristic impedance Z of the rod for each mode,

$$\begin{aligned} I_m(y) = &\frac{i}{Z(\theta+\pi)} \left(-A_1 \sin\beta y + A_2 \cos\beta y\right) e^{-im(\theta+\pi)} \\ &+ \frac{i}{Z(\theta)} \left(-A_3 \sin\beta y + A_4 \cos\beta y\right) e^{-im\theta}. \end{aligned} \tag{2.7}$$

The characteristic impedance is a function of both the geometry of the interdigital line (i.e. shapes of the conductors and distances between conductors) as well as the phase advance between resonators. Applying the voltage boundary conditions (2.3) to (2.6) eliminates A_3 and A_4. Then we have for A_1 and A_2:

$$A_1 = -A_4 \tan\left(\beta \frac{h}{2}\right) \tag{2.8}$$

$$A_2 = -A_3 \cot\left(\beta \frac{h}{2}\right). \tag{2.9}$$

Applying the current constraints (2.4) to (2.7) yields two waves

$$\text{Wave } 1 : A_2 = 0, \qquad \tan^2\left(\beta \frac{h}{2}\right) = \frac{Z(\theta+\pi)}{Z(\theta)} \tag{2.10}$$

$$\text{Wave } 2 : A_1 = 0, \qquad \cot^2\left(\beta \frac{h}{2}\right) = \frac{Z(\theta+\pi)}{Z(\theta)} \tag{2.11}$$

which are in fact identical in that each has the same voltage and current distributions. As this is the case, we arbitrarily choose $A_2 = 0$. Then

$$\tan^2\left(\beta \frac{h}{2}\right) = \frac{Z(\theta+\pi)}{Z(\theta)} \tag{2.12}$$

is a dispersion relation between the (phase) length of the resonators and θ, the phase advance of the zeroth mode.

Applying the complete set of boundary conditions we have for the voltage and

current on each resonator:

$$V_m(y) = A\cos(\beta y)\, e^{-im(\theta+\pi)} - A\cot\left(\beta\frac{h}{2}\right)\sin(\beta y)\, e^{-im\theta} \tag{2.13}$$

$$I_m(y) = -A\frac{i}{Z(\theta+\pi)}\sin(\beta y)\, e^{-im(\theta+\pi)} - A\frac{i}{Z(\theta)}\cot\left(\beta\frac{h}{2}\right)\cos(\beta y)\, e^{-im\theta}. \tag{2.14}$$

Even without solving for the characteristic impedance of the line, one observation can be made for the voltage and current near the center of the rods. Near the center, the $\sin(\beta y)$ term is small and we have $\arg(V) \sim -m(\theta+\pi)$ and $\arg(I) \sim \pi/2 - m\,\theta$. The phase advance for the voltage and current from rod m to rod $m+1$ for a given value of θ are

$$\phi_V \equiv \arg(V_{m+1}) - \arg(V_m) = -(\theta+\pi) \tag{2.15}$$

$$\phi_I \equiv \arg(I_{m+1}) - \arg(I_m) = -\theta \tag{2.16}$$

and are shown in Figure 2.2. An interesting result from this simple consideration is that the voltage and current waves have *opposite* (but not necessarily equal) phase velocities along the axis of the interdigital line, and for $0 \leq \theta < \pi$ the voltage — and thus the electric field — travels backwards toward the end of the line being fed the power.

Lastly we note that the because the characteristic impedance is invariant to the

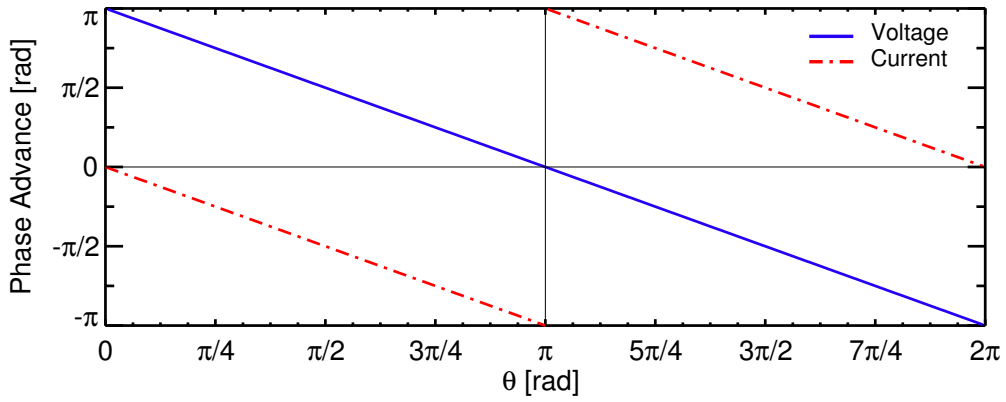

Figure 2.2: The phase advance of the voltage and current on the interdigital line for values of θ. A positive [negative] phase advance corresponds to a backward [forward] wave.

direction of the wave as well as to a phase addition of $2\pi n$, we have:

$$Z(\theta) = Z(-\theta) = Z(\theta + 2\pi n) \tag{2.17}$$

$$Z(\theta + \pi) = Z(\theta - \pi) = Z(\pi - \theta). \tag{2.18}$$

Equations (2.17) and (2.18) with the dispersion relation (2.12) imply that if we choose $\theta = \pi/2$, then $Z(\theta) = Z(\theta + \pi)$ and then $\beta h = \pi/2$, or $h = \lambda/4$. So by choosing the resonators to be one-quarter of a wavelength long, the phase advance is $\pi/2$ and is independent of the impedance of the circuit. Plugging this θ in to (2.6) and (2.7), we

have

$$V_m(y) = A\left(\cos(\beta y)\ e^{im\pi/2} - \sin(\beta y)\ e^{-im\pi/2}\right) \tag{2.19}$$

$$I_m(y) = -A\frac{i}{Z_0}\left(\sin(\beta y)\ e^{im\pi/2} + \cos(\beta y)\ e^{-im\pi/2}\right) \tag{2.20}$$

With $\theta = \pi/2$, we see that for both the voltage and current each has two counter-propagating waves moving at the same phase velocity. At the ends of the rods, these waves have the same magnitude and a standing wave forms. At the center of the rod where $\sin(\beta y)$ is small however, the cosine term dominates, and we see the same behavior that we saw in Figure 2.2.

2.1.2 Impedance of the Interdigital Line

To find the characteristic impedance of the interdigital line and thus the solution to the dispersion relation (2.12), we first calculate the electric field directly outside a conductor with surface charge density σ using Gauss' Law [13]:

$$\mathbf{E} = \frac{\sigma}{\epsilon}\hat{n} \tag{2.21}$$

where ϵ is the permittivity of the dielectric medium and $\hat{n}$ is the normal to the surface. Since we have $\mathbf{E} = -\nabla\varphi$, we can reformulate (2.21) as

$$\frac{\partial\varphi}{\partial n} = -\frac{\sigma}{\epsilon}. \tag{2.22}$$

The total (normalized) charge per unit length can be calculated by integrating

(2.22) around the boundary of the conductor:

$$q = -\epsilon \int_{\Gamma} \nabla\varphi \cdot \hat{n}, \tag{2.23}$$

and then we can calculate the capacitance, $C = q/V$, where V is the voltage on a resonator. The characteristic impedance of a uniform transmission line in TEM mode is related to its shunt capacitance [14] by

$$Z_0 = \frac{\eta}{\sqrt{\epsilon_r}\,(C/\epsilon)} \tag{2.24}$$

where ϵ_r is relative dielectric constant, and η is the impedance of free space.

We still require the potential φ as a starting point. In this case we want to solve Laplace's equation for our geometry. The partial differential equation is difficult to solve analytically except in very simple geometries, so we turn to finite element methods. See Appendix A for details.

For the problem, we require the geometry as well as the boundary conditions. Two different general forms of the interdigital line have been examined: one where the interdigital resonators are situated over a single ground plane and open on the other side as in Figure 2.1 — the "open" type, and the other where the resonators are sandwiched between a pair of grounded planes — the "closed" type. The addition of a second ground plane in the closed type adds to the capacitance of an individual resonator.

In both of these cases, the ground planes are set to $\varphi = 0$ and the resonators are set to a fixed voltage. The m'th resonator will be given a particular voltage depending

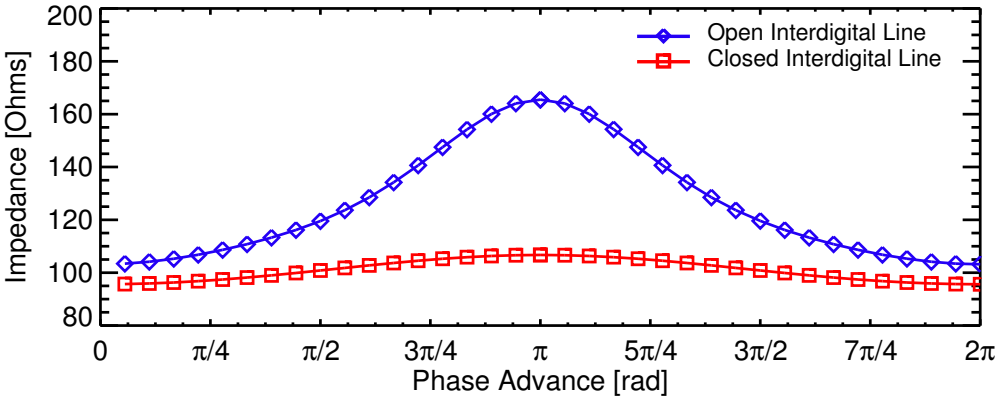

Figure 2.3: The impedance of the interdigital line relative to the rod-to-rod phase advance. Resonators are 2.38 mm in diameter, the distance from the center of the resonator to the groundplane[s] is 5 mm, and the center-to-center resonator distance is 12 mm.

on the phase advance:

$$\varphi_{\mathrm{rod}_m} = \cos\left(m\phi + \delta\right), \tag{2.25}$$

where ϕ is the phase difference between adjacent resonators and δ is an arbitrary constant to avoid voltage nodes. Solving for φ using the finite element code, we can apply (2.23) and (2.24) to calculate the impedance for a given phase advance. Figure 2.3 shows the results for both the closed and open interdigital models. From the inverse relationship between impedance and capacitance, it is not surprising that the open interdigital line has a higher overall impedance than the closed line. The data also shows that the impedance is symmetric about $\phi = \pi$ and verifies that when $\phi = \pi/2$, then $Z(\theta) = Z(\theta + \pi)$ as we calculated in the previous section. With the impedance and the dispersion relation in (2.12), we can relate the phase advance to the length of

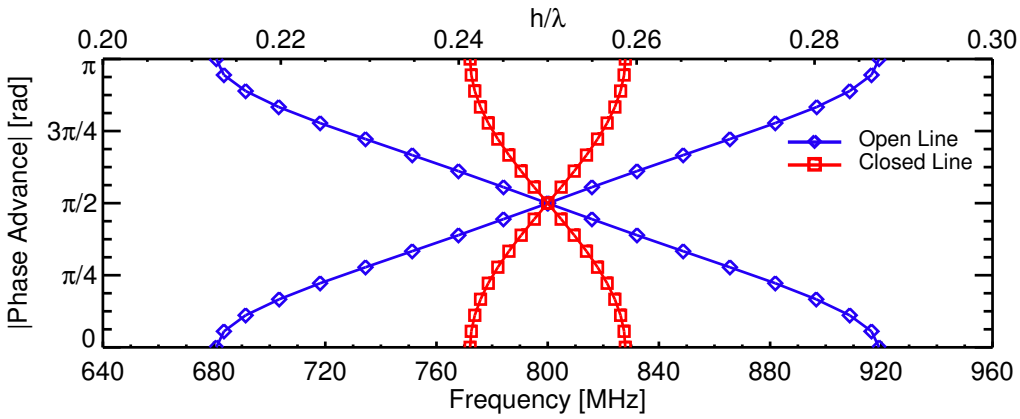

Figure 2.4: The phase advance of the interdigital line relative to the normalized resonator length. The frequency dependence is given for $h = 93.75$ mm, one-quarter of the vacuum wavelength at 800 MHz. The curves with negative gradients correspond to the backwards-traveling $(\theta + \pi)$ mode.

the resonators normalized to the wavelength. This relation is shown in Figure 2.4.

2.1.3 Observations

The previous two sections show that for any non-zero phase advance from rod to rod, the current and voltage waves (and thus the electric and magnetic field waves) propagate down the structure (in the z-direction) in opposite directions. This conclusion is a bit counter-intuitive, since it would seem to violate Maxwell's laws. We started the derivation with the assumptions that the structure propagates an electromagnetic wave transverse to the parallel conductors (the rods) forming it *and* that the field can be represented by TEM modes along those conductors. Walling [10] points out that these assumptions are actually inconsistent. In fact, the energy flow down the structure occurs only at the ends of the resonators rather than in the middle. Thus the "wave"

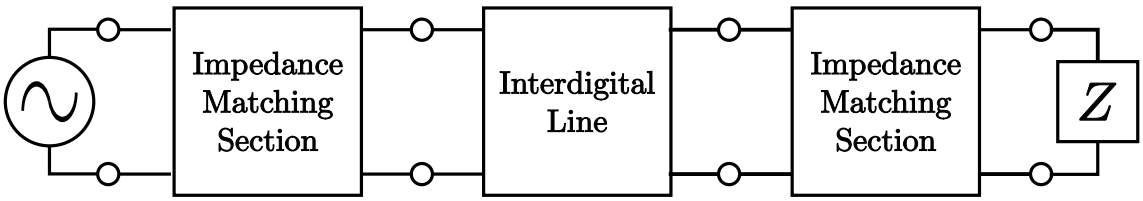

Figure 2.5: The antenna as a transmission line circuit.

traveling down the center of the structure is only a wave in the sense that there is a phase structure along the line that advances in time.

Despite that rod-to-rod energy transfer occurs at the ends of the rods, if the length of the conductors is large relative to their rod-to-rod separation then most of the energy stored in the fields will be in the region where the TEM approximation holds. In this region — with $\sin(\beta y) \ll 1$ — the voltage, and thus the electric field, is large only in the $\theta + \pi$ mode. The wave travels mostly in a single direction near the z-axis of the interdigital line.

2.1.4 The Antenna Circuit

Given the theory of the interdigital line, we can now construct an antenna that can launch a directional wave of 800 MHz at an $n_{\|} \sim 7.8$ and satisfies the required geometrical constraints. To actually perform a task, the antenna must also be connected to and fed by a power generation system. The antenna and its power feeds can be described as a transmission line circuit and is shown in Figure 2.5.

The interdigital line will be the launching section of the antenna. At an operating frequency of 800 MHz, a quarter-wave antenna would require resonators to be 93.75

mm long. 5 mm wide side rails like those in Figure 2.1 serve as attachment points for the resonators. So that the open-circuited end of the resonator is in fact open, the cavity formed between the side rails and groundplanes is wider than the resonators are long, chosen to be 95 mm. With the addition of 3.175 mm thick boron nitride cladding for protection, the antenna will still be narrow enough to fit through the largest porthole on MST, a requirement for installation [15].

Because the physical antenna has side rails, an additional source of capacitance exists that is not in the TEM model of the interdigital line. A finite element and capacitance solver [16] was used to estimate the contribution to the self-capacitance of the resonator from the side rail. With the additional capacitance, the length of the resonator was changed to 92.1 mm to compensate and move the phase advance back to $\pi/2$ [17].

Using an "open" interdigital line with a single ground plane as described in §2.1.2 will allow coupling of the fields on the line to the plasma. However, the open geometry exposes the resonator-ends where the two counterpropagating modes form a standing wave. Since we want to launch a directional wave, this is not ideal. On the other hand, a "closed" geometry is useless as an antenna, since no power can be coupled. A hybrid design that has an aperture cut into the ground plate proximate to the plasma that covers the ends of the rods and exposes the center where $\sin(\beta y) \ll 1$ will give the best directionality. The width of the aperture is chosen so that minimum ratio of the two mode amplitudes that is seen by the plasma is about $4:1$.

The height of the antenna is only slightly less prescribed than its width. Its height must be such that it does not protrude into the plasma, and it must not be too tall to

fit through the circular porthole. A second consideration is that a large characteristic impedance by definition keeps the voltage to current ratio high. Doing this will accomplish two goals. First, for a given input power the smaller current will reduce ohmic heating — and possible melting — of the antenna conductors, especially the resonators which will carry most of the current and have relatively small dimension. Second, a large impedance will reduce the competition between the magnetic and electric fields in coupling to the plasma. Ordinarily this would not be an issue, but since the voltage and current waves move in the opposite directions, this becomes relevant. A cavity height of 10 mm with resonator diameter of 2.38 mm will give an impedance of $\sim 100\Omega$ in the closed geometry.

To launch a wave at the required $n_{||}$, we need to specify the propagation constant. The phase velocity of a traveling wave on the line is

$$v_\phi = \frac{\omega}{k_z} = \frac{\omega\, L}{\theta \bmod \pi}. \tag{2.26}$$

For the interdigital line, setting a particular k_z amounts to prescribing the phase advance and spacing of the resonators. For 800 MHz and a target $n_{||}$ of ~ 7.8, a quarter-wave antenna requires a rod spacing of 12 mm.

The material for the antenna body was chosen to be copper for its conductivity and machinability. For the resonators, molybdenum is used instead of copper to minimize sputtering from multipactor or plasma interaction. For the same reason, the front plane of the antenna is faced by a thin sheet of molybdenum. Additionally, boron nitride limiters are used to protect the antenna from general plasma interaction.

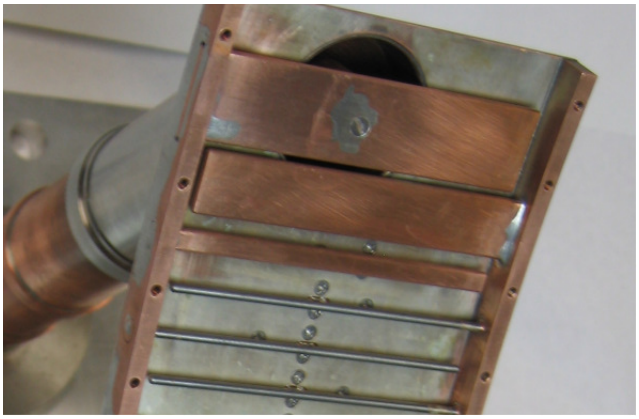

Figure 2.6: The impedance matching section for port 1 of the MkIII antenna with the frontplane removed. The characteristic impedance for the straps are approximately 35, 50, and 70 Ω. The attachment point of the feed to the large strap is 40 mm from the shorted end. Note that the backplane is cut away to accommodate the transmission line.

The generator and load and their associated transmission lines have a nominal characteristic impedance of 50Ω, and as Figure 2.3 shows, the interdigital line itself was chosen to have an impedance of over 100Ω. To prevent large reflections due to the impedance mismatch we have a pair of impedance matching sections between the coaxial feed line and interdigital line. A matching section consists of a set of resonators similar to the rods in the interdigital line, except that they are rectangular "straps" to provide more surface area, increasing their capacitance and thus reducing their characteristic impedance. Multiple straps are used in a similar fashion to the use of multisection quarter-wave transformers where the impedance is stepped up geometrically to increase the bandwidth [18]. The MkII antenna has a pair of straps, while the MkIII antenna uses three to improve the match. A photograph of a MkIII matching section is shown in Figure 2.6.

The transition from the transmission line to the first section of the impedance transformer is accomplished by tapping the first or feed strap at the point on the resonator where the voltage to current ratio of the backwards and forward waves (along the resonator) matches the characteristic impedance of the transmission line. In the case of a isolated resonator, this point can be determined by matching the input impedance equations of an open-circuit and short-circuited transmission line. A coupled resonator — the second stage of the matching section — adds a complication. The necessity to cut away part of the ground plane to accommodate a coaxial line with a diameter a significant percentage of the resonator length makes the problem intractable without using 3D modeling or trial-and-error.

One of the major advantages of the interdigital antenna concept is that it requires only two (small) feed ports, dovetailing well with the limited port access of MST. The feeds on either end of the antenna are coaxial transmission line. The inner conductor is attached to the first matching strap while the outer conductor attaches to the grounded backplane of the antenna. the MkII antenna used standard $^{7}/_{8}$" coax feeds because access was restricted to $1^{1}/_{4}$" diameter portholes. The MkIII antenna uses $1^{5}/_{8}$" coax after gaining access to 2" portholes. The increase in feed size should allow an increase of power handling above 300 kW. Since the antenna proper is under vacuum and the transmission line is not, vacuum feedthroughs are required. Each of these are several centimeters down the transmission line from the backplane.

A diagram of the MkIII antenna with the interdigital line, matching sections and feeds is shown in Figure 2.7. In Figure 2.8, the antenna is shown as constructed on the bench directly before installation. The upper three-quarters of the antenna including

Figure 2.7: A semi-transparent drawing of the MkIII antenna without limiter tiles.

Figure 2.8: Photograph of MkIII antenna on the bench before installation.

the feed port #1 are behind a box port on MST and so sit under machine vacuum. Feed port #2 does not, and so requires its own port flange to maintain vacuum integrity.

2.2 Antenna Modeling

While several packages and codes have been used to model different aspects of the antenna including SPICE and RANT3D [19], generally these have suffered from deficiencies that prevent an adequate prediction of the overall performance of the antenna. Recently, however, a pair of more sophisticated commercial software packages has shown good agreement with experimental measurements.

CST's Microwave Studio™ (MWS) is a general-purpose electromagnetic solver that

uses the Finite Integration Technique (FIT), which solves the integral form of Maxwell's equations [20]. The package was acquired late in the design phase of the MkIII antenna, and though it was used to configure the impedance matching sections, more full use of the code was limited to a *post-hoc* verification of an already-fabricated antenna.

The solver numerically solves the equations within a finite domain and can use multiple grid shapes, though for the present simulations, a hexahedral mesh is used. Depending on the problem type, either transient, frequency domain, or eigenmode solvers can be used. For the interdigital antenna, either the transient or frequency domain solvers are appropriate. The transient solver uses central differences to calculate the time derivatives and then does time stepping using the leap-frog scheme. The frequency domain solver assumes $\partial/\partial t \rightarrow i\omega$ and so only solves for discrete frequencies. This solver is sufficient as our antenna is driven at a pure 800 MHz, and the antenna is highly resonant. Since we are interested in the antenna's bandpass characteristics, however, and the transient solver returns the behavior over a broad frequency range with little time penalty and allows open boundary conditions, we use the transient solver.

To monitor the voltages and fields on the antenna a set of virtual diagnostics can be used. The components of the electric and magnetic fields can be measured at a specific coordinate, or the entire vector field at a specific frequency can be measured. A voltage can be found by integrating along a prescribed path: in our case, the voltages of interest include between neighboring resonators as well as between a resonator and the antenna backplane. While current probes are not currently supported, a magnetic field probe can act as a proxy at least for a current phase diagnostic. In addition to

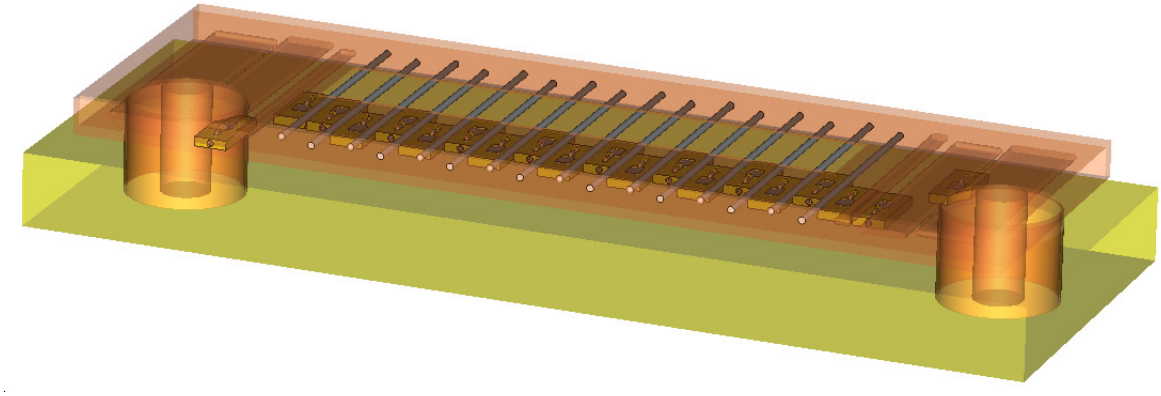

Figure 2.9: Microwave Studio flat model of MkIII antenna.

these simple diagnostics, the loop diagnostics can be modeled to verify their operation.

While the fabricated version of the antenna has been modeled, for most applications, a flattened version of the MkIII antenna is perfectly sufficient. A flat model has the advantages of being much simpler to (virtually) instrument, characterize, and mesh. For a given mesh density, a flat model simulation run takes approximately 4x less time. The model used is shown in Figure 2.9.

At the time of this writing MWS could not satisfactorily handle a cold plasma dielectric and so is limited to the vacuum solution. While this is an impediment to modeling the antenna response and coupling in plasma, the modeling is still useful in determining field strengths and the characteristics of the interdigital line.

COMSOL Multiphysics™ is a 3D Finite Element solver with multiple modules including an RF Module suitable for solving high frequency problems. Like Microwave Studio, both time domain and frequency domain solvers are available in COMSOL, though for this work, the frequency solver is used. Unlike Microwave Studio, COMSOL

allows the user to define arbitrary expressions on edges, surfaces, or subdomains as functions of x, y, and z. This capability will be used to model a cold plasma in front of the antenna. Figure 2.10 shows the vacuum and plasma subdomains of the antenna model that will be used.

The RF Module solves the general wave equation:

$$\nabla \times \left(\frac{1}{\boldsymbol{\mu}} \nabla \times \mathbf{E} \right) - k_0^2 \left(\boldsymbol{\epsilon_r} - j \frac{\boldsymbol{\sigma}}{\omega \, \epsilon_0} \right) \mathbf{E} = 0 \tag{2.27}$$

where $\boldsymbol{\mu}$, $\boldsymbol{\epsilon_r}$, and $\boldsymbol{\sigma}$ can be scalar or tensor expressions. For our case, $\mu \rightarrow 1$, and $\boldsymbol{\epsilon_r}$ is set to be the standard cold plasma dielectric tensor from (1.11) in the subdomain where we define the plasma. The conductivity is added as a damping term:

$$\sigma = \left(1 - (x/x_{ub})^{10}\right)^{-1/2} - 1, \tag{2.28}$$

where x_{ub} is the upper bound of the plasma subdomain. This damping is added to prevent reflections off the boundaries of domain, which are stipulated as perfect conductors.

The plasma model used will be a standard slab model, with $\mathbf{B} = \hat{\mathbf{z}} B \cos\theta + \hat{\mathbf{y}} B \sin\theta$. The density profile is a function only of the radial coordinate, x, and is defined as a vacuum gap followed by a density step and then a linear density gradient. Formally:

$$n_e(x) = \begin{cases} 0 & : \quad x < l_s \\ n_{e_0} + \frac{dn_e}{dx}(x - l_s) & : \quad x \geq l_s \end{cases} \tag{2.29}$$

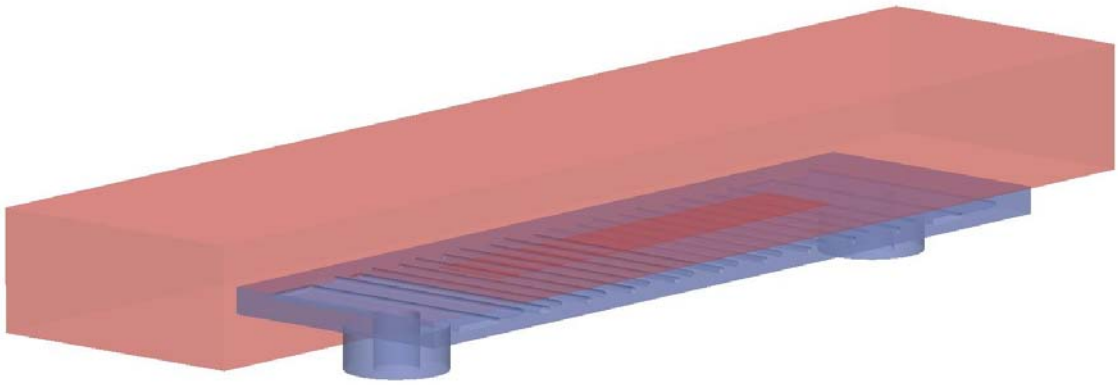

Figure 2.10: COMSOL model of flat MkIII antenna with vacuum subdomain in the antenna cavity and feeds and the plasma subdomain in the aperture and above the frontplane. The boundaries of the vacuum subdomain have the properties of copper or molybdenum, and the boundaries of the plasma subdomain are perfectly conducting.

where l_s is defined as the vacuum gap with $l_s = 0$ at the face of the antenna. This density profile is similar to those used with the SWAN code and others to model the coupling of grill antennas [21, 22]. In this case we add the vacuum gap term l_s to connect the modeling to the Golant theory to be discussed in §3.1. The flat antenna model from Microwave Studio is used as the COMSOL antenna, and similar voltage probes between the resonators and backplane are used to measure the response of the antenna to the plasma.

As an example, Figure 2.11 shows the electric field components at the antenna's midplane from a COMSOL simulation given a vacuum gap of 1 mm, a step of $n_{e_0} = 5 \times 10^{10}$ cm^{-3} and a density gradient $dn/dx = 1 \times 10^{11}$ cm^{-4}. Additional field plots are shown in Appendix B.

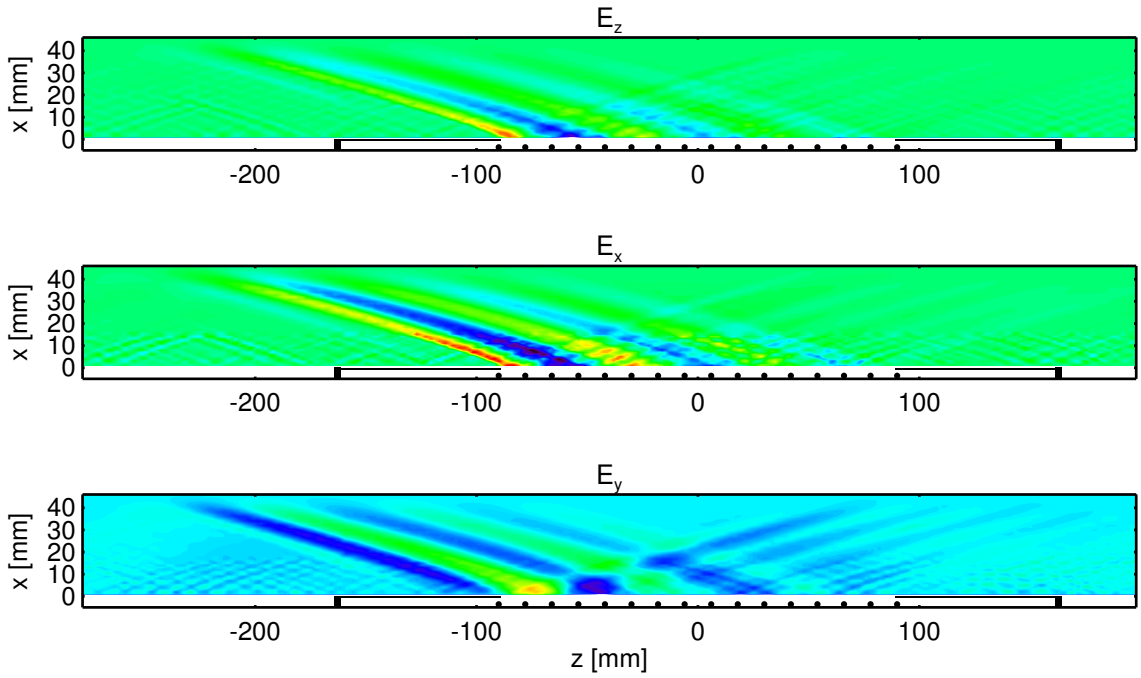

Figure 2.11: Electric field components on the antenna midplane from COMSOL simulation. A sketch of the antenna location is shown. Evident in the simulation are the resonance cones as the wave propagates into the plasma, the interference pattern caused by a small fraction of the power launched in the opposite direction, and the damping of the wave along the antenna as it couples into the plasma.

2.3 RF Power Generation

A Varian-955A 50 kW CW klystron on extended loan from PPPL is used as the lower hybrid system's primary amplifier. Designed to operate at 27 kV and a beam current of 8 A, the tube can be overdriven for high-power pulsed experiments to approximately 46 kV and 16 A. The klystron can be used within the frequency range of 694 to 850 MHz, but if tuned to deliver the gain required for $> 250\,\mathrm{kW}$ output, the bandwidth is reduced to $\sim$5 MHz of the chosen center frequency.

As the site does not have the requisite HV infrastructure to power the klystron, a pulse-forming network (PFN) was constructed to provide the necessary requirements. A schematic of the high power PFN is shown in Figure 2.12. The PFN is designed to deliver a square pulse of up to 50 kV to a 1000 Ω load for 30 ms. The nominal load for the klystron is 3 kΩ, so 3 such klystrons can be pulsed with the network. For the single klystron system, a recirculating water load doped with copper sulfate is placed in parallel to match the PFN. The circuit is modular so that by adding paired inductor/capacitor sections, the pulse length can be extended to 50 ms. The circuit is charged to 100 kV using a Glassman 30 mA power supply. A thyristor stack [23] acts as the switch to discharge the PFN. In the event of a reflection back from the load, a diode stack protects the power supply. Diagnostics monitor the voltage and current, and if more than ∼20 A of current are flowing to the klystron or if an arc is detected in the klystron, a crowbar circuit is fired with a second thyristor stack.

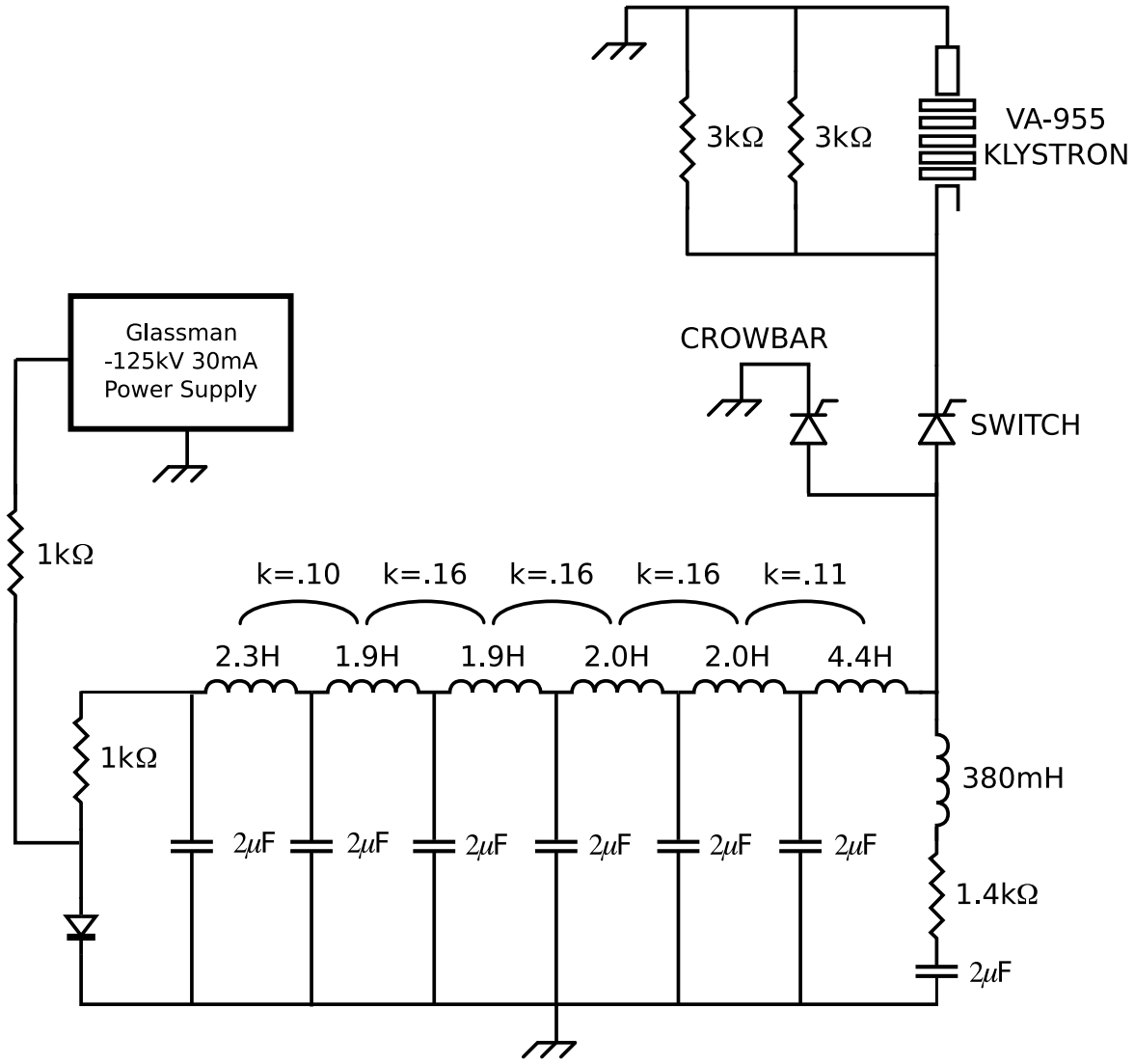

Figure 2.12: Schematic of pulse-forming network, power supply and klystron amplifier for the Lower Hybrid system.

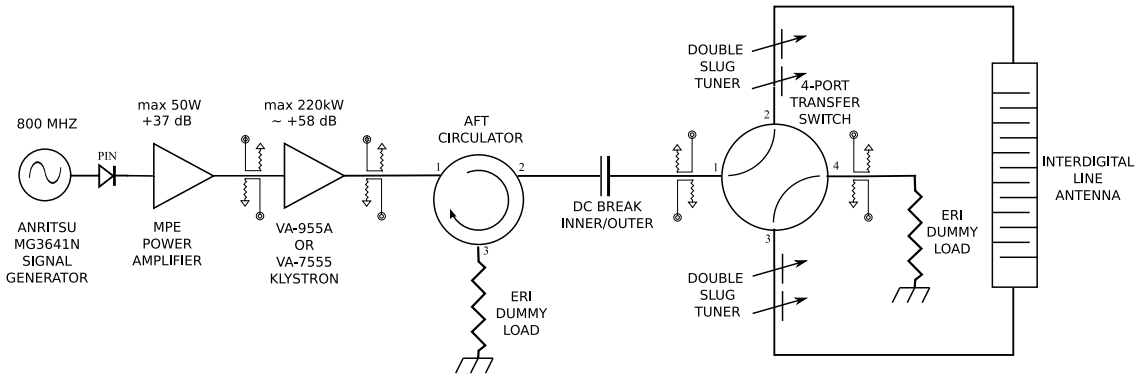

Figure 2.13: Schematic of the rf transmitter circuit.

2.4 The Transmission System

A transmission system is required to transmit the power from the rf generator to the antenna in MST. This system consists of the transmission line as well as its associated diagnostics and protection circuitry. The transmission system is illustrated in Figure 2.13.

The transmission line run consists of a run of approximately 200 feet of $3^1/_8$" coaxial transmission line up to and including the slug tuners. As alluded to in the previous section, the final run depends on which antenna is being used. For the MkII antenna, the $3^1/_8$" line is reduced and $^7/_8$" air-core Heliax™ is used to match the vacuum feedthrough size. This corrugated transmission-line has a nominal unpressurized peak power of 90 kW, though approximately 105 kW was achieved before uncontrollable arcing occurred — most likely in this line rather than in the antenna or vacuum feedthrough. The MkIII antenna uses $1^5/_8$" air-core Heliax rather than $^7/_8$" for increased power handling. Because of the reduced bend radius for the larger line, additional $1^5/_8$" rigid coax plumbing

is required for the final run beneath the machine vessel to the antenna on the lower inboard side.

A 4-port transfer switch allows either end of the antenna to be fed power. Any power not radiated to the plasma flows through the antenna to a dummy load. To improve the impedance match from the $50\,\Omega$ transmission line to the antenna, two pairs of $\lambda/4$ slug tuners — one pair for each feed direction — sit at the output ports of the switch. An inner and outer DC break prior to the 4-port switch isolates the rf power supply and the klystron vault from the MST machine area and vacuum vessel. Any reflected power from the antenna is absorbed by a second dummy load by way of a circulator, protecting the klystron.

The line is instrumented with a set of bidirectional couplers at the input and output of the klystron to monitor the amplifier's gain, and at the input and output of the antenna to monitor its performance. Arc detection is implemented with a circuit connected to the couplers at the input of the 4-port switch. If the ratio of reflected to forward power on the line exceeds a set value the arc detector trips the PIN diode at the output of the signal generator and shuts off power for $100\,\mu$s.

2.5 Power and Phase Diagnostics

Measurements of the rf power sourced to the antenna, the power flowing through it, and the power on the transmission lines are crucial for diagnosis of potential problems as well as producing feedback on how well the experiment is working. Power measurements on the transmission line are made using bidirectional couplers at the input

of the klystron, the output of the klystron but before the circulator, in the machine area cell directly before the 4-port switch leading to the antenna, and at the output of the antenna prior to the high-power matching load. On the antenna itself power measurements are made through 50Ω pickup loops embedded in the antenna backplane.

2.5.1 Bidirectional Couplers

The bidirectional coupler at the input of the klystron is a Narda™ coupler with ∼20dB of attenuation. The couplers on the transmission line are slug-type Jampro™ dual-directional couplers. Attenuation and directionality for these couplers can be independently adjusted. This type of coupler generally picks off about −60dB of the power in the transmission line. A calibration procedure of this type of coupler can be found in Appendix C.

2.5.2 Pickup Loops

Unlike in waveguide grills, where power and phase can be controlled and measurements can be made for each individual waveguide to diagnose the loading on the antenna, power flow along the traveling wave antenna is a function only of the microwave structure and plasma loading. In this case, power and phase sensors at various points along the antenna are important for diagnosing antenna performance.

For the MkII and MkIII antennas, small pickup loops are embedded in the antenna backplane underneath a resonator as shown in Figure 2.14a. The loop itself is a length of the inner conductor (bent to shape) of semirigid coaxial cable whose outer

conductor and dielectric has been stripped away. The conductor end is terminated by a 50Ω surface-mount chip resistor soldered to the end of the loop housing, shown diagrammatically in Figure 2.14b.

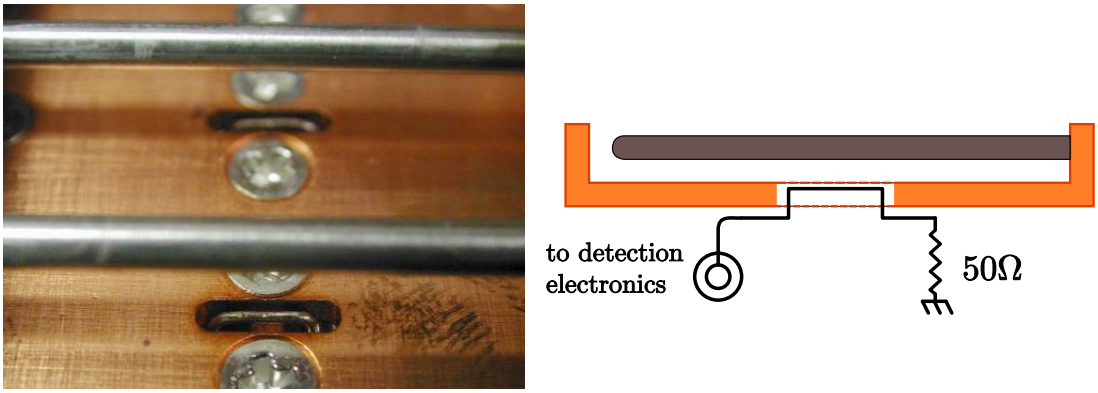

Figure 2.14: (a) A closeup of a couple of pickup loops embedded in the backplane of the MkII antenna. Each is placed directly underneath a resonator along the long axis. (b) A diagram of a pickup loop with antenna cross-section. Each loop is 50Ω terminated for impedance matching with the power and phase electronics.

As the antenna design evolved, there was a certain evolution in the loop diagnostics as well. The MkI antenna had no loop diagnostics. The MkII antenna had five loops underneath the middle five rods of the antenna. The MkIII antenna possesses 20 loops, one under each of the rods, and four offset from center underneath the straps of the impedance-matching sections.

The loop is coupled capacitively and inductively to the resonator above it. The amount of coupling is determined by the shape and location of the loop, the distance from the resonator, the shape of the resonator and the shape of the cavity. Figure 2.15 shows Microwave Studio modeling results for the attenuation of the pickup loop with respect to the height of the loop relative to the backplane. The loops as constructed

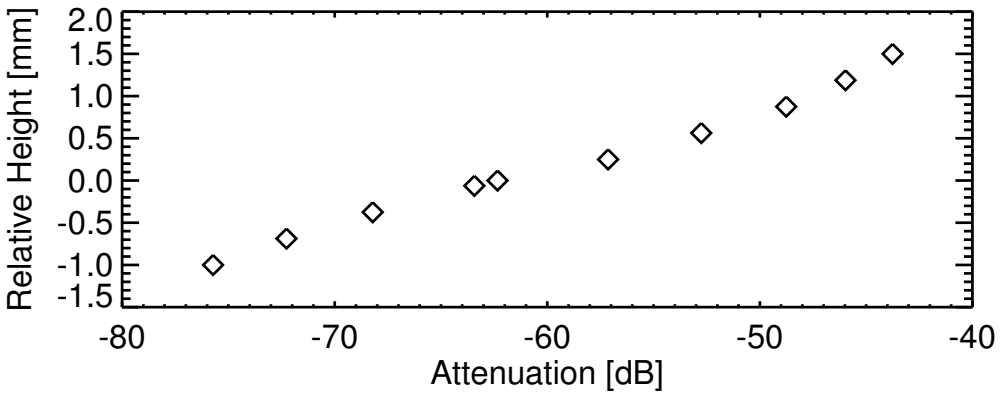

Figure 2.15: Relative attenuation of pickup loop couplers vs. the height of loop relative to the antenna backplane. Frequency is 800MHz. Zero height corresponds to the top of the loop conductor flush with the backplane.

show 10-15 dB less attenuation than the modeling, but the modeling demonstrates that a small change in loop height strongly affects the attenuation.

After the loops had been attached to antenna backplane during construction, a calibration jig with a single resonator was used to measure the attenuation of each loop relative to each other. Because of the coupling characteristics between resonators on the interdigital line, an absolute power measurement for each resonator is difficult. For investigating the power *flow* along the antenna, it is not strictly necessary; a relative measurement is adequate.

A calibration jig for the loops during antenna construction was not used for the MkII antenna. Instead a "pseudo-absolute" power calibration method is employed. A network analyzer's stimulus is applied to one antenna feed port with the other properly terminated. The loop output (which is being calibrated) is attached to the transmission port of the analyzer. In this way the attenuation of the loop can be

measured directly. It has the advantage that a real power measurement can be made relative to the input power of the antenna. The disadvantage is that any standing wave on the antenna — which may or may not be present during regular operation — is included in the calibration. ohmic losses in the structure also introduce a factor estimated from antenna scattering parameters and removed from the measurement. See Appendix C for more information.

2.5.3 Power and Phase Measurements

Power measurements on the MkII antenna used both HP 423B and HP8472B Schottky crystal diode detectors [24]. These detectors offered good sensitivity, but an operating range of only about 35 dB. Over most of this 35 dB, the output voltage is proportional to the input power (in dBm), but to make use of the full range, some curve fitting is required. As these are passive devices with output voltages on the order of mV, to make full use of the digitizer, a 60 dB isolation amplifier is used to boost the signal.

The diode detectors are relatively easy to use, but have been found to be susceptible to ambient rf noise. Additionally we want relative phase measurements for the loops which the diodes cannot do. Double-balanced mixers can be easily configured to act as phase detectors, but care must be taken to manage offsets. Instead of using both diodes and phase detectors in concert, a single hardware module with software processing was designed to get both amplitude and phase at significant cost savings.

Since directly digitizing the 800 MHz rf signal for the 40 ms of the experiment is cost prohibitive, frequency down-conversion is employed to get a signal that can be analyzed. Rather than being employed as a pure phase detector, ZP-2-S+ double-balanced mixers

from Mini-Circuits are used to produce an IF at a low enough frequency to be easily digitized. The down-conversion also preserves the phase, so the output signal can be used for both amplitude and phase measurements.

The digitizers used to record the IF output are Joerger 16 channel TR modules with 100 kΩ input impedance. They can use internal or external clock rates up to 10MHz. Each has 256k of memory per channel and 12 bits per sample. The voltage range is ±5 V. For the given pulse length of the experiment, a clock rate of 3MHz was chosen for a 200kHz signal from the mixer's IF. At 15 points per period, this gives fairly good resolution to make amplitude and phase measurements on the few μs scale.

The ZP-2-S+ mixer requires a local oscillator (LO) power of +7 dBm, has a maximum rf input power of 50 mW and an IF conversion loss of $\sim$ 6.5 dB at 800 MHz. The linear (in dB) region of the mixer however maxes out at ~ -3 dBm. With the conversion loss, the maximum usable IF output voltage is $\sim$ 1 mV. To make efficient use of the resolution of the digitizer, we designed an amplifier to boost our signal into the ±5 V range. The circuit is shown in Figure 2.16. The amplifier uses an AD826 op-amp in parallel mode to drive up to ±5 V at 50Ω load. A simple low pass filter with 3 dB cutoff at 1.94 MHz acts to attenuate the RF, LO, and their harmonics. The digitizer is isolated from the phase electronics by the use of a Mini-Circuits T1-6 1:1 rf transformer to prevent grounding issues. The rf signal (grounded at the machine vacuum vessel) is isolated by a inner-outer DC block.

The system is composed of three sets of eight IF amplifiers whose local oscillators are driven by a single signal generator at 800.2 MHz run through an RF amplifier and then split 3×8 ways. As the amplifiers are laid out four per PCB with a shared power

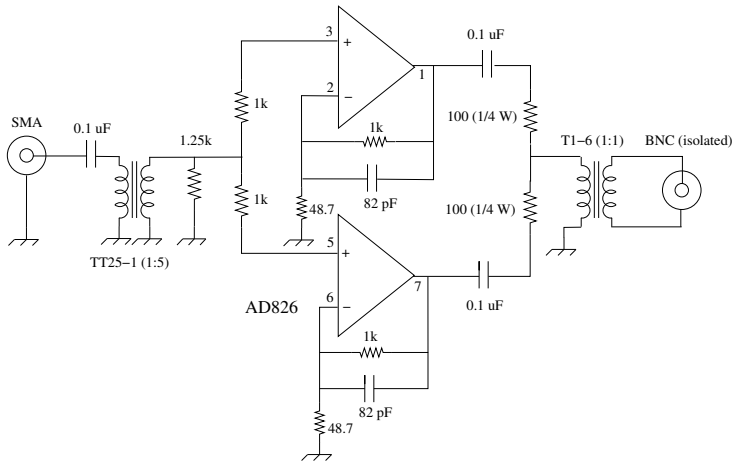

Figure 2.16: IF amplifier circuit. The output is isolated from the amplifier and it's power supply.

supply, there is some potential for cross-talk, but testing shows that with a neighboring amplifier running full-out at 10V pk-pk, only ∼10mV of cross-talk is seen.

To obtain the amplitude of the rf signal, we have:

$$v(t) = A(t)\cos\left(\omega_0\, t + \theta(t)\right), \tag{2.30}$$

where ω_0 is the modulating IF frequency and $A(t)$ is the desired amplitude, then we average the squared signal over the IF period,

$$\langle v^2(t)\rangle = \frac{1}{T}\int_0^T A^2(t)\cos^2\left(\omega_0\, t + \theta(t)\right) dt. \tag{2.31}$$

The integral is approximated by a low-pass filter created by the standard digital filter routine from IDL with a cut-off at 10% of the Nyquist frequency (150kHz). Then as

long as $A(t)$ and $\theta(t)$ are slowly changing relative to ω_0 then we have:

$$\langle v^2(t)\rangle \simeq \frac{1}{2}A^2(t) \tag{2.32}$$

and finally,

$$A(t) \simeq \sqrt{2\langle v^2(t)\rangle}. \tag{2.33}$$

The resulting signal is then resampled down to 400 kHz to conserve storage space. Figure 2.17 shows a sample of raw data with the processed signal superimposed. In this sample an arc occurs which causes the source power to be interrupted for 100 μs. The demodulation technique produces an envelope that matches the amplitude with excellent fidelity.

To obtain the phase of the signal, we follow Jiang [25]. Given a signal from one of the loop couplers:

$$x[n] = A(n)\cos\left[\,\omega_0' n + \theta\,(n)\right], \quad n = 0, 1, 2, \ldots, N-1 \tag{2.34}$$

where N is the signal length and $\omega_0' = \omega_0 \Delta t$. Before continuing with the phase extraction, the signal is bandpass-filtered around the IF frequency with a bandpass of 100 kHz, since fluctuations of interest will have frequencies less than this. To obtain a complex signal, we take the discrete Fourier transform [26] of $x[n]$:

$$X[k] = \frac{1}{N}\sum_{n=0}^{N-1} x[n]\, e^{-i2\pi kn/N} \tag{2.35}$$

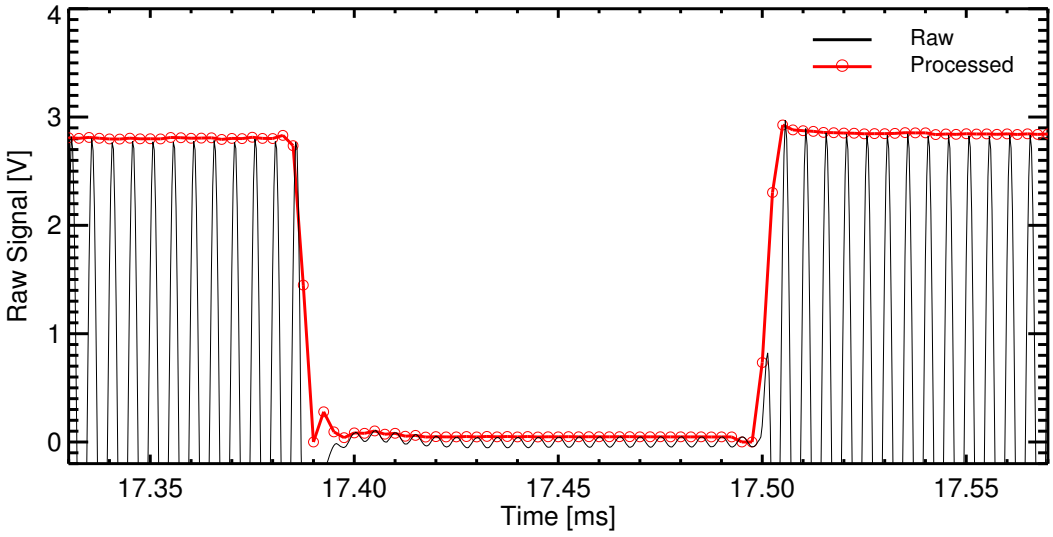

Figure 2.17: Raw signal of forward power from the power diagnostics with an arc occurring at 17.39 ms. The processed amplitude follows the raw signal through the arc.

We then define the sequence

$$X'[k] = \left\{ X[k] : 0 \leq k \leq \frac{N}{2} - 1 \right\} \tag{2.36}$$

which effectively zeroes all the elements above the Nyquist frequency. This also makes the inverse transform complex: $x'[n] \propto \exp\left[i\omega_0' + i\theta\left(n\right)\right]$. The same algorithm is applied to a reference signal, which in our case is the first loop coupler signal:

$$y[n] = B(n)\cos\left[\omega_0' n + \theta_r(n)\right], \quad n = 0, 1, 2, \ldots, N-1. \tag{2.37}$$

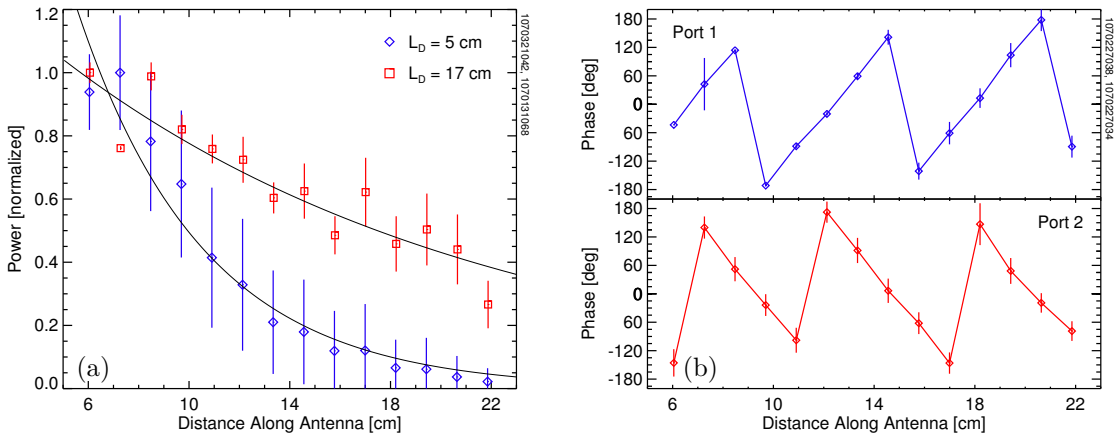

Figure 2.18: Measurement taken by the loop diagnostics in the antenna aperture. (a) The normalized power averaged over 0.25 ms. The e-folding length of the power (L_D) along the antenna is fitted. (b) The phase along the antenna for two different shots (in different feed directions) averaged over 0.25 ms.

Finally, we take the product of $x'[n]$ and $y'^{*}[n]$ to get

$$\alpha[n] = x'[n]\, y'^{*}[n] = C(n) \exp i\left[\theta\,(n) - \theta_r(n)\right]. \tag{2.38}$$

The phase between the two signals can be found by taking the argument of (2.38):

$$\phi\,(n) = \theta\,(n) - \theta_r(n) = \tan^{-1} \frac{\operatorname{Im}\,\alpha[n]}{\operatorname{Re}\,\alpha[n]} \tag{2.39}$$

Figure 2.18a shows two examples of the power measurement along the antenna and the fitted e-folding length of the power as it couples to the plasma. Figure 2.18b shows the rod-to-rod phase measurement for both feed directions.

2.6 Antenna Measurements in Air and Vacuum

The performance of the constructed antenna can be tested against theory by using a combination of field probe measurements, the embedded power and phase diagnostics and measurements of the antenna's scattering parameters from microwave network analysis.

Despite the complexity of the interdigital line itself, the antenna can be considered a microwave device that has a set of ports that have a prescribed or induced voltage and current. In the most general sense, the antenna is a three port network, with two of the ports being the two coaxial feeds one serving as the input of the interdigital line and the other serving as the output or "through" feed. The antenna aperture is the third port [27], where the electrostatic slow wave is launched.

In air or vacuum however, an electrostatic wave cannot be launched, and so the the antenna can be thought of as a two port device only. Any residual electromagnetic radiation through the aperture can be treated as part of the losses in the device.

Scattering parameters are a simple way to characterize a microwave device. An element of the scattering matrix $\mathbf{S}$ is defined as

$$S_{ij} = \left.\frac{V_i^-}{V_j^+}\right|_{V_k^+=0 \text{ for } k\neq j} \tag{2.40}$$

where S_{ij} is the ratio of driving port j with V_j^+ and measuring the voltage V_i^- coming out of port i where all ports are terminated in matched loads [18]. Since power is expressed as $P_i = V_i^2/Z_i$, where Z_i is the characteristic impedance of port i, then as long as the impedances of the ports are the same, the scattering parameters can

easily be expressed in terms of a ratio of powers, especially when working in units of decibels [28] since:

$$10 \log \frac{P_1}{P_2} \text{ dB} = 20 \log \frac{V_1}{V_2} \text{ dB}. \tag{2.41}$$

One of the initial uses for the interdigital line was for a microwave band-pass filter [14, 29]. As seen in Figure 2.4, the line only operates around a center frequency where the phase advance is $\pi/2$ and the width of the passband (as opposed to the actual bandwidth, the 3 dB point) corresponds to a phase advance of π around the center point.

Figure 2.19 shows the scattering parameters as a function of frequency around the passband of the antenna and measured at the four-port switch. Port 1 corresponds to the inboard feed and port 2 to the outboard feed with respect to the machine major radius. The response shows the passband expected in S_{21} and S_{12} which are symmetric. The passband's width is between what we expected from either the closed or open interdigital line in Figure 2.4 which is credible for a hybrid line — one that is closed but with an aperture. The loss of 2 dB at $\sim$800 MHz is taken to be the ohmic losses in the antenna structure itself. This will be the power lost whether a wave is launched or not.

The reflected power, S_{11} or S_{22} also shows characteristics of a filter in that outside the passband, all input power is reflected. S_{11} and S_{22} are asymmetric which indicates that most of the reflections in the antenna are occurring at the first impedance matching section that is encountered by the input wave. To avoid throwing away power that could be radiated to the plasma, the reflected power should be minimized. Unfortunately,

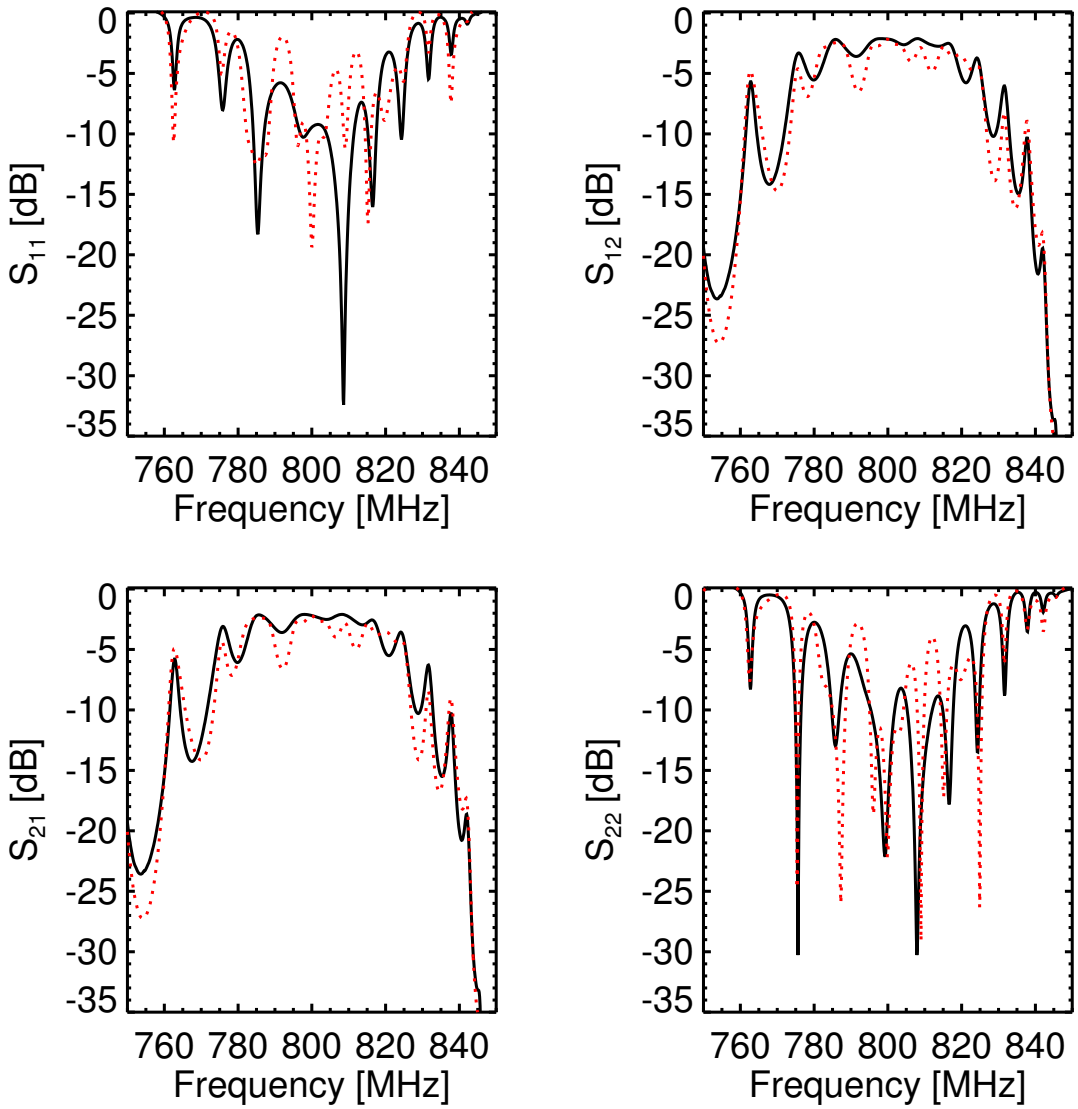

Figure 2.19: Scattering parameters of the MkIII antenna in vacuum. The solid line is the scattering parameter without external tuning. The red dotted line indicates the change in S_{xy} with a set of quarter-wave slug tuners on the port feeds. S_{21} and S_{12} are symmetric.

port 1 shows that almost 10% of the input power at 800 MHz is reflected despite the improved impedance matching section. Port 2 is much better at less than 1% reflected power, but still much poorer than the design goal of ~ -40 dB.

It is speculated that during the final fabrication step when the frontplane was soldered to the antenna, the antenna cavity was slightly twisted with the resulting effect to the reflection. To compensate for this, a pair of quarter-wave slugs are used to externally tune the antenna. As a result, S_{11} approaches -20 dB at 800 MHz, which, while not ideal, is sufficiently good for experiments.

While this section is primarily about vacuum and air measurements, the reflection characteristics of the antenna are important enough that a result in plasma should be reviewed. Figure 2.20 shows the probability distribution of an ensemble of S_{11} measurements taken for over 1600 shots. These comprise a variety of plasma conditions for plasmas between 380 and 430 kA. While the variability is significant, it is clear the S_{11} is consistently low with the peak of the distribution at -15.1 dB for port 1 and -18.2 dB for port 2. The vast majority of the data sits below 5% reflection.

The attenuation of S_{21} and S_{12} was attributed to ohmic losses with the assertion that no wave is launched by the wave in air or vacuum. To test this assertion, the scattering parameters of five-element test antenna are measured both with an aperture and again with a copper plate affixed to the frontplane, covering the aperture. The results are shown in Figure 2.21. While quantitatively different in that the resonant peaks are at different locations in S_{11}, the magnitude of S_{21} at the center frequency is very similar. This indicates that indeed no electromagnetic wave of significant power is being launched by the antenna.

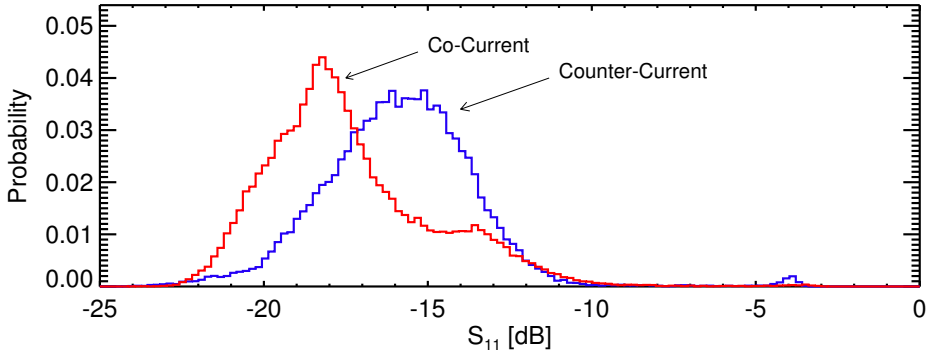

Figure 2.20: The probability distribution of S_{11} over a wide range of plasma conditions for both ports. The peak of port 1 is -15.1 dB. The peak of port 2 is -18.2 dB.

While the passband of the antenna is more or less in the correct location, and the reflection coefficient indicates that power can be delivered to the antenna without significant loss, field probe measurements can determine if a traveling wave with the correct propagation constant is produced by the antenna. Before the MkIII antenna was installed, a set of measurements were done on the bench to determine the $n_{\|}$ spectrum (in air).

The index of diffraction $\mathbf{n} = \mathbf{k}c/\omega$ in vacuum (or to good approximation in air) can be separated into components:

$$n^2 = n_x^2 + n_y^2 + n_z^2 = 1 \tag{2.42}$$

where $n_z \simeq 7.8$ by the rod spacing and $n_y = 1$ because of the nature of the TEM mode along the resonator. Then to satisfy (2.42) we must have the radial component $n_x \simeq 7.8\,i$. Plugging this result into the wave eikonal gives an exponentially decaying

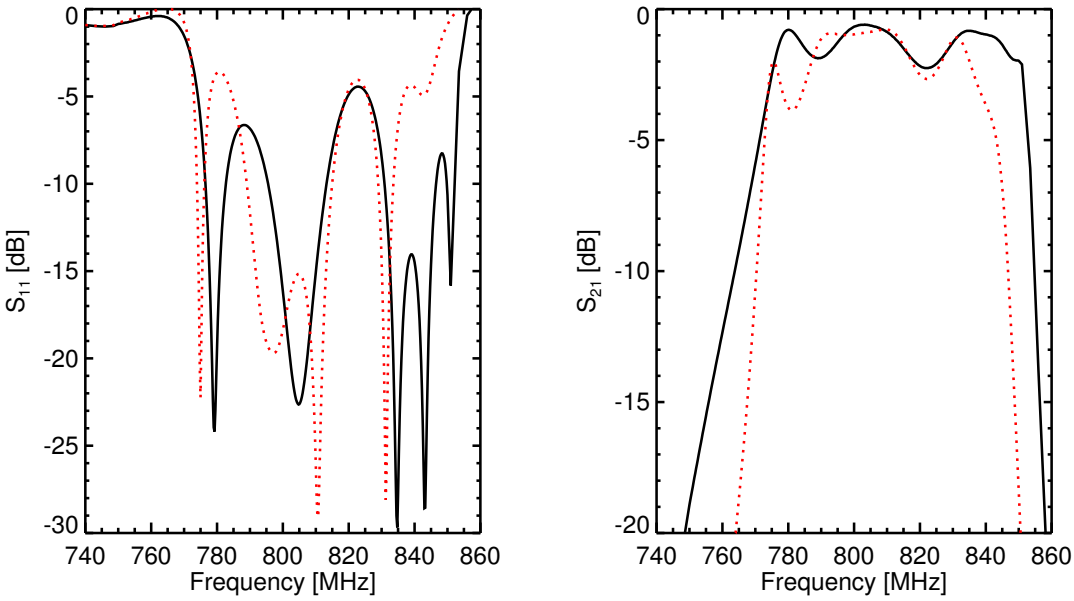

Figure 2.21: Scattering parameters of a 5-rod test antenna for an open aperture verses the aperture closed by copper plate. The solid lines are the scattering parameters with an open aperture. The dotted lines are S_{11} and S_{21} with no aperture.

wave in the radial direction corresponding to an evanescent wave. Despite the non-propagation of the slow wave in air, a measurement of n_z can be made if close enough to the aperture.

An electrostatic probe was mounted perpendicular to the antenna face on a movable jig that slides along the face of the antenna. For the measurements presented, the probe tip was $\sim$5.4 mm above the antenna face. This orientation measures $|E_x|$ rather than the more proper $|E_z|$; however, the probe's geometry is such that mounting parallel to the antenna face would reduce the resolution and modeling shows that E_z differs from E_x by a constant phase of $\pi/2$. A second probe was kept immobile and these probes

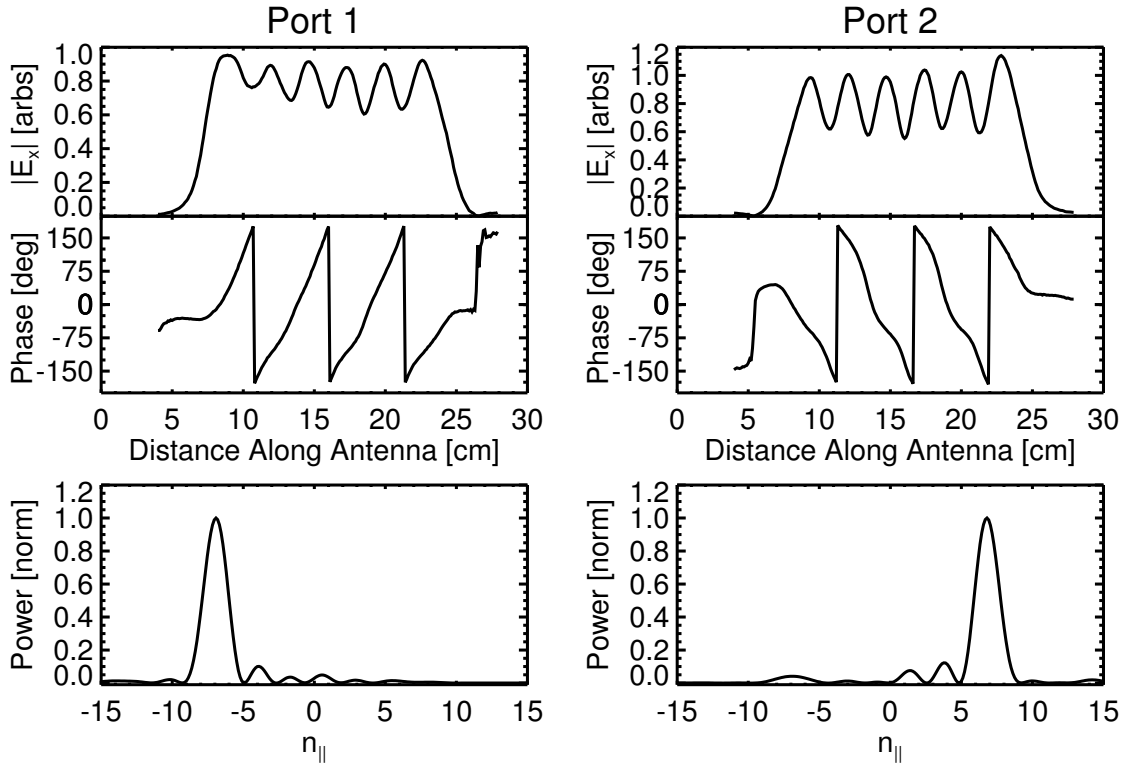

Figure 2.22: Voltage and phase measurements for $|E_x|$ above the antenna face and the resulting $n_{\|}$ spectrum for each port feed.

were attached to a vector voltmeter for a voltage and relative phase measurement. The voltage and relative phase were measured along the antenna centerline at 1 mm intervals.

Figure 2.22 shows the data as well as the spectra. The ripple in the magnitude is a result of the fact that each wavelength is composed of a quartet of resonators, and close to the antenna, the individual resonators become more resolved. The relative phasing point-to-point is not constant, but slowly varying, most likely due a small standing wave on the antenna.

The lower panels in the Figure for each of the port feeds shows the $n_{\|}$ spectrum in air. The directivity in each launch direction is good with very little power launched in the non-desired direction. The width of the main lobe is fairly broad, but is unavoidable with only about 4 wavelengths over the length of the aperture. The peak locations are $n_{\|} = -6.92$ and $n_{\|} = 6.80$ for ports 1 and 2 respectively and correspond to a mean phase advance of $\sim 79°$. These are quite a bit lower than than the design value of $n_{\|} = \pm 7.81$, and will allow the wave to propagate slightly deeper into the plasma before being absorbed.

To explore this discrepancy, we turn to Microwave Studio for modeling of the three dimensional problem. It is possible that the curved nature of the interdigital line is causing the downshift in $n_{\|}$, but initially we use the flat antenna model of Figure 2.9 and replicate the phase advance vs. frequency diagram of Figure 2.4.

Figure 2.23a shows the the phase dependence on frequency for the antenna with the constructed rod length of 92.1 mm or 0.246λ. The center frequency where the voltage and current waves both have a phase advance of $\pi/2$ is 785 MHz, 15 MHz lower than expected. To check the model, the diagnostic loops on the physical antenna are hooked up to a network analyzer and the relative phase advance of the voltage on a resonator is measured over a frequency sweep. The dotted line of Figure 2.23a shows the resulting curve which follows the modeled curve quite well, giving a slightly higher center frequency of 788 MHz.

Figure 2.23b shows the same measurement except that the aperture has been removed from the model giving a "closed" interdigital geometry. The width of the pass-band is much narrower as is predicted from the theory, and the center frequency is 798

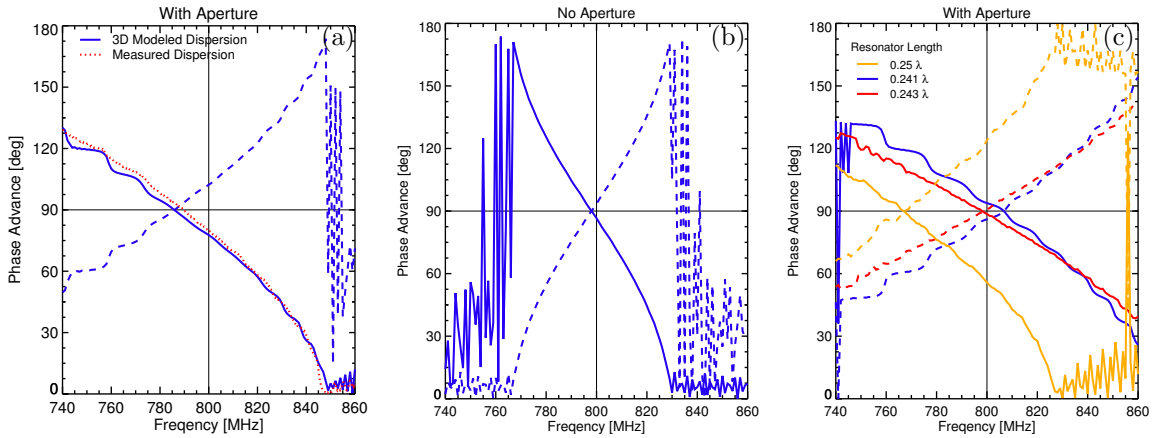

Figure 2.23: Phase advance of flat antenna model as a function of frequency in the passband. Solid lines are the phase advance of the voltage between each resonator and grounded backplane. The dashed lines are the phase advance of the current on each resonator. (a) Resonators at the designed 92.1 mm in length. The dotted line is the phase advance of the power in vacuum as measured by the loop diagnostics in the backplane of the constructed antenna. (b) Same as in (a) but with no aperture. (c) Resonators of different lengths with repect to the vacuum wavelength.

MHz, much closer to the design value of 800 MHz. It is clear from this result that presence of an aperture shifts the frequency down much farther than the 14 MHz that was expected by the capacitive contribution from the side rail.

Figure 2.23c shows a modeling run with resonator lengths of 0.241λ, 0.243λ, and 0.25λ (90.37 mm, 91.13 mm, 93.73 mm) and an open aperture. For 0.243λ, the center frequency has been shifted back up to $\sim$800 MHz as desired. From this, the modeling indicates that the presence of the aperture can be compensated for by altering the length of the resonators. For the present antenna, however, it is impossible to change the resonator length without essentially rebuilding the antenna. In this case, the pump frequency can be lowered to 788 MHz to give a phase advance of 0.25λ, and an $n_{\|} = 8.0$.

This corresponds to a 1.5% change in the frequency, and GENRAY modeling shows no significant change in the location of deposited power for 800 MHz and an $n_{\|} = 7.8$. The frequency shift will require retuning the klystron as its bandwidth is quite narrow, but this is much less onerous than changing the resonator lengths.

2.7 Radiated Power

To estimate the power that will be radiated to the plasma, we first need to know the power delivered to the antenna as well as the ohmic losses in the antenna. The inital losses occur in the transmission line. The 3⅛" transmission line from the klystron amplifier to the antenna is not lossless, and for our run of ∼60 m, there is about 0.6 dB of loss, or about 13% of the output power of the klystron.

Ideally all the power delivered to the antenna is radiated to the plasma. However, imperfect matching from the transmission line to the antenna and from the antenna to the plasma will either result in reflected power, ohmic losses to the structure, or since the the interdigital-line antenna is essentially a three port device, the power may pass through the antenna into a matched load (defined as *through* power). How much depends on the plasma parameters as reflected by the power e-folding length, but in general — except in the most loaded conditions — this will be on the order of several percent of the input power.

Refined construction techniques and external tuning have improved the structural impedance matching to the point where reflected power is on the order of one percent, and more involved modeling of the impedance matching sections may finally remove

the need for external tuning with a next generation antenna. Plasma impedance mismatching as a contribution to the *reflection* coefficient has been shown to be small in almost all plasma conditions.

The antenna is not a perfect conductor, so resistive losses are important, and in fact contribute to the most loss in the overall power budget. As shown in Figure 2.19, even with external tuning, S_{21} and S_{12} at 800 MHz in vacuum are measured to be -1.81 dB and -1.91 dB respectively for the MkIII antenna. Splitting the difference, only $\sim 65\%$ of the input (*forward*) power makes it through the antenna. The remainder is lost ohmically through heating the structure. This assumes that the antenna does not radiate into vacuum, and is not precisely true as we will see in §5.2.3, though experiments with the test antenna (see Figure 2.21) indicate that we can safely make this approximation.

With the input power and ohmic losses in the antenna, we can now estimate the radiated power. During plasma operation when the antenna is coupling well (and therefore radiating), any power received at the output feed (through power) is certainly not radiated. Additionally, any power reflected back to the input feed is also not radiated. In the reflected power case, we must assume that as the reflected power travels back toward the input feed, a percentage of its power will too be lost to the structure. The most conservative estimate would be a reflection off the far end of the antenna and then ~ 1.85 dB loss as it travels back down the antenna. Practically however, we may have multiple internal reflections anywhere on the structure, so the loss may not be so significant.

Adding these losses we have for the radiated power:

$$P_{rad} = 0.65 P_{forw} - \frac{1}{0.65} P_{refl} - P_{thru} \tag{2.43}$$

This estimate may also be conservative because if we assume that the ohmic loss in the structure is more or less constant per unit length, then if the power is well coupled, significant power will be radiated before it is lost to the structure.

For the highest power shot to date ($P_{forw} \simeq 220$ kW), the radiated power was approximately 100 kW, a consequence of almost 40 kW of through power. The amount of through power can be decreased by increasing the coupling (increasing the edge density), but even for an ideal case, the maximum radiated power would be 140 kW. To achieve the estimate of 2.1 MW for improved confinement, we would require 15 antennas: an impractical number. Increasing the maxmimum power input will reduce this number, but without a corresponding increase in the current drive efficiency, it may still be infeasible to implement an LHCD system on MST.

2.8 Summary

The interdigital-line antenna is in many ways ideally suited for MST. The thick conducting wall prevents the use of the standard grill antenna, and is conducive to the small feedthrough cross-section of the interdigital antenna. The naturally low profile of the interdigital circuit is advantageous since the plasma is close-fitting to the vacuum vessel. On the other hand, multiple antennas are expected to be needed for profile modification.

A power supply has been constructed and the Varian 955A klystron has been successfully overdriven to 46 kV and 16 A to provide > 250 kW of output power. The MkIII antenna has successfully handled 220 kW of input power in both feed directions with $\lesssim 4\%$ reflection. A power accounting has been made, and we have determined that more than 56% of the generated power is available to the plasma, which is on par with other high power (higher frequency) experiments [30]. With this degree of loss, many antennas will be required to achieve a power level necessary for improved confinement operation, substantially increasing the size of the LH system.

Power and phase diagnostics embedded in the antenna backplane have shown in vacuum and bench measurements that the constructed antenna can produce a $n_{\|}$ spectrum with good directivity. The peak of the spectrum is lower than the design value but still high enough to be accessible to the target absorption region. Theory and modeling show that lowering the pump frequency by 1-2% can compensate for this if needed without altering the geometry of the antenna.

Bibliography

[1] Brambilla, M. Slow-wave launching at the lower hybrid frequency using a phased waveguide array. *Nucl. Fusion*, **16**(1):47–54, 1976.

[2] Howell, R. and Vogel, H. Magnetic field perturbations due to a hole in a conducting wall on the ZT-40M reversed-field pinch. *Journal of Applied Physics*, **56**(7):2017–2022, 1984.

[3] Dexter, R. N., et al. The Madison Symmetric Torus. *Fusion Technology*, **19**:131–139, 1991.

[4] Haye, R. J. L., et al. Propagation of very slow lower hybrid waves in the Octopole Tokamak. *Physics of Fluids*, **23**(9):1862–1867, 1980.

[5] Chiu, S., et al. Study of the slow-wave structure as an ICRF launcher. *Nuclear Fusion*, **24**(6):717–723, 1984.

[6] Moeller, C. P., et al. Combline antennas for launching traveling fast waves. volume 289, pp. 323–326. AIP, 1994.

[7] Takase, Y., et al. Initial results from the TST-2 spherical tokamak. *Nuclear Fusion*, **41**(11):1543–1550, 2001.

[8] Takase, Y., et al. Development of a fishbone travelling wave antenna for LHD. *Nuclear Fusion*, **44**(2):296–302, 2004.

[9] Fletcher, R. C. A broad-band interdigital circuit for use in traveling-wave-type amplifiers. *Proceedings of the I.R.E.*, **40**(8):951–958, 1952.

[10] Walling, J. C. Interdigital and other slow wave stuctures. *Journal of Electronics and Control*, **3**(3):239–258, 1957.

[11] Bolljahn, J. and Matthaei, G. A study of the phase and filter properties of arrays of parallel conductors between ground planes. *Proceedings of the IRE*, **50**(3):299–311, 1962.

[12] Wu, P.-R. Dispersion characteristics of an open interdigital-line structure. *Microwave Theory and Techniques, IEEE Transactions on*, **17**(3):159–163, 1969.

[13] Griffiths, D. J. *Introduction to Electrodynamics*. Prentice Hall, 2nd edition, 1989.

[14] Cristal, E. Coupled circular cylindrical rods between parallel ground planes. *Microwave Theory and Techniques, IEEE Transactions on*, **12**(4):428–439, 1964.

[15] Goetz, J. A., et al. Design of a lower hybrid antenna for current drive experiments on MST. In T. K. Mau and J. de Grassie, editors, *Radio Frequency Power in Plasmas:14th Topical Conference on Radio Frequency Power in Plasmas*, volume 595, pp. 253–256. AIP, 2001.

[16] Nabors, K. and White, J. FastCap: a multipole accelerated 3-D capacitance extraction program. *IEEE Transactions on Computer-Aided Design of Integrated Circuits and Systems*, **10**:1447 – 1459, 1991.

[17] Thomas, M., 2009. Private communication.

[18] Pozar, D. M. *Microwave Engineering*. John Wiley and Sons, 3rd edition, 2005.

[19] Carter, M., et al. Three dimensional modelling of ICRF launchers for fusion devices. *Nuclear Fusion*, **36**(2):209–23, 1996.

[20] CST GmbH — Computer Simulation Technology. *CST Studio Suite 2006 Advanced Topics*, 2005.

[21] Litaudon, X., et al. Lower hybrid wave coupling in TORE SUPRA through multijunction launchers. *Nuclear Fusion*, **32**(11):1883–1898, 1992.

[22] Hillairet, J., et al. Modeling of lower hybrid antennas using the ALOHA code and comparisons with Tore Supra experiments. *Fusion Engineering and Design*, **84**(2-6):953–955, 2009.

[23] Kulpin, J. A 100 kilovolt phase control thyristor switch stack. pp. 378–380. 2008.

[24] Agilent Technologies. *Agilent 423B, 8470B, 8472B, 8473B/C Low Barrier Schottky diode Detectors*, 2002.

[25] Jiang, Y., et al. Application of a digital phase comparator technique to interferometer data. *Review of Scientific Instruments*, **68**(1):902–905, 1997.

[26] Haykin, S. and Veen, B. V. *Signals and Systems*. John Wiley & Sons, 2nd edition, 2003.

[27] Wolff, E. A. *Antenna Analysis*. John Wiley & Sons, 1st edition, 1966.

[28] Federal Telephone and Radio Corporation. *Reference Data for Radio Engineers*. J. J. Little & Ives Co. N.Y., 2nd edition, 1946.

[29] Matthaei, G. Interdigital band-pass filters. *Microwave Theory and Techniques, IEEE Transactions on*, **10**(6):479–491, 1962.

[30] Wallace, G., 2008. Private communication.

Chapter 3

Coupling and Antenna Performance in Plasma

3.1 Coupling Theory

While wave propagation and absorption are best handled with ray-tracing and Fokker-Planck codes such as GENRAY and CQL3D [1], the coupling of the wave from the antenna to the plasma edge can, to first approximation, be handled analytically. For this we follow Golant [2] given its applicability to traveling wave antennas.

For this analysis, we assume a slab-type geometry as shown in Figure 3.1. The domain is divided into three regions: the slow wave structure, a vacuum region of width l_s, and the plasma. The plasma is modeled as a slab where the density varies linearly in the radial direction x.

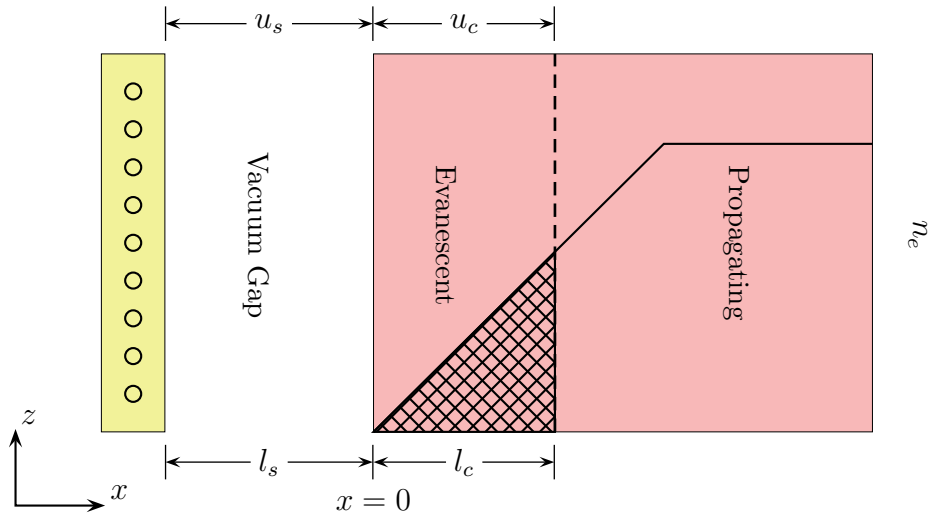

Figure 3.1: Sketch of antenna/vacuum/plasma geometry in the Golant coupling scheme. l_s is the width of the vacuum gap. l_c is the width of the opaque region. $u_{\{s,c\}} \equiv \omega\, l_{\{s,c\}}/c$ are normalized lengths.

3.1.1 Wave Solutions in the Plasma Edge

At the extreme edge of the plasma, we assume that $\omega_{pe}^2 \ll \Omega_{ce}^2$. The limitations of this assumption will be discussed later, but for any plasma with a vacuum region between the antenna and plasma, there will be some region (however small) which satisfies this condition. With this approximation, we have $\epsilon_\perp \simeq 1$ and $\epsilon_{xy}^2 \ll 1$. Then our solutions to the dispersion relation (1.15) become

$$n_{\perp 1}^2 = -\epsilon_{\|}\left(n_z^2 - 1\right), \quad n_{\perp 2}^2 = -\left(n_z^2 - 1\right). \tag{3.1}$$

At the plasma edge, the geometric-optics approximation is violated since the re-

fractive index is small and changes rapidly, so we use the wave equation:

$$\nabla \times \nabla \times \mathbf{E} - \frac{\omega^2}{c^2}\,\boldsymbol{\epsilon} \cdot \mathbf{E} = 0 \tag{3.2}$$

where $\boldsymbol{\epsilon}$ is the dielectric tensor from (1.11) and by Faraday's law,

$$\mathbf{H} = i\frac{c}{\omega}\nabla \times \mathbf{E} \tag{3.3}$$

is the corresponding magnetic field. For our slab geometry with the plasma varying along x, our wave incident to the plasma can be written as:

$$\mathbf{E}\,(x, z) = \mathbf{E}\,(x)\, e^{i n_z \frac{\omega}{c} z}. \tag{3.4}$$

Plugging (3.4) into (3.2), we can derive a set of differential equations for the field components,

$$E_z'' - \epsilon_{||}\left(n_z^2 - 1\right) E_z - n_z \epsilon_{xy} E_y' = 0 \tag{3.5}$$

$$E_y'' - \left[\left(n_z^2 - 1\right) - \frac{\epsilon_{xy}^2}{n_z^2 - 1}\right] E_y + \frac{n_z \epsilon_{xy}}{n_z^2 - 1} E_z' = 0 \tag{3.6}$$

$$E_x = \frac{i\epsilon_{xy}}{n_z^2 - 1} E_y - \frac{i n_z}{n_z^2 - 1} E_z' \tag{3.7}$$

where we have made the substitution $u = \omega x/c$ and derivatives are also respect to u. Writing (3.5) and (3.6) as

$$E_z'' + n_{\perp 1}^2 E_z + a E_y' = 0, \qquad E_y'' + n_{\perp 2}^2 E_y + b E_z' = 0, \tag{3.8}$$

we have a pair of coupled differential equations. If we assume a solution like $E_{\{x,y\}} = C_{\{x,y\}} e^{\int \lambda \, du}$, with λ slowing varying then we can use Cramer's Rule to solve for non-trivial solutions. The solutions show that we can neglect the coupled terms if $ab \ll n_{\perp 1}^2 + n_{\perp 2}^2$ which is the case if we use either $\epsilon_{xy} = 0$, true in the vacuum gap between the plasma and antenna, or $\epsilon_{xy} \ll 1$, true at the plasma edge. In either of these cases, we can write (3.5) and (3.6) with (3.1) as

$$E_z'' + n_{\perp 1}^2 E_z = 0, \qquad n_{\perp 1}^2 = -\epsilon_{||} \left(n_z^2 - 1 \right) \tag{3.9}$$

$$E_y'' + n_{\perp 2}^2 E_y = 0, \qquad n_{\perp 2}^2 = -\left(n_z^2 - 1 \right). \tag{3.10}$$

In vacuum this pair of waves corresponds to E ($E_z \neq 0, H_z = 0$) and H ($E_z = 0, H_z \neq 0$) waves respectively. In the plasma, they are the slow and fast waves as seen from (3.1). Since the fast wave is evanescent far into the plasma, we concentrate on the E wave.

The procedure will be to match the solution of (3.9) in the vacuum region — with $\epsilon_{||} = 1$ — to its solution at the plasma edge where

$$\epsilon_{||} \simeq 1 - \frac{\omega_{pe}^2}{\omega^2} = 1 - \frac{x}{l_c} \equiv 1 - \frac{u}{u_c} \tag{3.11}$$

where $u_c \equiv \omega \, l_c / c$ and $l_c = [1/n \, dn/dx]^{-1}_{\omega = \omega_{pe}}$ is the density gradient scale length. For our simple linear density model l_c corresponds to the width of the small evanescent region that the wave must tunnel through to be accessible to the plasma interior.

Using (3.11) in (3.9), we have

$$E_z'' + \gamma\left(u - u_c\right) E_z = 0 \tag{3.12}$$

where $\gamma = \left(n_z^2 - 1\right)/u_c$. The solutions to (3.12) are the Airy functions:

$$E_z\left(u\right) = A\ \mathrm{Ai}\left(\left(-1\right)^{1/3}\gamma^{1/3}\left(u - u_c\right)\right) + B\ \mathrm{Bi}\left(\left(-1\right)^{1/3}\gamma^{1/3}\left(u - u_c\right)\right). \tag{3.13}$$

These two solutions have opposite phase and group velocities. We choose the one that corresponds to a wave propagating into the plasma — $\mathrm{Ai}\left(u\right)$.

3.1.2 Impedance Matching

To match solutions in the three regions, we use the wave impedance — the ratio of transverse components E_z and H_y — at each interface:

$$Z = i\frac{E_z}{H_y} = -\left(n_z^2 - 1\right)\frac{E_z}{E_z'} \tag{3.14}$$

where i has been added to the definition of Z to simplify the math. $\epsilon_{||} > 0$ in this model fixes the scale length of the density gradient. For the pump frequency of 800 MHz, $\epsilon_{||} = 0$ corresponds to a density of $7.94 \times 10^9\,\mathrm{cm}^{-3}$. For a non-diverted machine like MST with no well-defined separatrix, we may only find densities of this magnitude behind a limiter. l_c will then be on the order of fractions of a millimeter, and so $u_c \ll 1$. With this, we expand Ai and Ai$'$ about $u_c = 0$ using *Mathematica*™ and get

the complex impedance at the vacuum/plasma interface:

$$Z_p \simeq \frac{\Gamma\left(\frac{1}{3}\right)}{3^{1/3}\Gamma\left(\frac{2}{3}\right)}\left(-1\right)^{2/3}\left(n_z^2-1\right)^{2/3}u_c^{1/3}. \tag{3.15}$$

In the vacuum region our solution to (3.9) is not propagating and reduces to

$$E_z\left(u\right) = C\, e^{\sqrt{n_z^2-1}u} + D\, e^{-\sqrt{n_z^2-1}u} \tag{3.16}$$

where C and D are constants. The wave impedance in this region is

$$Z = i\frac{E_z}{H_y} = \sqrt{n_z^2-1}\,\frac{De^{-2\sqrt{n_z^2-1}u}+C}{De^{-2\sqrt{n_z^2-1}u}-C}. \tag{3.17}$$

To solve for C and D, we use the boundary conditions of the vacuum gap. At the antenna/vacuum boundary $u = -u_s$ (where $u_s \equiv \omega\, l_s/c$), and we have the impedance $Z = Z_s$ with Z_s a property of the antenna structure. At the vacuum/plasma boundary, $u = 0$, we have $Z = Z_p$. With these boundary conditions for (3.17) we obtain the transcendental equation:

$$w = Z_s u_s \frac{1+e^{-2w}}{1-e^{-2w}}\left[1 - Z_p \frac{4u_s e^{-2w}}{w\left(1-e^{-4w}\right)}\right], \quad w \equiv \sqrt{n_z^2-1}\, u_s \tag{3.18}$$

for terms linear in Z_p. (See Appendix D.1 for the derivation.) To solve this equation for the parameter we care about, the normalized propagation constant n_z of the antenna, we apply perturbation theory.

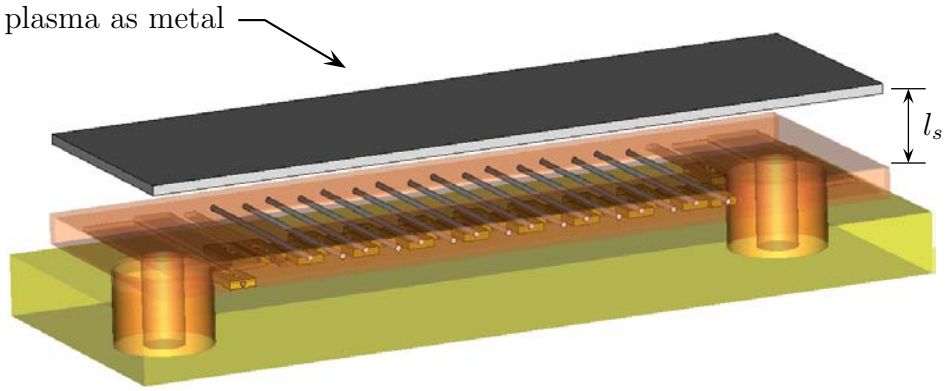

Figure 3.2: MWS flat model of the MkIII antenna with a perfectly conducting metal at distance l_s in front of the antenna aperture.

3.1.3 Exact Solution: n_{z_0}

Since (3.18) has terms linear in Z_p, we expand around $Z_p = 0$, which corresponds to the plasma as a perfect conductor. Then we let our perturbation $Z_p \neq 0$ be a correction to the index of refraction:

$$n_z = n_{z_0} + n_{z_1}, \tag{3.19}$$

where n_{z_1} is the result of the perturbation. To find the exact solution, n_{z_0}, we use Microwave Studio to simulate the response of an antenna model to a perfectly conducting metal placed in front of the aperture as shown in Figure 3.2.

We expect that n_{z_0} may change as a function of the conductor's distance from the antenna aperture, l_s, so multiple modeling runs are required. The launched wave spectrum of the model for a particular l_s is gotten from synthetic voltage and field diagnostics on the resonators in the same manner as in §2.1. For a realistic antenna

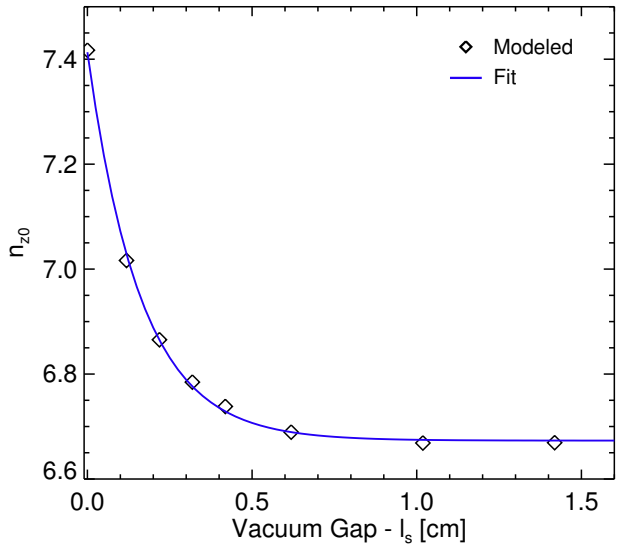

Figure 3.3: Modeled dependence of n_{z_0} as a function of l_s. The fit is an exponential with offset.

with aperture, the traveling wave does not have a single propagation constant, so the major spectral peak is fit and its maximum is used for the value of n_{z_0}.

Figure 3.3 shows the results of the modeling with a metal wall in front of the aperture. As the wall moves closer to the aperture the propagation constant increases until the limit of no aperture. Moving the wall away from the antenna approaches the vacuum behavior within 10 mm. The behavior can be modeled by a simple exponential decay with offset:

$$n_{z_0}(l_s) = e^{-(l_s+l_{s0})/\kappa_0} + n_{z_\infty} \tag{3.20}$$

where α_0 is the exact solution's scale parameter and n_{z_∞} is the value of the refractive index for vacuum or when the metal is at infinity. Doing a fit of the simulations, we

find $l_{s0} \simeq 0.049\,\mathrm{cm}$, $\kappa_0 \simeq 0.16\,\mathrm{cm}$, and $n_{z_\infty} \simeq 6.67$.

This modeling can be checked against the physical antenna by reference to n_{z_∞}, since we have for the MkIII antenna both bench measurements (in air) and vacuum measurements of $n_\parallel$ after the antenna was installed. The measurements in §2.6 gave $n_{z_\infty} \simeq -6.92$ and $n_{z_\infty} \simeq 6.80$ for ports 1 and 2 respectively. These are both larger than value for the flat antenna model, and furthermore have different values depending on the port. This must be accounted for later when we compare the spectral response of the antenna in plasma against theory, but for now we will simply note the disparity.

3.1.4 Perturbed Solution: n_{z_1}

Given the exact solution, n_{z_0}, we let $w = w_0 + w_1$ where $w_1 = w_1(n_{z_1})$ and apply the perturbation to (3.18). After some algebra and inverting w_1 such that $n_{z_1} = n_{z_1}(w_1)$, we have the first order term:

$$n_{z_1} = -\frac{4\left(n_{z_0}^2 - 1\right)^{1/2}}{n_{z_0}} Z_p\, F(w_0), \tag{3.21}$$

where F is

$$F(w_0) = \frac{e^{-2w_0}}{(1 - e^{-4w_0})(1-\nu) + 4w_0\, e^{-2w_0}}, \quad w_0 = \sqrt{n_{z_0}^2 - 1}\; u_s, \quad \nu = \frac{n_{z_0}^2 - 1}{n_{z_0}^2}\frac{1}{Z_s}\frac{\partial Z_s}{\partial n_z}.$$

See Appendix D.2 for the details. If our antenna is constructed so that the spatial period is smaller than a wavelength, which for our quarter-wave interdigital structure is approximately true, then the antenna impedance Z_s will slowly vary spatially as

well. Then $\nu \sim \partial Z_s/\partial n_z \approx 0$, and we can calculate n_{z_1} without knowing Z_s.

Plugging (3.15) into (3.21), we have the perturbation:

$$\boxed{n_{z_1} \simeq -4\,(1.19)\left(\frac{1}{\sqrt{3}} - i\right)\frac{\left(n_{z_0}^2 - 1\right)^{7/6}}{n_{z_0}}\left(\frac{\omega\, l_c}{c}\right)^{1/3} F.} \tag{3.22}$$

The real part of n_{z1} is a correction to (the real) n_{z_0} so the presence of plasma will shift the launch spectrum. Taking the imaginary part $\alpha \equiv \mathrm{Im}\,(n_{z1})$ gives us the decaying part of E:

$$|E| \sim e^{-(\alpha\omega/c)z} \longrightarrow l_D \equiv \frac{c}{\omega\alpha} \tag{3.23}$$

where we define l_D as the damping length of the field of the antenna. This parameter will be used as a metric for the tightness of the coupling of the antenna field to the plasma.

Up until now we have assumed a guide magnetic field parallel to the launched wave. If instead of (3.4), we add a pitch to the field lines with respect to the antenna axis, then our test solution is:

$$\mathbf{E}\,(x, y, z) = \mathbf{E}\,(x)\, e^{i\frac{\omega}{c}(n_y y + n_z z)}, \tag{3.24}$$

where the pitch angle is $\phi = \arctan\,(n_y/n_{z_0})$. We will subsequently show that for pitch angles available to MST, the modification to n_{z1} is insignificant. Therefore we simply

state Golant's result:

$$\alpha = \mathrm{Im}(n_{z_1}) = 4(1.19)\frac{\left(n_{z_0}^2-1\right)^{2/3}\left(n_{z_0}^2+n_y^2-1\right)^{3/2}}{n_{z_0}\left(n_{z_0}^2+2n_y^2-1\right)}\left(\frac{\omega\, l_c}{c}\right)^{1/3} G\left(w_0\right) \tag{3.25}$$

with

$$G\left(w_0\right) \simeq \frac{e^{-2w_0}}{\left(1-e^{-4w_0}\right)+4\frac{n_{z_0}^2-1}{n_{z_0}^2+2n_y^2-1}w_0\, e^{-2w_0}}, \quad w_0 = \sqrt{n_{z_0}^2+n_y^2-1}\; u_s$$

where we have already used the same approximation that $\partial Z_s/\partial n_z = 0$ from above.

3.1.5 Damping Length and Launch Spectrum

The damping length defined by (3.23) is a measure of the decay of the electric field strength as the wave travels down the antenna structure. This is equivalent to a transfer of power from the fields on the structure to the fields in the plasma. As power is transferred, there is an exponential falloff in the power along the antenna. The steepness of the falloff depends on the degree of coupling to the plasma, and the e-folding length of this decay we define as the *power* damping length L_D. Since it is the power rather than the field that is measured by the loop diagnostics embedded in the back of the antenna, we will use L_D rather than l_D as our figure of merit.

The exponential decay of the power along the antenna will distort the launch spectrum; however, what is important for the correction to the $n_{||}$ spectrum is decay of the electric field, rather than the power. Since power is proportional to E^2, the power

damping length is one-half the field damping length. Using (3.23), we have

$$P \sim |E|^2 = E_0^2 \exp\left(-2\frac{\omega\,\alpha}{c}\,z\right) = E_0^2 \exp\left(-\frac{z}{l_D/2}\right) \sim P_0 \exp\left(-\frac{z}{L_D}\right). \tag{3.26}$$

To find the effect of damping, we calculate the $n_{\|}$ spectrum by taking the discrete Fourier transform of

$$E\,(z) = \exp\left(ik_{\|}z\right) \exp\left(-\frac{z + d/2}{l_D}\right) \Theta\,(d/2 - z)\,\Theta\,(d/2 + z) \tag{3.27}$$

where d is the length of the antenna aperture, and the pair of Heaviside functions Θ serve as the aperture function. One should note that because the DTFT is periodic, we need to use the entire machine cross-section $2\pi a$ as the z domain. Both the aperture and the damping tend to reduce the spatial extent of the wave and thus broaden the peak of the spectrum. Figure 3.4 shows the calculated $n_{||}$ spectrum for various power damping lengths. The aperture length is 17.8 cm, so until the damping length becomes $\lesssim 30\%$ of the aperture length, the launching spectrum does not become much more distorted than for the spectrum with just an aperture.

The damping length is an indirect measure of the amount of power that is radiated to the plasma. If the damping length is short relative to the aperture, then most of the power will be radiated, but the launched spectrum will be broader than we want. On the other hand, if the damping length is on the order of the aperture length, then the spectrum will not significantly broaden, but we would lose over one third of the input power to the dummy load at the through port rather than to the plasma. In this respect, we have a "Goldilocks" situation: for maximum efficiency, we must have the

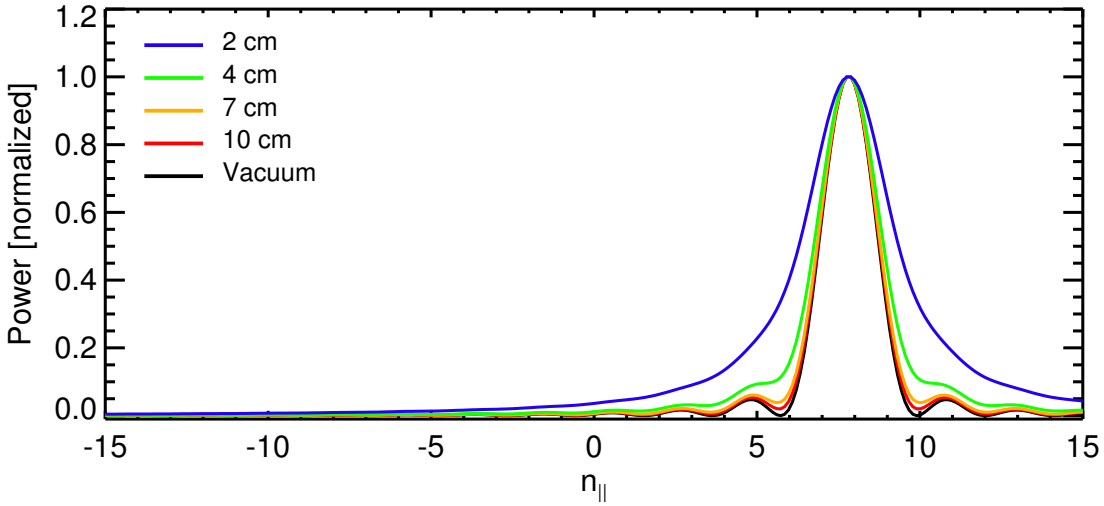

Figure 3.4: Normalized launched power spectrum for different values of the power damping length L_D.

damping length neither too short nor too long.

Figure 3.5a shows the variation of the damping length L_D for different values of l_s and dn/dx after plugging in the fitted n_{z_0} from (3.20) into (3.21). As may be expected, the damping length increases as the width of the vacuum gap increases, indicating weaker coupling. The damping length is also proportional to the density gradient. This behavior is counterintuitive as one would expect very diffuse plasmas to couple more weakly than denser plasmas. However, if the amount of coupling is proportional to the number of particles we have, decreasing dn/dx increases the number density near the antenna. The shaded region in the plot shows the experimental domain with respect to the parameters that will be presented in the following sections.

Figure 3.5b shows the damping length as a function of pitch angle and vacuum gap

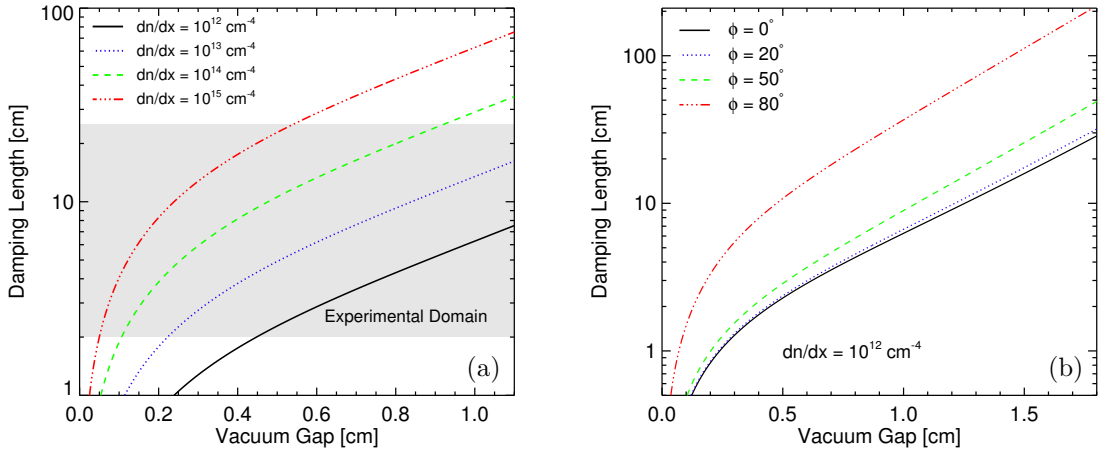

Figure 3.5: (a) Damping length as a function of vacuum gap and edge density gradient. The experimental constraints of the damping length are shown by the shaded region. (b) Damping length as a function of vacuum gap and pitch angle with $dn/dx = 1 \times 10^{12}$ cm^{-4}. Note that the damping length here is the power damping length as opposed to the field damping length. $|\Delta n_{z\infty}| \leq 1$ does not change the solution curves significantly.

with $dn/dx = 10^{12}$ cm^{-4}. The change in damping for angles less than about $\pi/4$ is quite small, although as $\phi \to \pi/2$, the damping length (for an infinite antenna) approaches infinity. For almost all plasma configurations, the pitch angle is never greater than $\sim \pi/6$, in which case we should be able to neglect the correction for pitch angle.

Using COMSOL, we can simulate the antenna response to a prescribed plasma and then compare that to the analytical model. A slab model is used and is described in §2.2. The magnetic field is chosen to be 1500 G and parallel to the long axis of the antenna. The density profile parameters are l_s, a step n_{e_0} and the gradient dn/dx. Eight different values of l_s are used: -0.08128, 0, 0.1, 0.3, 0.5, 0.7, 1.1, and 1.5 cm, where $l_s = 0$ has been defined as before as the plasma-facing surface of the antenna

frontplane. Figure 3.6a shows the results of the numerical model with different density gradients and the density step n_{e_0} set to zero so that it may be easily compared to the Golant formulation. Unlike the Golant model, however, the vacuum damping length due to ohmic loss of the antenna is accounted for, so $dn/dx = 0$ has a finite damping length. Golant fails in this limit ($l_c \to \infty$) because of the previous assumption that l_c is small.

For a gradient of $dn/dx = 1 \times 10^{10}$ cm^{-4}, very near the limit Golant's applicability, the COMSOL result shows the damping length very high, the opposite trend of the Golant model. As the gradient increases the numerical model recovers the same trend as the analytic model: the damping length increases as the gradient increases. This loading behavior is also seen in numerical modeling of waveguide grills where the reflection coefficient is high at a low density [gradient] but then decreases to a minimum where loading is best before increasing again as the density [gradient] is increased further [3]. Figure 3.6b shows a similar set of modeling runs, but with $n_{e_0} = 5 \times 10^{10}$ cm^{-3}. In this case, the density starts far enough above the evanescent region that the antenna loading is high even at $dn/dx = 0$, and so the proportionality of damping to dn/dx is the same as the analytic model.

For either of the numerical cases, the resulting damping length is much larger than the corresponding analytical results for a given gradient. For the Golant model, gradients of $\gtrsim 10^{12}\,\mathrm{cm}^{-4}$ must be posited to bring the damping length up into the experimental domain, while for the simulation, gradients much above that value will pull the damping length out of the experimental domain.

A short aside must be made here to discuss reasonable edge density gradients.

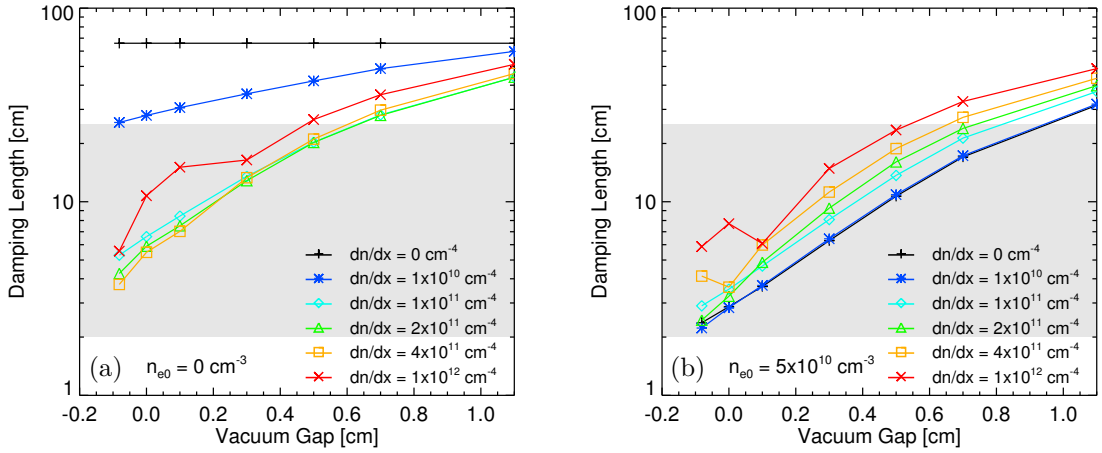

Figure 3.6: (a) Damping length as a function of vacuum gap and edge density gradient from COMSOL modeling. $n_{e_0} = 0$ cm^{-3}. The experimental constraints of the damping length are shown by the shaded region. (b) Same as (a) with $n_{e_0} = 5 \times 10^{10}$ cm^{-3}.

Probe measurements taken in 200 kA plasmas on the upper inboard side show density gradients of $2.8 \times 10^{11}\,\mathrm{cm}^{-4}$ for plasmas with line-average densities of $1 \times 10^{13}\,\mathrm{cm}^{-3}$ [4]. Interferometry at 400 kA shows slightly higher gradients, on the order of $4 - 9 \times 10^{11}\,\mathrm{cm}^{-4}$ depending on the location in the sawtooth cycle, but the outermost chord is at $r/a \sim 0.61$ making the density inversion at the edge fairly unreliable. Using the relation

$$l_c = \left[\frac{1}{n_e}\frac{dn_e}{dx}\right]^{-1}_{\epsilon_\parallel = 0} \tag{3.28}$$

discussed in §3.1.1, a gradient of $4 \times 10^{11}\,\mathrm{cm}^{-4}$ corresponds to $l_c \simeq 2 \times 10^{-2}$ cm.

The analytic model then requires gradients too large for reasonable experimental values while the range of gradients in the numerical simulation are reasonable and reproduce damping lengths that are within the experimental domain. One could bring

the analytic model back into line with the experimental damping length by requiring the vacuum gap, l_s, be on the order of centimeters rather than millimeters, but this conflicts with other experimental data that has density quite near the wall [4].

While the imaginary part of n_{z_1} predicts the loading on the antenna, the real part predicts the correction to the launch spectrum. Assuming $\partial Z_s/\partial n_z \approx 0$ as in the derivation, $F(w_0)$ in (3.21) can be well approximated by

$$F\left(l_s\right) \simeq \frac{1}{8\sqrt{n_{z_0}^2-1}} \frac{c}{\omega} \frac{1}{l_s}, \tag{3.29}$$

where we have expanded w_0. With (3.29), we can more easily pick out the dependence of l_s on n_{z_1}. The correction to the propagating (down the antenna) part of n_z with the real part of n_{z_1} is:

$$\begin{aligned} \mathrm{Re}\left(n_z\right) &= n_{z_0} + \mathrm{Re}\left(n_{z_1}\right) \\ &\simeq n_{z_0} - \frac{1.19}{2\sqrt{3}} \frac{\left(n_{z_0}^2-1\right)^{2/3}}{n_{z_0}} \left(\frac{\omega}{c}\right)^{-2/3} \frac{l_c^{1/3}}{l_s}, \end{aligned} \tag{3.30}$$

where n_{z_0} is again a function of l_s and fitting parameters. Unlike (3.27) where reducing the damping length narrows the extent of the field in configuration space which causes the main lobe of the launch spectrum to broaden, this correction shifts the location of the main lobe by the value of the second term in (3.30).

Figure 3.7a shows the variation of $\mathrm{Re}\left(n_z\right)$ with respect to l_s for different values of dn/dx. An offset, Δn_{z_∞}, is added to n_{z_0} to account for physical measurements as outlined in §3.1.3. Figure 3.7b shows the peak $n_\parallel$ of the spectrum for a set of COMSOL

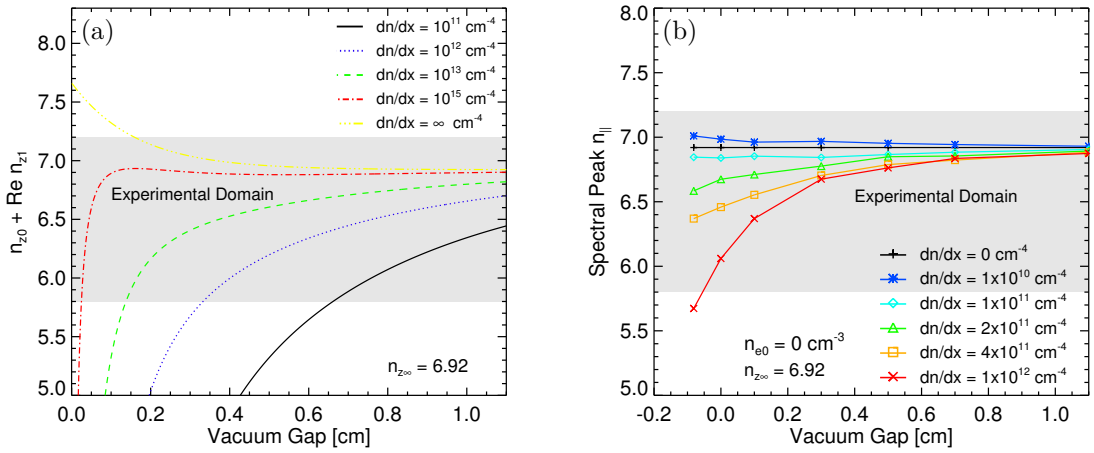

Figure 3.7: The propagating part of n_z as a function of l_s for different values of dn/dx. The value of $n_{z\infty}$ from (3.20) has been shifted by an offset to reflect measured vacuum spectra. The experimental constraints of the measured spectrum are shown by the shaded region. (a) The analytic solution. (b) Numerical solution from COMSOL.

runs. The vacuum $n_{\|}$ as predicted by COMSOL (with $dn/dx = 0$ and $n_{e_0} = 0$) is $\sim$6.26, lower still than Microwave Studio's underestimate of the spectral peak. It was found that lower mesh densities in the COMSOL model would produce a downward-shifted peak. Because the impedance of the cavity is critical in determining the propagation characteristics, this is not altogether surprising, and increasing the mesh density would upshift the spectral peak to the apparent limit of 6.26 where improving the mesh further had no effect. The cause of the final peak underestimate is unresolved. An offset is again used to bring $n_{z\infty}$ to the experimentally measured value.

Once again the analytic model requires large density gradients to span the experimental domain while the numerical results are within the experimental domain for reasonable values of the edge density gradient. A closer comparison to the experimental

data will be done in §3.2.3. Notwithstanding the magnitude issue with the analytical model, the functional dependence of the peak $n_{\|}$ with respect to dn/dx is of the opposite sense in the Golant model as opposed to the numerical model. The existing numerical dataset sheds little light on this discrepancy except that at $dn/dx = 1 \times 10^{10}$ cm^{-4}, the spectral peak increases slightly relative to the vacuum solution: the same sense as the analytical model.

3.1.6 Coupling to a Density Step Function

The magnitudes of the density gradients ($10^{12} - 10^{15}; \mathrm{cm}^{-4}$) required for the Golant model to be consistent with experiments correspond to $l_c < 10^{-2}$ cm. At these scale lengths, the density rises quickly and the antenna essentially faces a conductive wall rather than a diffuse plasma. In this case it may be instructive to model a density step, n_{e_0}, rather than a density gradient, with the height of the step serving as a proxy for the magnitude of the gradient.

The density step should be larger than the critical density, $n_e|_{\epsilon_{\|}=0}$ so that the wave actually propagates. In this case we can no longer assume that $\epsilon_{\perp} \simeq 1$ or $\epsilon_{xy}^2 \ll 1$ as in §3.1.1 because our density will be such that $\omega_{pe} > \omega$. Using the wave equation (3.2) and (3.4), we have for our differential equations:

$$E_z'' - \frac{\epsilon_{||}}{\epsilon_{\perp}}\left(n_z^2 - \epsilon_{\perp}\right) E_z - n_z \frac{\epsilon_{xy}}{\epsilon_{\perp}} E_y' = 0 \tag{3.31}$$

$$E_y'' - \left[\left(n_z^2 - \epsilon_{\perp}\right) - \frac{\epsilon_{xy}^2}{n_z^2 - \epsilon_{\perp}}\right] E_y + \frac{n_z \epsilon_{xy}}{n_z^2 - \epsilon_{\perp}} E_z' = 0. \tag{3.32}$$

Cramer's rule is again used to eliminate the coupled terms. For MST parameters of 1500 G, 800 MHz, and $n_z = 7$, the coupling can be neglected for densities $\lesssim 2 \times 10^{12}\,\mathrm{cm}^{-3}$, far above the cutoff density.

The perpendicular index of refraction for the slow wave is

$$n_\perp^2 = -\frac{\epsilon_{||}}{\epsilon_\perp}\left(n_z^2 - \epsilon_\perp\right) \tag{3.33}$$

which is a constant in the plasma because we assume a constant density and magnetic field and positive since $\epsilon_{||} < 0$ for $\omega_{pe} > \omega$. Our differential equation for the slow wave is then

$$E_z'' + n_\perp^2 E_z = 0 \tag{3.34}$$

which has the standard solution:

$$E_z\left(u\right) = Ae^{in_\perp u} + Be^{-in_\perp u}. \tag{3.35}$$

Because $Be^{-in_\perp u}$ has its phase velocity in the $-u$ direction and group velocity in the $+u$ direction, we set $A = 0$ and $E_z = Be^{-in_\perp u}$.

The vacuum solutions and matching conditions are identical to Golant's treatment with a density gradient. Only the plasma's surface impedance has changed. For a density step the impedance is

$$Z_p = i\frac{E_z}{H_y} = -\frac{n_z^2 - \epsilon_\perp}{\epsilon_\perp}\frac{E_z}{E_z'} = -i\frac{n_z^2 - \epsilon_\perp}{n_\perp \epsilon_\perp} \tag{3.36}$$

where we have applied Faraday's law to H_y. Expanding the $n_\perp$ term, the impedance is

$$Z_p = -i\frac{\sqrt{n_z^2 - \epsilon_\perp}}{\sqrt{\epsilon_\perp}}\left(\frac{\omega_{pe}^2}{\omega^2} - 1\right)^{-1/2} \tag{3.37}$$

Applying Z_p to (3.21), we have the correction to n_{z_0}:

$$n_{z_1} \simeq 4\,i\,\frac{\left(n_{z_0}^2 - 1\right)^{1/2}}{n_{z_0}}\,\frac{\sqrt{n_{z_0}^2 - \epsilon_\perp}}{\sqrt{\epsilon_\perp}}\left(\frac{\omega_{pe}^2}{\omega^2} - 1\right)^{-1/2} F(l_s) \tag{3.38}$$

where F is from §3.1.4. The equation (3.38) is interesting in that it is purely imaginary: unlike the gradient case, there is no real correction to n_{z_0} and so the peak of the launch spectrum is fixed by the width of the vacuum gap only.

Figure 3.8a shows the damping length as a function of l_s and n_{e_0} and Figure 3.8b shows some corresponding numerical results. The results mirror the analytical results closely as would be expected if a large density gradient is essentially a step function. The COMSOL results' behavior are also similar to those shown in Figure 3.6a. A more realistic model may be one similar to the density profile given by (2.29) and used by the COMSOL numerical model, but the development of such an model analytically is beyond the scope of this work.

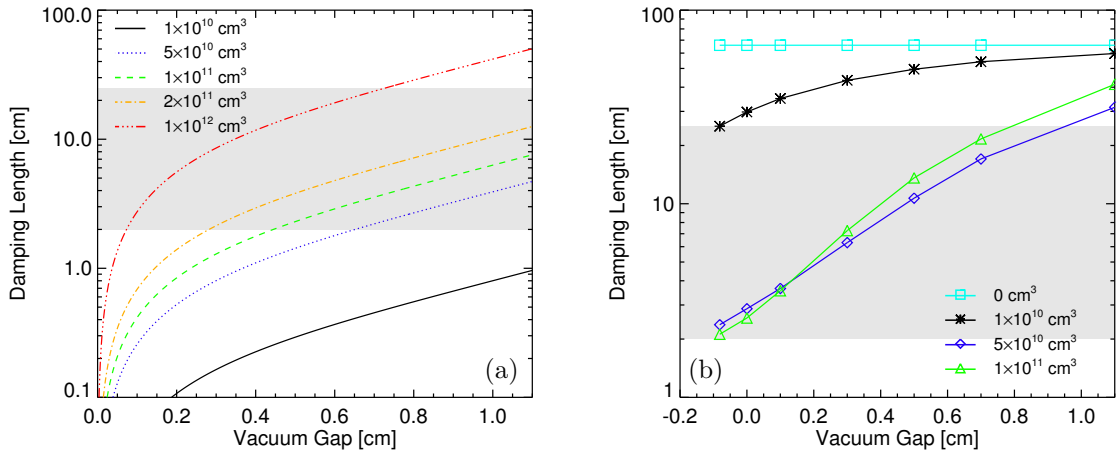

Figure 3.8: (a) Damping length as a function of vacuum gap and density step sizes. The experimental constraints of the damping length are shown by the shaded region. (b) COMSOL modeling of the same parameters. The density gradient dn_e/dx is set to zero.

3.2 Experimental Antenna-Plasma Coupling

3.2.1 Coupling and Plasma Parameters

From the §3.1, it is clear — and unsurprising — that the magnitude of the terms in the dielectric tensor have a considerable effect on the antenna response and its coupling to the edge plasma. From the treatment of Golant, we initially examine three plasma parameters and look at the variation of the antenna's coupling with respect to them. The primary metrics used to gauge the antenna behavior will be the damping length and launch spectrum as measured by the loop diagnostics introduced in §2.5.3.

To explore the data from the experiment, we use composite analysis. Since we expect that the antenna's coupling is a function of many variables, and since in general

MST's plasmas are quite variable shot to shot as well as intra-shot, we must control for each of these parameters as well as the performance of the antenna. The toolset for this analysis is an outgrowth of J. Chapman's sawtooth correlation code [5]; however, the correlation routines themselves are not used. Because of this variability, large ensembles of shots are required to determine the antenna's response to plasma conditions.

At the outset of the analysis, a particular ensemble of shots is picked depending on the experiment. For each shot a time range is selected, for example the nominal flat top of the plasma current waveform. At this point a window size is chosen. Because of the large variability in plasmas, a small window size is used. For these datasets, 0.1 or 0.25 ms is chosen. The data are then averaged over each window, and each of these time slices is defined as an event. After this, the first cut is made. The first cut can be with respect to any signal or set of signals, but this cut selects which data go into the final dataset. For example, any time slice whose average rf input power is less than 50 W will be excluded from the dataset. With these data, any series of additional cuts can be performed to constrain the dataset and isolate the parameter of interest.

We first compare the damping length of the antenna with respect to the pitch angle of the background magnetic field. To calculate the pitch angle for MST, we find the angle between the toroidal and poloidal fields at the wall. The toroidal field is determined by Ampere's law and a measurement of the currents flowing in the shell. The field at the wall varies as $1/R$, and is measured at $R = 0.97R_0$. Then

$$B_\phi = \frac{0.97 R_0 B_{\phi 0}}{R}, \tag{3.39}$$

where R now is measured at the location of the [center of the] antenna: 1.16 m for MkII and 1.12 m for MkIII. The poloidal field at a given poloidal angle θ is given by [6]

$$B_\theta(a,\theta) \simeq \frac{\mu_0 I_p}{2\pi a}\left[1+\frac{a}{R_0}\left(\beta_p+\frac{l_i}{2}-1\right)\cos\theta\right] \tag{3.40}$$

where l_i is the normalized internal inductance (~ 1.5) and $\beta_p \sim 0.15$. The pitch angle relative to the antenna is then:

$$\phi = \arctan\left(\frac{B_\phi}{B_\theta}\right) + 2.5^\circ \tag{3.41}$$

where we add 2.5° since the MkIII antenna itself is tilted with respect to the vertical.

The ensemble used is a set of 1801 shots collected from two years of experiments. The cuts made to pare events are $350 < I_p < 450$ kA with densities at $0.8 - 1.2 \times 10^{13}\,\mathrm{cm}^{-3}$ and $P_{\mathrm{forw}} > 500$ W. Figure 3.9a shows the measured damping length with respect to the pitch angle.

As noted in §3.1, the treatment of Golant indicates that until the field pitch relative to the antenna becomes on the order of $\phi \sim \pi/4$, the change in damping length is insignificant. A visual inspection of the data do not indicate a trend strong enough to contradict Golant and supports a weak dependence of L_D on ϕ, but doing a formal hypothesis testing for the (lack of) a trend is more problematic. As illustrated in Figure 3.9b, despite the fairly loose constraints of the dataset, over 70% of the data occurs between 3 degrees of pitch, which puts a large amount of weight to a fit in that region. A much bigger obstacle is the fact that the data outside that region are not normally distributed, failing a necessary condition to perform linear regression. At the

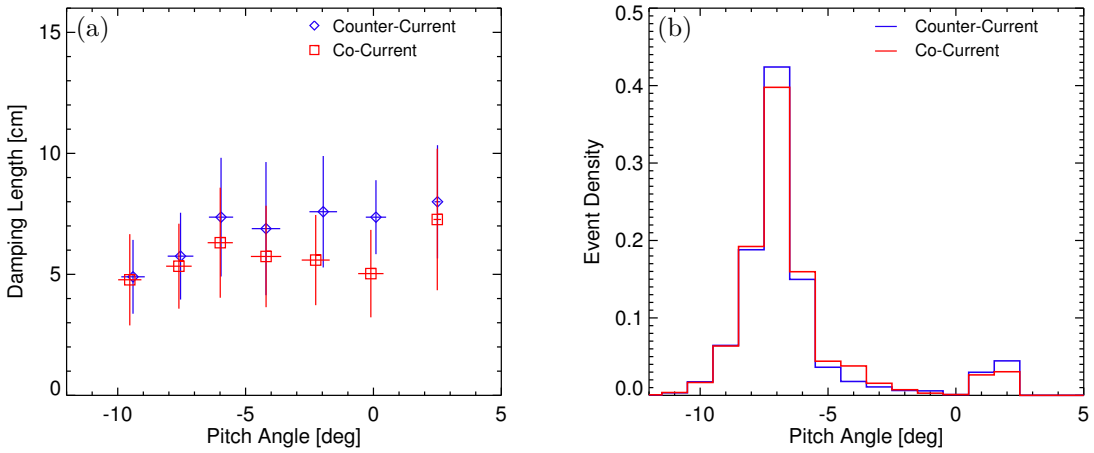

Figure 3.9: (a) Damping length vs. the pitch angle of the magnetic field relative to the antenna. (b) The event density with respect to the pitch angle.

minimum, more data across as many pitch angles as possible are necessary to perform a rigorous analysis.

In §3.1, we made the assumptions $\epsilon_\perp \simeq 1$ and $\epsilon_{xy} \ll 1$ in our derivation. Since $\epsilon_\perp$ and ϵ_{xy} depend on Ω_{ce} and thus $|B|$, we can attempt to test these assumptions by varying the magnitude of the edge field and measuring the coupling. $|B|$ is calculated by taking the norm of (3.39) and (3.40).

The same 1801 shot ensemble as before is used. The constraints applied to the dataset are densities of $0.8 - 1.2 \times 10^{13}\,\mathrm{cm}^{-3}$ and $P_{\mathrm{forw}} > 500$ W. Figure 3.10a shows the damping with respect to $|B|$. At first glance, we see that the damping length for the co-current phasing is fairly insensitive to the magnetic field. The behavior for the counter-current phasing is more muddled.

This dataset has a similar problem as the pitch angle data. As seen in Figure 3.10b,

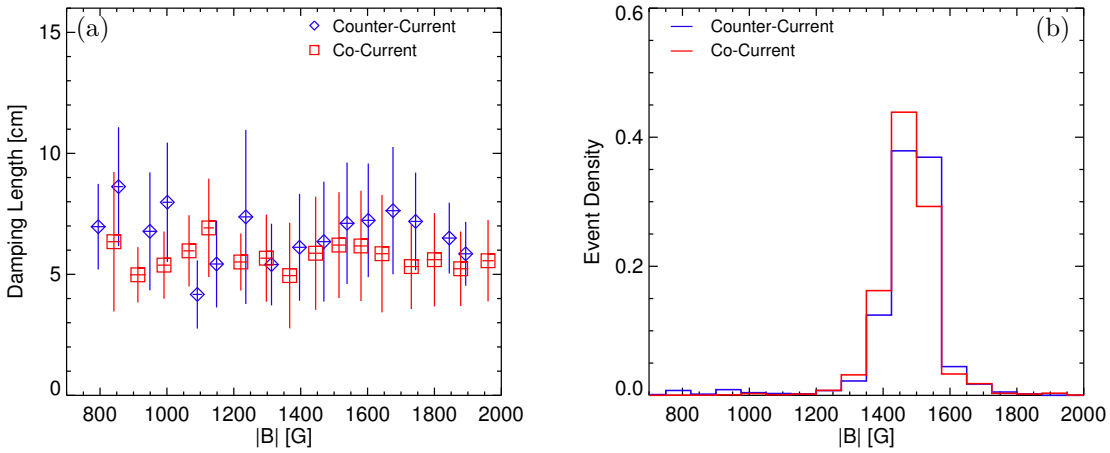

Figure 3.10: (a) Damping length vs. the magnitude of the edge magnetic field. (b) The event density with respect to the magnetic field.

a large majority of these data are between $1400 - 1600$ gauss. This certainly skews the weighting for a regression, but for these data, the necessary condition of normality is satisfied. To compensate for the skewed weighting the data are binned with bin size of 75 G. The error for each bin is given as $\sigma/\sqrt{N}$ where N is the number of events in each bin. This procedure reduces the number of degrees of freedom to $\nu = N_{bins} - 2$, but is an unavoidable tradeoff to compensate for the weighting.

The hypothesis tested is that the slope of the regression line is zero. Doing a standard Student's t-test, we reject the hypothesis for the counter-current phasing with only 41% confidence and the co-current phasing with 64% confidence: a far cry from the standard 95% level. Of course, the test requires the premise that the trend is linear in the first place. In the case of the coupling terms in (3.5) and (3.6), $\epsilon_{xy} \sim |B|^{-1}$ and for the approximation leading to (3.1), $\epsilon_{\perp} \sim |B|^{-2}$. As a test for sensitivity however,

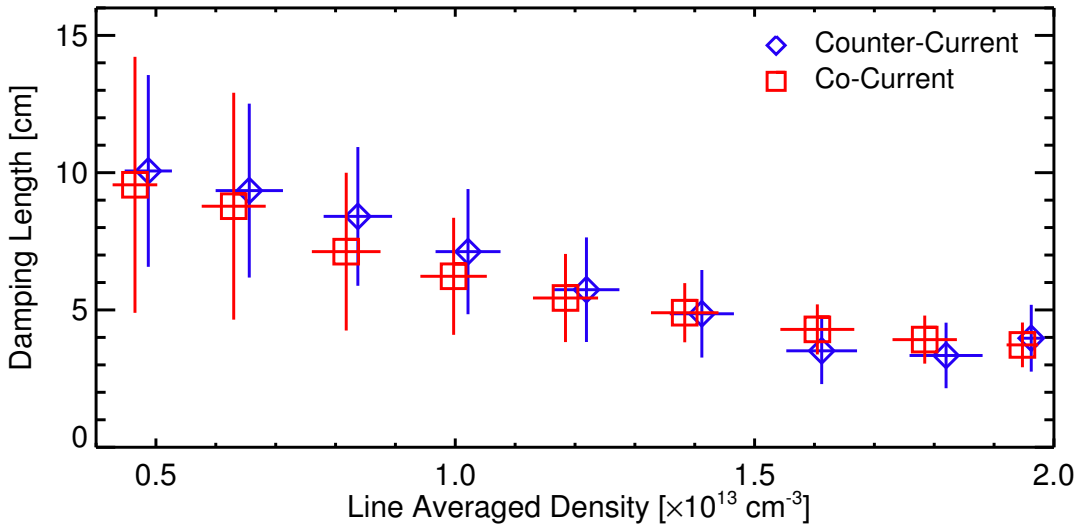

Figure 3.11: Damping length vs. line-average density.

we can be fairly confident that our approximations in §3.1 are alright.

The third parameter we will examine is the plasma's line-averaged density. Since l_c is the density gradient scale length and $L_D \sim l_c^{-1/3}$, we might expect the damping length to vary strongly as the density changes.

The same 1801 shot ensemble is again used for this dataset. The constraints on this dataset are $380 < I_p < 420$ kA, $P_{\text{forw}} > 500$ W, and the reversal parameter F is restricted to between -0.22 and -0.18. Figure 3.11 shows how the damping length varies relative to the density.

As expected, the coupling improves as the density increases, but the line-averaged density itself is only an indirect measure of the "hidden" variables that actually impact the damping length. From §3.1, we expect the vacuum gap l_s and width of the opaque region l_c to be the quantities directly governing the coupling. Unfortunately, a direct

measurement of either of these is difficult.

Given the local edge density we could infer both l_c and l_s. However, edge density measurements on MST are problematic. MST, at the time of writing, has no dedicated edge density diagnostic. At low currents insertable Langmuir probes can be used as long as they are appropriately shielded from fast electrons. At higher currents, probes are generally impractical.

Edge density was measured for the MkII antenna experiments, but for these data the probe was located on the upper outboard side of the machine while the antenna is located on the lower inboard side. Additionally, the probe tips were located at 1 cm in from the wall. Although for our purposes, the density a centimeter or so from the wall is what we want, the porthole through which the probe is inserted will distort the measurement. Nevertheless, we can use these measurements as a bridge to motivate the use of the line-averaged density as a parameter of interest. Figure 3.12 shows the variation of edge density as measured by the Langmuir probe in 400 kA standard plasmas. While the data must be taken with a large grain of salt for the aforementioned reasons, it is clear that for MST operating densities, the edge density — in an equilibrium sense — increases exponentially as a function of average density.

It is clear from Figure 3.11 that line-average density is at best a mediocre metric for what is taking place in the edge. The variance of the damping length is quite large at low densities and becomes smaller as the density increases. This is indicative of an unaccounted for variable. As will be described in the next section, while the equilibrium edge density may covary with the average density, the MHD relaxation cycle causes the edge to vary independently as well.

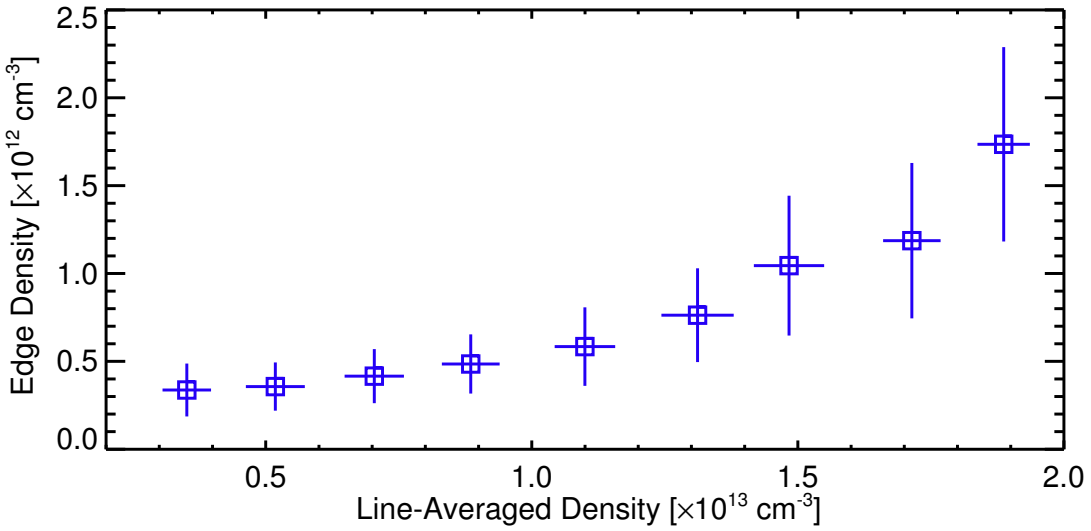

Figure 3.12: Edge density vs. line-average density for 400 kA plasmas. The edge density is measured by Langmuir probe inserted 1 cm into the plasma.

Despite the missing variance there is, for some mean measure, quite good correlation between average density and the antenna's damping length. To motivate this, we look again at the damping length's dependence on l_c and l_s. With the approximation of $F(w_0)$ in (3.29), we plug in to (3.22) and (3.23) to write the damping length as

$$L_D = \underbrace{\frac{1}{1.19}\, n_{z_0} \left(n_{z_0}^2 - 1\right)^{-2/3} \left(\frac{c}{\omega}\right)^{1/3}}_{K} l_c^{-1/3}\, l_s. \tag{3.42}$$

where K is strictly a function of l_s, though it has a very weak dependence.

As the density increases, the profile may steepen, increasing the edge density gradient — and decreasing l_c — while the plasma extent and the vacuum gap remains constant. However, decreasing l_c increases L_D, which is the opposite sense of the den-

sity covariance. On the other hand, we might expect that as the density increases, the plasma edge is pushed farther out into the shadow of the limiters, thus decreasing the width of the vacuum gap. In this case, we may see little change in the density gradient.

Taking the latter case to be true (in the equilibrium sense), and since we know that l_s is inversely proportional to $\langle n_e \rangle$, we presume that l_s is of the geometric form:

$$l_s = a \langle n_e \rangle^b , \tag{3.43}$$

where n_e is in units of $10^{13}\,\mathrm{cm}^{-3}$. Plugging into (3.42), and taking the log, we have

$$\ln L_D = \ln \left(K l_c^{-1/3} \right) + \ln a + b \ln \langle n_e \rangle \tag{3.44}$$

which we can fit to the data in Figure 3.11. Unfortunately, we have three free parameters in a, b, and l_c giving a family of solutions, but the form in (3.43) does allow us to constrain b. Using a weighted fit as before, we find that for both phasings, $b \simeq -3/4$, demonstrating the inverse proportionality between density and l_s.

3.2.2 Coupling and Sawteeth

The sawtooth cycle is a characteristic phenomenon of standard MST plasmas. The sawtooth is an MHD relaxation event which drives edge current and generates toroidal flux. The crash leads to a degradation in overall confinement from increased radial transport [7]. For our purpose, the more important sawtooth effect is the increased plasma-wall interaction. The injection of impurities into the edge and the associated

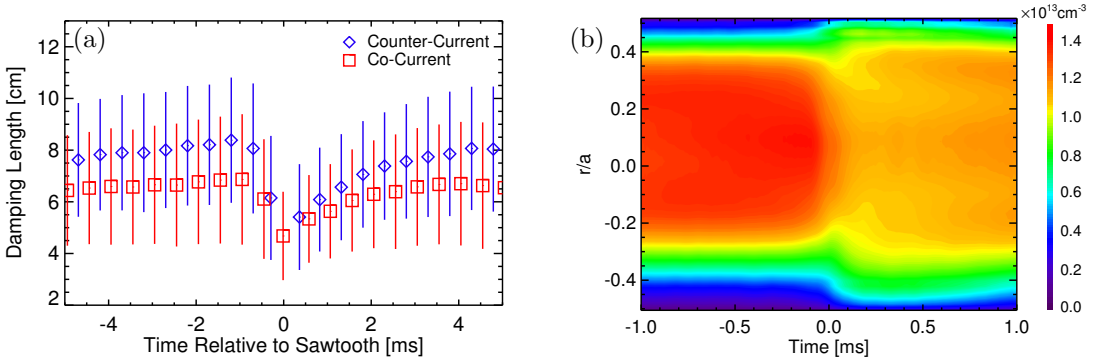

Figure 3.13: (a) The antenna damping length relative to the sawtooth cycle in 400 kA plasmas. (b) The density profile at the midplane for these plasmas. Zero milliseconds corresponds to the sawtooth crash.

increase in edge density has the potential to affect the antenna's coupling. If so, then we should see the damping length covary with the sawtooth cycle.

The same ensemble as above is used. The line-averaged density is set between 0.8 and $1.2 \times 10^{13}\,\mathrm{cm}^{-3}$. The reversal parameter is between -0.22 and -0.18 and the plasma current is fixed between 380 and 420 kA. Figure 3.13a shows how the damping length varies relative to the sawtooth crash. Figure 3.13b shows an ensembled density profile through the sawtooth as measured by the FIR interferometry diagnostic.

As hypothesized, the sawtooth cycle has a significant effect on the loading of the antenna. At the crash the damping length drops by almost a factor of two even as the line-averaged density remains constant. The density profile shows a peaked profile leading up to the crash; the core flattens directly before the crash with the edge density commensurately increasing. As Chapman [7] notes, it is observed that impurity injection can happen just prior to the crash. The antenna follows this behavior with

its damping length dropping before the crash as well.

The antenna has been observed — depending on its conditioning — to arc or at least trip the arc detector at sawtooth crashes. This behavior has been interpreted as a blob of charged particles entering the antenna cavity and drawing an arc. The prerequisite for this occurrence is for the plasma edge to fill the vacuum gap and thus increase the antenna-plasma coupling. As confinement improves after the crash, the density profile begins peaking and the vacuum gap increases, bringing the damping length up and the loading down.

The disparity in damping length between phasings is also apparent in the sawtooth ensemble data. As in the case of line-averaged density, the difference between ports shrinks as we expect the vacuum gap to shrink. In the case of the sawtooth crash, equilibrium reconstruction shows that the last closed flux surface [LCFS] moves inward by approximately 1 mm. The data hint that despite the design goal of the MkIII antenna face to be better matched to the LCFS, during inter-sawtooth periods, it is not.

3.2.3 Coupling and Launch Spectrum

Up to now, we have used the damping length as the metric for the antenna response to plasma parameters. As noted in §3.1.5 however, the index of refraction should change in response to the plasma as well. The coupling theory assumes an infinitely long antenna with a pure propagation constant. To connect the theory to experiment we define $\mathrm{Re}\,(n_z)$ as the location of the peak of the main spectral lobe and hereafter refer to this as n_z.

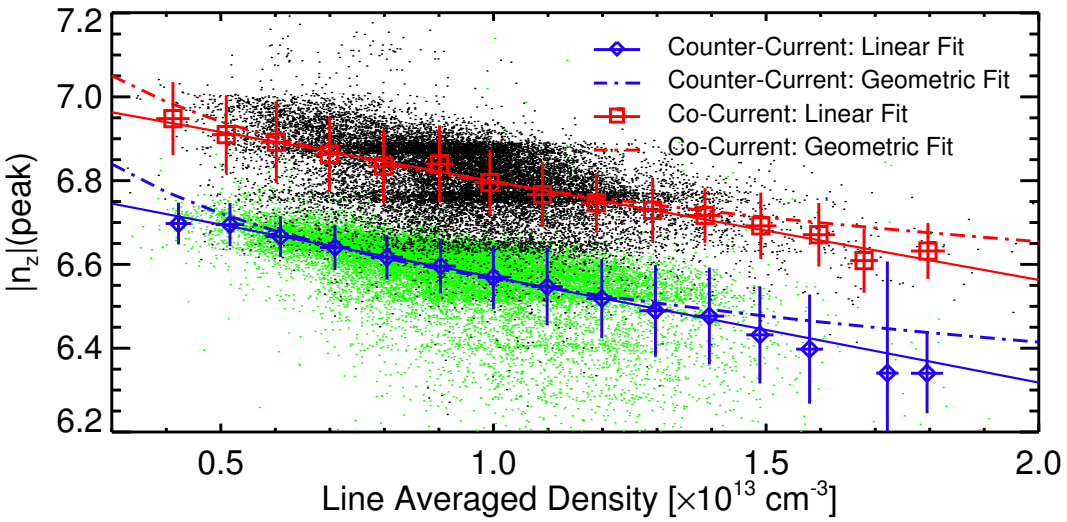

Figure 3.14: The measured $n_{\|}$ spectral peak with respect to line-averaged density. Green or black dots are individual events for counter- and co-current feed directions respectively. Solid trendlines are simple linear fits. The dashed lines are fits assuming a geometric model for $l_s(\langle n_e \rangle)$.

An ensemble of 946 shots in the port 1 launch direction and 1041 shots in the port 2 direction with constraints similar to those in §3.2.1 is used in this analysis. Figure 3.14 shows the position of the main measured spectral peak n_z as a function of line-averaged density $\langle n_e \rangle$ for each launching direction. It should be noted that as $|n_z|$ decreases, the spectrum tends to become quite distorted and the directivity becomes poor. For this analysis, events with spectra with less than 40% of the power in the main lobe are neglected. The results are not especially sensitive to this as using anything in the range of 20-60% does not significantly change the result.

The binned data have a correlation coefficient of $r^2 \simeq 0.98$ indicating that a linear fit may be appropriate. Indeed, the slope of the fits for each launch direction are quite

similar; evidence that despite the offset of ~ 0.25 in n_z between the two ports over the entire density range, the equilibrium response to plasma is the same. On the other hand, the unbinned data have an $r^2 \lesssim 0.3$ so the majority of the variance in the data cannot be explained by a linear fit. If we again make the assumption:

$$l_s = a \langle n_e \rangle^b , \tag{3.43}$$

then we can plug this into the equation (3.30) for $\mathrm{Re}\,(n_z)$ and fit the ensembled data. Unfortunately we have at the least four free parameters, $n_{z_{0\infty}}$, l_c, a, and b, which makes the fit fairly vacuous, but if we let $n_{z_{0\infty}}$ be either 6.80 or 7.05 depending on the port direction, and fix $a = 1$, then fit to the parameters l_c and b, we get for port 1: $l_c \simeq\ 0.007, b \simeq -0.018$ and for port 2: $l_c \simeq 0.007, b \simeq -0.016$.

The values for l_c are very close, and are similarly close if we were to fix l_c and vary a instead. The values of b are also similar to each other, again demonstrating that the coupling of the plasma to each port is much the same. The value of b however is more problematic when evaluating the soundness of the hypothesis (3.43). Making the same hypothesis for the damping length relative to the density in §3.2.1, we got $b \simeq -3/4$ which is a long way from $b \simeq -0.017$. The disparity indicates that the variation of the coupling parameters with respect to the line-averaged density is more complicated than a geometric dependence on l_s. A good measurement of the local density may yield a firmer connection between n_e, l_c, and l_s, but at present the broad trends with respect to $\langle n_e \rangle$ must suffice.

Verifying the coupling theory with the experimental data is difficult not only be-

cause of the difficulty in measuring either l_s or l_c but also because these two parameters are essentially coupled free parameters. With data for n_z and L_D however, we can provide an additional constraint to the equations to eliminate one parameter and solve for the other.

If we fix l_c and then invert (3.30), we get l_s as a function of n_z:

$$l_s = l_s\left(n_z, n_{z_\infty}, l_c\right) \tag{3.45}$$

where we add the parameter $n_{z_{0\infty}}$ — the vacuum n_{z_0} — to compensate for the disparity between the modeling and the physical measurements. We initially choose $l_s\left(n_z\right)$ instead of $l_s\left(L_D\right)$ because as is seen in Figure 3.7a, n_z is multivalued over a range of l_s that is of potential interest.

Plugging (3.45) into the equation for L_D (3.42), we have

$$L_D = L_D(n_z, n_{z_\infty}, l_c) \tag{3.46}$$

where we have eliminated l_s. We can now compare this equation for different parameters to the experimental data. Figure 3.15 shows the the ensembled spectral data plotted as a function of the damping length and (3.46) for different values of l_c. Each point in the Figure corresponds to a different realization of the density profile in front of the antenna and the antenna's response to that profile. Because of this, it makes little sense to attempt a fit to the data. Instead, a family of curves is used to assess the usefulness of the theory.

For density gradients on the order of the experiment, or the largest values of l_c

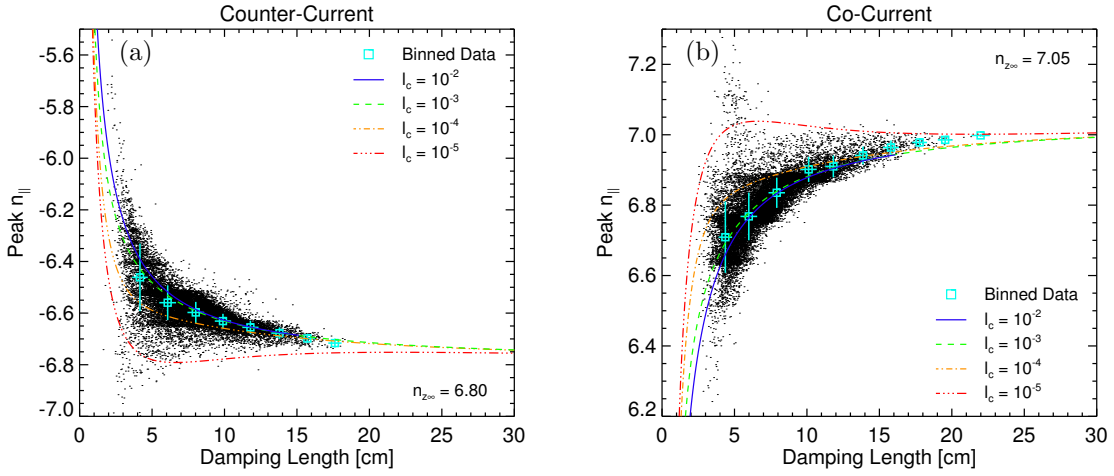

Figure 3.15: The measured $n_{\parallel}$ spectral peak (black dots) vs. damping length for (a) counter-current launch. and (b) co-current launch. Overlaid are the Golant theory predictions. Each trace is parametrized by l_s with a set $n_{z\infty}$ and for different values of l_c.

plotted, the theoretical curves tend to approach the edge of the lower bound (in terms of $n_{\parallel}$) of the experimental data. At small values of l_c, the values of $n_{\parallel}$ increase and the curve turns over and can sample some of the phase space at high $n_{\parallel}$ and low L_D. Qualitatively, the curves from the theory have the same shape as the experimental data and depending on the density gradient can access all the experimental domain. Quantitatively, to sample the low L_D and high $n_{\parallel}$ region of the domain, the gradients must be much larger than expected from the experiment, so this comparison to the data suffers the same problems as the analytical results in §3.1.5.

Figure 3.16 shows the results of the COMSOL modeling for four different density steps and six gradients. The vacuum $n_{\parallel}$ of $\sim$6.26 as described previously is corrected by applying an offset to bring the vacuum solution in-line with experimental vacuum

measurements.

For the smaller n_{e_0}, the numerical models show remarkable agreement with the experimental profile estimates. Only at $n_{e_0} = 1 \times 10^{11}\text{cm}^{-3}$ or at gradients above $1 \times 10^{12}\,\text{cm}^{-4}$ do the simulations underestimate the data. At the shallower gradients ($1 \times 10^{11}\,\text{cm}^{-4}$) and low n_{e_0}, the peak $|n_{z_0}|$ becomes larger than $n_{z_{0\infty}}$ as is required by the experimental data in the lower-left corner of the graphs. The modeling and the antenna response indicates that at least for some plasmas, the edge profile may be much shallower than interferometry implies.

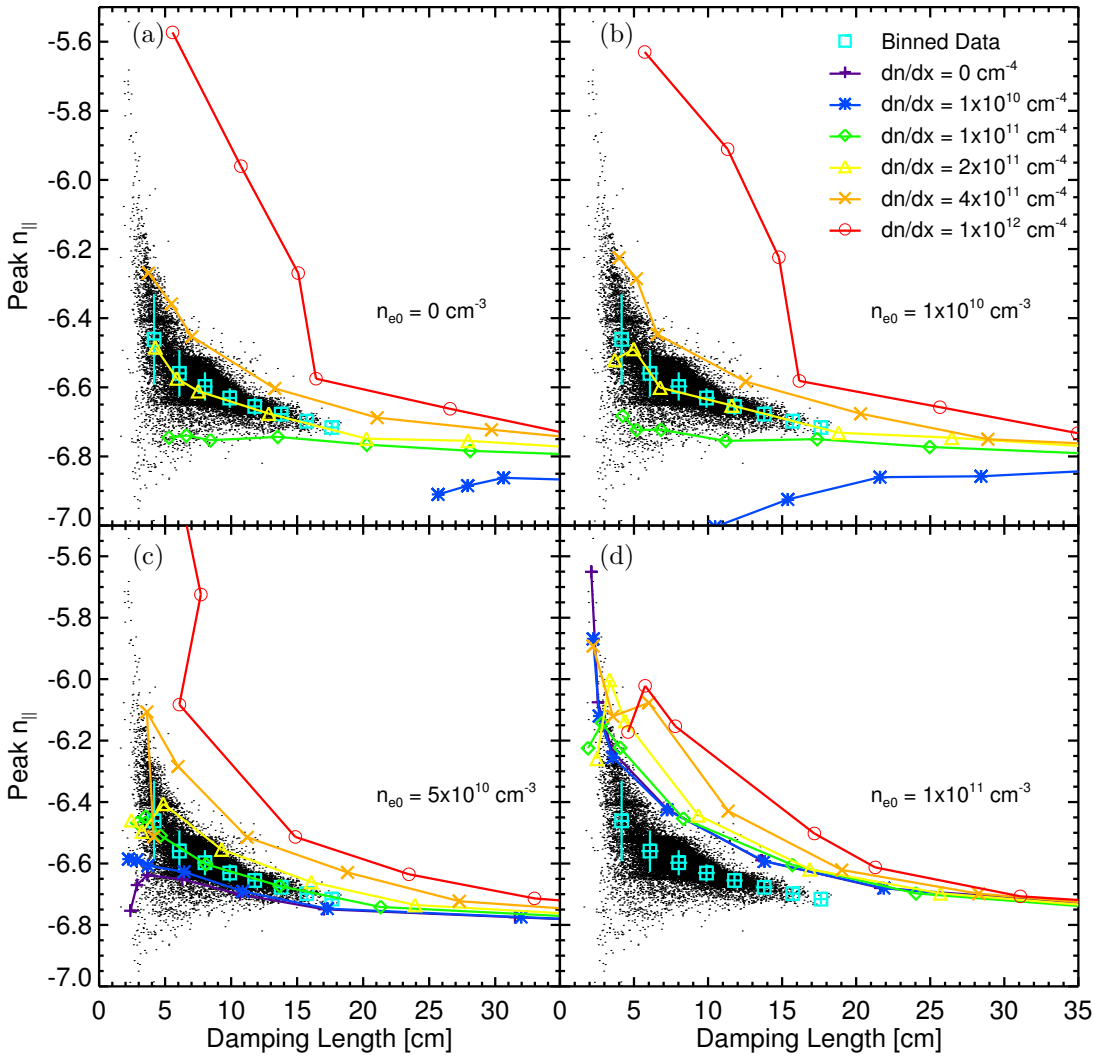

Figure 3.16: The measured $n_{\|}$ spectral peak (black dots) vs. damping length overlaid by predictions from COMSOL with various density profiles. The profile shape consists of a vacuum gap l_s followed by a density step n_{e_0} and a density gradient dn/dx. (a) $n_{e_0} = 0\text{cm}^{-3}$, (b) $n_{e_0} = 1 \times 10^{10}\text{cm}^{-3}$, (c) $n_{e_0} = 5 \times 10^{10}\text{cm}^{-3}$, (d) $n_{e_0} = 1 \times 10^{11}\text{cm}^{-3}$. Each trace is offset by the difference between the vacuum n_{z_0} predicted by COMSOL (n_{z_∞}) and the measured bench value of 6.82.

3.3 Controlling Antenna-Plasma Coupling

While changing overall plasma conditions to regulate the antenna-plasma coupling is sufficient, it would be preferable to alter local parameters or change the antenna geometry itself to affect the coupling. The Alcator C-Mod grill antenna's radial position can be moved relative to the LCFS although its limiters remain fixed [8]. The JET grill and its limiters can also be moved, and in addition it has a gas puffing system to change the local density [9]. MST's antenna is fixed in place; however, the local limiter can be changed and local gas puffing can be employed.

3.3.1 Antenna Limiter

Given the arcing problems of the MkI antenna [10], it was thought that plasma was finding its way into the antenna waveguide cavity, thus causing the arcing. To remedy this, a plasma limiter for the MkII antenna was implemented. The limiter is a set of interlocking boron nitride tiles that are placed on top of the antenna frontplane as shown in Fig. 3.17b. A small opening in the limiter above each resonator allows the fringing fields to couple to the plasma edge.

The MkII antenna was installed with the limiter in place and its initial conditioning and coupling experiments were performed with the limiter. Later, the limiter was removed and the coupling experiment was repeated. An ensemble of 1121 shots without limiter and 1018 shots with limiter were used in the composite analysis. Each shot was subdivided into 0.1 ms windows, and only windows with at least 500 W of rf forward power, $380\,\mathrm{kA} < I_p < 450\,\mathrm{kA}$, and $-0.22 < F < -0.18$, were used.

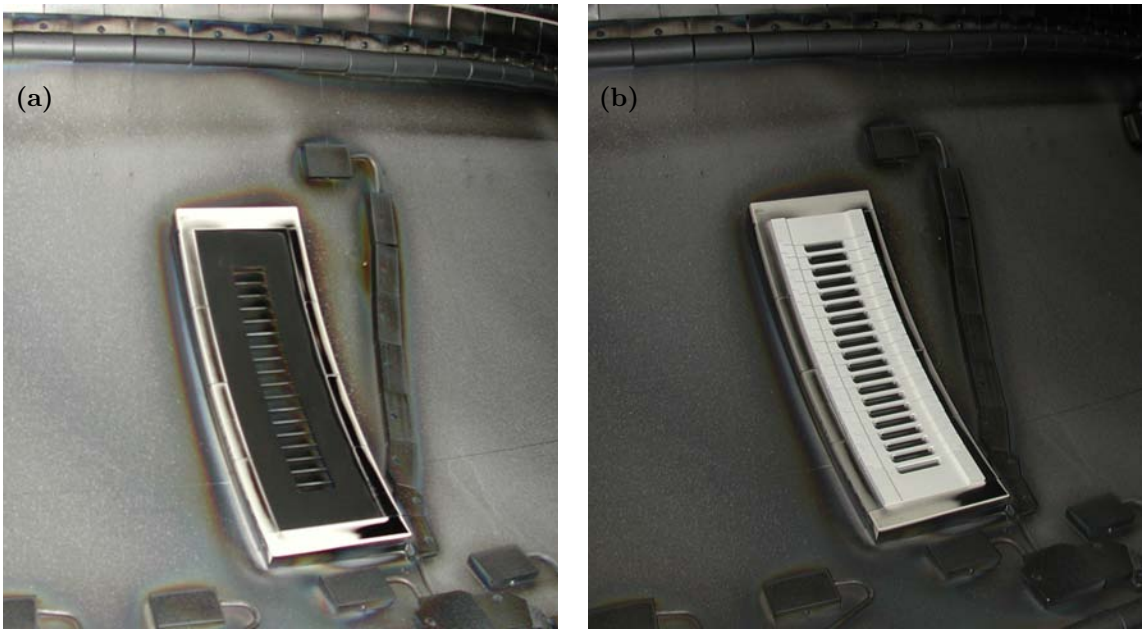

Figure 3.17: The MkII antenna installed on MST. (a) Without front limiter. (b) With front limiter installed.

Figure 3.18 shows the results of the experiments. Without the limiter, the damping length relative to the density behaves quite similarly to the MkIII antenna in §3.2: the coupling increases as density increases. On the other hand, coupling of the antenna with the limiter in place as in Figure 3.18b shows almost no correlation with density.

More difficult to explain is the distinct difference in average damping length between launching directions with the limiter in place. Unlike the MkIII antenna, the MkII antenna is not raised off the machine wall to more closely match the plasma's LCFS. In this case with the Shafranov shift, the port 1 or counter-current drive direction is farther away from the plasma that the port 2 direction. Given the variance of damping length with respect to density it is counter-intuitive that port 1 appears more tightly

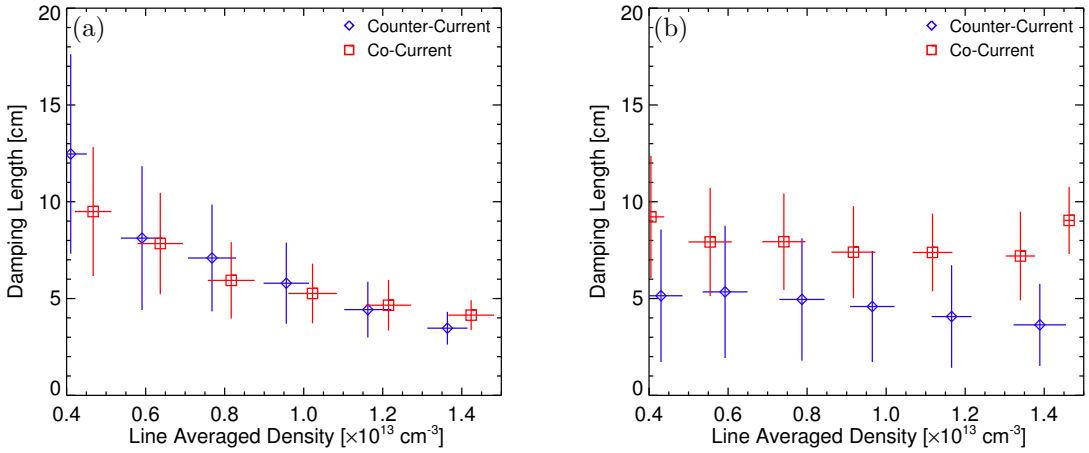

Figure 3.18: The damping length with respect to the line-averaged density with (a) no limiter (b) the limiter covering the aperture. Plasma conditions are $380 - 450$ kA and $F \simeq -0.2$

coupled than when port 2 is driven.

The analysis of Golant may explain the discrepancy. As shown in Eq. 3.42, the width of the vacuum gap is proportional to the damping length while the edge density gradient (or our proxy of line-averaged density) is inversely proportional to the damping length. In this case, the limiter may be serving to fix the width of the vacuum gap, and the variation of the damping length between ports is due to the edge density.

A limited antenna is generally advantageous with respect to coupling behavior as it would allow antenna operation over MST's full range of densities. However, the presence of the limiter kept the damping length high and prevented the achievement of the best loading for port 2. Additionally, the presence of the limiter made conditioning extremely difficult, and in fact the MkII antenna with the limiter never achieved more

than $\simeq 50$ kW of input power. After the limiter was removed, conditioning was quite fast and the antenna was able to handle the limit of the power supply at the time and eventually over 100 kW.

3.3.2 Local Puffing Into Standard Plasmas

The antenna loading as seen in §3.2 has been found to be poorer in standard plasmas when the density is low. Previous results with the LHCD grill antenna on JET [9, 11] shows that coupling can be improved in ITB plasmas having very low edge densities with gas puffing near the antenna. With these results in mind, we can attempt to increase the local density in front of MST's antenna with a similar system.

CD_4 was used as the doping gas in the JET experiments to counteract deleterious effects of D_2 on the H- or ITB-mode. Our experiment used He as a doping gas to calibrate the puff timing. A spectrometer set to view the HeI line was placed on an off-axis chord across from the antenna to gauge when the doping gas entered the plasma. Future experiments can change the gas in the manner of [11] as required.

A diagram of the local gassing system for the MkII antenna is shown in Figure 3.19. A puff valve from the MST doping system is installed on the machine's pumping duct with a pipe conducting the doping gas up through a pumping duct hole near the antenna. The pipe outlet is at the base of the antenna just below the port 2 feed.

To diagnose the effect of gassing near the antenna, we choose 240-280 kA plasmas with densities at $\sim 0.5 \times 10^{13}\,\mathrm{cm}^{-3}$. The antenna has empirically coupled poorly with plasmas of these parameters. A set of 24 shots without puffing and 15 shots with a moderate amount of puffing (~ 10 torr liters/s) were ensembled. The results of the

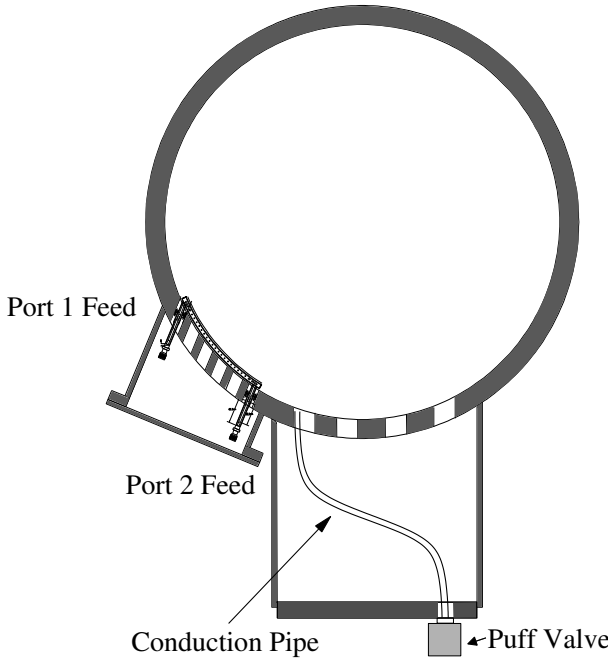

Figure 3.19: Location of local gas puffing source relative to the antenna.

experiment are shown in Figure 3.20. Edge density is measured by a triple Langmuir probe inserted to 1 cm inside the wall, but the probe is located 30° away from the antenna toroidally and is on the outboard side. As previously mentioned, it is at best an indirect measurement of the density in front of the antenna.

At this low level of local puffing we see no significant change to the damping length for a port 1 feed, with respect to either edge or line-averaged density. The damping length for the port 2 feed does show a significant difference with local puffing becoming shorter by about 2 cm. This dissimilarity is most likely due to the fact that the gas injection pipe is much nearer the port 2 feed than the port 1 feed.

To increase the coupling for the port 1 feed, we increase the flow rate of the local

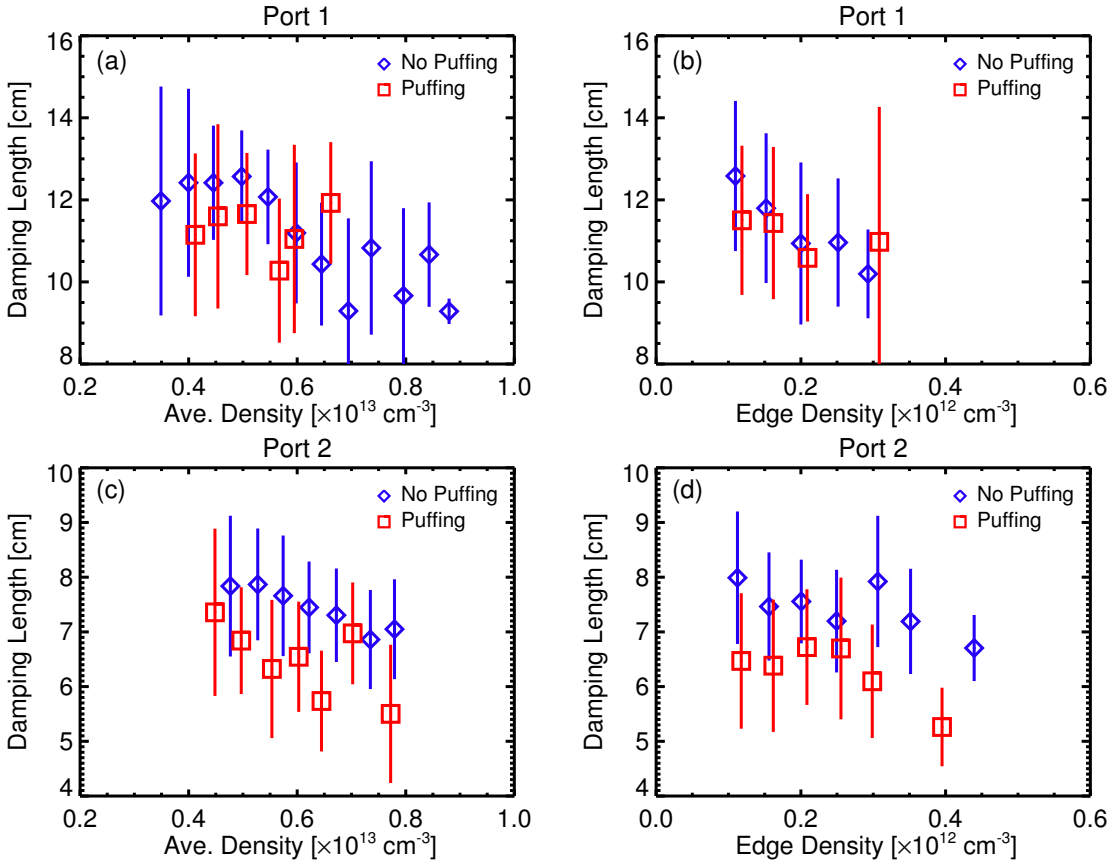

Figure 3.20: Damping length vs. line-averaged and edge density with and without local gassing. (a),(b): Port 1. (c),(d): Port 2.

gas injection. The results of the 4 shot ensemble are displayed in Figure 3.21. The larger puff pushes the damping length below 10 cm. The Langmuir probe shows the edge density to be about 25% higher with the local puff, but the line-averaged density does not significantly change giving some confidence that coupling to standard plasmas can be improved without altering overall plasma conditions.

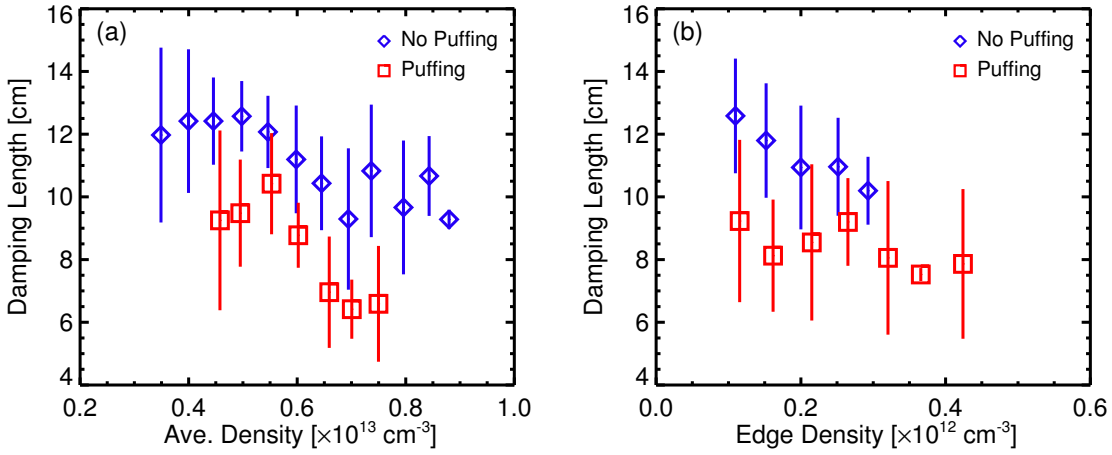

Figure 3.21: Port 1 damping length with puffing at high flow rate for (a) line-averaged density and (b) edge density measured by a Langmuir probe.

3.3.3 Local Puffing Into PPCD

Coupling rf into improved confinement plasmas is a potentially more interesting and important proposition than coupling into standard RFP plasmas. Since we expect that a full power LH system would have the same effects as the current PPCD system (increased confinement, temperatures, lower fluctuations), sustaining this regime with rf requires that we can maintain good coupling to the plasma.

With a low-power system, we can test the coupling requirements by injecting power into PPCD plasmas. A 500 kA discharge is shown in Figure 3.22. At 15 ms, 80 kW of power is applied to the MkII antenna. PPCD has started at 12 ms with power applied to the toroidal circuit, $B_\phi\,(a)$ increases and drives the pitch angle very high relative to the antenna axis. At $\sim 19.5\,\mathrm{ms}$, the D_α signal increases markedly, indicating the transition out of the improved confinement regime.

The effect on antenna performance is no less significant. During PPCD almost 30% of the input power ends up as through power indicating that coupling is very weak. At the transition out of PPCD, the coupling becomes much stronger and much more rf power is radiated. The line-averaged density changes marginally or decreases so cannot explain the increase in coupling. Looking at the density profiles in Figure 3.22b provides the now-familiar explanation. At the transition out of PPCD, the edge density increases at the expense of central peaking. In this case as well, we have a clear indication that the edge profile is critical in determining the amount of antenna coupling.

Using local gassing with the same setup as in §3.3.2, we can attempt to change the density profile (or at least the density) at the edge at the antenna. An ensemble of 105 400 kA PPCD discharges with 80 kW of injected rf power was used as a baseline for the coupling experiment. Because of the shot-to-shot variation in PPCD quality and timing, time windows within each shot were chosen for good rf power and good PPCD and only these windows were used in the ensemble.

For local puffing, 20 and 65 shots are chosen for gas injection of $\sim 6.8\,\mathrm{T}\cdot\mathrm{L/s}$ and $\sim 32\,\mathrm{T}\cdot\mathrm{L/s}$ respectively. Figure 3.23 shows the results. In the improved confinement regime without puffing, the damping length is $2-3\,\mathrm{cm}$ larger than in standard plasmas. At $6.8\,\mathrm{T}\cdot\mathrm{L/s}$, there is no change in port 1 coupling. Feeding port 2, we see a small decrease in the damping length which can be ascribed to the location of the gas conduction pipe just below the port 2 end. At $32\,\mathrm{T}\cdot\mathrm{L/s}$, the damping length significantly decreases in both feed directions indicating much better coupling even in PPCD plasmas.

A potential problem exists with local puffing during PPCD to improve antenna

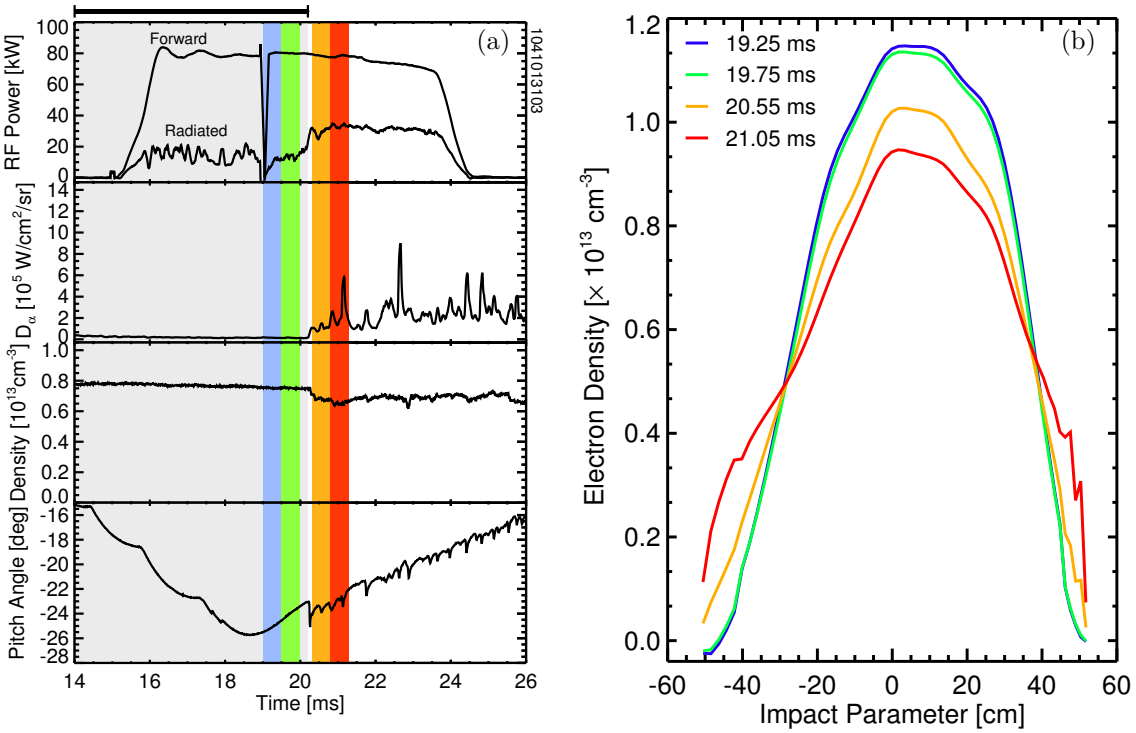

Figure 3.22: (a) Selected signals at a transition out of improved confinement. The shaded region is during PPCD. (b) Radial density profiles about the transition. Each is averaged over 0.5 ms.

coupling. It has been observed that edge fueling during PPCD tends to increase the $m = 0$ mode and degrade confinement [12]. Local puffing (of He) in these experiments to increase antenna coupling had no significant impact on the quality of plasmas. This risk may increase for lower density plasmas or for stronger puffing. Despite this, local gassing can be a potent tool to compensate for plasma conditions that normally cause poor antenna coupling.

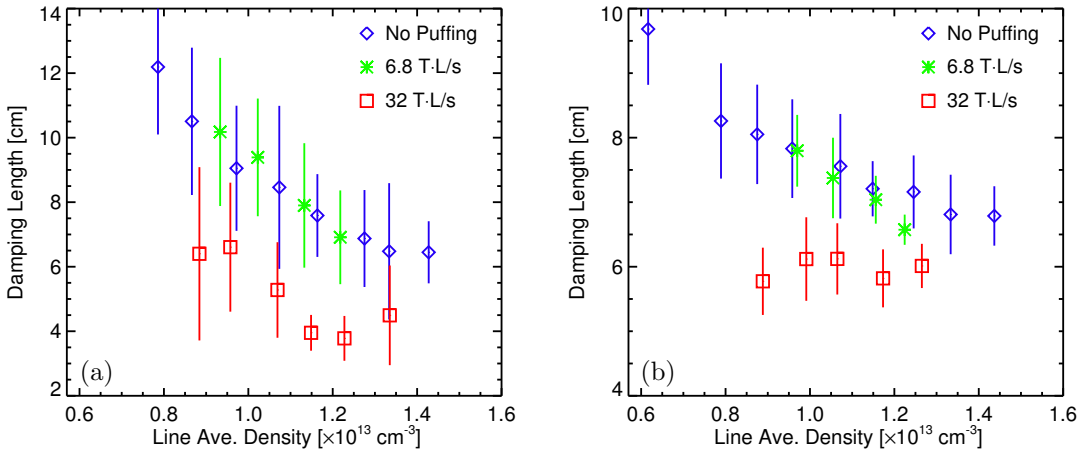

Figure 3.23: Damping length of the MkII antenna during PPCD for three different levels of puffing. (a) Port 1. (b) Port 2 nearer the local puffing source.

3.4 Summary

Coupling experiments in plasma demonstrate that the interdigital-line antenna design performs well in high current standard plasmas. In lower current plasmas, where the wave is inaccessible to the target absorption region, the antenna's power handling becomes quite poor. In high current PPCD plasmas, the antenna is unloaded as evidenced by an increase in the damping length. As with other lower hybrid experiments, plasma density is shown to be the principal driver in antenna loading. Other experiments that alter the edge magnetic field strength and pitch have no effect on coupling as expected.

With the use of a plasma limiter in front of the antenna, the amount of coupling can be kept relatively constant, but with the serious drawback that conditioning to high power becomes quite difficult. Using local gas puffing, the antenna loading can be be maintained even in low density or higher confinement plasmas.

In line with theoretical and numerical predictions, the density profile can shift the peak of the $n_{\|}$ spectrum, in some cases far enough down that the accessibility condition may become an issue. Increasing the amount of loading on the antenna will cause the damping length of the antenna to decrease and will broaden the launch spectrum.

Bibliography

[1] Harvey, R. W. and McCoy, M. G. The CQL3D Fokker-Planck code. Technical Report GA-A20978, General Atomics, 2005.

[2] Golant, V. Plasma penetration near the lower hybrid frequency. *Sov. Phys.-Tech. Phys.*, **16**(12):1980–8, 1972.

[3] Stevens, J., et al. Edge density profile effects for lower hybrid waveguide coupling. *Nuclear Fusion*, **21**(10):1259–1264, 1981.

[4] Miller, M., 2009. Private communication.

[5] Chapman, J. T. *Spectroscopic measurements of the MHD dynamo in the MST reversed field pinch.* Ph.D. thesis, University of Wisconsin-Madison, 1998.

[6] Anderson, J. *Measurements of the electrical resistivity profile in the Madison Symmetric Torus.* Ph.D. thesis, University of Wisconsin-Madison, 2001.

[7] Chapman, B. E., et al. Sawteeth and energy confinement in the Madison Symmetric Torus reversed-field pinch. *Physics of Plasmas*, **3**(3):709–711, 1996.

[8] Loesser, G., et al. Design and engineering of the Alcator C-Mod lower hybrid current drive system. In *Fusion Engineering, 2002. 19th Symposium on*, pp. 20–22. 2002.

[9] Ekedahl, A., et al. Long distance coupling of lower hybrid waves in JET plasmas with edge and core transport barriers. *Nuclear Fusion*, **45**(5):351–359, 2005.

[10] Goetz, J. A., et al. Design of a lower hybrid antenna for current drive experiments on MST. In T. K. Mau and J. de Grassie, editors, *Radio Frequency Power in Plasmas:14th Topical Conference on Radio Frequency Power in Plasmas*, volume 595, pp. 253–256. AIP, 2001.

[11] Ridolfini, V. P., et al. LHCD coupling during H-mode and ITB in JET plasmas. volume 595, pp. 245–248. AIP, 2001.

[12] Wyman, M. *The physics of high-density, high-β reversed-field pinch plasmas.* Ph.D. thesis, University of Wisconsin-Madison, 2007.

Chapter 4

X-Ray Observations

The acceleration of particles to suprathermal energies is a phenomenon which is prevalent over a broad range of plasmas including the magnetosphere and solar corona. These fast particles can produce extensive radio and x-ray emission which can be used as probes into these usually remote phenomena [1]. Laboratory plasmas, especially those at the high temperatures used for fusion experiments, can also produce high levels of x-ray flux [2]. In particular, rf waves in combination with the ohmic electric field can pull out high energy electron tails, and the use of x-ray diagnostics has verified their presence on many of the larger machines [3, 4].

On MST, soft x-ray tomography has been used to map magnetic islands [5] as well as measure the core bulk electron temperature in PPCD plasmas [6]. At higher energies, hard x-ray observations have been used to model the radial diffusion coefficient in standard and PPCD plasmas [7]. This work will focus on the hard x-ray regime that is loosely defined as photons with energies greater than 10 keV. While the measurement

of the hard x-ray flux will be used primarily to verify the existence of rf-induced fast electrons, it is also possible to calculate or at least to discuss other more interesting quantities related to the x-ray flux. To motivate this discussion, a brief review of bremsstrahlung is warranted.

4.1 Bremsstrahlung

In the energy regime of interest the primary x-ray production mechanism is electron-ion bremsstrahlung: the process by which a photon is emitted when an electron is decelerated in the field of an atomic nucleus. The probability of an electron interacting, and emitting a photon, is:

$$P = n_b \sigma \delta \tag{4.1}$$

where n_b is the bulk density, δ is the distance the electron travels over some time interval, and $\sigma = \sigma\left(p, k, Z, ...\right)$ is the cross-section of the bremsstrahlung interaction, p is the momentum of the incident electron, k is the energy of the emitted photon and Z is the atomic number of the nucleus. The cross-section is for thin targets, which are defined as media in which the electron scattering and loss (as it travels through the media) have a negligible effect on the angular distribution of the bremsstrahlung [8]. Magnetically confined plasmas qualify as thin targets, and for the rest of this work "thin-target bremsstrahlung" and "plasma bremsstrahlung" will be used interchangeably. If it takes a time t for the incident particle to traverse δ, then we have an interaction rate,

$$\nu \equiv \frac{dP}{dt} = n_b \, \sigma \frac{\delta}{t} = n_b \, \sigma v_f, \tag{4.2}$$

where v_f is the velocity of the particle. To get a counting rate, we need the number of incident particles N_f, so we have

$$\frac{dN}{dt} = n_b \, \sigma N_f v_f. \tag{4.3}$$

If instead we use a density of incident particles, then we have

$$\frac{dN}{dt \, dV} = n_b \, \sigma n_f v_f. \tag{4.4}$$

Discriminating the energy of the photon, and the solid angle into which it is emitted,

$$\epsilon \equiv \frac{dN}{dt \, dV d\Omega dk} = n_b \frac{d\sigma}{dk d\Omega_k} n_f v_f. \tag{4.5}$$

where ϵ is defined as the emissivity and $d\sigma/dkd\Omega_k$ is the probability that the interaction results in the emission of a photon of energy k and into a solid angle Ω_k. Equation 4.5 is good for a mono-energetic beam of incident electrons. If instead we have a distribution, then

$$\frac{dN}{dt \, dV d\Omega dk} = n_b \int \frac{d\sigma \left(p, k, \chi, Z\right)}{dk d\Omega_k} v_f f \left(p_{\parallel}, p_{\perp}\right) d^3 p \tag{4.6}$$

where χ is the angle between the incident electron and emitted photon.

To relate (4.6) with our hard x-ray measurement, we let $dV = dA \, dl$ and integrate ϵ over l to get the x-ray flux,

$$\phi \equiv \int \epsilon \, dl = \frac{dN}{dt dA \, d\Omega \, dk}, \tag{4.7}$$

where l is along the line of sight of the detector.

In general, instead of the cross-section $n_b\, d\sigma/dk\, d\Omega_k$ in (4.6), we have

$$n_e \frac{d\sigma_{ee}}{dk d\Omega_k} + Z_{eff} n_e \frac{d\sigma_{ei}}{dk d\Omega_k} + \frac{n_i}{n_e} \frac{d\sigma_r}{dk d\Omega_k} \tag{4.8}$$

where the first term is the cross section of electron-electron bremsstrahlung, the second is electron-ion bremsstrahlung, and the third is the cross section of recombination radiation. For electrons with relatively low energies ($T_0 \ll 511\,\mathrm{keV}$) and $Z_{eff} > 1$ the e-e cross-section is small relative to the e-i cross section [9] so we can neglect it. With our detectors' lower limit of $\sim 10\,\mathrm{keV}$ and impurities in MST with $Z \lesssim 13$, we can also neglect the cross section from recombination [10].

To calculate $d\sigma/dk\, d\Omega$, or integrating over the angle between electron and photon, $d\sigma/dk$, we use formulas 2BN or 3BN from Koch and Motz [8]. These formulas are derived from the relativistic Sommerfeld-Maue wave functions using the Born approximation. The Born approximation cross-section formulas are in general valid for initial and final electron energies that both satisfy:

$$\frac{2\pi Z}{137\beta} \ll 1, \tag{4.9}$$

where Z is the atomic number of the ion and β is the fraction of the speed of light of the electron. For 50 and 10 keV electrons, this corresponds to 0.310 and 0.795 respectively for Z of 3. This isn't very good, but moving to non-relativistic equations is no better as they cannot predict potentially important effects like beaming. Instead the Elwert

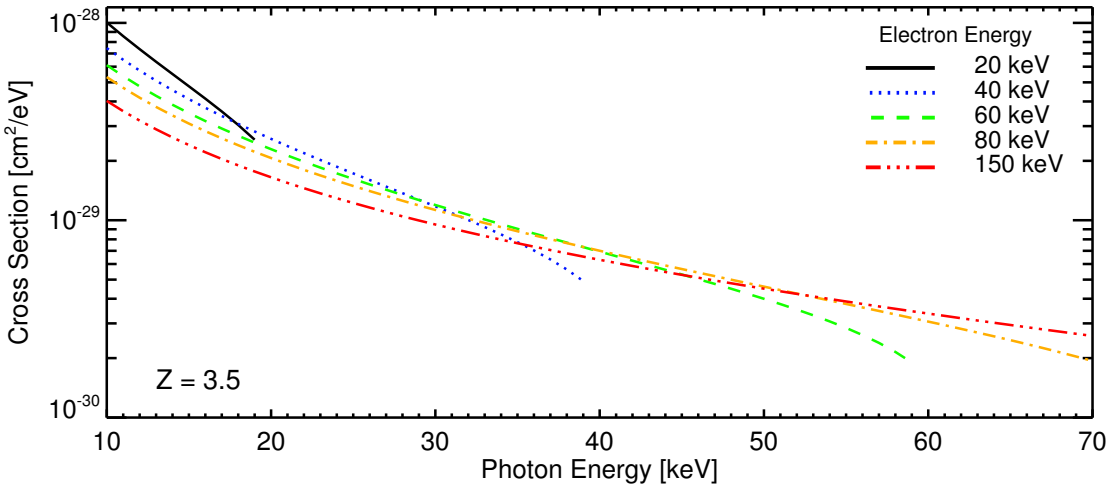

Figure 4.1: Relavistic electron-ion bremsstrahlung cross-sections for the resultant photon energy. The lines represent different incident electron kinetic energies T_0.

correction can be applied [8]:

$$\frac{\beta_0 \{1 - \exp[-(2\pi Z/137\beta_0]\}}{\beta \{1 - \exp[-(2\pi Z/137\beta]\}} \tag{4.10}$$

where β_0 and β are respectively the initial and final velocities of the electron. For lower energies this gives cross-sections with errors less than 10%. Figure 4.1 shows cross-sections $d\sigma/dk$ with the Elwert correction for $Z = 3.5$.

For plasmas, the Born cross-sections are appropriate since the plasma is "thin" in terms of collisionality. As we will discuss in the next sections, data indicate that some fast electrons are hitting solid targets, namely the antenna. In general, the thick-target formulas are obtained from the thin-target cross-sections by calculating the electron energy loss with target depth as it scatters off atomic electrons [11]. The procedure

is to integrate along the electron path up to the photon energy k — since the photon cannot have an energy greater than the incident electron — using an expression for the electron stopping power to find the intensity [12]. When combined with corrections for characteristic radiation, these sophisticated methods compare well with experiment, but only after some semi-empirical fiddling.

The non-relativistic semiclassical formula due to Kramers is often used and compares favorably to the more sophisticated formulations [13]. Because of this and its simplicity, we will use it here. The Kramers' formula is:

$$I_k = KZ\left(T_0 - k\right), \tag{4.11}$$

where I_k is the intensity (in ergs/s/sr/mA/keV) at the photon energy k and T_0 the incident electron kinetic energy, both in keV. Z is the atomic number, and K is a constant. K has been evaluated to $27.6/4\pi$, but has been found to have some dependence on T_0 [13]. Unlike thin targets, this formula predicts that a mono-energetic beam of electrons hitting a thick target will yield an x-ray intensity with a linear repsonse. Both the Kramers' formula and the more sophisticated formulations discussed in [11] have integrated out the angular dependence.

To relate (4.11) to the measured flux (4.7), we convert units from mA of incident current (carried by electrons) to a counting rate of incident electrons, and ergs to emitted photons (where the energy is carried by each photon). Then

$$\phi = I_k \frac{1}{k} 10^{-10} \frac{1}{A} \frac{dN_f}{dt} \tag{4.12}$$

where dN_f/dt is the number of fast electrons per second incident on an area of size A. Finally, for a density of fast electrons:

$$\phi = I_k \frac{1}{k} 10^{-10} n_f v_f. \tag{4.13}$$

Lastly it should be noted that the Z in the bremsstrahlung formulas is not the charge of the ion, but instead the atomic number (and can be applied to neutrals). Because the cross-section goes as Z^2 (with the Elwert correction, the proportionality is $\sim Z^{2.09}$), the flux is also proportional to Z^2 or just Z for the thick-target formulas. We can define an effective atomic number:

$$Z_{eff} = \frac{\sum Z_j n_j}{\sum n_j} \tag{4.14}$$

which can be used for Z. This modification can become important in the cold plasma edge where we may have high impurity influx and either high neutral pressures or non-fully-stripped ions. In this case $Z_{eff} \gtrsim Z^+_{eff}$ where the latter is the effective ionic charge. Because either of these quantities is so poorly known in MST plasmas, this is mostly a distinction without a difference, but unless noted, we refer to the the effective atomic number.

4.2 The Hard X-Ray Diagnostic

The hard x-ray (HXR) diagnostics on MST consist of a set of single channel CdZnTe crystal detectors manufactured by eV Products™ and also a 16-channel detector (also

by eV Products) of CdZnTe crystals arranged in a linear array. The detectors are rated to be sensitive to photons in the 10-250 keV range. As the detectors were designed for medical applications rather than fusion applications, they needed to be structurally modified to reduce noise issues. Despite this, the practical lower limit for the multi-channel detector is $\sim$12 keV.

Each type of detector records single x-ray events and discriminates photon energy by pulse height. The multi-channel detector has on-board shaping that delivers an asymmetrical bipolar pulse whose width is about $1\mu s$. The single channel detectors use shaping electronics that create a Gaussian pulse whose extent is over $2\mu s$. The pulse width gives the maximum counting rate the detector can sustain before x-ray pileup makes it difficult to get accurate counting statistics and energy resolution [14].

The detector events are directly digitized at 10MHz and 12 bits of resolution. The height and thus the energy of the Gaussian-shaped pulses is determined by locating a peak above the noise floor and then performing a Gaussian fit on the pulse. The bipolar pulse's energy is found by taking the maximum voltage of the upper lobe and subtracting the noise floor. The voltage amplitude for each fit is calibrated against the peaks of an ^{241}Am standard source.

The single channel detectors are $10 \times 10 \times 2$ mm giving a surface area of 1 cm^2. Each channel of the multichannel detector is $6.9 \times 3.2 \times 3.2$ mm; however, for the experiments to be discussed, the set of channels is operated as a single detector with total surface area of 3.5 cm^2. The detectors are shown in Fig. 4.2. A CdZnTe crystal thickness of $\gtrsim 2$ mm is sufficient for a stopping efficiency of $\simeq 100\%$ for x-rays below about 50 keV [4]. As will be shown, most HXR production in standard plasma with and without

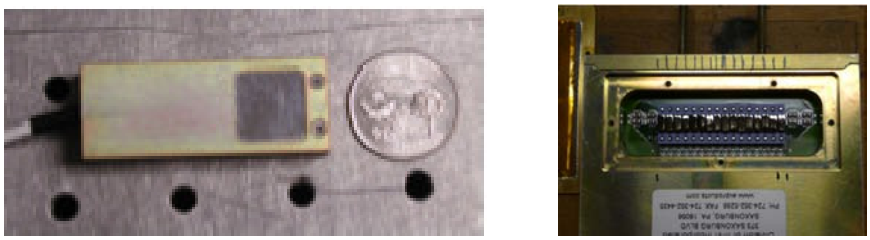

Figure 4.2: Hard x-ray detectors used for measuring emission from rf injection. The detector on the left is the single channel detector with the CdZnTe crystal hidden by the Mylar film. The multi-channel detector on the right with access cover removed.

rf is below this energy, so detector efficiency will be ignored for purposes of calculating the absolute flux.

The detectors are movable and can be mounted at any open porthole on the machine. The single channel detectors for the most part were mounted on a set of "radial" chords as shown in Fig. 4.3a and will hereafter be referred to as the radial array. The multichannel detector was mounted at several toroidal locations, but the line-of-sight always looked through the magnetic axis of the plasma. The detector positions are shown in Figure 4.3b.

To ensure that the detectors were correctly collimated, i.e. not picking up HXR emission from plasma we weren't looking at, the detectors were encased in lead with an appropriate aperture as the initial collimator. Generally small apertures are used to reduce the flux to avoid saturating the detectors. For the low fluxes encountered here, large apertures (which cannot be approximated as pinholes) must be used. Calculation of the etendue for the detectors is discussed in Appendix E.

Since the x-ray energies of most interest are in the 10-50 keV range, the detector window becomes critical. For aluminum and borosilicate glass, the materials of which

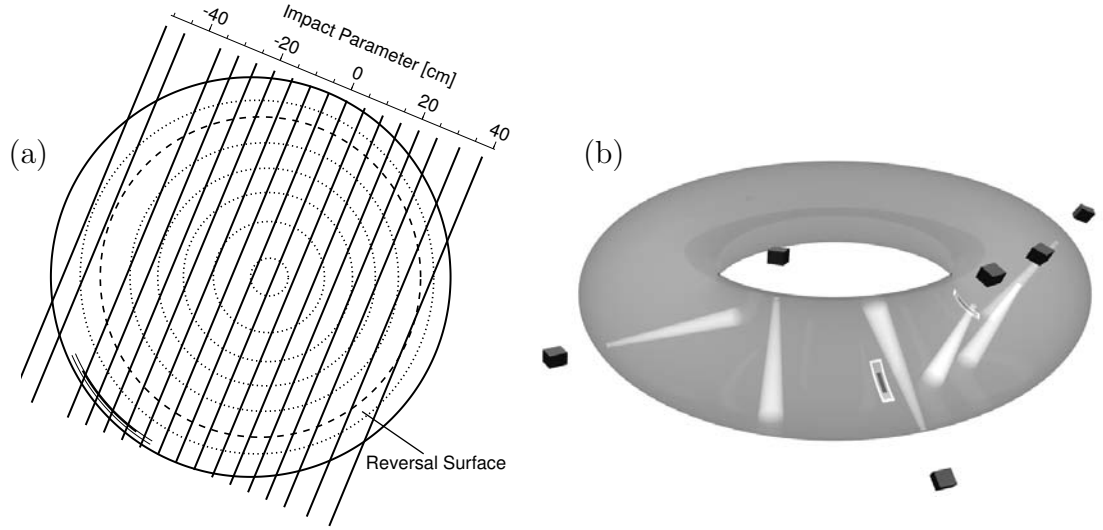

Figure 4.3: (a) Chord locations for HXR radial array. The middle 13 chords of the array are at the same toroidal location as the MkII antenna (150°T) shown on the lower inboard side. The outer 4 chords from inboard to outboard are at 156T, 144T, 154T, and 146T. The array is +60°T from the MkIII antenna. Shown are equilibrium flux surfaces, with the dashed line the $q = 0$ surface. The impact parameter (in cm) is measured from the magnetic axis. (b) Viewing angles of toroidal survey with the MkII and MkIII antennas shown at 150T and 90T respectively. Viewing angles are 30T+15P, 60T+105P, 90T-22.5P, 105T+75P, 120T+75P, and 150T+67.5P. All toroidal positions except that at 150T use the multichannel detector.

our windows are made, the flux attenuation becomes quite significant at the lower energies. The attenuation law for gamma rays is

$$I/I_0 = e^{-(\mu/\rho)\rho x} \tag{4.15}$$

where x is the thickness of the absorber, μ is the linear attenuation coefficient which depends on the energy of the photon, ρ is the density of the absorber [14]. The quantity

(μ/ρ) is called the mass attenuation coefficient and is tabulated for various materials and energies [15]. Figure 4.4 shows the attenuation of aluminum and borosilicate glass for the thicknesses of our windows. While much more transparent than lead, the attenuation must still be accounted for at the lower energies in order to get an accurate emission rate.

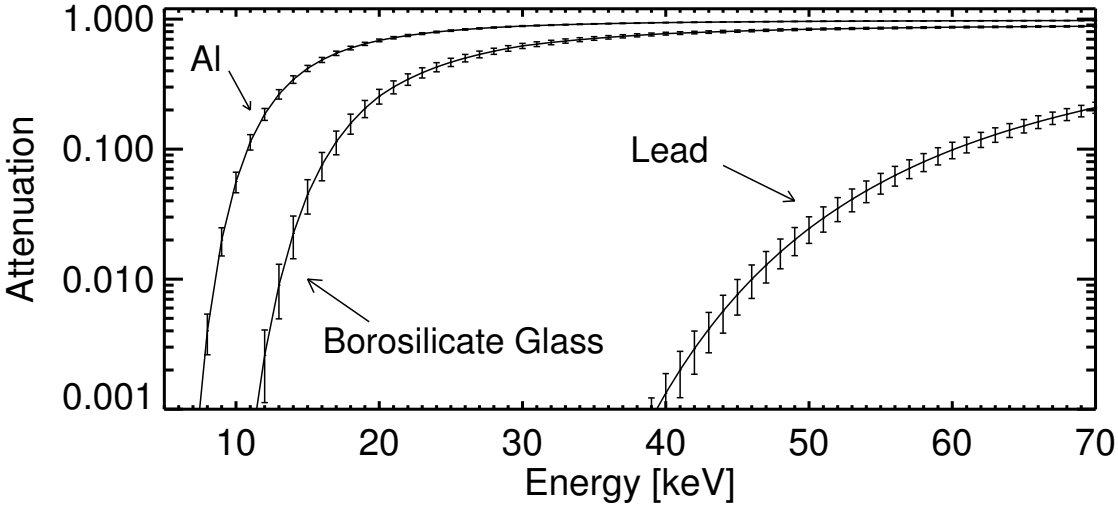

Figure 4.4: Attenuation of x-ray windows used for rf measurements. The aluminum windows used for the single channel detectors are 0.016" thick. The borosilicate glass used by the multichannel detector is 0.105" thick. The attenuation of 0.016" of lead is included for reference.

Despite the pains taken to prevent noise pickup, some steps must be taken in the pre-analysis phase to reject events resulting from a noisy environment. For the Gaussian-shaped events of the single channel detectors, the Gaussian fitting routine rejects noise that it cannot fit and the relatively wide and slowly varying shape with respect to the digitizer rate means that fast transients are less likely to be interpreted

as real x-rays.

Noise rejection for the bipolar shaping of the multichannel detector is more complicated. The faster response time gives more immunity to event pileup, but that and the more complicated shape, especially for x-rays at low energies, makes distinguishing between transients and true events difficult. The first try at filtering rejected an event as noise if the ratio between the magnitude of the first and second peak was outside the range of 1.0-3.0.

Though automated, this procedure was quickly determined to be insufficient, so a system of accepting or rejecting *by hand* each event was put in its place. Though tedious, it had the advantage of good, though not perfect, accuracy. For the x-ray fluxes that present power levels of rf produce, the number of events per shot is — in general — acceptably low to make manual filtering a just-workable solution.

Some operating modes and detector positioning give flux levels that make a manual filtering scheme impractical. An optimized backpropagating neural network was developed [16] to filter events automatically. The network was trained using previously manually filtered data. Though not quite as accurate as manual filtering, overall false positives and false negatives are in the area of a couple percent with most of the errors occurring with the lowest and highest energy events.

An aside on the error analysis is warranted. Since the etendue of the detector and possibly the transmission coefficient may change for different shots, to get an estimate of the total error, we must have appropriate Poisson statistics for an individual energy bin for each shot. The problem arises that for many bins, and especially for the higher energies, there are simply no counts for a particular shot. If that is the case, then the

Poisson error is $\sqrt{n} \rightarrow 0 \pm 0$ counts.

To mitigate this issue, we note that if we know the *rate* at which events happen, then multiply that rate by an amount of time, the result will be Poisson [17]. Given a set of N shots, we divide each time series into bins and use a bin if it satisfies our criteria (rf power, density, etc.). X-rays are then counted for all time bins for each shot and each energy bin. c_{ik} is the result where i indexes an individual shot and k indexes an energy bin. Then we sum over all shots:

$$C_k = \sum_{i}^{N} c_{ik}. \tag{4.16}$$

To get an estimate for the counting rate Λ_k for x-rays of a given energy, we count up all the time bins we used to get τ the total time. The counting rate is then $\Lambda_k = C_k/\tau$. With this we have the variance for an individual shot: $\sigma_{ik}^2 = \Lambda_j t_i$ where t_i is the sum of time bins in the i'th shot. It should be noted that this does not completely solve the problem since some energy bins will have no counts over the entire ensemble of shots. Thus the rate is unknowable with the information we have. To ease computation in this situation we arbitrarily assign $C_k = 0.5$ counts to avoid divide by zero problems in the error propagation.

Once, we have an error estimate, we can proceed to calculate the flux. The counting rate per shot is

$$\lambda_{ik} = c_{ik}/t_i. \tag{4.17}$$

However, we are viewing the plasma through a window, and thus we must divide by

the window's transmission coefficient T_{ik}:

$$\lambda'_{ik} = \lambda_{ik}/T_{ik} \tag{4.18}$$

which is the counting rate that we would see if the window weren't there. Finally, we divide by the width of the energy bin Δk_k (in eV) as well as the etendue G_i of the detector for this shot to get the flux as a function of shot and energy

$$\phi_{ik} = \frac{\lambda'_{ik}}{\Delta k_k G_i}. \tag{4.19}$$

$\sigma_{\phi ik}$, the error in the flux as a function of shot and energy is determined by standard error propagation from the error in the counting rate, σ_{ik}, as well as the errors in transmission coefficient and etendue, σ_{Tik} and σ_{G_i} respectively. Then the flux and its error can be found by calculating the weighted average:

$$\phi_k = \frac{\sum \phi_{ik}/\sigma^2_{\phi ik}}{\sum 1/\sigma^2_{\phi ik}}, \qquad \sigma^2_{\phi k} = \frac{1}{\sum 1/\sigma^2_{\phi ik}}, \tag{4.20}$$

where all variables are averaged over the shot.

4.3 Experimental Observations

With the available set of hard x-ray diagnostics, we now turn to a set of experiments that attempt to gauge the plasma's response to launching lower hybrid waves. In some operating regimes, MST is an excellent testbed for observing rf-induced x-rays. In

standard and non-reversed plasmas up to ~ 450 kA — which will be the case for the remainder of the Chapter — there is almost no background x-ray emission unless the plasmas are very diffuse: $\langle n_e \rangle \lesssim 0.8 \times 10^{13}\,\mathrm{cm}^{-3}$. For low-density plasmas, the edge plasma can become decoupled and form a very non-Maxwellian distribution which can spawn many fast electrons and high-energy photons. While of interest in its own right, this background will pollute the lower hybrid hard x-ray spectrum and can be difficult to subtract. As a result, the following experiments are done with line-averaged densities $\geq 1 \times 10^{13}\,\mathrm{cm}^{-3}$.

It is typical in antenna analysis to divide the overall field of the antenna into three regions: the near field, the Fresnel region, and the far field [18]. It will be convenient to separate these experiments into two main categories: those observations of x-rays in the far field and those in the near field. While there are various definitions of what constitutes which region, most are only reasonable for free-space antennas launching an electromagnetic wave. We will use the definition of Karpman [19] where the near field will be defined as distances from the antenna that are small in comparison to the wavelength of the radiated wave. The wavelength of the launched wave changes rapidly as it penetrates, but looking at results of ray-tracing, we can make the approximation $\lambda \sim 1$ cm. The far field will be at distances much farther away from the antenna than that.

4.3.1 The Far Field

Early hard x-ray experiments using the MkII antenna at ~ 80 kW showed no x-ray production at toroidal angles off the antenna (at 150T), and only a hint when the

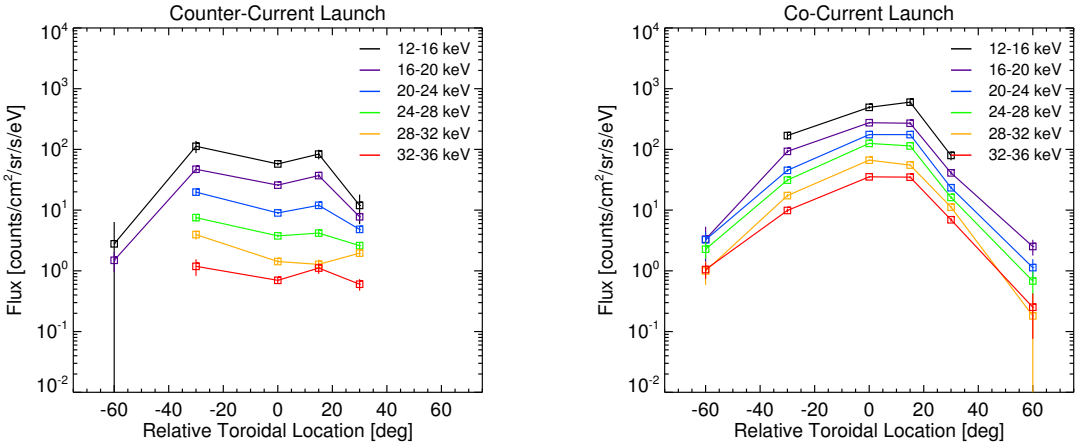

Figure 4.5: Toroidal survey of HXR flux for both launch directions with 160 kW of input power. The plasmas are standard 400 kA with densities $1.0 - 1.5 \times 10^{13}\,\mathrm{cm}^{-3}$ The detector chords look through the magnetic axis.

viewing chord at 150T was not looking at the near field. With the increase in power handling capability of the MkIII antenna, a new survey was performed at the multiple toroidal locations shown in Figure 4.3b. For rf input powers above about 100 kW, we start to see x-ray emission at toroidal angles not in-line with the antenna.

Due to the low overall counting rate, a large ensemble of shots was used for each toroidal location and was subject to the analysis method of §4.2. Even so, the poor statistics of the background spectrum makes the magnitudes in the higher energies higher than they might be. For this ensemble the MkIII antenna was operated at 160 kW input power in 400 kA standard plasmas. Only events away from sawteeth with average densities between $1 - 1.5 \times 10^{13}\,\mathrm{cm}^{-3}$ were used and Figure 4.5 shows the flux for different x-ray energies at toroidal angles up to 60° away from the antenna.

There is a marked toroidal asymmetry. For the port 1 or counter-current drive

launch direction, the flux over about 40° is fairly flat with the flux dropping down to just above background levels at 60° away from the antenna, but with the flux level at +60° higher at all energies than at −60°. The co-current drive direction, port 2, shows a slightly different toroidal shape. The flux falls off faster than in the counter-current direction, and there appears to be an asymmetry about the antenna location where the flux at all energies is at a lower level at +30° and +60° than at −30° and −60° relative to the antenna. The peak flux in the co-current direction is also higher by almost an order of magnitude than the counter-current launch. In both feed directions, however, measurements taken 90° away show x-ray production at the background level.

While B_ϕ is small relative to a typical tokamak, it is not zero. As shown in Figure 3.9b, standard plasmas — with a reversal parameter of $F \simeq -0.2$ — have a field line pitch of about −7° with respect to the antenna. This pitch might itself lead to the asymmetry seen in the flux produced by a co-current launch. To explore this, another experiment was done with non-reversed plasmas. These plasmas have the safety factor go to zero at the edge of the plasma ($F = 0$). With the antenna slightly tilted, the pitch angle (with respect to the antenna) is actually about +2.5°. Results are shown in Figure 4.6.

Unfortunately, data is not available at ±60°, but some comments can be made in comparing the flux to that of the standard reversed case. Overall, the differences are quite small, despite the significant change in the q-profile. The flux as a function of toroidal angle stays relatively constant in the counter-current direction while the flux in the co-current direction loses some of the asymmetry about 0°.

The fact that the flux has a dependence on the toroidal angle is not particularly

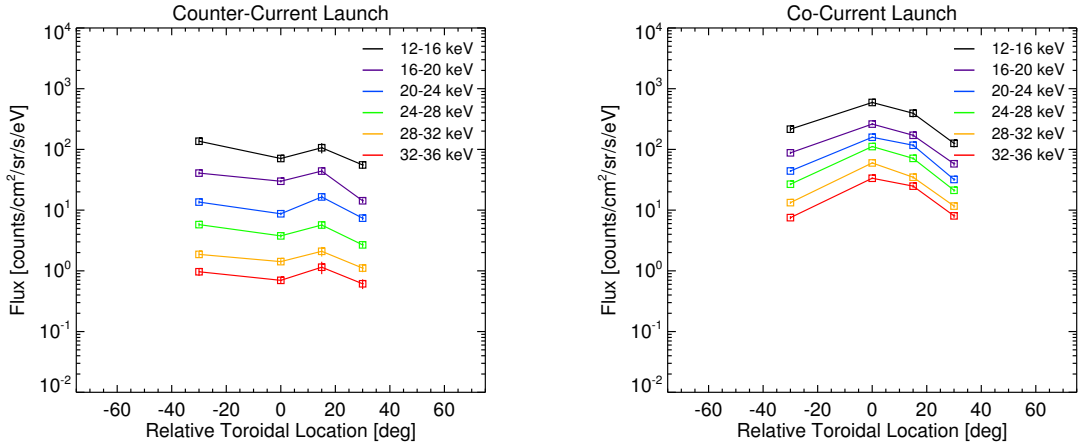

Figure 4.6: Toroidal survey of HXR flux for both launch directions with 160 kW of input power. The plasmas are non-reversed 400 kA with density $1.0 - 1.5 \times 10^{13}\,\mathrm{cm}^{-3}$. The detector chords look through the magnetic axis.

surprising in plasmas with low energy confinement since fast electrons are lost quickly. What is surprising is that the toroidal dependence does not seem to change as a function of photon (and by inference electron) energy.

One normally expects that injected rf power Landau damps on electrons in the absorption region after which the ohmic electric field pulls the now-decoupled electrons into a high energy tail in the distribution. Anderson *et al.* [20] have calculated that the parallel electric field in standard 400 kA plasmas to be on the order of 0.5 V/m. Assuming a generous 4 keV starting energy from Landau damping, for the tail electrons to reach energies high enough to produce hard x-rays in the 40 keV region (which we see), electrons would need to travel over 70 kilometers, generally making many toroidal transits. If this were the case, then to first order we should see similar x-ray flux for comparable viewing chords at any toroidal angle.

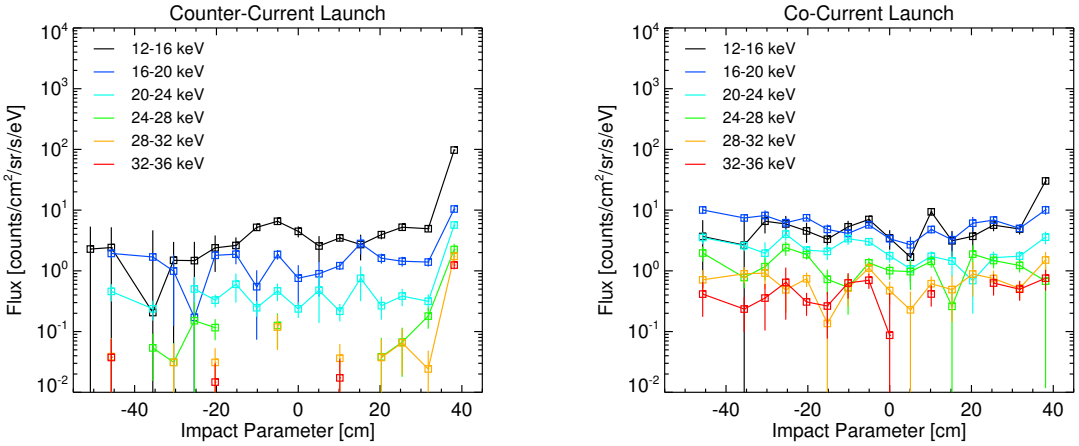

Figure 4.7: Radial survey of HXR flux 60° away from the MkIII antenna.

Since this is not the case, either the mechanism for producing the fast electrons (and high energy x-rays) is not by way of the ohmic field, or there is a structure (for example near the $q = 0$ surface where the field lines are purely poloidal) that allows electrons to gain high energies without circumnavigating the vessel. The latter hypothesis must also account for similar observations in both the reversed and non-reversed configurations.

A radial survey of the hard x-ray flux may be instructive in determining if absorption of the LH wave is taking place at the predicted radial location. Because only thirteen detectors were available for the seventeen chordal views and the count rate was so low (the detectors are 60° away from the MkIII antenna), an ensemble of shots with the same constraints as the toroidal survey is used. The data are shown in Figure 4.7. As seen from the toroidal survey, far from the antenna, the flux is just above background and leads to poor statistics especially at energies above 20 keV. Despite this issue, several observations can be made.

The radial profile is quite flat across the majority of the plasma cross-section. If

one takes the x-ray emissivity to be a function of the poloidal flux, ψ, then a flat flux profile corresponds to an thin annulus of current from fast electrons at a radial location outside the viewing region. This observation supports the conclusion that the antenna is launching a wave that propagates and deposits it's power at the edge rather than the core.

The outermost viewing chord at $x = +38.1$ cm shows an order of magnitude more flux than the rest of the chords for the counter-current drive launch, and a smaller but significant uptick in the co-current launch direction. Equilibrium reconstruction shows that this particular chord is more or less tangent to the reversal surface for these plasmas. The initial assessment is that this chord is looking precisely at the annulus of current that produces the flat profile over the rest of the cross-section.

In the toroidal survey the flux in the co-current direction is higher than in the counter-current direction so it is peculiar that the outermost viewing chord should have its flux juxtaposed in magnitude. Ray-tracing and Fokker-Planck modeling [21] shows that counter-driven current is absorbed deeper into the plasma than co-driven current. If the absorption region for the counter-driven current coincided with the outermost viewing chord then we might expect the higher x-ray flux while the detector missed the co-driven current farther out radially.

While the current can be considered a flux function, the x-ray emissivity is not by virtue of the phenomenon of relativistic beaming of the x-rays. At higher energies the bremsstrahlung cross-section $d\sigma/dkd\Omega_k$ is higher in the direction of the incident electron. Figure 4.8 shows the asymmetry for an incident 50 keV electron. The ratio of forward to backward cross-sections is fairly constant across the emitted photon energies.

This effect will be particularly pronounced in the RFP where poloidal viewing chords can be almost tangent to field lines (especially at the reversal surface) [22]. The electron direction for standard MST plasma is up on the outboard side so electrons are moving toward outboard detectors and away from inboard detectors.

The innermost chords at $x = -50.8$ cm and -45.7 cm are farther out than the +38 cm chord (in terms of ψ_N), and they see no similar uptick. Either the fast electron current sheet is narrow enough that the these chords completely miss it or the beaming effect is strong enough to account for the difference. For counter-current launch, this ratio between the +38 and -45 chords – around the same ψ_N — is about 50:1. This is much larger than would be expected for beaming unless the incident electron energies were hundreds of keV. Since we have no evidence of x-rays above ~ 80 keV, this is unlikely.

The peaking on the outboard chord is not only an rf effect. In plasmas without injected rf power, this chord also sees above-average fluxes as shown in Figure 4.9. The condition for thermal electrons to runaway is [23]

$$E_c = \frac{4\pi n_e e^3}{T_e}\left(\ln\Lambda + \ln\left(\frac{4\pi n_e e^3 \ln\Lambda}{T_e E_\parallel}\right)\right), \tag{4.21}$$

where the onset of runaway production occurs at $E_\parallel/E_c \sim 3\%$. Standard MST plasmas have parameters very close to this 3%. As expected from (4.21), the magnitude of the flux is highly dependent on the plasma density. At higher densities, the flux is so scant that a large ensemble of shots is required to assemble a spectrum.

The observations of both the apparent production of an rf-induced fast electron

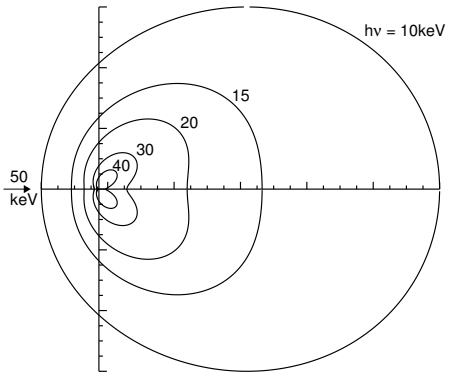

Figure 4.8: Relativistic forward beaming for bremsstrahlung. The cross-section will be higher in the direction of motion of the incident electron. The effect becomes more pronounced for higher energy electrons.

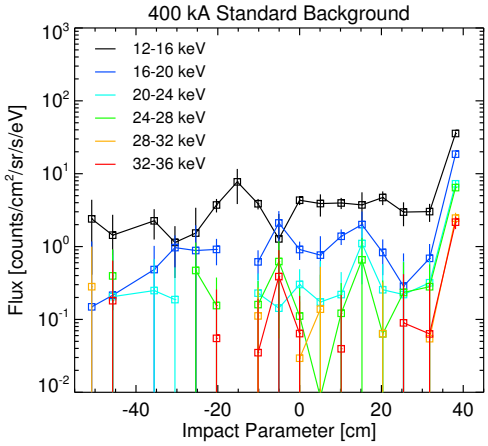

Figure 4.9: Radial survey of background HXR flux in 400 kA standard plasmas with line-averaged densities $0.5 - 0.8 \times 10^{13}\,\mathrm{cm}^{-3}$.

current sheet (or at least a region of high emissivity in the edge) and the toroidal asymmetry we see are difficult to reconcile. If the lower hybrid wave absorbs just inside the reversal surface, some class of superthermal electrons (via Landau damping) will be resonant with a drift velocity. This class might be localized to a particular toroidal angle while they are accelerated by the ohmic field. While possible, all the various drifts must be finely balanced even as the the particle's parallel velocity increases (causing a certain change in the curvature drift). Since an electron will need tens of kilometers to accelerate to 40 keV, this scenario is unlikely.

There is another possibility in the same category as the reversal surface trapping that should at least be mentioned. The perpendicular velocity rather than the parallel

velocity could be the driver of the high energy x-ray flux. If Landau damping drives the parallel energy up to $\sim$4 keV and then parallel and perpendicular diffusion moves the electron higher into perpendicular velocity space, it will slow below the Landau resonance. A second pass through the absorption region and another round of diffusion will allow the electron to move yet higher in velocity space. Can this cycle get the fast electrons to $E_\perp \gtrsim 40$ keV?

Figure 4.10 shows the distribution function from the results of CQL3D modeling of 100 kW of co-current drive. While there is a significant spread in perpendicular velocity space, the contours show clearly that for perpendicular energies at all close to approaching the measured flux energies, the parallel energies by themselves would be easily sufficient to obtain those same fluxes. So this mechanism cannot explain the toroidal asymmetry in x-ray flux.

Lastly we look at the shape of the HXR spectra. Figure 4.11a shows the background spectra for three different density ranges seen from the +38 cm radial x-ray chord. Figure 4.11b shows the spectra from the same chord, but with 160 kW of rf power in high density plasmas ($1 - 1.5 \times 10^{13}\,\mathrm{cm}^{-3}$). Qualitatively there appears to be a "kink" at 30 keV, so a two-temperature fit to the tail can be used to characterize the spectrum [2, 24]. For the background spectra, the "characteristic" temperature increases slightly as the density increases. The higher energy tail falls off roughly half as quickly for each density, though the statistics are quite poor for the high density spectrum.

The rf spectra whose density corresponds to the triangles in Figure 4.11a shows a much steeper falloff in the spectrum for each of the launch directions than the back-

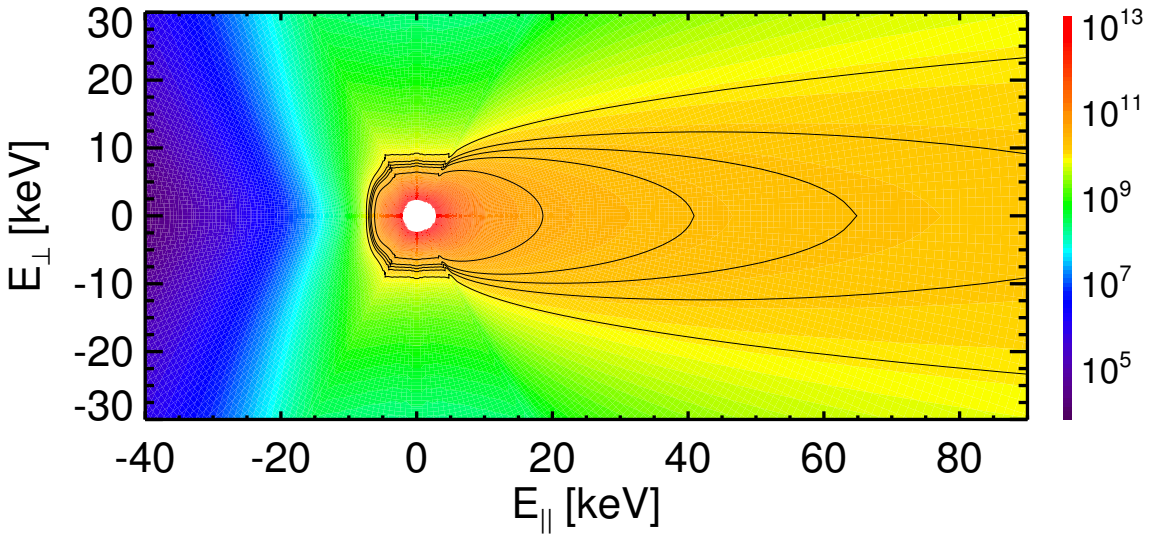

Figure 4.10: Distribution function from CQL3D at r/a=0.8, near the absorption region for 100kW of rf power and $D_\rho = 1\text{m}^2/\text{s}$

ground at a similar density. Both of the characteristic temperatures are about half as large as the background temperatures. The magnitudes for co-current and counter-current launch are similar indicating that the x-ray production mechanism is probably also the same. The disparity between the background and rf spectra however suggests a differently-shaped fast electron distribution and thus the mechanism for producing that distribution might also be different.

We certainly expect the origin of the fast electrons — either background or rf-induced — to be different: the background electrons will either be thermal or "fast" where fast in this context means drifted but still less than 1 keV [23]. The rf-induced electrons are normally boosted by Landau damping to the phase velocity of the wave at absorption: 2-4 keV. In either case the background ohmic field takes over and pulls

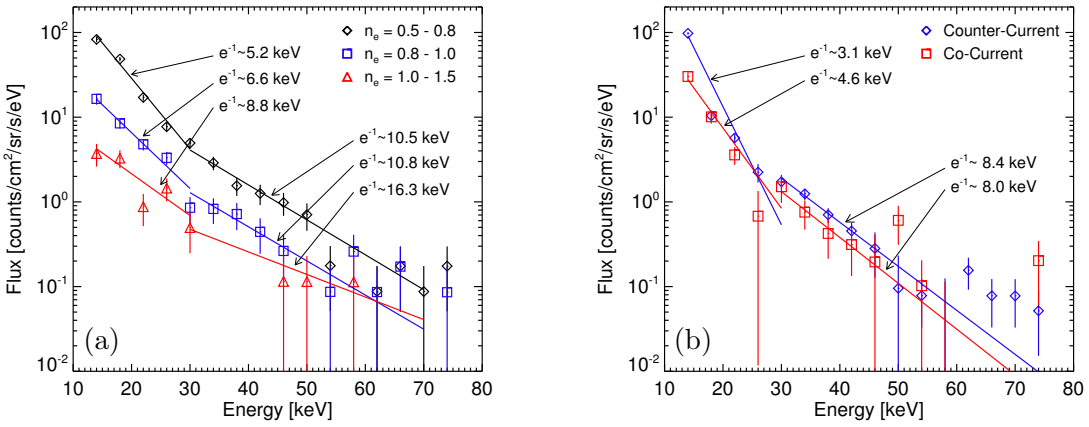

Figure 4.11: Hard x-ray spectra detector chord at $x = 38.1$ cm. (a) Background spectra for three different density ranges ($\times 10^{13}\text{cm}^{-3}$) (b) Spectra for MkIII antenna in both launch directions. Density is $1 - 1.5 \times 10^{13}\text{cm}^{-3}$. Fits are 12-30 keV and 30-80 keV, with the characteristic temperature corresponding to the e-folding length.

the tail out to high energies. CQL3D modeling predicts that while a clear knee at the Landau resonance is seen, above about 14 keV, the only difference in the shape of the spectra is in the magnitude.

4.3.2 The Near Field

As noted in the previous section, while low power experiments found no discernible rf-induced x-ray flux at toroidal angles away from the antenna location, the radial array at 150T — at the same angle as the MkII antenna — observed significant flux. When the MkII antenna is operating, the array's viewing chords intersect the near field zone of the antenna.

An ensemble of shots at 400 kA and line-average densities between $1-1.5\times10^{13}$ cm^{-3}

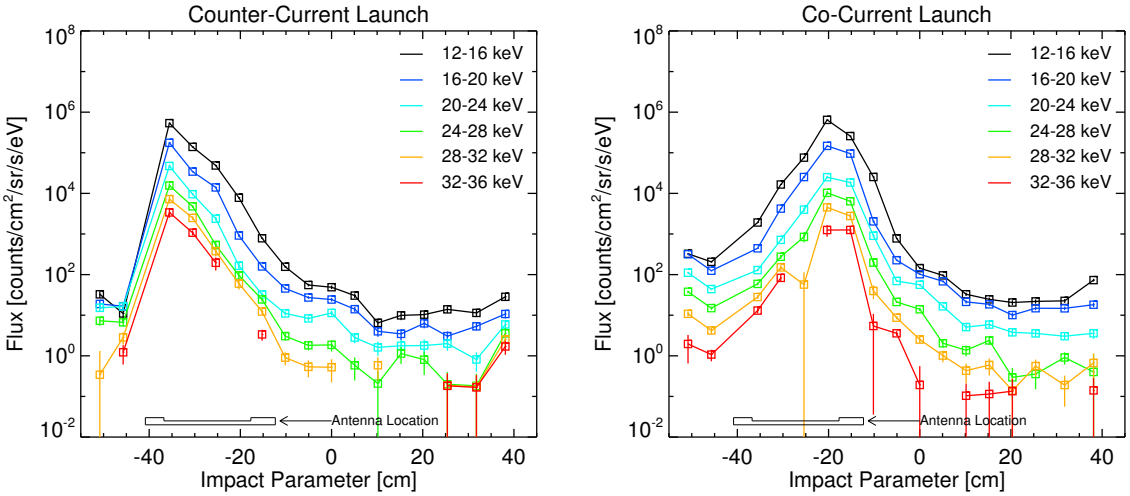

Figure 4.12: Hard x-ray flux from a set of radial chords looking at the MkII antenna. The peak flux is centered at the port being fed power.

were used with the MkII antenna operating at ~ 90 kW input power. The radial measurements of x-ray flux are shown in Figure 4.12 for both launching directions. A sketch of the antenna is superimposed where the viewing chords would intersect it.

The results are dramatic. The chords that intersect the antenna face (*on-antenna* chords) show much more flux than the chords that do not (*off-antenna* chords). The peak flux for either launching direction ($\sim 10^6\,\mathrm{cm}^{-2}\mathrm{sr}^{-1}\mathrm{s}^{-1}\mathrm{eV}^{-1}$ at 12-16 keV) is more than 3 orders of magnitude higher than any off-antenna chord. Moreover, this peak flux is also much larger than the flux seen by all (off-antenna) chords when the MkIII antenna is operating at almost double the input power.

Also clear from the Figure is the fact that the location of the peak flux depends significantly on the launching direction. The peak appears to be centered nearest the end of the antenna from which the power is being fed. It should be noted that since

the power is presumably being coupled to the plasma and damped as the wave travels down the antenna, the feed end will possess the most power.

With the amount of flux available from the on-antenna chords in the radial survey it becomes feasible to attempt a confinement time measurement of these fast electrons that are (presumably) generating the observed high energy x-rays. Such a measurement is not practical for the toroidal survey since the flux is simply too low.

To measure the confinement time of fast electrons generated by the LH antenna, the input power was square-wave modulated with a period of 2 ms. A set of 60 shots in standard plasmas was ensembled and the x-ray counts were binned with a 5 μs width relative to the rising and falling edges of the rf modulation. The modulation is not perfect, so the edges also have a width of about 5 μs. A typical modulated shot is shown in Figure 4.13.

Figure 4.14 shows the ensembled falling edge of the rf modulation while Figure 4.15 shows the ensemble of the rising edge and the associated x-ray flux at the rf power transition. These data are from the viewing chord at -35.6 cm and a co-current launch. Both Figures show that to within the width of the transition, the x-ray flux appears and ceases immediately with the application or cessation of rf power.

By (4.3) or (4.13), we assume that the x-ray flux is proportional to some population of fast electrons n_f in the volume of our viewing chord. Constructing a simple continuity equation for the fast electrons, we have

$$\frac{\partial n_f}{\partial t} \simeq -\nabla \cdot (n_f \mathbf{u}) - \nu_s \, n_f + S_{ohmic}\,(t) + S_{rf}(t) \tag{4.22}$$

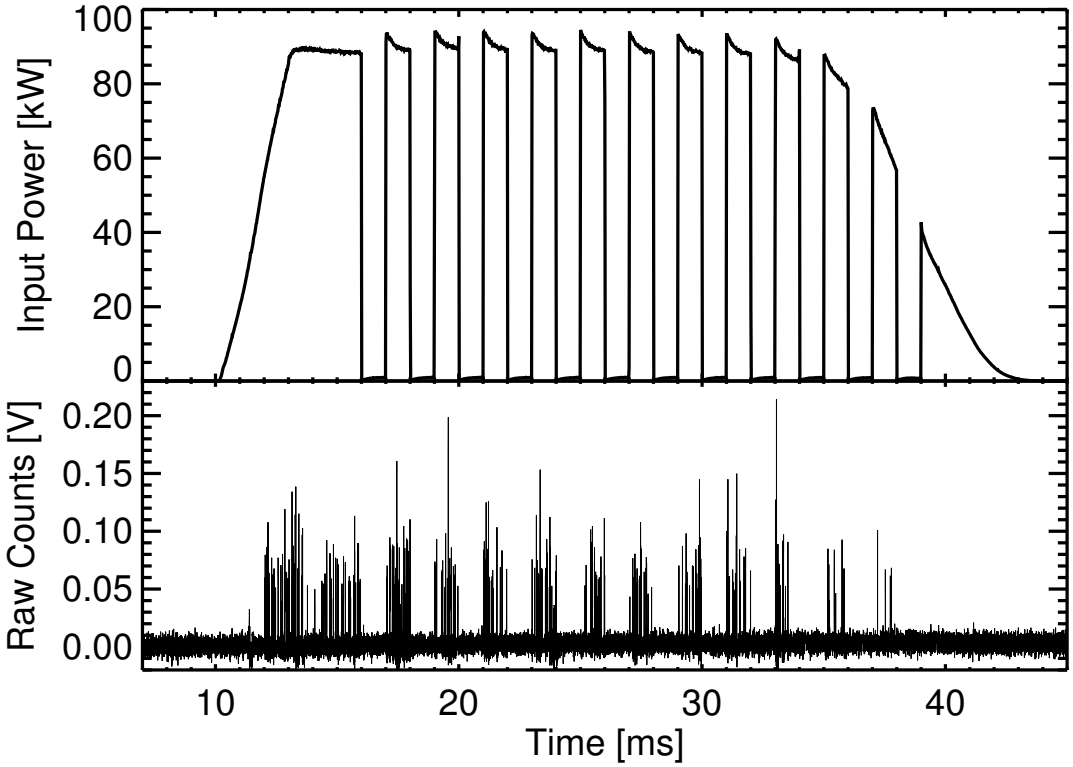

Figure 4.13: Modulation of the rf input power and the typical hard x-ray flux of a detector looking at the face of the MkII antenna.

where the first term on the right is the flux of particles entering or leaving the viewing volume, the second is the collision term where $\tau_s = 1/\nu_s$ is the slowing down time for the fast electrons, S_{ohmic} is the source term representing electrons accelerated into the *fast* population by the ohmic electric field and S_{rf} is the source term for other rf-induced effects on the electrons include Landau damping. For our purposes, given the fact that the diagnostics are sensitive to x-rays above $\sim$10 keV, we will define those electrons with energies above 10 keV as fast electrons.

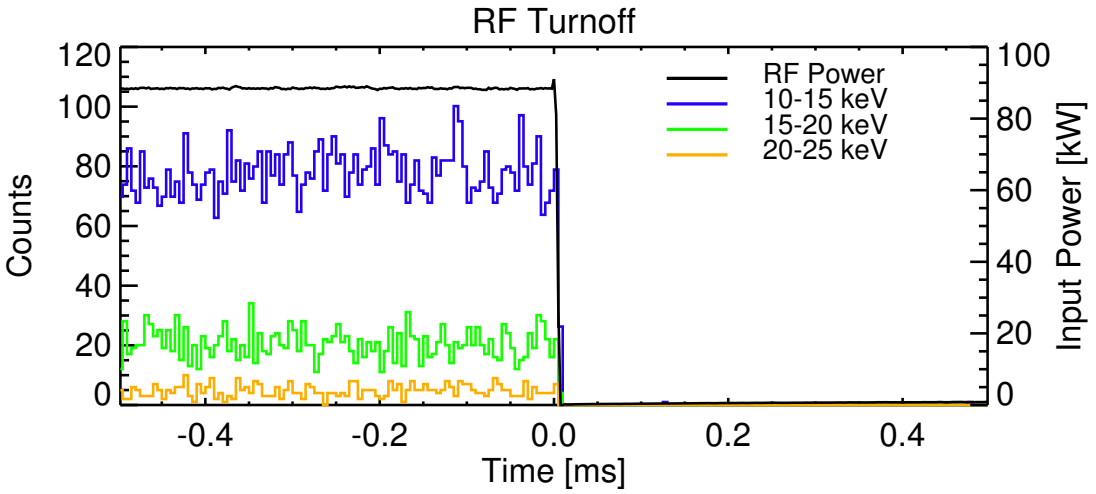

Figure 4.14: Hard x-ray flux relative to the turn off of rf modulation.

Taking the rf turn-off experiment first, we have at $t_{off} > 0$, $S_{rf} \rightarrow 0$. For an equilibrium background field, S_{ohmic} is constant; however, we will assume for now that the accelerating field cannot significantly inhibit the losses and show *a posteriori* that this is the case. Then losses by particle flux out of the viewing volume as well as losses due to fast electrons slowing down can be aggregated to first order as

$$\frac{\partial n_f}{\partial t} \sim -\nu_f n_f, \qquad t_{off} > 0 \tag{4.23}$$

where $\tau_f = 1/\nu_f$ is the characteristic confinement time for these fast electrons. Considering the rate of decay of the x-ray flux, we can estimate the fast electron confinement time is on the order of 5 μs. For 10 keV electrons, the slowing down time is about 5 ms, so on the time scale of interest, the electrons are collisionless, and all the loss is due to particle flux out of the viewing region (and presumably the plasma).

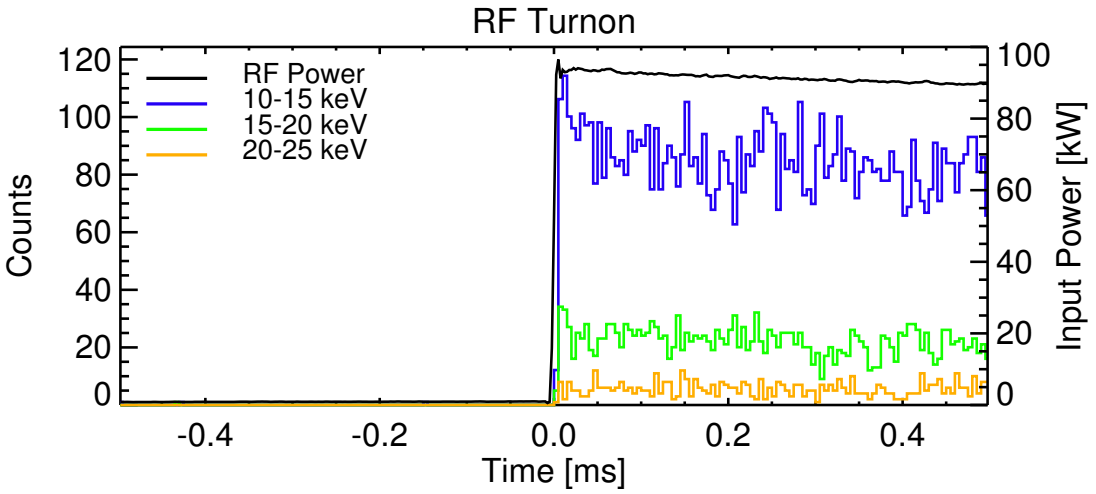

Figure 4.15: Hard x-ray flux relative to the turn on of rf modulation.

For the rf turn-on experiment, the x-ray flux (and presumably the fast electron) growth rate is also on the order of 5 μs. For a Landau damped electron starting at (a quite generous) 4.6 keV, at $\sim$0.5 V/m, accelerating to 10.5 keV would require 0.25 ms and 16.7 keV would take almost 0.4 ms. (For a thermal electron the required time is 0.65 and 0.8 ms.) Then even if S_{rf} provided the Landau damping, the S_{ohmic} source cannot contribute anything to the population (and cannot inhibit the losses either).

S_{rf} must then solely generate the fast electron population. Considering that the decay time τ_f is also on the order 5 μs, then the source must accelerate electrons (either thermal or possibly Landau damped) up to 20-50 keV in at most that time.

4.3.3 Antenna Interaction

The mechanism for the production of high velocity electrons in front of the antenna (and away from it) as observed in the previous sections must in some way be explained.

The question of the bremsstrahlung process itself is a slightly different one. Conservation of energy requires that any fast electron colliding with a (cold) ion must have a kinetic energy greater than the photon produced, so observation of high energy photons requires an mechanism for yet higher energy electrons. There are two possibilities for the background nuclei: bulk plasmas ions directly in front of the antenna, and/or the lattice nuclei of the antenna itself. The observations from Figure 4.12 illustrating the difference between on-antenna and off-antenna x-ray emission suggest that the antenna may be acting as a target for fast electrons.

MST has a set of eight 2" ports directly opposite the MkIII antenna at 90T. Having been previously used as Thomson scattering viewing windows, a set of quartz lenses on these ports had already been installed. Mounting a CCD camera at the focal point of a subset of these lenses allows a good closeup view of the antenna.

A Dalstar CA-D1 CCD camera with 128×128 resolution and exposure time of 1.276 ms was used to capture the images. Figure 4.16 shows a set of frames captured by the CCD camera during a pair of high power rf pulses. It was noted that there appeared to be damage to the antenna face at the port 2 end near the aperture. Further inspection showed that a manufacturing defect of the molybdenum PFC had allowed it to slip down the antenna face exposing the copper frontplane.

The exposed copper appears to have been eaten away, presumably by the impact of high energy particles. Indeed, the lower sequence of images of Fig. 4.16 shows light from the the exposed copper region saturating the camera when 160 kW of power is applied to the port 2 antenna feed.

The upper sequence shows the antenna interaction near the port 1 feed when 195

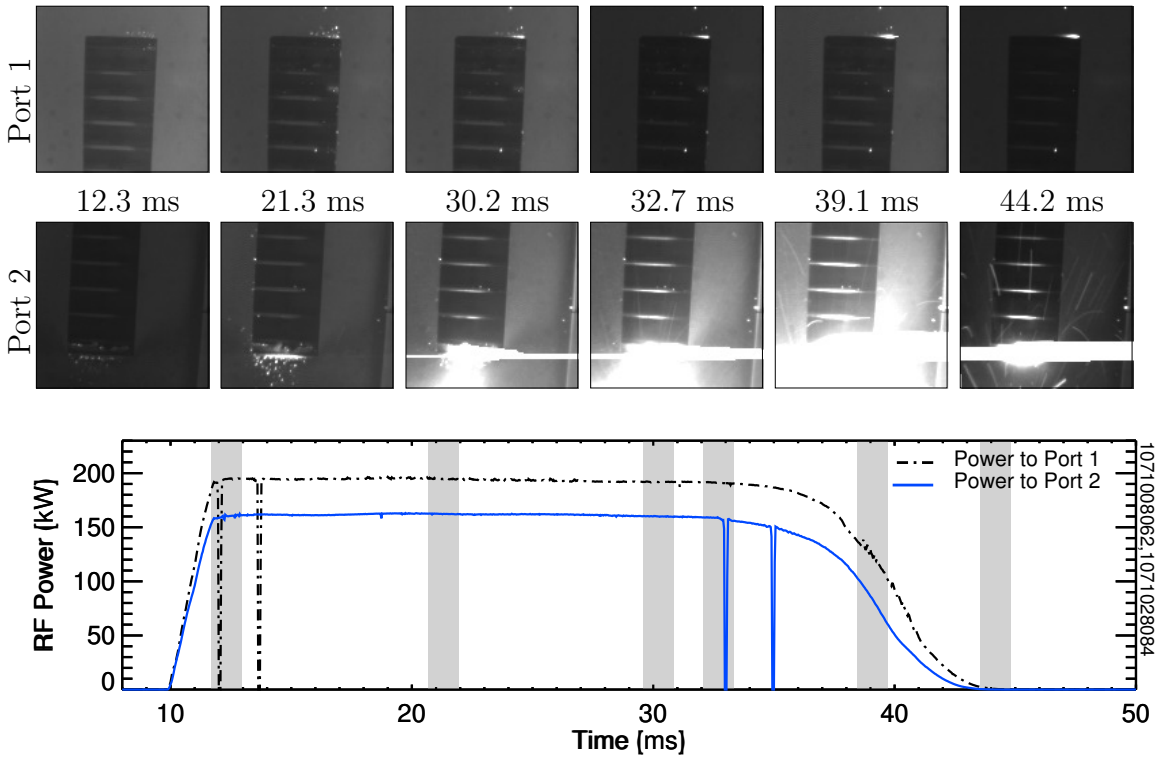

Figure 4.16: CCD camera view of the MkIII antenna showing fast electron interaction with antenna prior to correcting the molybdenum front cover. Each frame has an exposure time of 1.28 ms.

kW of power is applied to port 1. There is visible interaction at the upper right-hand edge of the aperture, but unlike port 2 side there is no exposed copper to sputter.

Interaction with the antenna is visible only at the feed end of the antenna. For example, looking at the port 2 end of the aperture with power is fed at port 1 shows no apparent brightening, even with the copper exposed. This observation is a verification that the (backwards) phase velocity of the ohmic field pulls out the fast electron tail in the phase velocity direction.

As an aside, the sequences also reveal the pitch angle of the guide field relative to the antenna. The electrons being accelerated into the aperture are following the field lines such that most of the apparent interaction occurs on the upper-right and lower-left edges of the aperture.

4.3.4 Discussion

The visible interaction with the antenna is further evidence that the cause of the large on-antenna flux is from fast electrons hitting the antenna itself rather than interacting with plasma ions directly in front of the antenna. Assume for the moment the alternate hypothesis: it is the plasma rather than the antenna. Starting then with (4.4) and taking the differential with respect to the energy of the emitted photon, we have

$$\epsilon \equiv \frac{dN}{dt\, dV d\Omega\, dk} = \frac{1}{4\pi} n_b \frac{d\sigma}{dk} n_f v_f, \tag{4.24}$$

where we have integrated over the angle between the incident electron and emitted photon, and we have assumed isotropic emission.

If we then take $dV = dAdl$ and integrate ϵ over l assuming that the emmisivity is constant in a certain region of width Δl and zero everywhere else, then we have

$$\phi\,(k) \equiv \frac{dN}{dt\, dA\, d\Omega\, dk} = \int \epsilon\,(k,l)\ dl \simeq \Delta l \sum \epsilon\,(k,l) = \Delta l\, \epsilon\,(k) \tag{4.25}$$

where ϕ is the measured x-ray flux. Combining (4.24) and (4.25),

$$\frac{1}{\Delta l}\phi = \frac{1}{4\pi} n_b \frac{d\sigma}{dk} n_f v_f. \tag{4.26}$$

For the sake of argument, we will choose $\Delta l \simeq 1$ cm, $n_b = 1 \times 10^{12}\,\mathrm{cm}^{-3}$, $Z_{eff} = 6$, and for the incident electrons a monoenergetic beam with $T_0 = 15$ keV. The last two are likely too large and too small respectively, so these choices will underestimate the fast electron population required. For the flux, we choose the peak measured value of 10^6 at 14 keV. Evaluating the cross-section and plugging in,

$$\frac{1}{1} 10^6 \simeq \frac{1}{4\pi} \left(10^{12}\right) \left(4 \cdot 10^{-28}\right) n_f \left(7.1 \cdot 10^9\right), \tag{4.27}$$

yields a required fast electron density of $n_f = 4.4 \times 10^{12}\,\mathrm{cm}^{-3}$. A fast density on the order of the bulk density — which is an *underestimate* — is simply unrealistic.

What if instead the x-ray emission were from thick-target bremsstrahlung? The viewing chord at -35.6 cm looks onto the antenna face with two-thirds of its spot is the molybdenum of the antenna frontplane and one-third looks through the aperture into the antenna cavity. The backplane is silvered, but we will assume that our x-ray emission is from the molybdenum frontplane.

While the characteristic radiation for most of the materials in MST occurs beneath the instrumental threshold of the hard x-ray detectors, the K_α and K_β transitions for molybdenum are at 17.4 and 19.7 keV respectively [25]: well within the sensitivity of the diagnostic. One would expect to see these peaks easily, but we do not. However, experiments by Chervenak [13] have shown that the angle of incidence and emission

matter a great deal in the production of line radiation. For shallow incident angles, which we might expect from our geometry, Chervenak found that the molybdenum characteristic radiation was completely absent.

With this concern allayed, we combine (4.11) and (4.13),

$$\phi = \frac{27.6}{4\pi} Z \left(T_0 - k\right) \frac{1}{k} 10^{-10} n_f v_f. \tag{4.28}$$

For molybdenum $Z = 42$. Evaluating as before,

$$10^6 \simeq \frac{27.6}{4\pi} \left(42\right) \left(15 - 14\right) \frac{1}{14} 10^{-10} \, n_f \left(7.1 \cdot 10^9\right) \tag{4.29}$$

gives a density of $n_f = 2 \times 10^5 \, \mathrm{cm}^{-3}$, a much more plausible value. For the thick-target formulas, using $T_0 = 15$ keV overestimates the fast electron population, since the observations show incident electrons beyond 30 keV.

Repeating the exercise for off-antenna viewing chords and assuming plasma bremsstrahlung, we get fast electron densities 4 to 5 orders of magnitude smaller than the bulk (plasma) density. These numbers are not implausible; we may not need to invoke thick-target bremsstrahlung with the wall to explain the magnitude of the flux. Without knowing the source and mechanism for fast electron acceleration, however, it is difficult to evaluate the relative probablility.

By inspection of the data we can come to the conclusion that wave absorption by Landau damping and acceleration of the progenitor electrons by the ohmic field cannot by themselves explain the x-ray emission at the line-of-sight of the face of the MkII antenna and the apparent lack of confinement by these same electrons. While the

background spectra hint that it is at least possible to confine some fast electrons long enough to attain high energies, the toroidal asymmetry in the far field and difference in spectral shape indicates that the ohmic field is not the primary mechanism for acceleration of these electrons up to and beyond 50 keV.

The apparent rejection of the aforementioned parallel ohmic field mechanism means that more unorthodox processes must be considered. Mechanisms for fast electron and/or x-ray production from something other than an electric field should at least be mentioned. These are beta decay, internal excitation of ions or atoms, emission following beta decay, annihilation, nuclear reactions, and line radiation following internal excitation [14]. Many of these can be discarded out of hand because they generate electrons or photons only away from the observation range or at narrow energy spectra. The rest can be eliminated by noting that the x-rays observed are apparently rf-induced, and for the [small] power injected, we cannot expect the rates of any of these mechanisms to change in any discernible degree. Fast electrons as a result of rf-induced fields are then what is required to explain the observations.

As mentioned in §4.3.2, the rf source S_{rf} must generate some part of the fast electron population directly. It happens that the antenna itself — or the electric fields directly in front of the antenna — may be sufficient to generate our fast electrons. These more or less thermal electrons in the plasma edge must be accelerated to energies in excess of 40 keV in a single pass through the antenna fields. Then they will either undergo thick target bremsstrahlung when they impact the antenna structure, with the resulting high x-ray flux and the visible antenna interaction, or will be confined long enough by the guide field for bremsstrahlung to occur seen by detectors toroidally off the antenna.

4.4 Antenna Field Modeling

The problem of interaction of plasma electrons with lower hybrid antennas has been discussed in the context of high heat loads and damage to divertor and first wall components in TdeV and Tore Supra [26–28]. In particular, Goniche *et al.* found that with near-antenna fields of 5 kV/cm, electrons could achieve energies as high as 3 keV.

As seen in Figure 4.12, even at relatively low power levels, high hard x-ray fluxes with energies greater than 30 keV are seen which implies that the interdigital-line antenna near field must somehow be capable of accelerating electrons to the minimum 30 keV — well beyond what the waveguide-grill antenna modeling suggests is achievable.

The two cases are not directly analogous, however. Typical peak $n_{\|}$ spectra for the tokamak models range from $2.0 - 3.3$ whereas the MST antennas have $n_{\|} \sim 7$. Since electrostatic Landau damping is essentially the process by which the electrons are accelerated, the MST antenna should be more efficient than the fast wave antennas which must rely on high $n_{\|}$ sidebands with little power to do the accelerating. The structure of the near-fields for the MST antennas are also substantially different than the waveguide grill with substantial power in the E_y fringing fields at the edge of the aperture. The question of whether these distinctions are enough to explain the observations is the focus of this section. To determine if the fields on the antenna are responsible for the x-ray flux seen by the HXR detectors, the fields must be able to accelerate electrons to energies at least as high as the photons presumed to be the result of bremsstrahlung.

4.4.1 1D Potential Well Model

The simplest model of the antenna field is a one dimensional sinusoidal potential as a traveling wave with wave number k and frequency ω. If we assume a monochromatic spectrum, then our electric field looks like (3.27), but for the simple model can be described as

$$E(z) = E_0 \sin(kz - \omega t + \delta), \tag{4.30}$$

and the potential: $V(z) = \int E\, dz$. The magnitude of the electric field E_0 is obtained from numerical modeling (with a flat antenna model) by either Microwave Studio or COMSOL. For 85 kW of input power 2 mm in front of the antenna, the vacuum model shows fields up to 4.5 kV/cm. Plasma models show even higher fields are possible, above 6 kV/cm. For the following calculation we shall use a $E_0 = 5$ kV/cm.

As we have more or less definite boundaries with the aperture of the antenna, we can arbitrarily choose at what phase δ the test particle enters the field potential to obtain an upper limit on the energy gain of the test particle.

The first step is to Lorentz boost the electron entering the antenna field into the rest frame of the traveling wave:

$$v_i' = \frac{v - v_\phi}{1 - v v_\phi / c^2} \tag{4.31}$$

where $v_\phi = \omega/k$ is the phase velocity of the wave. At the same time we have to boost the electric field into the moving frame as well. The magnitude of the E_z' component is equal to E_z and since we are concerned only about the z component, we have $E_0' = E_0$.

The wave itself is a function of z and t so we have:

$$\begin{aligned} E'(z) &= E_0 \sin\left(k\,\gamma\,(z' + v_\phi t') - \omega\gamma\left(t' + \frac{v_\phi}{c^2}z'\right) + \delta\right) \\ &= E_0 \sin\left(k\,\gamma\left(z' + \frac{\omega}{k}t'\right) - \omega\gamma\left(t' + \frac{\omega}{k^2c^2}kz'\right) + \delta\right) \\ &= E_0 \sin\left(kz'\gamma - kz'\gamma\beta^2 + \delta\right) \\ &= E_0 \sin\left(\gamma^{-1}kz' + \delta\right). \end{aligned} \tag{4.32}$$

The wave becomes a standing wave as intended, and we see that the wave number is transformed as $k' = \gamma^{-1}k$, though for the phase velocity of the wave, $v_\phi \simeq 4.54 \times 10^7$ m/s or $0.15c$, this is a small modification.

Now integrating to find the amplitude of the potential,

$$V_0' = \frac{E_0}{k'} = \frac{E_0\gamma}{k} = \frac{E_0\gamma}{k_0 n_\parallel} = E_0\frac{1}{k_0}\left(n_\parallel^2 - 1\right)^{-1/2} \tag{4.33}$$

where $k_0 = \omega/c \simeq 0.1675$ cm^{-1} is the vacuum wave number, and we have made the standard substitution $n_\parallel = kc/\omega$. As (4.33) makes clear, the lower our launch spectral peak, the larger the potential. The data from Chapter 3 show that depending on the feed, $n_\parallel$ varies mostly between 6 and 7. We shall use a value of $n_\parallel = 6.6$ for this calculation giving $V_0' \simeq 4.6$ kV.

The initial kinetic energy in the moving frame is $T_i' = (\gamma_i' - 1)\,m_e c^2$. Suppose, in our first case, that $T_i' > 2eV_0'$. The potential then cannot stop the electron (in the wave's frame) no matter what phase the particle enters the field and can only increase

its energy by a maximum of $2eV_0'$. In this case, $T_f' = T_i' + 2eV_0'$ and so

$$v_f' = c\sqrt{1 - 1/\gamma^2}, \qquad \gamma = \frac{T_f'}{m_e c^2} + 1. \tag{4.34}$$

Finally we must transform back to the lab frame:

$$v_f = \frac{v_f' + v_\phi}{1 + v_f' v_\phi / c^2}. \tag{4.35}$$

For an electron entering the field moving in the same direction as the phase velocity, it can achieve energies of more than 45 keV, but only if it initially had a kinetic energy above 30 keV which is exceedingly unlikely in 40 eV edge plasmas. On the other hand, an electron moving in the opposite direction can start at a more reasonable 375 eV (but still quite far out in the tail of the Maxwellian) and will achieve 4.3 keV, a much larger relative energy gain. Either is apparently useless in achieving the the energies required to produce the bremsstrahlung observed.

If we take a second case, $T_i' < 2eV_0'$, then there is enough energy in the wave to bring the electron to a stop in the wave frame. To get maximum energy in this case, we let the electron come to a stop at the very top of the potential well. Here $v' = 0$. Then the drop through the entire potential gives the electron a kinetic energy of $2eV_0'$ for a final velocity of $v_f' = 5.6 \times 10^7$ m/s as calculated by (4.34). For electrons initially traveling opposite to v_ϕ, gaining maximum energy means that the electron will be "reflected" off the wave back to the direction it entered the wave field.

Transforming back using (4.35), the final velocity in the lab frame is 9.9×10^7 m/s or a kinetic energy of 30.2 keV. This is remarkable since the electron can be essentially

at rest in the lab frame to achieve these energies and in times on the order of a wave period. This mechanism could explain a large amount of the x-ray flux that we see, and indeed the transition in Figure 4.11 between the higher and lower flux regimes occurs at $\sim$30 keV.

Still there is x-ray flux, albeit on much lower levels, out to 50 keV and beyond. Some numerical models show fields in front of the antenna to be higher than our stipulated $E_0 = 5$ keV, and the higher fields could produce the higher energy x-rays, or another mechanism must be present.

4.4.2 Gyromotion Model

The one-dimensional traveling wave model is unmagnetized. In the edge we have a guide field which adds gyromotion to the mix. In the previous sections much attention was placed on the parallel velocities of the fast electrons, because of the standard focus on Landau damping and the parallel ohmic electric field. High perpendicular velocities can be just as important: for bremsstrahlung, in the view of the cold ion, an incident electron with a high $v_\parallel$ or a high $v_\perp$ amount to the same thing. Certainly the bremsstrahlung cross-section will be unlike what we expect for purely parallel electrons, but will not change the energy of the emitted photon.

There are three hypotheses we will consider. The first is that thermal electrons coming into the antenna's near field are boosted (in their perpendicular velocities) through the relativistic Doppler-shifted cyclotron resonance [29]

$$\omega - k_\parallel v_\parallel - \frac{n\Omega}{\gamma} = 0 \tag{4.36}$$

where $\Omega \equiv \omega_{ce}$. The $n = 0$ case corresponds to the one-dimensional model in the previous section. When $n = \pm 1$, we have the Doppler-shifted frequency seen by the electron moving at $v_\parallel$ equal to its own gyrofrequency.

Solving (4.36) for the antenna parameters and the cyclotron frequency at 1500 G, 4.2 GHz, we get two solutions for $v_\parallel$: 1.93×10^8 and -1.41×10^8 m/s. These correspond to kinetic energies of 157 keV and 68 keV respectively. Clearly we would not require a resonance condition if the necessary incident energies are already sufficient to produce the bremsstrahlung we observe. Thus we can discard Doppler-shifted resonance as the primary acceleration mechanism.

For resonances at higher harmonics, the fields must have spatial variation in the perpendicular direction [30]. One case of such variation occurs not when the wave itself changes, but when the direction of the parallel field changes. If we add a slight tilt to the guide field — as is the case for the physical antenna — then the gyromotion can interact with the spatial variation of the traveling wave. Figure 4.17 gives a picture of an electron with gyromotion interacting with the antenna field.

To characterize this case, we take the change in energy for an electron subject to a Lorentz force. Ignoring motion in the parallel direction,

$$\frac{dW_\perp}{dt} = \frac{d}{dt}\frac{mv_\perp^2}{2} = m\mathbf{v}_\perp \cdot \frac{d\mathbf{v}_\perp}{dt} = q\,\mathbf{v}_\perp \cdot (\mathbf{E}_\perp + \mathbf{v} \times \mathbf{B}) = q\,\mathbf{v}_\perp \cdot \mathbf{E}_\perp \tag{4.37}$$

Rotating the coordinate system so that $\hat{z} \to \hat{b}$ and assuming for the moment that our

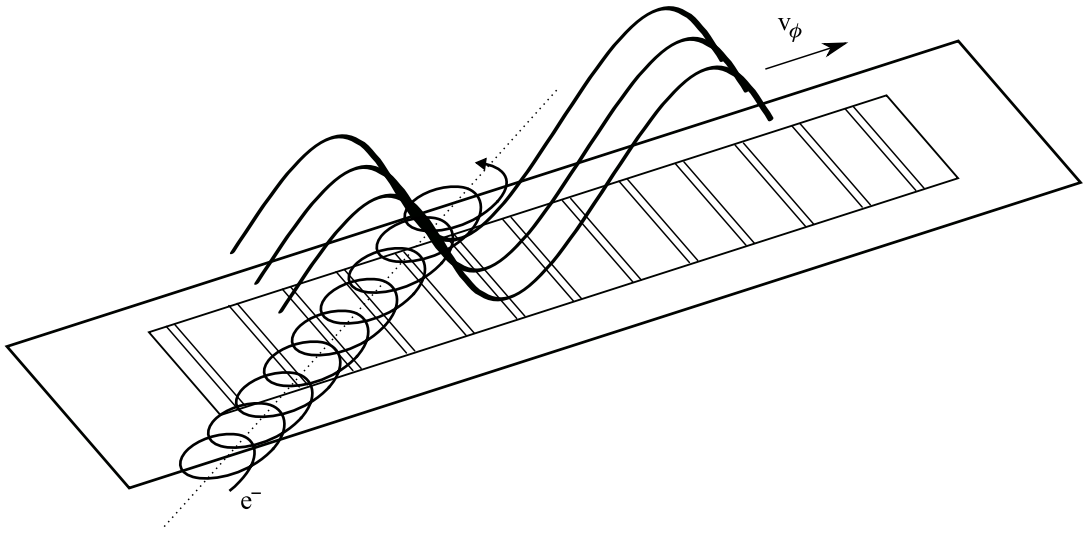

Figure 4.17: Diagram of tilted-field gyromotion model. The guide field is at an angle θ with respect to the long axis of the antenna, giving a perpendicular spatial variation. Not to scale.

perpendicular field is only in the $\hat{x}$-direction, we have:

$$\mathbf{E}_\perp = \hat{\mathbf{x}} E_x \cos\left(k_\perp y - \omega t\right) = \hat{\mathbf{x}} E_x \cos\left(k_0 \sin\theta\, y - \omega t\right) \tag{4.38}$$

where θ is the angle between the guide field and the long axis of the antenna. The gyromotion in the y-direction is

$$y = \rho_L \cos\left(\Omega_{ce} t + \phi\right) \tag{4.39}$$

where $\rho_L = m_e v_\perp / |q| B$ is the Larmor radius. Plugging (4.38) and (4.39) into (4.37)

with $\mathbf{v}_\perp = \hat{\mathbf{x}}\,\Omega\rho_L \cos(\Omega t + \phi)$, we get

$$\frac{dW_\perp}{dt} = qE_x\Omega\rho_L \cos\left(k_0 \sin\theta\, \rho_L \cos(\Omega t + \phi) - \omega t\right) \cos(\Omega t + \phi) \tag{4.40}$$

$$= qE_x\Omega\rho_L \mathrm{Re}\left[\sum_{n=-\infty}^{\infty} J_n\left(k_0 \sin\theta\, \rho_L\right) e^{in(\Omega t+\phi-\pi/2)-i\omega t}\right] \mathrm{Re}\left[e^{i(\Omega t+\phi)}\right], \tag{4.41}$$

where (4.41) is found by applying Jacobi's expansion [31]. Then when $\omega = (n+1)\,\Omega$ there will be an increase in $W_\perp$ proportional to $J_n\left(k_0 \sin\theta\, \rho_L\right) \cos\left((n+1)\phi - n\pi/2\right)$ on average. For the MST antenna parameters, however, the resonance condition cannot be satisfied since the the gyrofrequency is larger than the pump frequency.

While the variation of (4.38) cannot satisfy our requirements, the tilt of the guide field is not the only source of spatial variation in the perpendicular direction. By virtue of being a physical device, the wave field has a finite extent and its boundary constitutes a spatial variation. The transition between the antenna aperture where the electric field is high and the grounded frontplane where the field is zero provides a gradient that will provide a mechanism to pump energy into electrons entering the region. A sketch of the model is shown in Figure 4.18.

We can model the gradient at the aperture edge as a plateau (in front of the aperture itself) with an linear falloff down to zero field on the frontplane. The falloff will have a scale length λ_a that is on the order of one millimeter. Neglecting E_y, we have the perpendicular field at the aperture edge:

$$\mathbf{E}_\perp \Big|_{edge} = \hat{\mathbf{x}} E_x \left(-\frac{y - y_0}{\lambda_a}\right) \cos\left(k_\parallel z - \omega t\right) \tag{4.42}$$

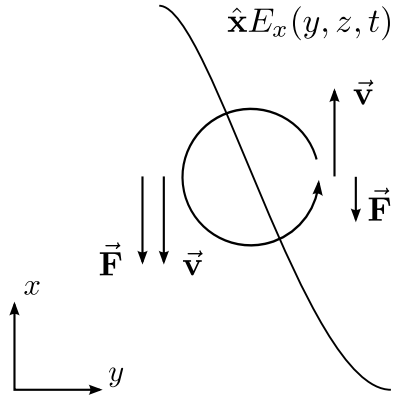

Figure 4.18: Diagram of gradient gyromotion model. The fields fall off at the edge of the antenna aperture. Not to scale.

with $y = y_0 + \rho_L \cos(\Omega t + \phi)$. Using the same perpendicular velocity as above with (4.37), the change in energy is

$$\frac{dW_\perp}{dt} \simeq eE_x\Omega\frac{\rho_L^2}{\lambda_a}\cos^2(\Omega t+\phi)\cos\left(k_\parallel z - \omega t\right). \tag{4.43}$$

Since the gyroradius is a function of $v_\perp$, it is also a function of $W_\perp$ so (4.43) is strictly a differential equation. If the gyroradius does not change too much over one orbit, we can neglect the time dependence or use an iterative method to find the energy gain.

For illustration, we assume that the electron is moving at a parallel velocity $v_\parallel = v_\phi$, the phase velocity of the wave, and enters the fields at the correct phase, then the rightmost cosine term goes to unity. The equation is then non-negative, and energy will be pumped into the electron. Integrating over a gyro-orbit:

$$\int_0^{2\pi/\Omega}\frac{dW_\perp}{dt}dt = \Delta W_\perp = eE_x\frac{\rho_L^2}{\lambda_a}\pi \tag{4.44}$$

is the kinetic energy gain of the electron in the gradient over one orbit. For $E_x = 2.92$ kV/cm, $\lambda_a = 1.3$ mm, $B_0 = 1500$ G, and an initial $v_\perp = 4 \times 10^6$ m/s (45 eV), the electron gains $\sim$16.2 eV per orbit. This corresponds to 68 keV in 1μs, enough to satisfy our observations, but we know that as the perpendicular energy goes up, the Larmor radius increases and makes the pumping more efficient. Using the result of (4.44), we find $v_\perp$ and ρ_L and then iterate. If the electron remains in the gradient, it will achieve 100 keV in about 6 ns. For $v_\parallel \simeq v_\phi = 3.87 \times 10^7$ m/s, the electron will travel 23 cm, on the order of the length of the aperture.

While the initial phase and velocity are contrived to obtain a sufficient energy, the model succeeds in accelerating an electron well in excess of what is required for the highest energy x-rays observed. That said, the mechanism must at the same time accelerate the electron to the required parallel velocity to make the example above work. Also because the force is unidirectional, the electron will quickly drift out of the gradient.

This model is still quite simple as it doesn't take into account several features of the physical picture. The field tilt of the second case must be accounted for since it will serve to prevent the electron from coasting along the aperture edge where the gradient is strongest. The polarization drift mentioned above must also be included. The antenna not only has E_z and E_x components, but also develops a strong E_y component at the aperture edges — right where we expect most if not all of the $v_\perp$ pumping to occur. Depending on the phase of the wave when the electron enters, E_y could provide additional pumping. These additions make calculations to find the maximum energy gain complicated enough that a "brute force" method becomes more practical.

4.4.3 3D Full Fields Model

At this point, it becomes more efficient to solve the full Newton-Lorentz equations of motion. For this we develop an Antenna Lorentz Field (ALF) code that takes a set of test particles in some initial velocity distribution and follows them through the fields in front of the antenna. As before, we make the assumption that at the plasma edge we have a very diffuse, low temperature, quasineutral plasma with collision rates much slower than the antenna interaction time. Our equations of motion for an individual test electron are:

$$\frac{\mathrm{d}\mathbf{p}}{\mathrm{d}t} = q\left(\mathbf{E} + \mathbf{v} \times \mathbf{B}\right) \tag{4.45}$$

$$\frac{\mathrm{d}\mathbf{x}}{\mathrm{d}t} = \mathbf{v} \tag{4.46}$$

where using the momentum $\mathbf{p} = \gamma m \mathbf{v}$ in (4.45) allows us to use the relativistic formulation. To solve this system of equations we use the leap-frog method as outlined by Birdsall and Langdon [32],

$$\frac{\mathbf{u}^{n+1/2} - \mathbf{u}^{n-1/2}}{\Delta t} = \frac{q}{m}\left(\mathbf{E}^n + \frac{\mathbf{u}^{n+1/2} - \mathbf{u}^{n-1/2}}{2\gamma^n} \times \mathbf{B}^n\right) \tag{4.47}$$

$$\frac{\mathbf{x}^{n+1} - \mathbf{x}^n}{\Delta t} = \mathbf{v}^{n+1/2} = \frac{\mathbf{u}^{n+1/2}}{\gamma^{n+1/2}} \tag{4.48}$$

where $\mathbf{u} \equiv \gamma \mathbf{v}$, the relativistic momentum divided by the mass, γ can be formulated as $\gamma^2 = 1 + u^2/c^2$, and the time $t^n = n\Delta t$.

For the relativistic calculation, it is easier to use the method by Boris [33] and

separate the **E** and **B** fields completely by letting

$$\mathbf{u}^{n\pm1/2} = \mathbf{u}^{\pm} \pm \frac{q\mathbf{E}\Delta t}{2m}. \tag{4.49}$$

Then using (4.49) we can rewrite (4.47) as:

$$\frac{\mathbf{u}^{+} - \mathbf{u}^{-}}{\Delta t} = \frac{q}{2\gamma^{n} m} \left(\mathbf{u}^{+} - \mathbf{u}^{-}\right) \times \mathbf{B}^{n}. \tag{4.50}$$

Using (4.50), $\mathbf{u}^{+}$, and thus $\mathbf{u}^{n+1/2}$ can be recovered given $\mathbf{u}^{-}$. An implementation of this method can be found in Appendix F.

For this model we use a slab geometry, so the antenna is flat, and the static magnetic field is parallel to the antenna face. Like the experiment, the guide field can be pitched at an angle relative to the antenna axis. The default guide field strength was chosen to be 1500 G, within a couple of percent of typical edge fields for 400 kA standard plasmas.

The antenna fields $\mathbf{E} = \mathbf{E}(\mathbf{x}, t)$ and $\mathbf{B} = \mathbf{B}(\mathbf{x}, t)$ are obtained from the aforementioned COMSOL simulation of fields — in vacuum or plasma — in front of the antenna. The outputs of the model are actually the complex fields with a harmonic time dependence. Then for example, the electric field is:

$$\mathbf{E}(\mathbf{x}, t) = \mathrm{Re}\,\mathbf{E}(\mathbf{x}) \cos(\omega_0 t + \delta) - \mathrm{Im}\,\mathbf{E}(\mathbf{x}) \sin(\omega_0 t + \delta) \tag{4.51}$$

where ω_0 is the pump frequency and δ is the phase at $t = 0$. The phase angle is chosen at random. The plasma model used in the following runs is cold with a vacuum gap of

1 mm, a density step of $5 \times 10^{10}\,\mathrm{cm}^{-3}$ and a density gradient of $1 \times 10^{11}\,\mathrm{cm}^{-4}$.

Our simulation domain is a three-dimensional box above the antenna. The **E** and **B** fields are imported from the COMSOL run on a $477 \times 105 \times 46$ grid, with 1.0 mm spacing. To retrieve the fields at a particular point (x, y, z) within the domain, we use a three-dimensional tricubic interpolation routine [34].

Each run consisted of at least 10000 particles and a time step of 2×10^{-12} s, Each particle was followed for one million steps, but stopped if the particle moved outside the force field and was determined not to return.

The initial parallel and perpendicular velocities of the particle are chosen from Maxwellian tail distributions. If desired, one-sided distributions can be used to explore the relationship between the directions of the parallel velocity, gyromotion, and the pump wave phase velocity. The tail distribution is cut off below 1 eV to increase the interaction with the pump fields. It was found that many very low velocity electrons never made it to the aperture where the highest fields and the most interaction took place in the simulation time. For the following simulations, a 40 eV distribution was used.

For the starting position of the particle, a plane normal to the field line is chosen, and a rectangular region on this plane is defined by choosing all field lines that intersect the plane and antenna aperture. The particle's position on this region is chosen from a uniform distribution and then translated to the face of the simulation domain as the fields outside the domain are zero. Figure 4.19 shows the starting positions for a pair of runs. The starting positions can be further constrained to pick out certain spatial gradients.

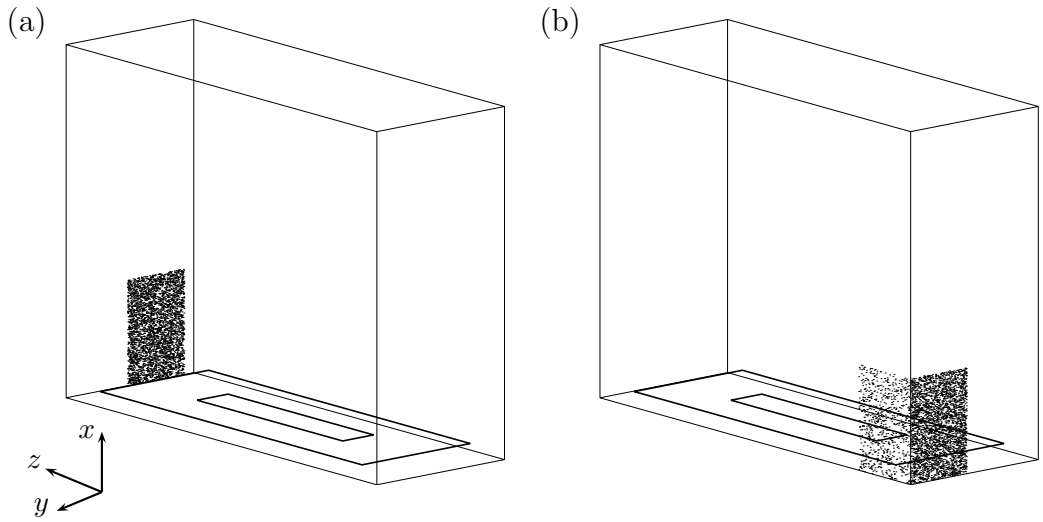

Figure 4.19: Starting positions of electrons for a simulation run. The antenna face and aperture are shown along with the simulation domain (box). Dimensions are not to scale. (a) Field line pitch of 8° and a negative temperature distribution. (b) Field line pitch of 12° and a positive temperature distribution.

The first result of the code is to verify the 1D potential model of §4.4.1. Though the fields used in ALF are 3D vector fields, the code can be configured to scale field components independently. For comparison to the 1D model, the perpendicular fields E_x and E_y are set to zero, the pitch angle is set to zero so the guide field is parallel with the antenna axis, and the strength of the E_z field is scaled to 85 kW of input power as in the modulation experiment of §4.3.2. The spatial distribution is set for the electrons to start 1-2 mm above the antenna face. The results for both vacuum and plasma are shown in Figure 4.20.

As we expected from the 1D model, a tail is pulled out in the direction of the phase velocity of the wave. With no perpendicular components of the field or pitch to the guide field, the energy in the perpendicular direction does not change. The peak

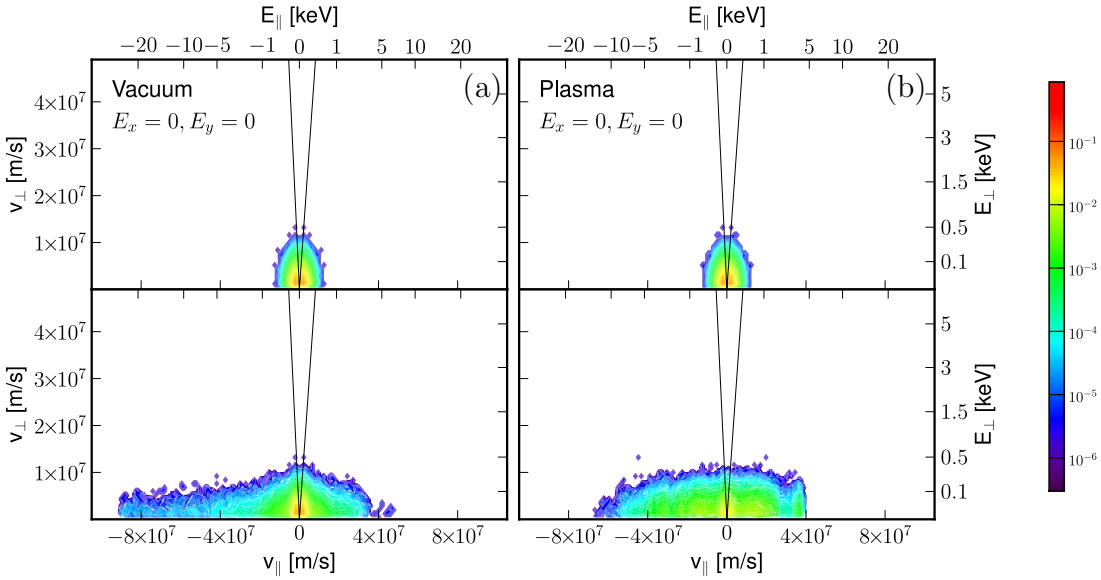

Figure 4.20: Results of near field modeling reproducing 1D potential well model. Here the perpendicular fields E_x and E_y are set to zero. The geometry corresponds to a port 1 feed. Units of velocity and kinetic energy are shown. (a) The initial velocity distribution (top) and the response from vacuum fields (bottom). (b) Similar distributions with the antenna fields in the presence of plasma with a 1 mm vacuum gap. The black lines indicate the trapped/passing boundaries.

energy of the tail for the vacuum field is $\sim$25 keV but no more. For the plasma the tail achieves only about $\sim$15 keV due to the fact that the plasma causes damping of the electric field while the vacuum field does not. Either result corroborates the prediction that the parallel component of the field is not enough to drive electrons to energies expected to produce the observed HXR flux.

The 2D gyromotion hypothesis can now be checked by restoring the perpendicular field components. Figure 4.21 shows the final velocity distribution with the plasma case for a field pitch of 0° and 180°, corresponding to co- and counter-current launch.

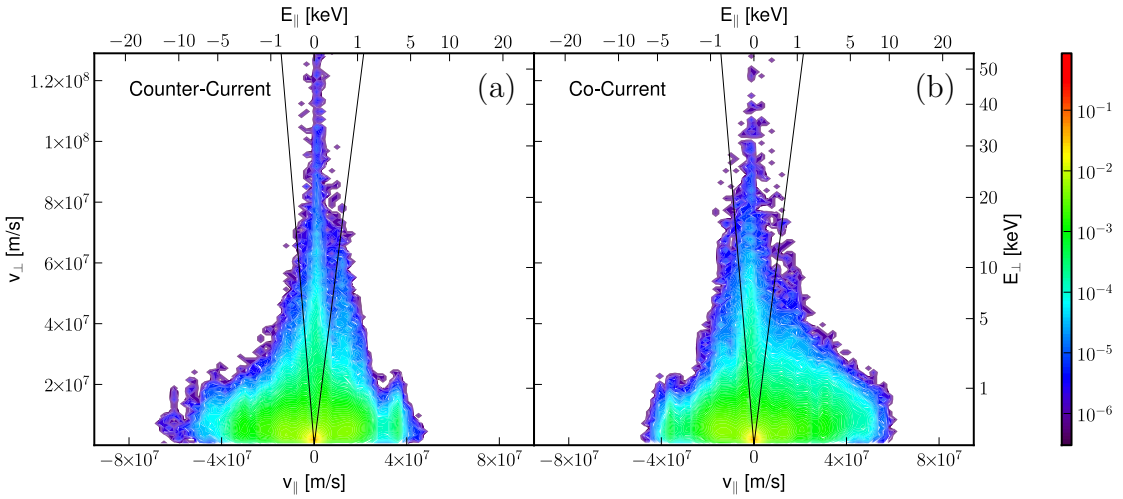

Figure 4.21: Results of near field modeling with all field components for the plasma case with 1 mm vacuum gap. (a) The final velocity distribution for geometry corresponding to a port 1 or counter-current launch. (b) The final velocity distribution for a port 2 or co-current launch.

These runs start the initial electrons between 1 and 5 mm above the frontplane. With all field components, a parallel tail is pulled out in the direction of the phase velocity as expected, though barely to 10 keV in the co-current direction. More importantly, we see the formation of a perpendicular tail that extends above 50 keV.

The fraction of the distribution greater than 10 keV is 0.09% and 0.04% respectively, which is on the order of what is needed to produce the magnitude of off-antenna flux as discussed in §4.3.4. The results then predict that thermal edge electrons entering the antenna field are accelerated to high perpendicular velocities. Some fraction of these fast electrons hit the antenna and produce the the x-ray emission seen in Figure 4.12. The rest leave the antenna region and contribute either heavily or entirely to the flux seen in the far field.

To check if superthermal parallel velocities are required to produce high perpendicular velocities, a pair of runs were performed with the E_z field components set to zero. Other parameters of the simulation are the same as previously stated. The results of the runs are shown in Figure 4.22. Without the parallel electric field, no tail in the parallel direction develops. On the other hand, an extremely large perpendicular tail is seen with 0.88% and 0.23% of the final distibutions for the vacuum and plasma cases respectively attaining energies greater than 20 keV. Moreover, the tail extends to 80 keV in the plasma case and above 100 keV in the vacuum case. This perpendicular tail is seen without requiring that the parallel velocity be on the order of the phase velocity as was premised in §4.4.2, and apparently avoids drifting out of the gradient via the polarization drift. Both E_x and E_y components are not required, either alone can pull out a perpendicular tail, but not one as robust.

Several caveats must be mentioned. The simulations discussed have no field pitch, which is present for standard plasmas. No plasma cases with a non-zero field pitch were available, but ALF runs with pitch using vacuum fields show the perpendicular tail remaining, though with the high energy electrons having even less parallel velocity. Secondly, the model uses a flat antenna and fields for a slab plasma instead of the physical curved antenna. Nominally, however, the antenna is constructed so that its face matches the flux surfaces. Lastly, the COMSOL model has an anomalously low $n_{\|}$ spectrum which cannot be compensated as was done in Chapter 3. This will produce a faster phase velocity than we would see in the experiment. The consequences of this are uncertain.

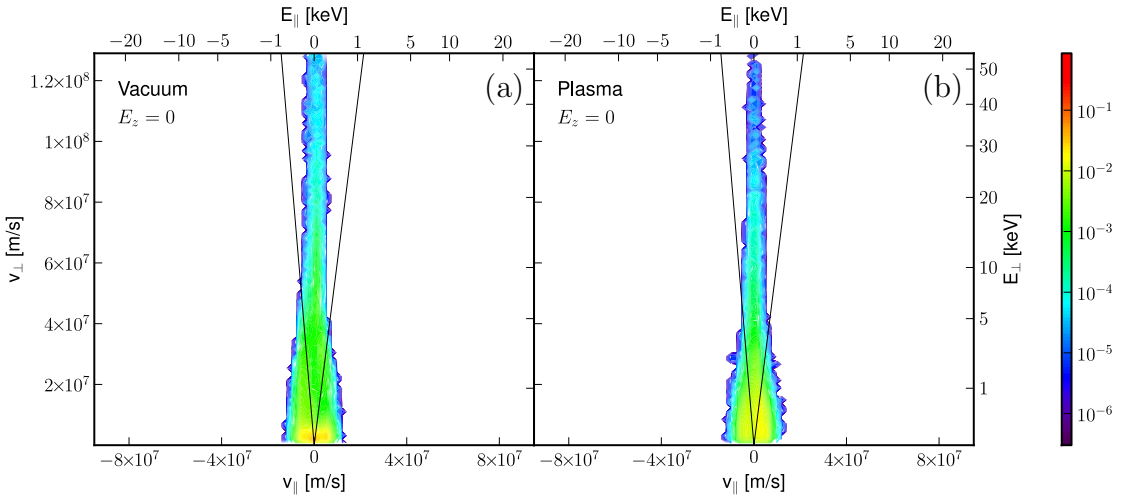

Figure 4.22: Results of near field modeling verifying 2D gradient gyromotion model. Here the parallel fields E_z is set to zero. The geometry corresponds to a port 1 feed. (a) The final velocity distribution with vacuum fields. (b) The final velocity distribution for antenna fields in the presence of plasma with a 1 mm vacuum gap.

4.4.4 Trapped Fast Particles

Figure 4.21 shows that almost all of the electrons above 10 keV, that is those that can contribute to the hard x-ray flux, are trapped. With a trapping condition, a multi-pass acceleration of fast electrons in the antenna field becomes a real possibility. Multiple passes through the near field allow for electrons with an already high $v_\perp$ to be boosted to higher energies. The definition for trapping [35] is

$$\frac{v_\parallel}{v_\perp} < \left(\frac{B_{max}}{B_0} - 1\right)^{1/2}, \tag{4.52}$$

where B_0 is the field at the location where the fast particle is born. For our particular case this will be at the poloidal angle of either antenna aperture edge. The poloidal

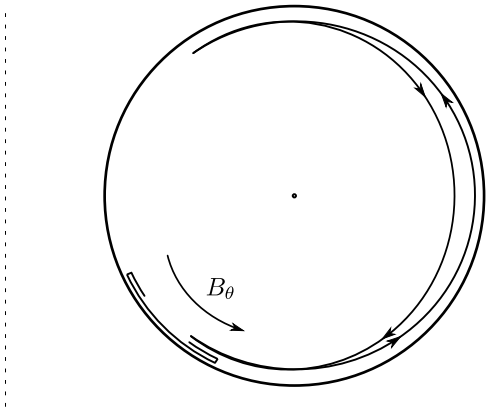

Figure 4.23: The banana orbit of a trapped particle produced by the antenna near field projected onto a single toroidal angle. The particle is born at the antenna aperture moving in the $+\hat{b}$ direction. The banana width is not to scale.

dependence of the magnetic field in the RFP is similar to that of a tokamak with the maximum $|B|$ on the inboard side at $\theta = \pm\pi$. Figure 4.23 shows a sketch of a banana orbit for a particular particle exiting the antenna near field. Since the magnetic moment $\mu = m\, v_\perp^2/2B$ is conserved, the smallest possible orbit will still take the particle back to the poloidal angle where it was "born". To determine B_0 at the antenna aperture, we use (3.39) and (3.40) for $B_z\,(\theta)$ and $B_\theta\,(\theta)$. Because the inboard feed of the antenna is nearer B_{max}, the mirror ratio for electrons born on the inboard side will be smaller than for those born on the outboard feed. It is this effect that makes the trapping cone asymmetric in Figure 4.21.

To determine if a trapped particle will make a second pass through the antenna near field (without making a full toroidal transit), we must calculate the toroidal drift of the electron as it completes a single banana orbit. The significant particle drifts are

the curvature drift

$$\mathbf{v}_R = \frac{1}{2}\frac{v_\parallel^2}{B\,\Omega_{ce}}\frac{1}{r}\left(B_z\hat{\theta} - B_\theta\hat{z}\right), \tag{4.53}$$

the grad-B drift

$$\mathbf{v}_{\nabla B} = \frac{1}{2}\frac{v_\perp^2}{B^2\,\Omega_{ce}}\left(\frac{B_z}{r}\frac{\partial B}{\partial\theta}\hat{r} - B_z\frac{\partial B}{\partial r}\hat{\theta} + B_\theta\frac{\partial B}{\partial r}\hat{z}\right), \tag{4.54}$$

and the $E\times B$ drift:

$$\mathbf{v}_E = \frac{\mathbf{E}\times\mathbf{B}}{B^2}, \tag{4.55}$$

where $\mathbf{E}$ is the ambipolar electric field. Equilibrium reconstruction and simple transport analysis are used to calculate the parameters for each of these drifts. The toroidal component of all these drifts is in the negative toroidal direction. There are two different cases to consider for trapped electrons. The first case is an electron that is born on the inboard side traveling in the $-\hat{b}$ direction. The inboard aperture edge of the MkIII antenna is at $-142.9°$: quite close to B_{max}. Highly trapped electrons — those with very high $v_\perp$ — will almost immediately turn around back into the antenna field. However, at the turning point, their parallel velocity is lowest, and they will spend quite a bit of time in this region.

The second case is an electron born at the outboard edge of the aperture ($-122.9°$ for MkIII). It will then complete the majority of a banana orbit before reentering the antenna near field. In both cases, all three drifts are acting on the electron as it makes its transit. The antenna aperture has a toroidal extent of 3 cm, so if the electron drifts more than 3 cm in its single (fraction of the) banana orbit, it will not be able to make

a second pass over the antenna.

The distance that the electron will drift over $\Delta\theta = \theta_1 - \theta_0$ via the grad-B drift is

$$\mathbf{s}_{\nabla B} = 2\int_{t_0}^{t_1} \mathbf{v}_{\nabla B}\, dt = 2\int_{\theta_0}^{\theta_1} \frac{\mathbf{v}_{\nabla B}(\theta)}{v_{\parallel}(\theta)}\, r\, d\theta \tag{4.56}$$

where the factor of two is for the reciprocal transit back from the turning point. Similar expressions can be derived for $\mathbf{s}_R$ and $\mathbf{s}_E$. To solve for $\mathbf{s}$, we require $v_{\parallel}(\theta)$ as well as the location of the turning points. By conservation of energy and the invariance of μ, we have

$$\frac{1}{2}mv_{\parallel}^2 = W - \mu B \tag{4.57}$$

where W is the total (relativistic) energy of the electron. θ_1 is found by setting $v_{\parallel} = 0$ and θ_0 is at the pertinent aperture edge.

Figure 4.24 shows the toroidal drift as a function of $E_{\perp}$ for a electron with $E_{\parallel} = +1$ eV which corresponds to an electron born on the outboard side of the antenna and traveling toward the outboard side. As expected for electrons with such small $v_{\parallel}/v_{\perp}$, the curvature drift contributes little. For electrons with low perpendicular velocities, making $\mathbf{v}_{\nabla B}$ small, the $E\times B$ drift compensates since the bounce period will be longer. This class of electron will then always drift too far to be able to pass over the aperture on its return trip.

Figure 4.25a shows the total toroidal drifts for the outboard transit for a set of different parallel energies. It is clear from the curves that electrons produced by the antenna near field and travel in the $+\hat{b}$ direction will never make a second pass back through the antenna field without circumnavigating the machine. Figure 4.25b on the

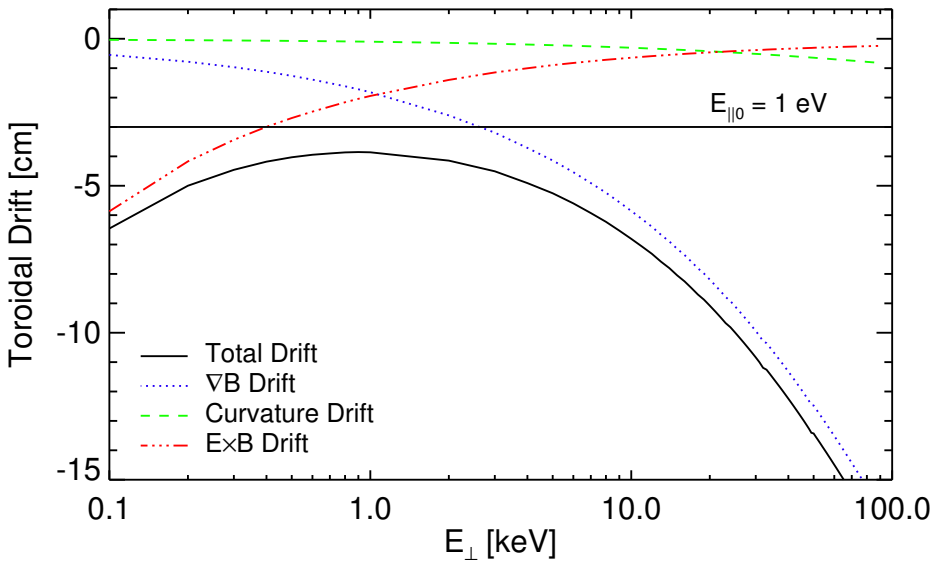

Figure 4.24: Toroidal drifts during a banana orbit for a given initial perpendicular energy. The initial parallel energy is 1 eV and the electron is born on the outboard side of the antenna. The transit path is antenna to turning point to antenna.

other hand shows electrons with initial $v_{\|} < 0$ and so will transit their banana orbit on the inboard side. Because the antenna is on the inboard side of the machine, these electrons have much less distance to travel before reaching the turning point and will have much less time to drift. The difference between the drifts for initially positive and negative velocity electrons is stark. Almost all of the inboard trapped electrons produced by the antenna field will get a second pass through the field as they cannot drift far enough to avoid the aperture.

We now can see how trapping further distorts the velocity distribution for a second pass through the antenna field. The final velocity distributions of the ALF runs illustrated in Figure 4.21 are used as the initial distribution. Any electrons with $v_{\|} > 0$

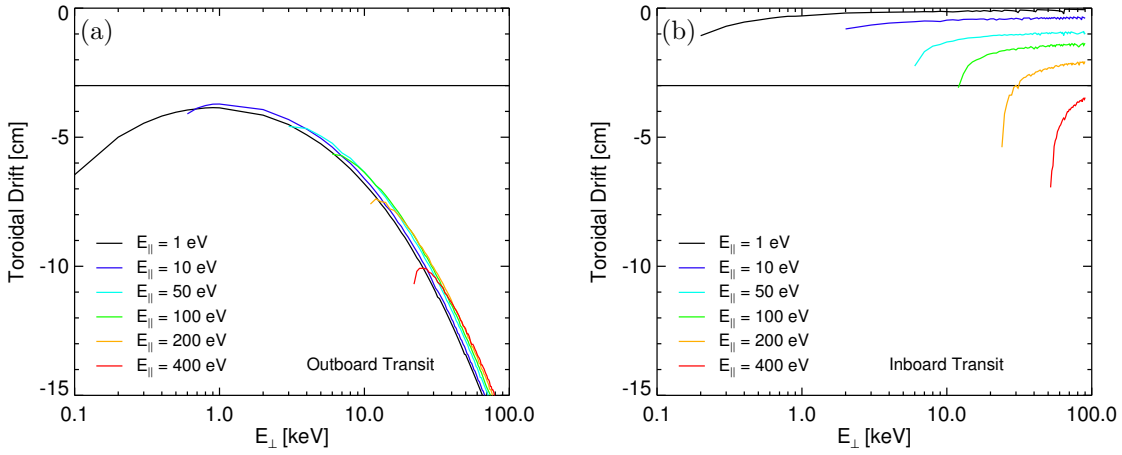

Figure 4.25: Total toroidal drift during a banana transit for a given initial perpendicular energy and for several initial parallel energies. The transit path is antenna to turning point to antenna. The lower $E_\perp$ cutoff on each of the curves is due to the trapped/passing boundary. (a) The electron is born and transits on the outboard side. (b) The electron is born and transits on the inboard side.

(outboard transit) are discarded per the previous analysis. Electrons with $v_\parallel < 0$ and within the trapped boundary are kept, but since they will reenter the antenna field after bouncing, their parallel velocity is reversed. Finally, any electrons whose trajectory intersected the antenna frontplane are eliminated as they cannot participate in a second pass. Figure 4.26 shows these initial and the final distributions after an ALF run for co- and counter-current drive phasings.

As expected, the fraction of electrons at high energies increases after a second pass. On the other hand, the second pass distribution appears to produce fewer of the the very highest energy electrons. The average parallel speed at $E_\perp \gtrsim 20$ keV increases relative to the single-pass case making it more likely that higher energy electrons (producing

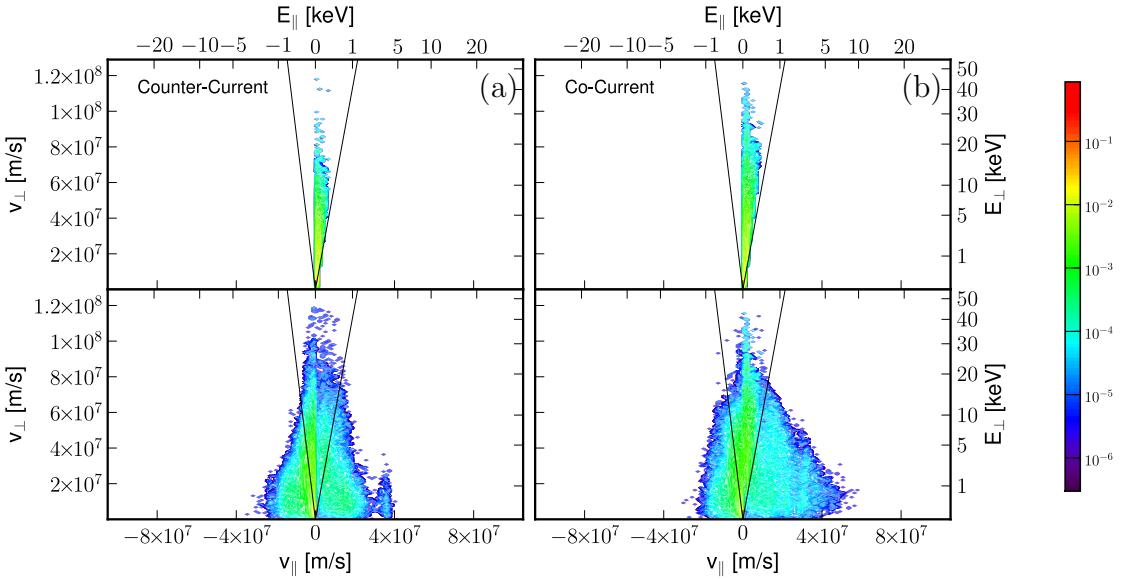

Figure 4.26: ALF results for second-pass acceleration for a plasma model with 1 mm vacuum gap. The input distribution is that trapped fraction which bounces off the inboard turning point. The black lines indicate the trapped/passing boundaries. (a) Co-current drive phasing. (b) Counter-current drive phasing.

hard x-rays) will become untrapped.

Inspection of the final distributions reveals that multi-pass acceleration may explain the observation from the toroidal survey that the hard x-ray flux at the antenna angle is almost an order of magnitude higher for the co-current phasing than for the counter-current phasing. The single-pass simulation shows a higher fraction of fast electrons for the counter-current phasing, opposite of what the observations show. The second-pass simulation on the other hand shows the fast electron fraction higher for the co-current phasing — in line with the observations.

The negative toroidal drift for these trapped electrons also serves to nicely explain

the observation of left/right HXR asymmetry about the antenna. Figure 4.5 showed that x-ray production was higher at toroidal angles $\phi < \phi_{antenna}$ than for $\phi > \phi_{antenna}$ for both phasings. Since all the trapped (fast) electrons will drift to smaller toroidal angles, the higher fast electron population there should result in higher x-ray flux, which is what is observed. In fact, this mechanism presents the problem of producing any flux at all at angles $\phi > \phi_{antenna}$. Clearly, enough passing (but still fast) electrons must be created to produce the observed high energy x-rays. It should be noted that as plasma conditions evolve, the equilibrium changes in ways that can significantly change the trapping ratio. Looking at (3.40) for example, if β_p increases, then the mirror ratio will decrease thus freeing electrons that were previously trapped.

4.5 Power Losses

As outlined in §2.7, a substantial percentage of the power available from the klystron is not radiated to the plasma, and this reduces the efficiency of the system. Even power radiated by the antenna may not be absorbed in the target region which will further reduce the efficiency. Assuming the modeling is correct, fast electron generation by the antenna near field functions as a loss mechanism. Power dumped into far-edge electrons which are subsequently lost do nothing for driving current just inside the reversal surface.

As noted in the previous section, viewing the antenna in the visible shows enough antenna interaction — presumably by fast electrons — to give an conspicuous afterglow. Goniche, *et al* [28] used IR cameras to calculate the absolute heat flux incident on the

antenna limiters and magnetically connected surfaces of Tore Supra and TdeV. Without an IR diagnostic on MST, we can only look at the hard x-ray flux and attempt to back out a figure of merit for the losses into edge electrons.

There are two possible loss channels for these near-field accelerated electrons. First, fast electrons could be immediately lost by impacting the antenna structure itself, producing x-rays by thick-target bremsstrahlung. Second, the fast electrons could simply follow the background magnetic field away from the antenna to be lost to the toroidal limiter or wall by radial diffusion.

4.5.1 Losses to the Antenna Limiter

We start with the first loss channel. In §4.3.4, we used the magnitude of the observed x-ray flux to corroborate our hypothesis that on-antenna flux must be the result of thick-target bremsstrahlung. We refine that analysis here to estimate the losses as well as to check the ALF modeling. Starting with the equation for x-ray flux from a thick target, we modify (4.28) for an electron distribution function:

$$\phi\left(k\right) = \frac{27.6}{4\pi} Z\, 10^{-10} \int_{k}^{\infty} \left(T_0\left(v\right) - k\right) \frac{1}{k}\, f(v)\, v\, d^3v, \tag{4.58}$$

where the kinetic energy T_0 is a function of v and the integral only contributes to the flux for electron energies above k.

The fast electron distribution $f(v)$ will be defined as

$$n_f = \int_{v_{f_0}}^{\infty} f(v)\; d^3v, \tag{4.59}$$

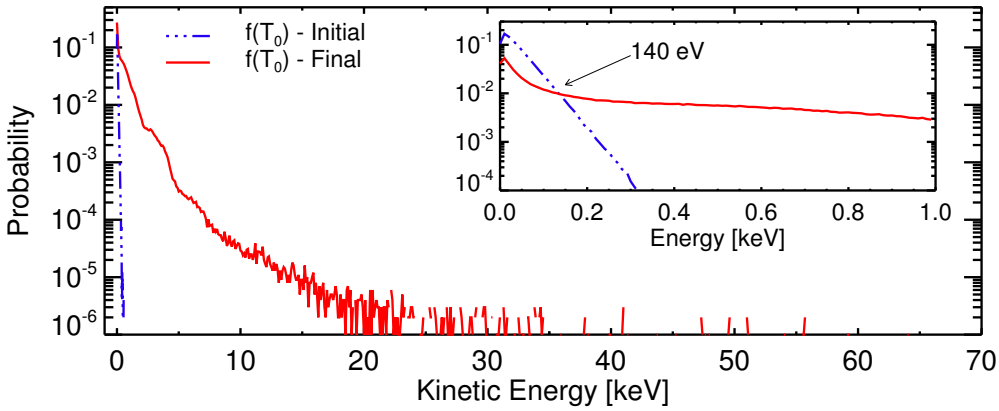

Figure 4.27: 1D energy probability distribution for ALF model. Inset shows location of v_{f_0} where final probability exceeds the initial probability.

where v_{f_0} is a cutoff velocity that separates the distribution of interest from the bulk. This cutoff velocity can be specified in several different ways. An initial Maxwellian distribution will necessarily become distorted as a fast tail develops. We could then define v_{f_0} as the location in velocity space where the distorted distribution probability first becomes larger than the initial Maxwellian. Figure 4.27 shows the initial and final distribution from the ALF model in terms of kinetic energy. The inset plot shows that $v_{f_0} = 7.02 \times 10^6$ m/s corresponding to 140 eV. More practically, we can define a n_f^{obs} to be those electrons in the distribution whose energies are higher than the instrumental cutoff of our hard x-ray detectors ($\sim$12 keV). This will be the population required to produce the x-ray flux that we see. Lastly, we can define an n_f to be that part of the distorted distribution that does not interact with the bulk. This definition is more ambiguous, and so we will not deal with it.

The output of the ALF model as well as a monoenergetic beam is a discrete set of

particles. The distribution function can be approximated as a sum over the N particles' location in velocity space:

$$f(\mathbf{v}) = \frac{n_f}{N} \sum_i^N \delta(v_x - v_{x_i}) \delta(v_y - v_{y_i}) \delta(v_z - v_{z_i}) \tag{4.60}$$

$$= \frac{n_f}{N} \sum_i^N \frac{1}{2\pi v_\perp} \delta(v_\perp - v_{\perp_i}) \delta\left(v_\parallel - v_{\parallel_i}\right) \tag{4.61}$$

$$= \frac{n_f}{N} \sum_i^N \frac{1}{4\pi v^2} \delta(v - v_i), \tag{4.62}$$

with the last two equations derived by general coordinate transformations [36]. Plugging (4.62) into (4.58), we have

$$\phi(k) = \frac{27.6}{4\pi} Z\, 10^{-10} \frac{n_f}{N} \sum_{i=1}^N (T_0(v_i) - k) \frac{1}{k} \delta(v - v_i)\, v_i\, \Theta(v_i - v_k) \tag{4.63}$$

where v_k corresponds to the velocity of an electron with an energy k. n_f in (4.63) is determined by normalizing ϕ against the integrated flux measured on a viewing chord. Figure 4.28 shows the hard x-ray spectra from the ALF model and a 50 keV beam normalized against the flux on the radial chord at -35.6 cm. The data are from the experiment shown in Figure 4.12.

The Figure shows clearly that the monoenergetic beam overestimates the flux for all energies above 20 keV. This isn't surprising since we expect that electrons of that energy will be rare. Much more surprising is that the flux calculated from the numerical model is a worse predictor with significant flux past 90 keV. The thick-target formulas are quite sensitive to very high energy electrons. Removing the electrons above 54 keV

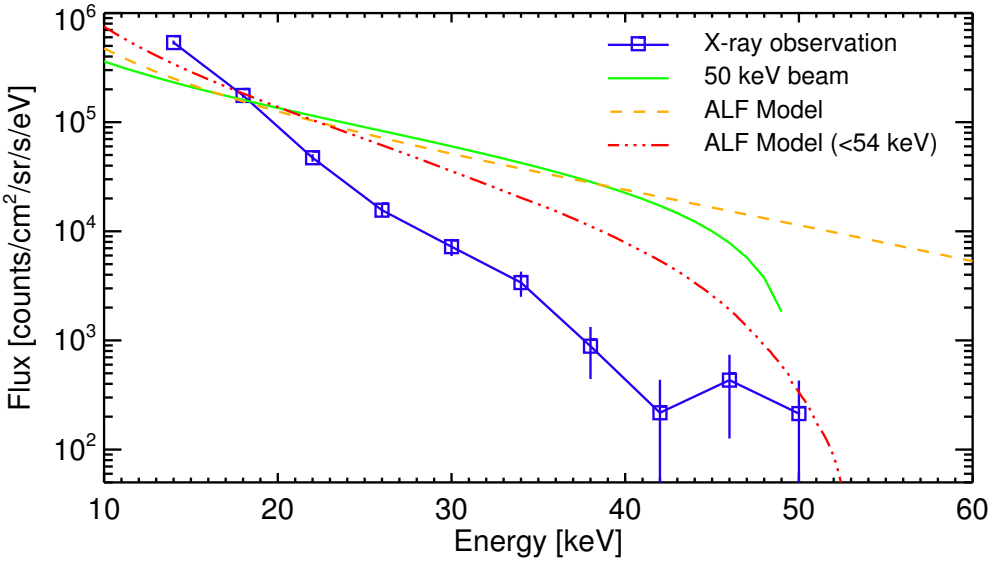

Figure 4.28: Modeled and observed hard x-ray spectra for thick-target bremsstrahlung. The measured flux is with a counter-current launch for a on-antenna viewing chord at −35.6 cm. The modeled spectra are normalized to the observed integrated flux above 12 keV.

(5% of n_f^{obs}), shows significantly better agreement with the observed flux, though still quite a bit higher from 30-40 keV.

This result shows that ALF is overproducing high energy electrons. The final distribution is for all electrons at the end of 10^6 steps wherever they are in the computation domain, not just the ones that hit the aperture. The electric field domain also starts 1 mm above the aperture, so the code is accounting for field interactions very close to the antenna (or inside the cavity). Adding these fields and including a more accurate aperture bounding function may limit the fraction of high energy electrons, but in the end it is easier to find loss mechanisms for fast electrons than a production mechanism.

	50 keV Beam	ALF	ALF $<$ 54 keV
n_f (cm^{-3})	7.9×10^2	2.7×10^6	6.5×10^6
n_f^{obs} (cm^{-3})	7.9×10^2	3.9×10^3	8.8×10^3
Q_f $(\mathrm{W/cm}^{-2})$	78	120	270
Q_f^{obs} $(\mathrm{W/cm}^{-2})$	78	14	24

Table 4.1: Modeled fast electron density and heat flux for HXR spectra for thick-target bremsstrahlung looking at the antenna face.

The sensitivity of the spectra to a very small number of electrons means that a good match to the observed flux would be very difficult in any case.

Table 4.1 gives the values of the fast electron densities required to normalize the calculated flux to measurements. It is remarkable that such a small density is required to produce the observed flux. The last two rows of the table are the results for the heat flux onto the antenna face. The heat flux Q_f from the fast electron population is

$$Q_f^{(obs)} = \int_{v_{f_0}}^{\infty} T_0\,(v)\, v f(v)\, d^3v \tag{4.64}$$

where we have Q_f or Q_f^{obs} depending on the value of v_{f_0}. As expected from the low density, Q_f is quite small. Comparing to the radiated power for the experiment, $\sim$55 kW and a spot size for the detector on the antenna face of approximately $10\,\mathrm{cm}^2$, the power lost to that area with the truncated ALF result is 2.7 kW. This is for all electrons faster than a Maxwellian, essentially extrapolated from the observed flux above 12 keV. Using Q_f^{obs} instead, we have a loss of 240 W.

Table 4.2 shows the heat flux for the three models for each of the 5 detector chords

	ALF < 54 keV		50 keV Beam
Chord	Q_f (W/cm^{-2})	Q_f^{obs} (W/cm^{-2})	Q_f (W/cm^{-2})
-35.6 cm	270	24	78
-30.5 cm	67	5.8	19
-25.4 cm	23	2.0	6.8
-20.3 cm	3.2	0.27	0.90
-15.2 cm	0.35	0.03	0.10

Table 4.2: Heat flux estimates from on-antenna detector chords for counter-current launch with 85 kW of input power. For the beam, $Q_f = Q_f^{obs}$.

intersecting the antenna face. The spot size for the chords becomes slightly larger going outboard since larger apertures were used, but as an estimate, we will use the same 10 cm^2 as the spot area. Then we have 3.6 kW or 320 W of power lost for 85 kW of input power.

There is at least one reason to believe that Q_f may be lower than the value presented in the Tables. The large gyroradius of high (perpendicular) energy electrons (3 mm at 20 keV) allows them to more easily hit the antenna even if their guiding center is deeper in the plasma. Because of this, the higher energy electrons will be overrepresented. From the middle column of Table 4.1, we see that $n_f^{obs}/n_f = 0.0014$. Looking at the actual distribution of particles intersecting the antenna frontplane in the simulation, the fraction is 0.063, almost 2 orders of magnitude greater. We then expect Q_f^{obs} to be closer to the actual flux lost to the antenna face.

4.5.2 Losses to Edge Fast Electrons

From the modeling we expect that only a minority of electrons entering the antenna near-field will hit the antenna limiter and be lost. The rest of the now-distorted distribution will continue to follow the guide field out of the antenna region. We propose that electrons accelerated sufficiently by the antenna field will cease to significantly interact with the rest of the plasma (with the exception of bremsstrahlung). This population is collisionless and sufficiently near the plasma edge that most will be lost to the toroidal limiter or wall. Even if not lost immediately, this power is unavailable to Landau damp at the target absorption region.

As the fast electrons pass through the bulk plasma, we have bremsstrahlung, and we use the Born cross-sections to estimate the flux from the modeled distributions. To begin we take (4.6) and (4.7) and replace v_f by its expression in terms of momentum. Then we have an expression for the x-ray flux:

$$\phi\left(k\right) = \int dl\, n_b \int_k \frac{d\sigma\left(p, k, \chi, Z_{eff}\right)}{dk d\Omega_k} \frac{c\, p}{\sqrt{p^2+1}} f\left(p_{\parallel}, p_{\perp}\right) d^3p. \tag{4.65}$$

The integral for dl is calculated by assuming the emissivity is constant in a plasma slice Δl and zero elsewhere as in (4.25). The distribution is a sum of delta functions from (4.61). Integrating, we then have

$$\phi\left(k\right) = \Delta l\, n_b\, c\, \frac{n_f}{N} \sum_{i=1}^{N} \frac{d\sigma\left(p_i, k, \chi, Z_{eff}\right)}{dk d\Omega_k} \frac{p_i}{\sqrt{p_i^2+1}} \Theta\left(p_i - p_k\right). \tag{4.66}$$

The dependence of (4.66) on the parallel and perpendicular components occurs in the

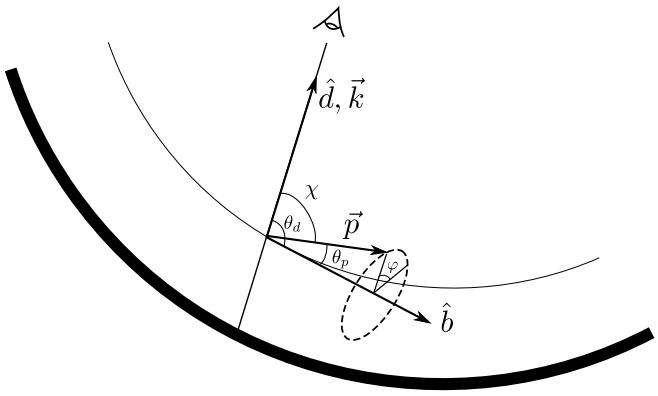

Figure 4.29: Local coordinate system $(\hat{p}, \hat{k}, \hat{b})$ for bremsstrahlung. The vectors correspond to the momentum of the incident electron $\vec{p}$, the energy or momentum of the emitted photon $\vec{k}$ (which is also the detector direction $\hat{d}$), and the local magnetic field diction $\hat{b}$.

angle between the incident electron and emitted photon, χ, which is given by the expression

$$\chi = \cos^{-1}\left(\frac{p_\perp \cos\varphi \sin\theta_d + p_\parallel \cos\theta_d}{p}\right), \tag{4.67}$$

where θ_d is the angle between the photon and the magnetic field, and $\varphi = \tan^{-1} p_y/p_x$ the phase of the gyromotion. The local coordinate system and important angles are shown in Figure 4.29. The phase φ is not known as it is the ignorable coordinate, so we treat it as a uniform random variable. For the i'th particle, we take M particles with the same $p_\parallel$ and $p_\perp$ and pick a random $\varphi \in [0, \pi]$ (π rather than 2π since φ is symmetric). Then instead of N particles in our distribution, we have $M \times N$.

To compare the modeled to observed flux, we choose a representative hard x-ray spectrum from the detector at +15.2 cm. In this case we choose spectra resulting from a co-current launch since our off-antenna radial chords are situated on the outboard side,

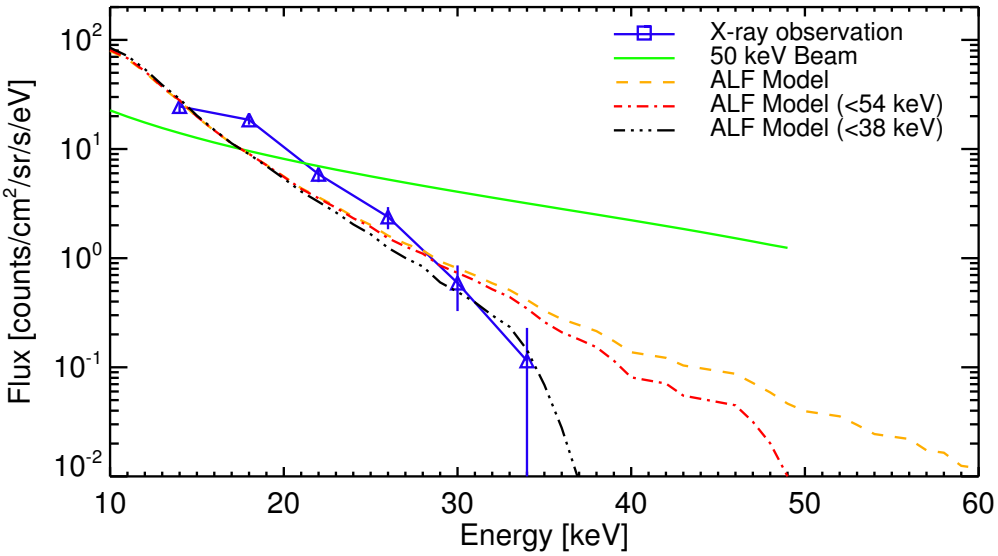

Figure 4.30: Modeled and observed hard x-ray spectra for plasma bremsstrahlung. The measured flux is with a co-current launch for the off-antenna viewing chord at +15.2 cm. The modeled spectra are normalized to the observed integrated flux above 12 keV.

the direction we expect most of the fast electrons to travel coming out of the antenna region. The modeling results are normalized as before to the integrated flux above the instrumental floor (12 keV). The results are compared to the observed spectra in Figure 4.3. The results shown are for a bulk density of $n_b = 1 \times 10^{12}$, a $\Delta l = 1$ cm, and $Z_{eff} = 6$, values reasonable for the edge plasma where impurities are expected to be high.

The 50 keV beam once again produces spectra far larger than the observed flux. Using a 35 keV beam instead removes flux at energies larger than 35 keV, but does not reduce the overall flux. The ALF result on the other hand shows much better agreement with the observed flux than it did the thick-target results. Without truncating the

highest energy electrons, there is still a substantial tail at higher energies that are not seen in the data. If we truncate the ALF results at 38 keV, then the agreement with the observed spectra is quite good.

The simple Kramers formulation for thick-target bremsstrahlung requires only the normalization to the observed flux to find n_f since we've assumed that the target is molybdenum. The thin-target formulas have three additional free variables: n_b, Δl, and Z_{eff}. The effective atomic number is inside the integral, but the flux is directly proportional to n_b and Δl. Q_f and n_f then are inversely proportional to n_b and Δl.

Table 4.3 shows the corresponding fast electron density and heat flux for the models shown in Figure 4.30. Also shown for reference are those quantities for $Z_{eff} = 4$. Clear at the outset are that the fast electron densities required to achieve a commensurate flux are far higher than for a solid target. Since for this model, the distributions are the same as in the previous section, the heat flux will also be much higher. In particular, for the ALF result truncated to 38 keV, closest to the observed spectra, the heat flux from just the observed part of the spectrum is $Q_f^{obs} = 11\,\mathrm{kW/cm^2}$.

For the total power lost to these electrons, we take one dimension to be the width of the antenna aperture — 3 cm, then the area through which the electron population flows is $3 \times \Delta l = 3\,\mathrm{cm}^2$ (so Δl drops out from from power loss formula). This yields a power loss of over 30 kW from the observed population for 85 kW of input power ($\sim$55 kW radiated). The other models discussed give comparable losses. This incredible result — if accepted — is extremely serious with respect to the prospect of driving sufficient current at the reversal surface.

The primary reason to take pause before accepting this result is to examine Q_f

		50 keV Beam	ALF	ALF $<$ 54 keV	ALF $<$ 38 keV
$Z_{eff} = 6$	n_f (cm^{-3})	1.2×10^8	3.0×10^{11}	3.1×10^{11}	3.3×10^{11}
	n_f^{obs} (cm^{-3})	1.2×10^8	4.1×10^8	4.2×10^8	4.5×10^8
	Q_f $(\mathrm{W/cm}^{-2})$	1.2×10^4	1.7×10^5	1.7×10^5	1.9×10^5
	Q_f^{obs} $(\mathrm{W/cm}^{-2})$	1.2×10^4	1.0×10^4	1.0×10^4	1.1×10^4
$Z_{eff} = 4$	n_f (cm^{-3})	2.8×10^8	7.9×10^{11}	8.7×10^{11}	8.7×10^{11}
	n_f^{obs} (cm^{-3})	2.8×10^8	1.1×10^9	1.2×10^9	1.2×10^9
	Q_f $(\mathrm{W/cm}^{-2})$	2.7×10^4	4.3×10^5	4.7×10^5	4.7×10^5
	Q_f^{obs} $(\mathrm{W/cm}^{-2})$	2.7×10^4	2.5×10^4	2.8×10^4	2.8×10^4

Table 4.3: Modeled fast electron density and heat flux for HXR spectra from plasma bremsstrahlung.

rather than Q_f^{obs}. The ALF simulations show over 150 kW/cm^2 when accounting for the electrons in n_f — far in excess of the total power available. This point serves to illustrate the fact that the ALF code may not be sophisticated enough to predict the velocity distribution at the low end. If the model is not remotely correct in the lower energy domain, however, then it is difficult to trust the results in the higher energy domain. It is troubling enough that reducing Z_{eff} to a still reasonable value of 4 gives power losses in the observed energies on the order of the radiated power.

The hard x-ray observations must still be explained. Instead of bremsstrahlung from electron-ion collisions in the plasma, we still have the possibility that we are seeing high energy electrons from the antenna field that hit the vessel wall. In this case we must again use the thick-target formulas with a $Z = 13$ for aluminum. Using (4.63) and normalizing with respect to the flux from the x-ray spectra seen at +15.2 cm, we

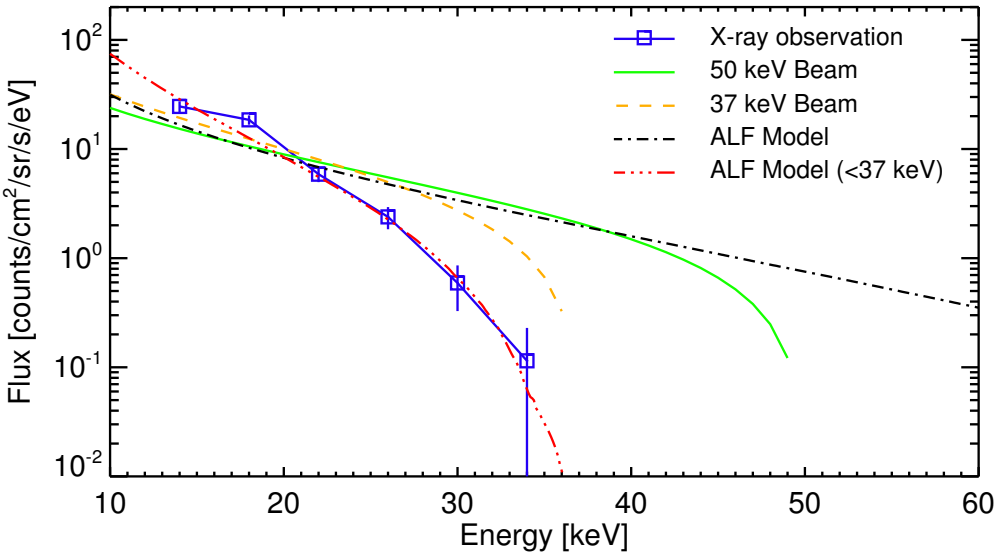

Figure 4.31: Modeled and observed hard x-ray spectra for thick-target bremsstrahlung assuming the target is the aluminum wall. The measured flux is for a co-current launch at +15.2 cm. The modeled spectra are normalized to the observed integrated flux above 12 keV.

have results shown in Figure 4.31. Again we have poor agreement for the ALF model and beam distributions since the observed flux drops rapidly past 35 keV. Using the ALF model truncated to 37 keV, however gives excellent agreement, better than for the plasma bremsstrahlung.

Table 4.4 shows the required fast electron densities and the resulting heat flux. In any of the cases, the necessary fast electron density is minuscule relative to the that for the plasma bremsstrahlung case. The truncated ALF simulation gives a total fast density n_f of 3000 cm^{-3} and an $n_f^{obs} = 3.8$ cm^{-3}. It should be mentioned that for the wall interaction scenario, the densities quoted are only for those electrons that actually

reach the wall. For every one of these, there may be a larger density (but not large enough to contribute significantly to the x-ray flux from plasma bremsstrahlung) that hits the toroidal limiter out of our field of view.

There are a couple possible mechanisms for this small density of electrons to reach the wall behind a 1 cm toroidal limiter. First, as was discussed in §4.4.4, these electrons are trapped which means that their transit time around the machine may be quite slow depending on the parallel velocity. In particular at the turning points, $v_{\|} \to 0$. The perpendicular velocity is still quite high and so the collision frequency is low, but averaged over the larger unseen fast electron density, there may be enough collisions to knock the small number of electrons into the wall.

Second, most of the x-ray diagnostics look across into portholes where a substantial B_r error field can develop. A porthole can produce a local error field on the order of 10% of $|B|$ [37]. This effect combined with the stochastic field at the plasma edge may be enough to push enough fast electrons to the wall. Because of the high perpendicular energies of the electrons, either mechanism need only get the electron part way to the wall since the large gyroradius of the electrons will get it the rest of the way.

Because we do not see the part of the population hitting the toroidal limiter, estimating the power loss from these electrons is more difficult. If we assume that these electrons do not have a high enough density to contibute significantly to the flux by plasma bremsstrahlung, then we may downgrade our density estimate from Table 4.3 by a couple orders of magnitude and use those estimates. The power losses are then on the order of kilowatts rather than tens or hundreds of kilowatts.

	50 keV Beam	37 keV Beam	ALF	ALF $<$ 37 keV
n_f (cm^{-3})	0.169	0.38	585	2.98×10^3
n_f^{obs} (cm^{-3})	0.169	0.38	0.84	3.8
Q_f $(\mathrm{W/cm}^{-2})$	0.017	0.024	0.025	0.122
Q_f^{obs} $(\mathrm{W/cm}^{-2})$	0.017	0.024	2.8×10^{-3}	8.56×10^{-3}

Table 4.4: Modeled fast electron density and heat flux for numerical HXR thick-target spectra for an aluminum target (the vessel wall) at +15.2 cm.

4.6 Summary

Applying power to the lower hybrid antennas in MST produces some puzzling x-ray phenomena. Observations in the antenna far field show an unexpected toroidal asymmetry in the x-ray flux and would seem to dismiss the standard mechanism for producing fast electrons — the ohmic electric field. More exotic scenarios such as localization by drift resonance are rejected by seeing the same asymmetry in non-reversed plasmas. A radial survey shows a flat profile, indicating that x-ray emission is occurring in the edge of the plasma. Emission from the outermost viewing chord shows very high flux (with and without rf) and is not yet fully explained.

Hard x-ray measurements of the near field of the antenna shows very high flux indicative of fast electrons striking the molybdenum limiter covering the antenna front-plane. Numerical modeling supports the hypothesis that gradients in the rf electric fields at the antenna face are pulling out a high energy perpendicular tail in the distribution. Some fraction of these are lost to the antenna structure while the rest follow the stochastic field out of the near field zone and are eventually lost. It is these fast

electrons that give rise to the x-rays seen in the far field. Most of the fast electrons are found to be trapped which explains a left/right asymmetry in the HXR flux about the antenna as well as the flux asymmetry between the antenna phasings.

Calculating the expected bremsstrahlung from a set of test distributions shows that the power lost from antenna interaction may be on the order of several percent of the total radiated power. This loss is important, but not critical for overall operation of the antenna. The far field spectra are most likely from these antenna-field fast electrons striking the vessel wall, and the power lost to these is insignificant.

Bibliography

[1] Lin, R. P. and Hudson, H. S. 10-100 keV electron acceleration and emission from solar flares. *Solar Physics*, **17**:412–435, 1971.

[2] Rice, J. E. and Chamberlain, K. L. X-ray observations between 10 and 150 keV from the Alcator-C tokamak. *Physical Review A*, **38**(3):1461–1467, 1988.

[3] Brusati, M., et al. Determination of the suprathermal electron distribution function during lower hybrid current drive in JET. *Nuclear Fusion*, **34**(1):23–42, 1994.

[4] Peysson, Y. and Imbeaux, F. Tomography of the fast electron bremsstrahlung emission during lower hybrid current drive on TORE SUPRA. *Review of Scientific Instruments*, **70**(10):3987–4007, 1999.

[5] Franz, P., et al. Observations of multiple magnetic islands in the core of a reversed field pinch. *Phys. Rev. Lett.*, **92**(12):125001, 2004.

[6] Franz, P., et al. Two-dimensional time resolved measurements of the electron temperature in MST. *Review of Scientific Instruments*, **77**(10):10F318, 2006.

[7] O'Connell, R., et al. Observation of velocity-independent electron transport in the reversed field pinch. *Phys. Rev. Lett.*, **91**(4):045002, 2003.

[8] Koch, H. W. and Motz, J. W. Bremsstrahlung cross-section formulas and related data. *Reviews of Modern Physics*, **31**(4):920–955, 1959.

[9] Stevens, J., et al. Modelling of the electron distribution based on Bremsstrahlung emission during lower-hybrid current drive on PLT. *Nuclear Fusion*, **25**(11):1529–1541, 1985.

[10] Hutchison, I. H. *Principles of Plasma Diagnostics*. Cambridge University Press, 1st edition, 1987.

[11] Storm, E. Calculated bremsstrahlung spectra from thick tungsten targets. *Phys. Rev. A*, **5**(6):2328–2338, 1972.

[12] Birch, R. and Marshall, M. Computation of bremsstrahlung x-ray spectra and comparison with spectra measured with a Ge(Li) detector. *Physics in Medicine and Biology*, **24**:505–517, 1979.

[13] Chervenak, J. G. and Liuzzi, A. Experimental thick-target bremsstrahlung spectra from electrons in the range 10 to 30 keV. *Phys. Rev. A*, **12**(1):26–33, 1975.

[14] Knoll, G. F. *Radiation Detection and Measurement*. Wiley, 3rd edition, 2000.

[15] Hubbell, J. H. and Seltzer, S. M. *Tables of x-ray mass attenuation coefficients and mass energy-absorption coefficients*. NIST, 1989,1990,1996. http://physics.nist.gov/PhysRefData/XrayMassCoef/tab3.html.

[16] Harris, B. J., Kaufman, M. C., and Goetz, J. A. Filtering noisy x-ray data from MST using a backpropagation neural network, 2008. Undergraduate Thesis.

[17] Walpole, R. E., Myers, R. H., and Myers, S. L. *Probability and Statistics for Engineers and Scientists*. Prentice Hall, 6th edition, 1998.

[18] Walter, C. H. *Traveling Wave Antennas*. McGraw-Hill, 1st edition, 1965.

[19] Karpman, V. Ponderomotive effects in the near zone of an antenna in a magnetized plasma. *JETP Letters*, **41**:455 – 458, 1985.

[20] Anderson, J. K., et al. Dynamo-free plasma in the reversed field pinch. *Physics of Plasmas*, **11**(5):L9–L12, 2004.

[21] Burke, D. R., 2009. Private communication.

[22] Peysson, Y. and Decker, J. Fast electron bremsstrahlung in axisymmetric magnetic configuration. *Physics of Plasmas*, **15**(9):092509, 2008.

[23] Stoneking, M. R. *Fast electron generation and transport in a turbulent, magnetized plasma*. Ph.D. thesis, University of Wisconsin-Madison, 1994.

[24] von Goeler, S., et al. Angular distribution of the bremsstrahlung emission during lower-hybrid current drive on PLT. *Nuclear Fusion*, **25**(11):1515–1528, 1985.

[25] Deslattes, R. D., et al. X-ray transition energies: new approach to a comprehensive evaluation. *Rev. Mod. Phys.*, **75**(1):35–99, 2003.

[26] Fuchs, V., et al. Acceleration of electrons in the vicinity of a lower hybrid waveguide array. *Physics of Plasmas*, **3**(11):4023–4035, 1996.

[27] Fuchs, V., et al. Tokamak edge electron diffusion and distribution function in the lower hybrid antenna electric field. *Nuclear Fusion*, **43**(5):341–351, 2003.

[28] Goniche, M., et al. Enhanced heat flux in the scrape-off layer due to electrons accelerated in the near field of lower hybrid grills. *Nuclear Fusion*, **38**(6):919–937, 1998.

[29] Forest, C. B., et al. Off-midplane launch of electron Bernstein waves for current drive in overdense plasmas. *Physics of Plasmas*, **7**(5):1352–1355, 2000.

[30] Stix, T. H. *Waves in Plasmas*. Spinger, 1992.

[31] Watson, G. N. *A Treatise on the Theory of Bessel Functions*. Cambridge at the University Press, 2nd edition, 1966.

[32] Birdsall, C. and Langdon, A. *Plasma Physics via Computer Simulation*. Bristol : Institute of Physics Pub., 2005.

[33] Boris, J. Relativistic plasma simulation—optimization of a hybrid code. In *Proceedings from the Fourth Conference of Numerical Simulation of Plasmas*, pp. 3–67. Naval Research Laboratory, 1970.

[34] Lekien, F. and Marsden, J. Tricubic interpolation in three dimensions. *International Journal for Numerical Methods in Engineering*, **63**:455–471, 2005.

[35] Goldston, R. J. and Rutherford, P. H. *Introduction to Plasma Physics*. IOP Publishing, Bristol, UK, 1st edition, 1995.

[36] Hassani, S. *Mathematical Physics*. Springer-Verlag, New York, Inc., 1st edition, 1999.

[37] Almagri, A., 2009. Private communication.

Chapter 5

Conclusions

5.1 Results

The major results of this thesis are as follows:

A high power interdigital-line antenna has been constructed, installed, and extensively operated in MST. This antenna has achieved $\gtrsim 220$ kW of applied power with over 100 kW radiated to the plasma despite unexceptional antenna coupling. With external tuning, the reflection coefficient averages -15.1 dB and -18.2 dB for ports 1 and 2 respectively. More extensive modeling of the impedance matching sections in the antenna design phase and better construction technique may reduce the reflection further still.

Measurement of the vacuum $n_\parallel$ spectrum shows excellent directivity for each of the antenna phasings. The peak of the spectrum is 6.80 and -6.92 for the co- and counter-current phasings respectively, lower than the design value of $n_\parallel = 7.8$. Antenna theory

and modeling show that the capacitive contribution of the aperture was overlooked in the antenna design phase. Lowering the pump frequency from 800 MHz to 788 MHz can compensate for this oversight without requiring extensive modification of the antenna geometry.

Coupling experiments demonstrate that an interdigital-line antenna performs well in high current standard plasmas and is unloaded in high current PPCD plasmas. A high percentage of the available power can be coupled to the plasma without significantly distorting the $n_{\|}$ spectrum. Plasma density is shown to be the key parameter with respect to antenna loading, while magnetic field and pitch have no significant effect: in-line with theoretical expectations.

Changes in plasma loading are shown to shift of the peak of the $n_{\|}$ spectrum, in some cases far enough to potentially make the accessibility of the wave an issue. Experimental measurements of the damping length and spectrum are compared to analytical and numerical models with the numerical model showing good qualitative agreement.

A plasma limiter placed in front of the antenna aperture has been used successfully to minimize the variability in the antenna loading but with the drawback that it becomes difficult to condition to high power. Local gas puffing has been used to maintain good coupling in low density and PPCD plasmas where in general coupling is poor.

Hard x-ray flux associated with LHRF has been observed in MST. Unfortunately, the present lack of reliable Fokker-Planck modeling of standard plasmas prevents an estimate of any current drive at present power levels. The observed x-ray flux has a toroidal asymmetry with emission localized about the antenna location, and a dis-

cernible left/right asymmetry relative to the toroidal antenna angle, as well as an almost order of magnitude difference in flux between antenna phasings. Additionally a large flux at the antenna face is observed. The toroidal asymmetry and high energy of the flux tends to reject the standard mechanism for producing fast electrons: Landau damping with ohmic field acceleration.

Numerical modeling with a Monte Carlo code and power balance accounting support the hypothesis that gradients in the rf electric fields near the antenna face pull out a high energy perpendicular tail in the velocity distribution. The tail is found to be trapped which allows for multi-pass acceleration of electrons in the antenna near-field. This tail and trapping can explain the asymmetries in the x-ray observations as well as the high flux from the antenna face: thick-target bremsstrahlung with the molybdenum antenna limiter. Power loss from these fast electrons is calculated to be several percent of total radiated power.

5.2 Future Work and Prospects

As always, interesting (or even uninteresting) results invariably lead to new questions and experiments that may answer those questions.

5.2.1 Power Handling Limits

As discussed in Chapter 1, it may require 1-2 MW of rf power to accomplish the goal of the program, namely reducing tearing mode fluctuations to levels comparable to that of PPCD. Additional CQL3D modeling will be required improve this estimate. Based

on the size of the power feeds and radial antenna profile, there is a distinct power limit for a single antenna that is much less than the total power required. The exact power limit is a complicated function of the feed size, the ambient pressure, and magnetic field strength [1]. A full production system then will require multiple separate antennas to achieve the required power.

A certain incident in October of 2008 may have considerable bearing on the power limits or overall feasibility of the MST lower hybrid antenna design. In the middle of October an unrecoverable arc occurred at an input power of ~ 170 kW. Subsequent to this incident, the antenna was unable to be conditioned beyond 140 kW, and in fact the power handling slowly degraded. An in-situ inspection of the antenna at the first available machine vent found what appeared to be a small flake of unknown composition had nestled into a loop diagnostic slot in a vertical orientation. A photo of the debris is shown in Figure 5.1. Unfortunately this debris was not recovered for analysis, but if the flake was in any respect conductive, it could easily be the cause of the conditioning issues.

After the debris was discovered, the antenna was removed from the machine for further inspection. It was found that serious arcing had occurred in both feeds between the vacuum feedthroughs and the primary impedance matching section. The largest impedance matching strap of port 1 also showed extensive arcing. Representative photographs are shown in Figure 5.2.

It is unclear at this time the precise cause of the arcing in the feedthroughs, in particular the whether the entirety of this arcing happens after the flake settled into the antenna cavity. It is probable that once the flake began an arc, the high VSWR

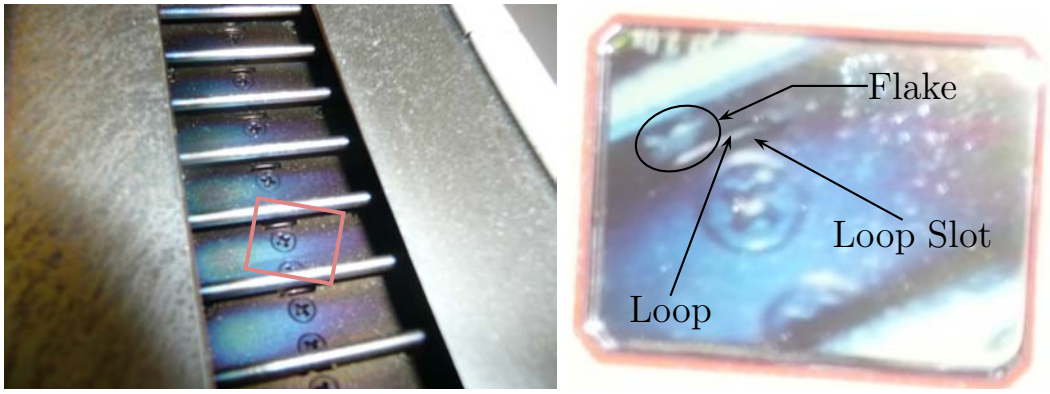

Figure 5.1: MkIII antenna on the bench looking at the center of the aperture. Inset shows an in-situ inspection of the antenna and a small flake of unknown composition.

from the reflection exceeded the breakdown voltage at the feed. Once arc residue formed in this region, arcing only became more likely. On the other hand it may be that the original high power experiments at $>$ 200 kW was the initial cause of the arcing. If this is the case, then we may be approaching or are at the power limit of the the antenna design.

To more fully test this, an additional klystron and an 3 dB Hybrid to be used as a combiner have been acquired. The added source power should be enough to determine if the $\sim$220 kW level attained so far is the upper limit of the launching structure.

5.2.2 PPCD

PPCD with LHRF is a topic that has seen preliminary work, but a more complete understanding is required. Since we expect that a successful rf experiment, i.e. fluctuation reduction, will result in improved confinement, it is necessary that the antenna can operate with temperature and density profiles similar to that of PPCD. Additionally,

Figure 5.2: Arcing problems in MkIII antenna feedthroughs. (a) Arcing on port 1 feed connector. (b) Arcing on port 2 feed connector. (c) Arcing on port 1 outer feed and first strap of impedance matching section.

with standard plasma confinement being so poor, PPCD itself probably will need to be applied before rf power is injected [2]. Previous experiments as outlined in §3.3.3 were performed with the MkII antenna and its limited loop diagnostics. The MkIII antenna, with its extended set of diagnostics will be able to measure any changes in the launching spectrum.

Unlike in standard plasmas, Fokker-Planck modeling has been fairly successful in PPCD with not unreasonable predictions of the x-ray flux. Though the magnitude and variability of the background emission in PPCD is an issue, better confinement gives the x-ray diagnostic a better chance to get an estimate for LH current drive. A diagnostic in the soft x-ray regime may also have better luck looking for the Landau resonance rather than the secondary effect of ohmic acceleration.

5.2.3 Parametric Decay and Scattering

Nonlinear three-wave interaction with rf injection has been reported in a wide variety of rf experiments at different frequencies [3–8]. Many decay channels exist for the lower

hybrid frequency regime, but two in particular may be of interest for MST: that of the decay of the pump wave into a lower hybrid wave and ion cyclotron quasi-mode and also the decay of the pump wave into a pair of lower hybrid waves.

The ion cyclotron quasi-mode decay mode has $\omega \simeq n\,\Omega_{ci}$, n an integer. The lower hybrid wave associated with this mode will follow selection rules and have $\omega \simeq \omega_0 \pm n\,\Omega_{ci}$, where ω_0 is the pump frequency. For the low field of MST, f_{ci} is on the order of 1 MHz instead of the tens of MHz on tokamaks. The lower hybrid-lower hybrid decay channel has the requirement that $\omega_0 \geq 2\omega_{LH}$. For MST operating conditions this requirement is never violated.

Additionally, experiments on ASDEX [9] demonstrate that scattering off of density fluctuations in the edge plasma can broaden the injected rf frequency as well as having a detrimental effect on current drive efficiency. Since the fluctuation level in MST standard plasmas is 20-40% [10], scattering may be a good candidate for a power loss mechanism.

Preliminary evidence for parametric decay and/or scattering was collected by the use of an electrostatic rf probe with an impedance of 50Ω similar to the type of probe used by Pinsker [3]. The probe was inserted into the plasma edge 2 cm from the machine wall at the same toroidal angle as the antenna and 90° poloidally displaced. The co-current drive (positive) phasing was used in 400 kA standard plasmas with $n_e \simeq 1 \times 10^{13}\,\mathrm{cm}^{-3}$. Ray tracing shows that a wave with positive antenna phasing passes very close poloidally to the probe tip as it descends radially to the absorption region.

The probe output was isolated using an inner and outer DC break and was split into

a pair of spectrum analyzers. Both were set to manual sweep at the center frequency. The first analyzer was used as a reference with its center frequency fixed at 800 MHz. The second analyzer's center frequency was set to the frequency of interest. Both have a bandwidth of 1 MHz. While this resolution might be just enough to resolve individual peaks from ion cyclotron quasi-modes, these experiments were designed to do a broad survey, with prospects of more detailed (and efficient) experiments in the future.

In vacuum, we find that the antenna does indeed launch some sort of EM wave as the electrostatic probe picks up signal when as little as 20 kW of power is applied to the antenna. Moving the probe from flush with the wall ($x = 0\,\mathrm{cm}$) to $x = +2\,\mathrm{cm}$, increases the signal at 800 MHz by almost 10 dB. The second and third harmonic of the 800 MHz pump wave are also present, although the peak at 2400 MHz is down more than 30 dB from the primary peak and the peak at 1600 MHz is down more than 50 dB. The widths of these peaks is on the order of the bandwidth resolution of the spectrum analyzer down to its detection threshold.

Figure 5.3 shows the results of a frequency scan from 10 MHz past the third harmonic on the pump frequency. The peaks at each of the harmonics show significant broadening relative to the vacuum width as seen in the ASDEX scattering experiment. The power on the low frequency side of the pump is much greater than that on the high frequency side. This result is in agreement with other LH experiments, though the power in the high side of the pump doesn't drop as abruptly in this experiment.

Figure 5.4b shows the response of the electrostatic probe as the rf power is decreased. The low-frequency side of the peak initially falls off faster than the peak magnitude consistent with the falloff of the PDI ion-cyclotron sidebands in the ATC

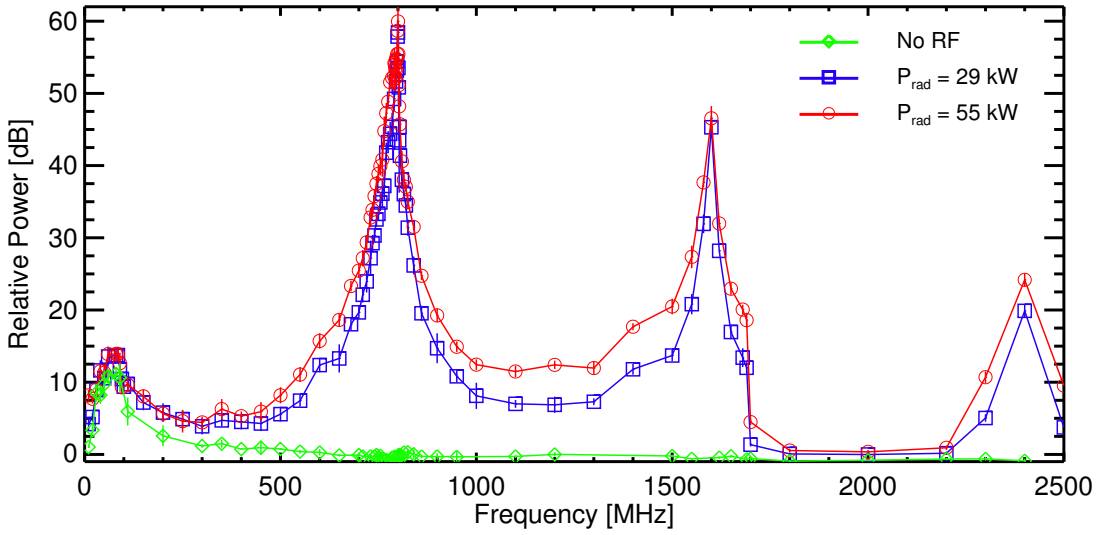

Figure 5.3: Frequency response of 50Ω electrostatic probe for two different rf radiated powers and a case with no rf.

experiment [4]. At lower powers however, the broadness of the peak does not decrease, indicating another mechanism for the peak width. Figure 5.4a shows the response at low frequencies. Although the spectral power increases when rf power is applied, there is still significant power from 30-100 MHz without rf.

The preliminary experiment presented here shows tantalizing hints of a parametric decay and/or scattering mechanism in MST plasmas. More in-depth experiments at higher frequency resolution and higher rf power are warranted.

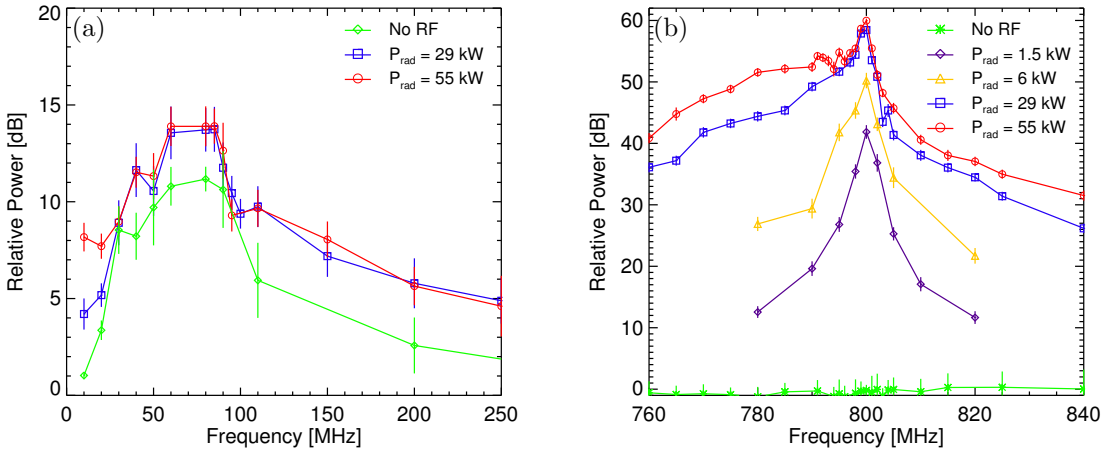

Figure 5.4: (a) Close-up of low frequency spectrum with and without rf. (b) Spectrum around 800 MHz pump frequency for different levels of rf power.

Bibliography

[1] Caughman, J. B. O., et al. Factors that influence RF breakdown in antenna systems. *APS Meeting Abstracts*, pp. 8104P–+, 2007.

[2] Hokin, S., et al. Confinement improvement with RF poloidal current drive in the reversed field pinch. *Nuclear Fusion*, **34**(11), 1994.

[3] Pinsker, R. *Fast wave current drive experiments on the Princeton Large Torus.* Ph.D. thesis, Princeton University, 1988.

[4] Porkolab, M., et al. Observation of parametric instabilities in lower-Hybrid radio-frequency heating of tokamaks. *Phys. Rev. Lett.*, **38**(5):230–233, 1977.

[5] Rost, J. C., Porkolab, M., and Boivin, R. L. Edge ion heating and parametric decay during injection of ion cyclotron resonance frequency power on the Alcator C-Mod tokamak. *Physics of Plasmas*, **9**(4):1262–1270, 2002.

[6] McDermott, F. S., et al. Observation of the parametric decay instability during electron cyclotron resonance heating on the Versator II tokamak. *Physics of Fluids*, **25**(9):1488–1490, 1982.

[7] Takase, Y. and Porkolab, M. Parametric excitation of ion-sound quasimodes during lower-hybrid heating experiments in tokamaks. *Physics of Fluids*, **26**(10):2992–3003, 1983.

[8] Biewer, T. M., et al. Edge ion heating by launched high harmonic fast waves in the National Spherical Torus Experiment. *Physics of Plasmas*, **12**(5):056108, 2005.

[9] Cesario, R., et al. Density fluctuations and spectral broadening during the lower hybrid current drive experiment on ASDEX. *Nuclear Fusion*, **32**(12):2127–35, 1992.

[10] Rempel, T. D., et al. Edge electrostatic fluctuations and transport in a reversed-field pinch. *Phys. Rev. Lett.*, **67**(11):1438–1441, 1991.

Appendix A

Finite Element Antenna Analysis

To calculate the characteristic impedance of our interdigital line, we need to solve for the potential. The general form of Poisson's equation (for our coordinate system) is

$$-\Delta\varphi(x,z) = f\,(x,z) \tag{A.1}$$

in some domain Ω. This partial differential equation is difficult to solve analytically except in very simple geometries even for trivial functions of f, so we turn to finite element methods. The FreeFem++ code [1] is used to solve (A.1). This package does not solve the PDE directly, but instead uses the "weak" or variational form of the equation. The variational form of Poisson's equation is

$$\int_\Omega \nabla\varphi \cdot \nabla w = \int_\Omega fw \quad \forall w \in \mathcal{X} \tag{A.2}$$

which minimizes an "energy" functional $I(w)$ to solve for φ. Here w is any function in the appropriate vector space $\mathcal{X}$, a subspace of the Sobolev space $H^1(\Omega)$. In the case at hand, we want to solve for the potential (2.2) which satifies Laplace's equation, so $f = 0$ in (A.2). We also must specify the boundary conditions $\Gamma = \partial\Omega$ which will be non-homogeneous Dirichlet type. The ground planes will be set to $\varphi = 0$ while the boundary of the m'th resonator will be given a particular voltage depending on the phase advance:

$$\varphi_{\mathrm{rod}_m} = \varphi_0 \cos\left(m\phi + \delta\right). \tag{A.3}$$

Once we have the potential, the charge per unit length can be found by integrating around the boudary of a resonator:

$$q = -\epsilon \int_\Gamma \nabla\varphi \cdot \hat{n}, \tag{2.23}$$

and then using the standard definition of capacitance, $C = q/\varphi$, the characteristic impedance of a uniform transmission line in TEM mode is related to its shunt capacitance [2] by

$$Z_0 = \frac{\eta}{\sqrt{\epsilon_r}\,(C/\epsilon)} \tag{2.24}$$

where ϵ_r is relative dielectric constant, and η is the impedance of free space.

With these boundary conditions, Figure A.1 shows the mesh used in the calculation. A seven-element interdigital line of circular conductors are sandwiched between pair of ground planes. The rod spacings and diameters correspond to the physical antenna geometry. Figure A.4 shows the resulting potential of the calculation for different

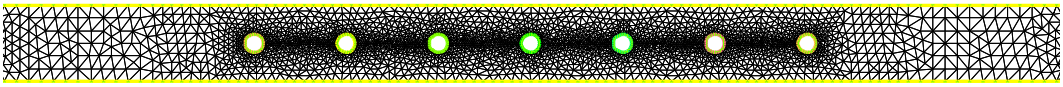

Figure A.1: FEM mesh for "closed" boundaries where the interdigital elements are between a pair of ground planes.

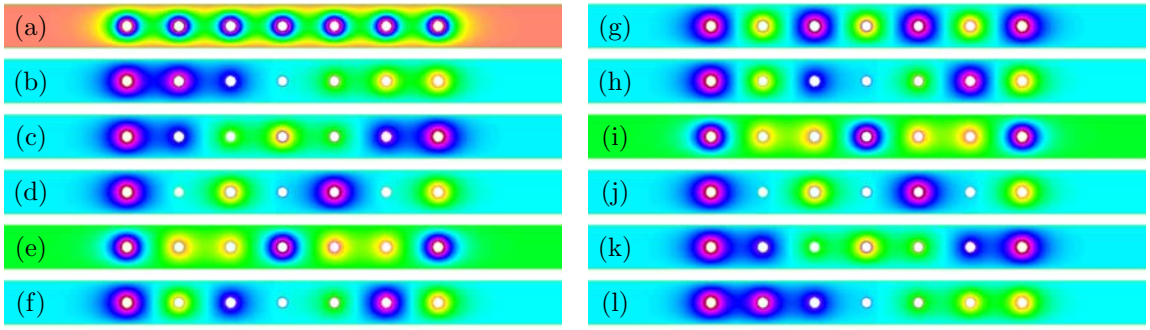

Figure A.2: FreeFem++ finite element solution for the potential φ for a seven element interdigital line sandwiched between two ground plane. (a)-(l) The phasing between resonators in 30° increments starting at $\phi = 0°$.

phasings between the conductors.

Figure A.3 shows the mesh for a similar model except that one of the ground planes has been replaced by an "open" boundary, or in this case the ground has been moved far away to simulate infinity. Figure A.4 shows the results for four different values of ϕ.

Seven conductor elements are used to minimize the effects of using a finite interdigital line, and the impedance is calculated from the center conductor. It should be noted that this is a two-dimensional problem and that interdigital is used in a loose sense as the voltage on each "rod" is applied externally and not with respect to the boundary conditions (2.3) and (2.4).

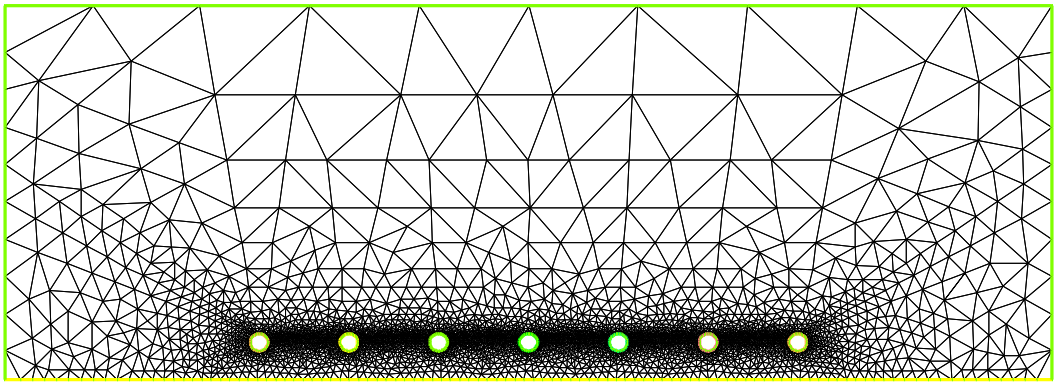

Figure A.3: FEM mesh for "mixed" boundary where one side is a grounded plane and the other is open — far away from the resonators.

The following program calculates the potential for a set of circular conductors (our interdigital line) that are sandwiched between a pair of grounded planes. A prescribed voltage, modulated by a phase shift, is applied to the conductors.

```
/*****************************************************************
 Copyright (C) 2009 - M.C. Kaufman

 Permission is hereby granted, free of charge, to any person obtaining
 a copy of this software and associated documentation files (the
 "Software"), to deal in the Software without restriction, including
 without limitation the rights to use, copy, modify, merge, publish,
 distribute, sublicense, and/or sell copies of the Software, and to
 permit persons to whom the Software is furnished to do so, subject to
 the following conditions:

 The above copyright notice and this permission notice shall be
 included in all copies or substantial portions of the Software.

 THE SOFTWARE IS PROVIDED "AS IS", WITHOUT WARRANTY OF ANY KIND,
 EXPRESS OR IMPLIED, INCLUDING BUT NOT LIMITED TO THE WARRANTIES OF
 MERCHANTABILITY, FITNESS FOR A PARTICULAR PURPOSE AND NONINFRINGEMENT.
 IN NO EVENT SHALL THE AUTHORS OR COPYRIGHT HOLDERS BE LIABLE FOR ANY
```

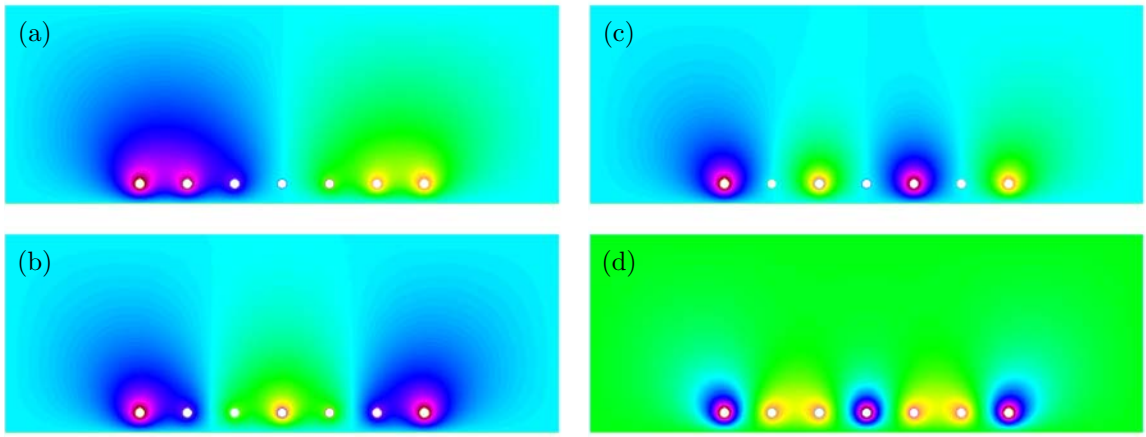

Figure A.4: FreeFem++ finite element solution for the potential φ for a seven element interdigital line with a single ground plane and an "open" boundary. The phase between resonators is (a) $\phi = 30°$ (b) $\phi = 60°$ (c) $\phi = 90°$ (d) $\phi = 120°$.

```
 CLAIM, DAMAGES OR OTHER LIABILITY, WHETHER IN AN ACTION OF CONTRACT,
 TORT OR OTHERWISE, ARISING FROM, OUT OF OR IN CONNECTION WITH THE
 SOFTWARE OR THE USE OR OTHER DEALINGS IN THE SOFTWARE.
*************************************************************************/

// interdigital line (double ground planes)

// border enumeration
int G=98;
int INF=99;

// mesh density
int nm = -25;
int ni = -10;
int ng = -40;
real m;

/* use cristal terms for geometry
 *
 * c = center-center
```

```
 * b = cavity height
 * d = rod diameter
 * s = side-side (s = c-d)
 */
real c = 12;
real d = 2.38;
real b = 10;
real s = c - d;

real iwid = 140;
real ihei = 50;
real[int] V0(7);
int n = 35;
real start = 10;
real offset = 0.04;
real[int] th(n), Z0(n);
real q0, c0;
real eps0 = 1.0;
real eta = 376.7;

// conductor borders defining the geometry
border LN3(t=0,2*pi) {
  m=-3; x = m*c + d/2 * cos(t); y = b/2 + d/2 * sin(t);
}
border LN2(t=0,2*pi) {
  m=-2; x = m*c + d/2 * cos(t); y = b/2 + d/2 * sin(t);
}
border LN1(t=0,2*pi) {
  m=-1; x = m*c + d/2 * cos(t); y = b/2 + d/2 * sin(t);
}
border L0(t=0,2*pi)  {
  m=0;  x = m*c + d/2 * cos(t); y = b/2 + d/2 * sin(t);
}
border LP1(t=0,2*pi) {
  m=1;  x = m*c + d/2 * cos(t); y = b/2 + d/2 * sin(t);
}
border LP2(t=0,2*pi) {
  m=2;  x = m*c + d/2 * cos(t); y = b/2 + d/2 * sin(t);
```

```
}
border LP3(t=0,2*pi) {
  m=3;  x = m*c + d/2 * cos(t); y = b/2 + d/2 * sin(t);
}

border G1(t=-0.7,-1) { x = iwid/2 * t; y = 0; label=G; }  // bottom
border G2(t=0.7,-0.7) { x = iwid/2 * t; y = 0; label=G; } // bottom
border G3(t=1,0.7) { x = iwid/2 * t; y = 0; label=G; }    // bottom
border G4(t=-1,-0.7) { x = iwid/2 * t; y = b; label=G; }  // top
border G5(t=-0.7,0.7) { x = iwid/2 * t; y = b; label=G; } // top
border G6(t=0.7,1) { x = iwid/2 * t; y = b; label=G; }    // top

border B1(t=0,1) { y = b * t; x = -iwid/2; label=INF; }   // left
border B2(t=1,0) { y = b * t; x = iwid/2; label=INF; }    // right

plot(B1(ni) + B2(ni) +
     G1(ni/3) + G2(ng*2) + G3(ni/3) +
     G4(ni/3) + G5(ng*2) + G6(ni/3) +
     LN3(nm) + LN2(nm) + LN1(nm) + L0(nm) +
     LP1(nm) + LP2(nm) + LP3(nm),
     bb=[[-iwid*0.6,0],[iwid*0.6,b*0.1]], wait = 0);

// finite-elements mesh
mesh Th = buildmesh(B1(ni) + B2(ni) +
                    G1(ng / 3) + G2(ng * 2) + G3(ng / 3) +
                    G4(ng / 3) + G5(ng * 2) + G6(ng / 3) +
                    LN3(nm) + LN2(nm) + LN1(nm) + L0(nm) +
                    LP1(nm) + LP2(nm) + LP3(nm));
plot(Th, wait=1, ps = "ps/fem_mesh_closed.ps");

fespace Vh(Th,P2); // P2 conforming triangular FEM
Vh phi, ww, f=0;

for (int i = 0; i < n; i++) {

  // phase shift
  th[i] = (start + i*10) * pi/180;
```

```
  // voltage on resonating conductors
  for (int j = 0; j < 7; j++) {
    V0[j] = cos(j * th[i] + offset);
  }

  // weak or variational form of Laplace's equation plus borders
  solve P(phi, ww) = int2d(Th)(dx(phi) * dx(ww) + dy(phi) * dy(ww))
                - int2d(Th)(f * ww)
                + on(INF, phi = 0)
                + on(G,   phi = 0)
                + on(LN3, phi = V0[0])
                + on(LN2, phi = V0[1])
                + on(LN1, phi = V0[2])
                + on(L0,  phi = V0[3])
                + on(LP1, phi = V0[4])
                + on(LP2, phi = V0[5])
                + on(LP3, phi = V0[6]);

  // integrate over the L0 boundary to get the charge per unit length
  q0 = int1d(Th,L0)(eps0 * (dx(phi) * N.x + dy(phi) * N.y));

  // get the characteristic impedance for the i'th phase shift
  Z0[i] = eta / q0 * V0[3];

  cout << "Z0(" << (th[i] * 180/pi) << ") = " << Z0[i] << endl;

  // output the potential as a function of (x,y)
  plot(phi, fill = 1, nbiso = 150, value = 0,
       bb = [[-iwid*0.51,0],[iwid*0.51,1.0]],
       wait = 0, ps = "ps/fem_pot_" + th[i]*180/pi + "_closed.ps");
}

// print out results
cout << "================================================" << endl;
cout << "s = " << s << endl;
cout << "d = " << d << endl;
cout << "c = " << c << endl;
cout << "b = " << b << endl << endl;
```

```
cout << "  ph = [";
for (int i = 0; i < n; i++) {
  cout << (th[i] * 180/pi);
  if (i < n-1) cout << ", ";
}
cout << "]" << endl;

cout << "  Z = [";
for (int i = 0; i < n; i++) {
  cout << Z0[i];
  if (i < n-1) cout << ", ";
}
cout << "]" << endl;
cout << "================================================" << endl;
```

Th following program calculates the potential for a set of circular conductors (our interdigital line) with a single ground plane on one side and an "open" boundary elsewhere. A prescribed voltage, modulated by a phase shift, is applied to the conductors.

```
/*********************************************************************
 Copyright (C) 2009 - M.C. Kaufman

 Permission is hereby granted, free of charge, to any person obtaining
 a copy of this software and associated documentation files (the
 "Software"), to deal in the Software without restriction, including
 without limitation the rights to use, copy, modify, merge, publish,
 distribute, sublicense, and/or sell copies of the Software, and to
 permit persons to whom the Software is furnished to do so, subject to
 the following conditions:

 The above copyright notice and this permission notice shall be
 included in all copies or substantial portions of the Software.

 THE SOFTWARE IS PROVIDED "AS IS", WITHOUT WARRANTY OF ANY KIND,
 EXPRESS OR IMPLIED, INCLUDING BUT NOT LIMITED TO THE WARRANTIES OF
```

```
 MERCHANTABILITY, FITNESS FOR A PARTICULAR PURPOSE AND NONINFRINGEMENT.
 IN NO EVENT SHALL THE AUTHORS OR COPYRIGHT HOLDERS BE LIABLE FOR ANY
 CLAIM, DAMAGES OR OTHER LIABILITY, WHETHER IN AN ACTION OF CONTRACT,
 TORT OR OTHERWISE, ARISING FROM, OUT OF OR IN CONNECTION WITH THE
 SOFTWARE OR THE USE OR OTHER DEALINGS IN THE SOFTWARE.
*************************************************************************/

// interdigital line with an "open" boundary (single ground plane),
// cylindrical resonators.

// border enumeration
int G=98;
int INF=99;

// mesh density
int nm = -30;
int ni = -10;
int ng = -40;
real m;

/* use cristal terms for geometry
 *
 * c = center-center
 * b = cavity height
 * d = rod diameter
 * s = side-side (s = c-d)
 */
real c = 12;
real d = 2.38;
real b = 10;
real s = c - d;
real iwid = 140;
real ihei = 50;
real[int] V0(7);
int n = 35;
real start = 10;
real offset = 0.04;
real[int] th(n), Z0(n);
```

```
real q0, c0;
real eps0 = 1.0;
real eta = 376.7;

// conductor borders defining the geometry
border LN3(t=0,2*pi) {
  m=-3; x = m*c + d/2 * cos(t); y = b/2 + d/2 * sin(t);
}
border LN2(t=0,2*pi) {
  m=-2; x = m*c + d/2 * cos(t); y = b/2 + d/2 * sin(t);
}
border LN1(t=0,2*pi) {
  m=-1; x = m*c + d/2 * cos(t); y = b/2 + d/2 * sin(t);
}
border L0(t=0,2*pi)  {
  m=0;  x = m*c + d/2 * cos(t); y = b/2 + d/2 * sin(t);
}
border LP1(t=0,2*pi) {
  m=1;  x = m*c + d/2 * cos(t); y = b/2 + d/2 * sin(t);
}
border LP2(t=0,2*pi) {
  m=2;  x = m*c + d/2 * cos(t); y = b/2 + d/2 * sin(t);
}
border LP3(t=0,2*pi) {
  m=3;  x = m*c + d/2 * cos(t); y = b/2 + d/2 * sin(t);
}

border G3(t=1,0.7) { x = iwid/2 * t; y = 0; label=G; }    // bottom
border G2(t=0.7,-0.7) { x = iwid/2 * t; y = 0; label=G; } // bottom
border G1(t=-0.7,-1) { x = iwid/2 * t; y = 0; label=G; }  // bottom

border B1(t=0,1) { y = ihei * t; x = -iwid/2; label=INF; } // left
border B2(t=1,0) { y = ihei * t; x = iwid/2; label=INF; }  // right
border B3(t=-1,1) { x = iwid/2 * t; y = ihei; label=INF; } // top

plot(B1(ni) + B2(ni) + B3(ni) +
        G1(ni/3) + G2(ng*2) + G3(ni/3) +
        LN3(nm) + LN2(nm) + LN1(nm) + L0(nm) +
```

```
        LP1(nm) + LP2(nm)+LP3(nm),
        bb=[[-iwid*1.0,0],[iwid*1.0,ihei*0.2]], wait = 0);

// finite-elements mesh
mesh Th = buildmesh(B1(ni) + B2(ni) + B3(ni) +
                    G1(ng/3) + G2(ng*2) + G3(ng/3) +
                    LN3(nm) + LN2(nm) + LN1(nm) + L0(nm) +
                    LP1(nm) + LP2(nm) + LP3(nm));
plot(Th, wait=0, ps="ps/fem_mesh_open.ps");

fespace Vh(Th,P2); // P2 conforming triangular FEM
Vh phi, ww, f=0, g=0, v=0, ex, ey;

for (int i = 0; i < n; i++) {

  // phase shift
  th[i] = (start + i*10) * pi/180;

  // voltage on resonating conductors
  for (int j = 0; j < 7; j++) {
    V0[j] = cos(j * th[i] + offset);
  }

  // weak or variational form of Laplace's equation plus borders
  solve P(phi,ww) = int2d(Th)(dx(phi) * dx(ww) + dy(phi) * dy(ww))
                - int2d(Th)(f * ww)
                + on(INF, phi = 0)
                + on(G, phi = 0)
                + on(LN3, phi = V0[0])
                + on(LN2, phi = V0[1])
                + on(LN1, phi = V0[2])
                + on(L0,  phi = V0[3])
                + on(LP1, phi = V0[4])
                + on(LP2, phi = V0[5])
                + on(LP3, phi = V0[6]);

  // integrate over the L0 boundary to get the charge per unit length
  q0 = int1d(Th,L0)(eps0 * (dx(phi) * N.x + dy(phi) * N.y));
```

```
  // get the characteristic impedance for the i'th phase shift
  Z0[i] = eta / q0 * V0[3];

  cout << "Z0(" << (th[i] * 180/pi) << ") = " << Z0[i] << endl;

  // output the potential as a function of (x,y)
  plot(phi, fill = 1, nbiso = 100, value = 0,
       bb = [[-iwid*0.51,ihei*0.2],[iwid*0.51,ihei*0.3]],
       wait = 0, ps="ps/fem_pot_" + th[i]*180/pi + "_open.ps");
}

// print out results
cout << "================================================" << endl;
cout << "s = " << s << endl;
cout << "d = " << d << endl;
cout << "c = " << c << endl;
cout << "b = " << b << endl << endl;

cout << "  ph = [";
for (int i = 0; i < n; i++) {
  cout << (th[i] * 180/pi);
  if (i < n-1) cout << ", ";
}
cout << "]" << endl;

cout << "  Z = [";
for (int i = 0; i < n; i++) {
  cout << Z0[i];
  if (i < n-1) cout << ", ";
}
cout << "]" << endl;
cout << "================================================" << endl;
```

Appendix B

Antenna Fields

CST Microwave Studio™ is used to simulate the electric and magnetic fields on a flat model of the MkIII antenna in vacuum. The following fields are normalized to 1 sqrt(W) peak power of at the input port of the model. To recover the vacuum fields, the magnitude should be multiplied by $\sqrt{2P_{in}}$ where P_{in} is the *average* input power (not the radiated power) in watts.

COMSOL is used to simulate the same antenna fields but in the presence of plasma. The shape of the density profile is given in §2.2. The fields shown here have a vacuum gap of 1 mm, a density step of $n_{e_0} = 5 \times 10^{10}$ cm^{-3}, a density gradient $dn/dx = 1 \times 10^{11}$ cm^{-4} and a guide field of 1500 G. The COMSOL fields are normalized to 1 W of average power at the input port.

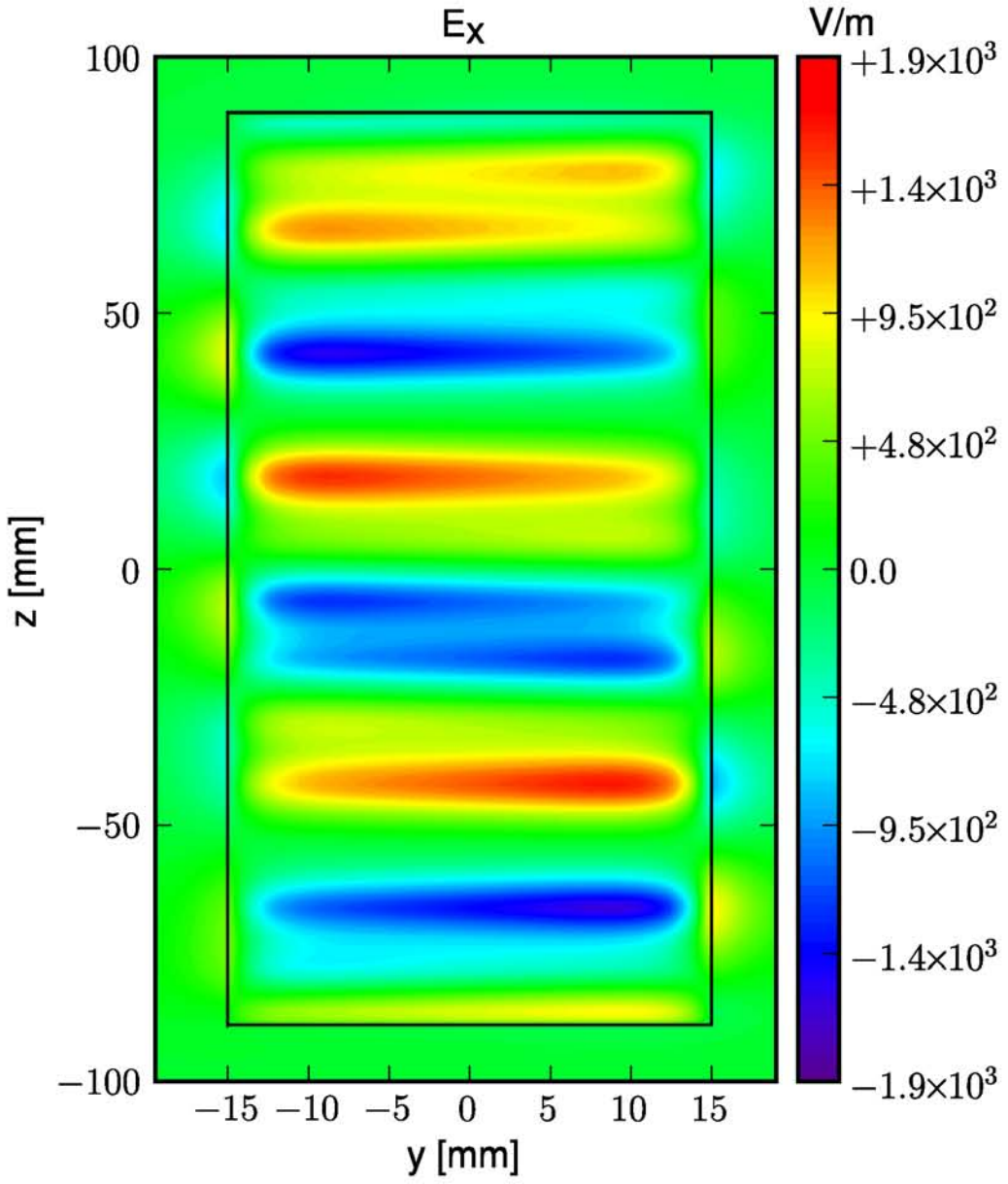

Figure B.1: E_x component of antenna vacuum field 2 mm in front of the antenna. The rectangle is the extent of the aperture on the antenna face.

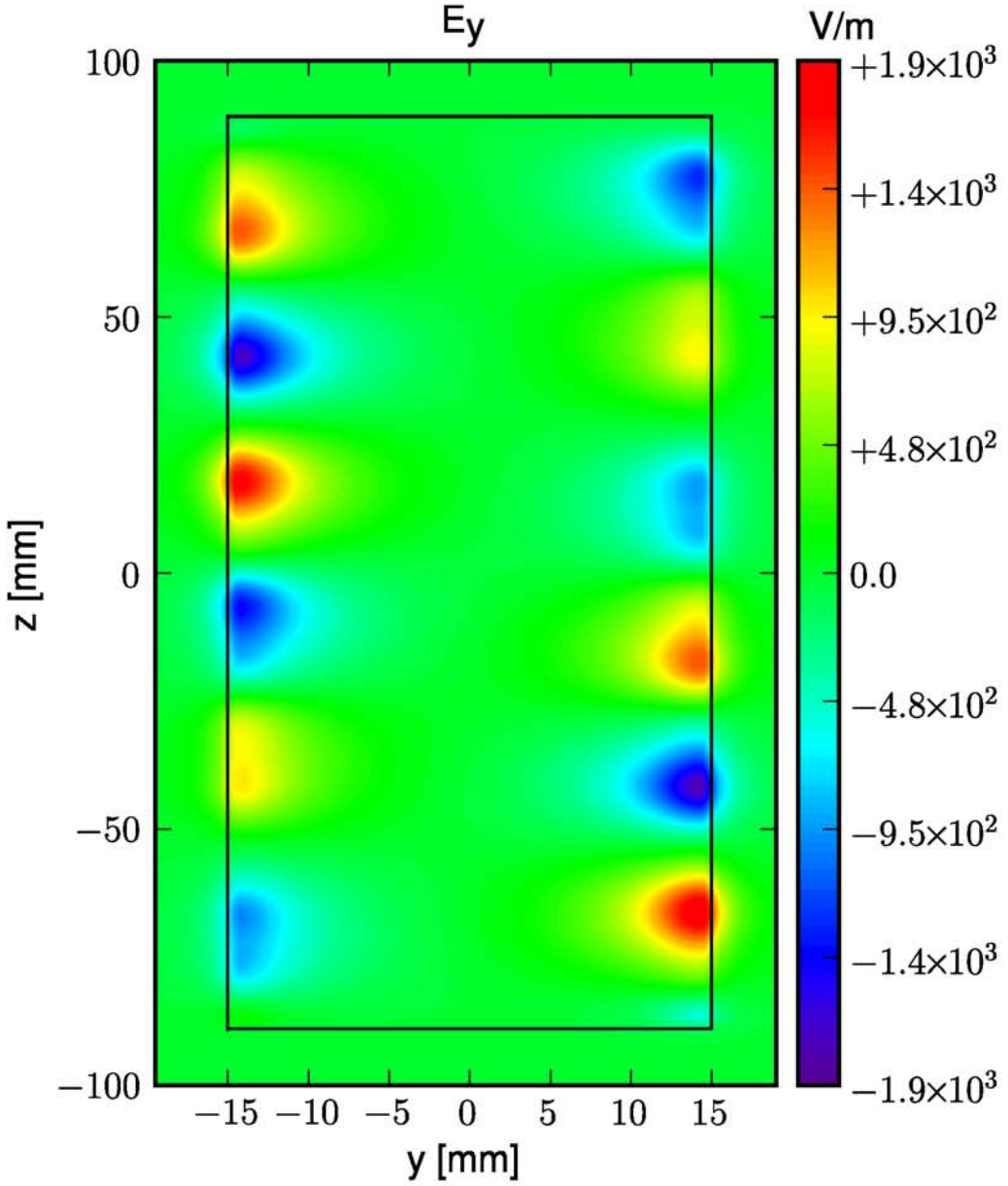

Figure B.2: E_y component of antenna vacuum field 2 mm in front of the antenna.

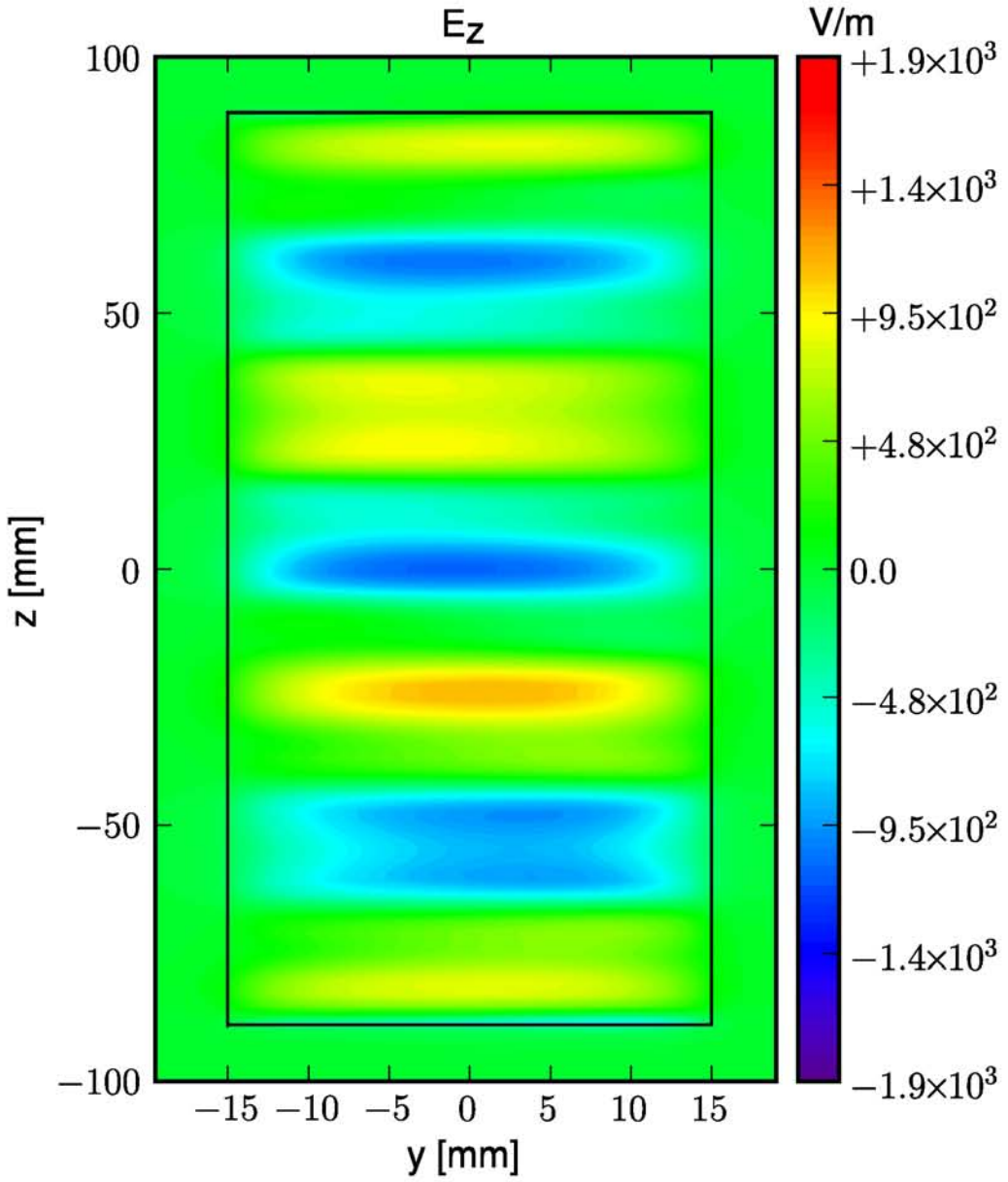

Figure B.3: E_z component of antenna vacuum field 2 mm in front of the antenna.

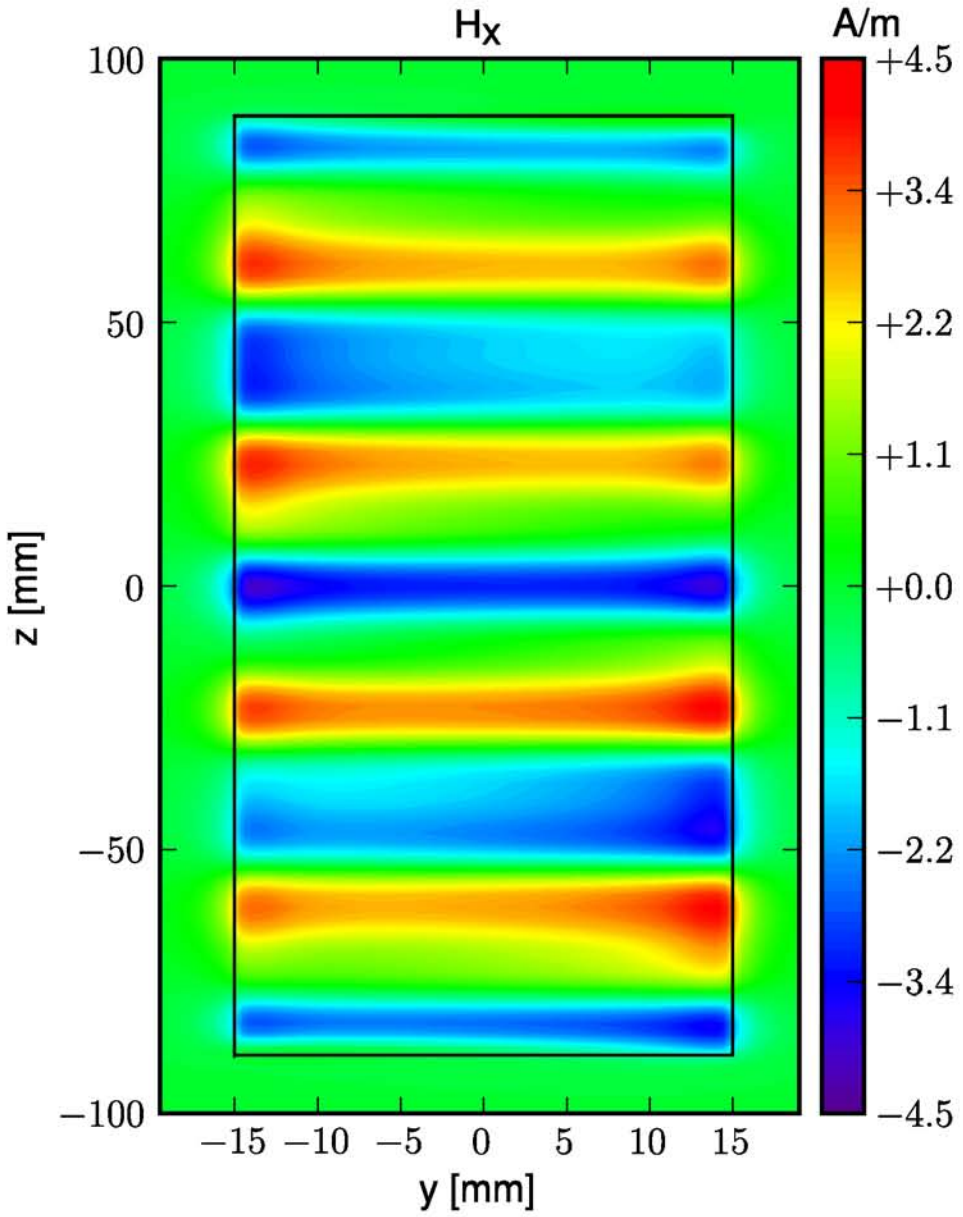

Figure B.4: H_x component of antenna vacuum field 2 mm in front of the antenna.

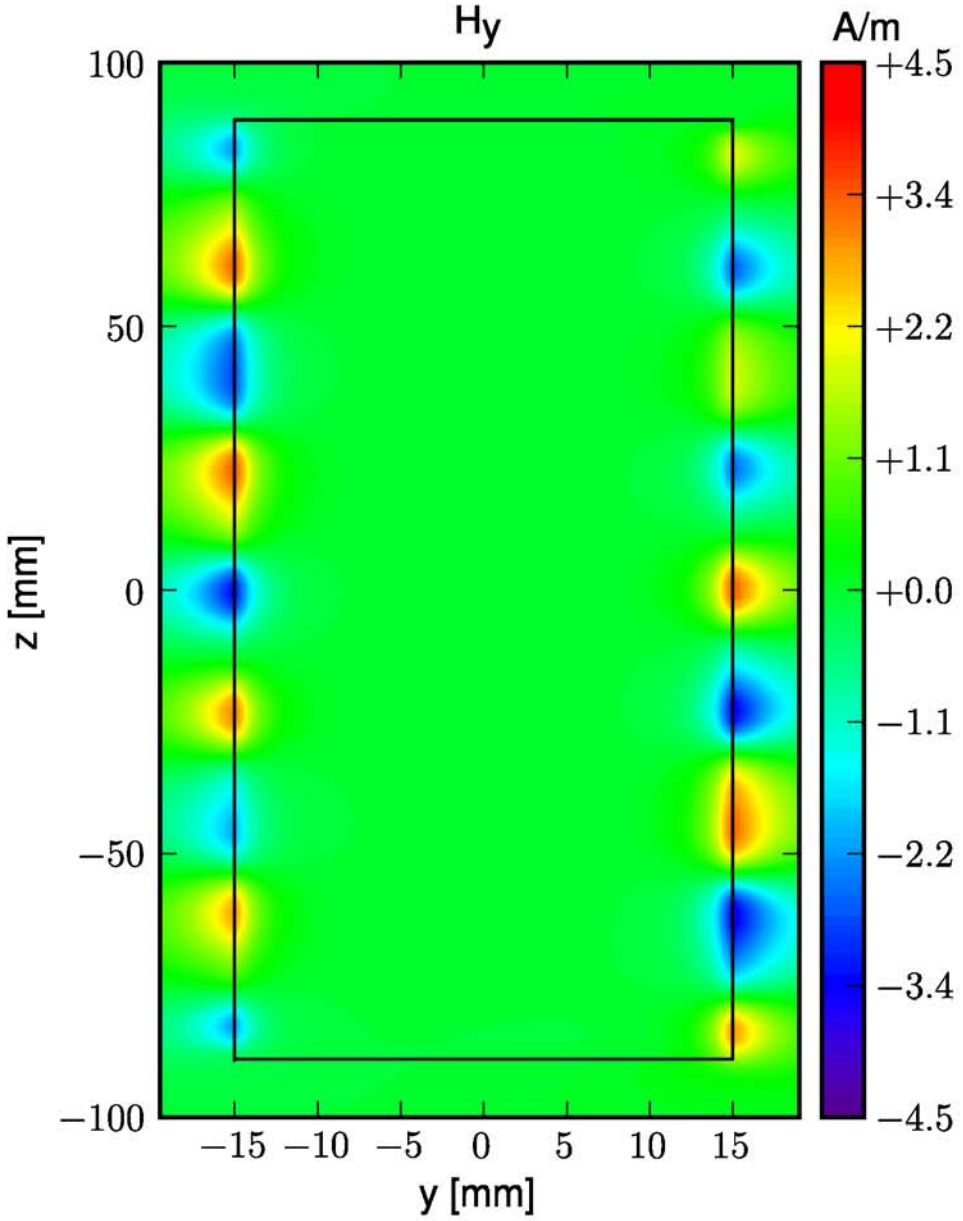

Figure B.5: H_y component of antenna vacuum field 2 mm in front of the antenna.

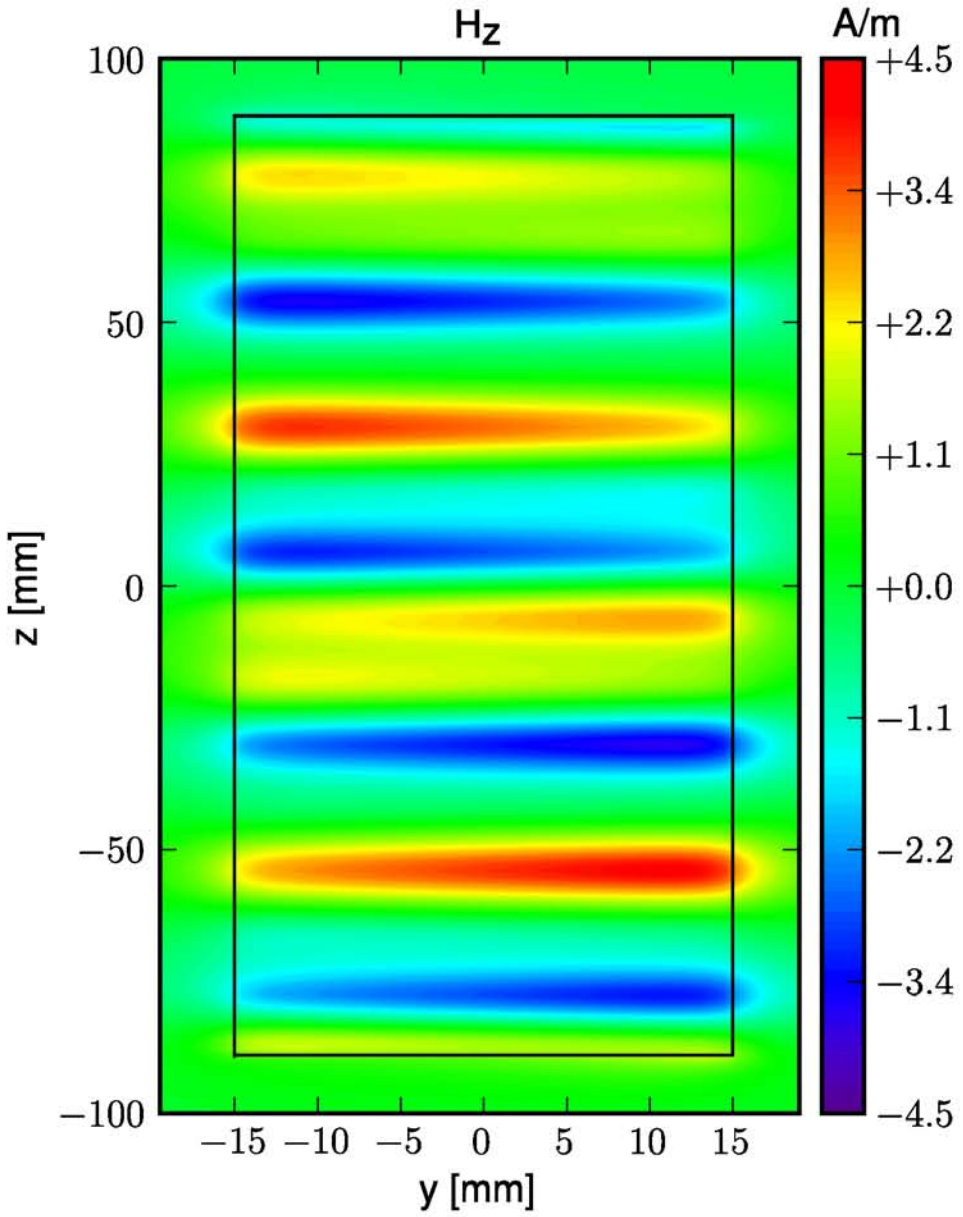

Figure B.6: H_z component of antenna vacuum field 2 mm in front of the antenna.

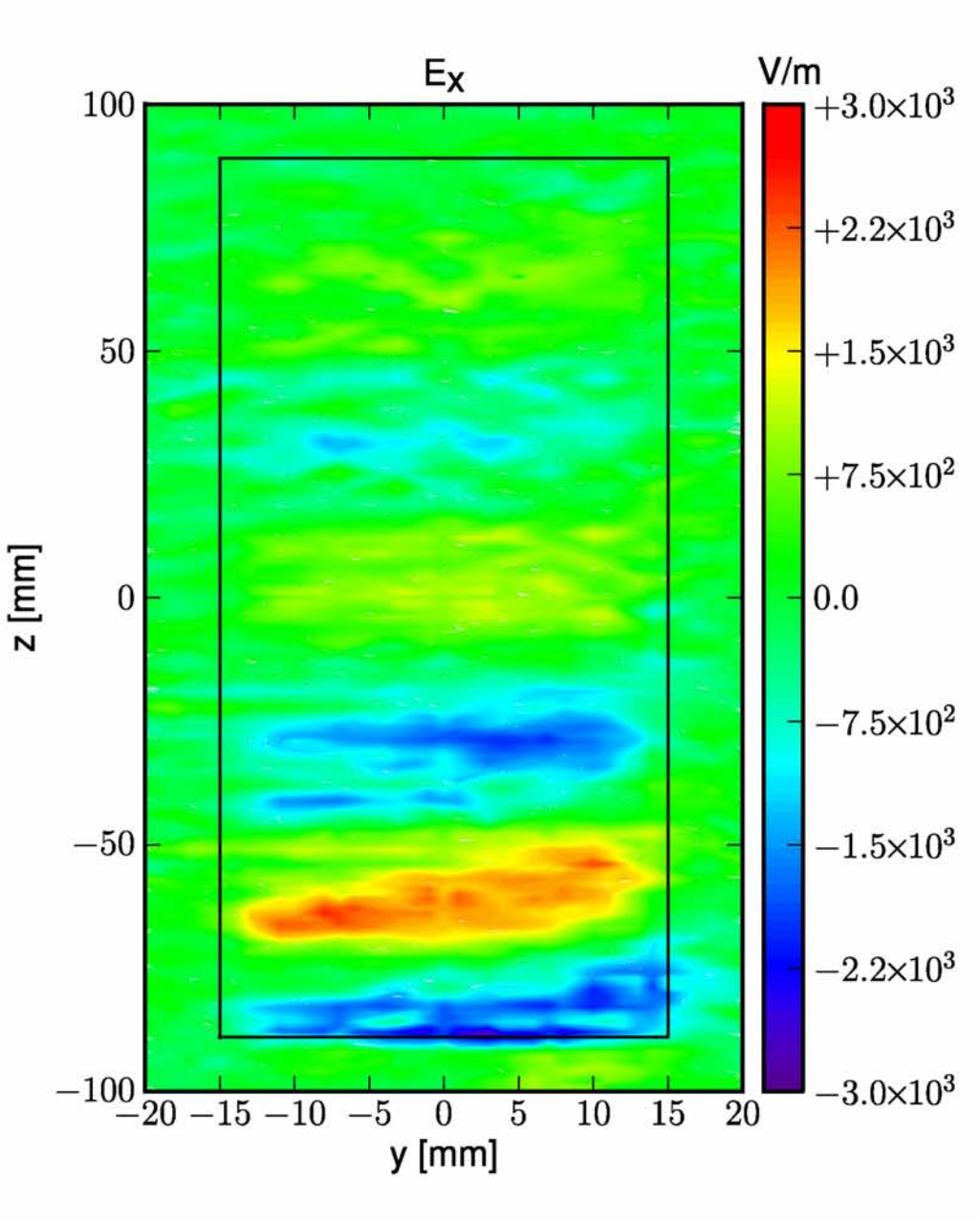

Figure B.7: E_x component of antenna field in the presence of plasma. The field shown is 2 mm in front of the antenna. The rectangle is the extent of the aperture on the antenna face.

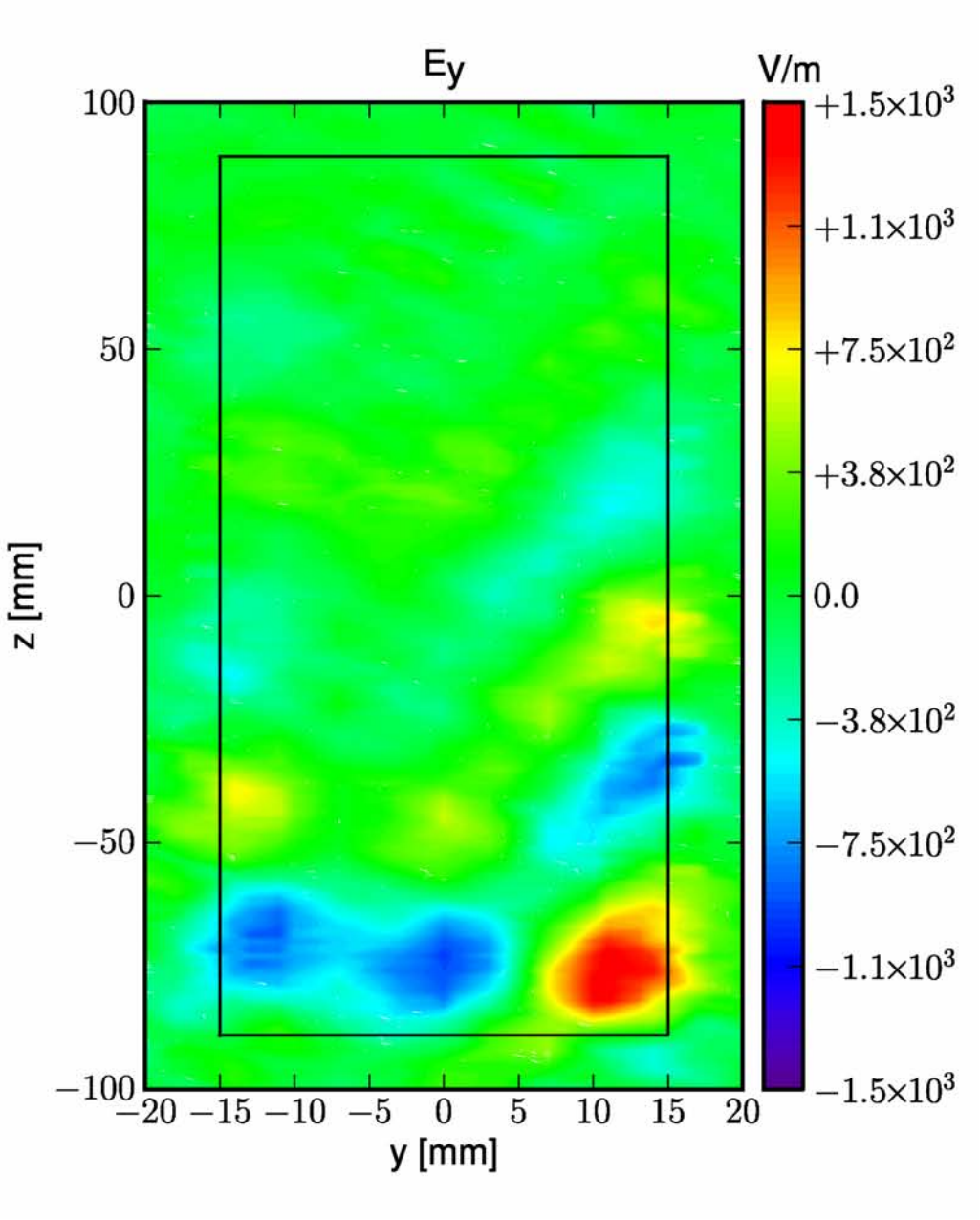

Figure B.8: E_y component of antenna field in the presence of plasma. The field shown is 2 mm in front of the antenna. The rectangle is the extent of the aperture on the antenna face.

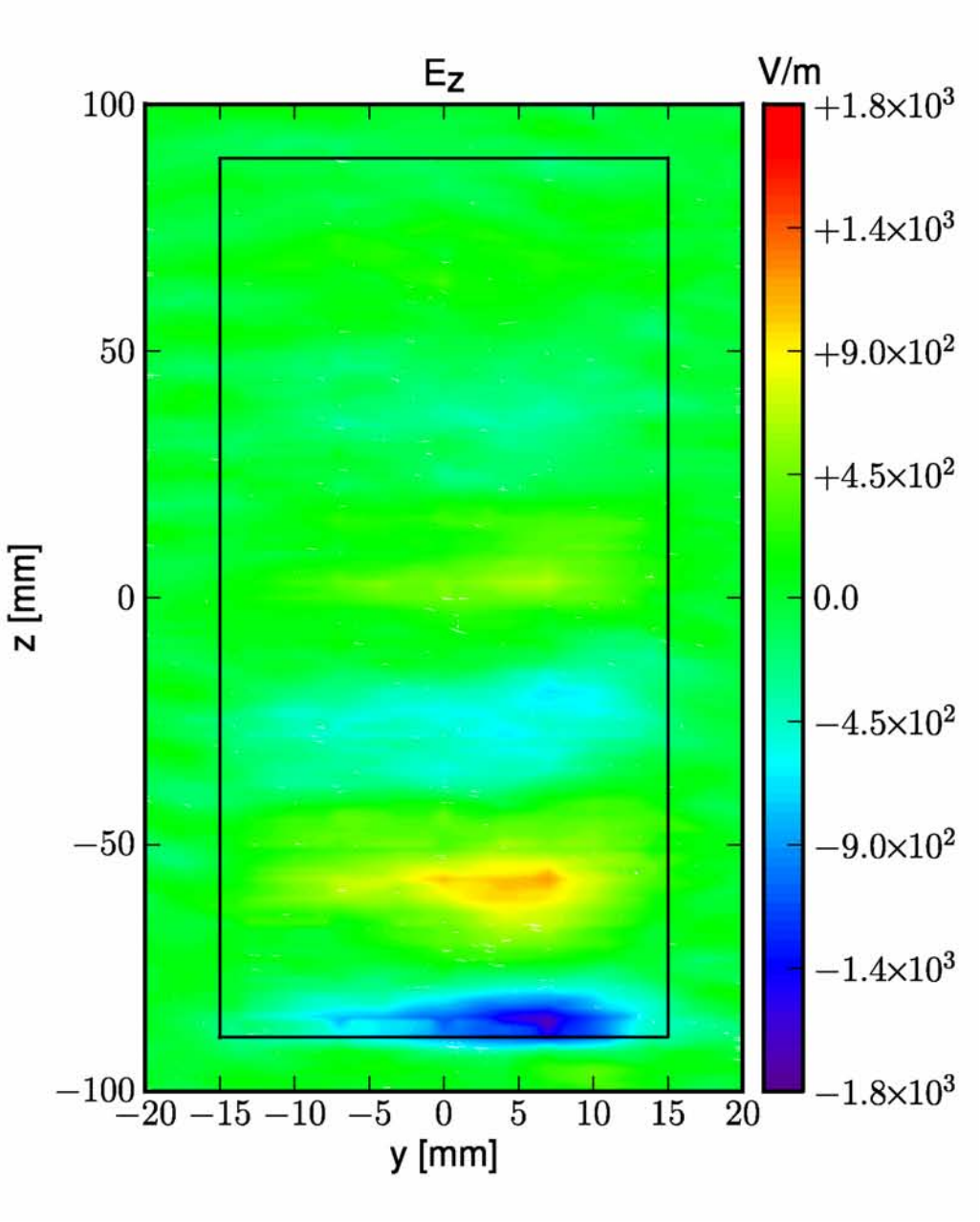

Figure B.9: E_z component of antenna field in the presence of plasma. The field shown is 2 mm in front of the antenna. The rectangle is the extent of the aperture on the antenna face.

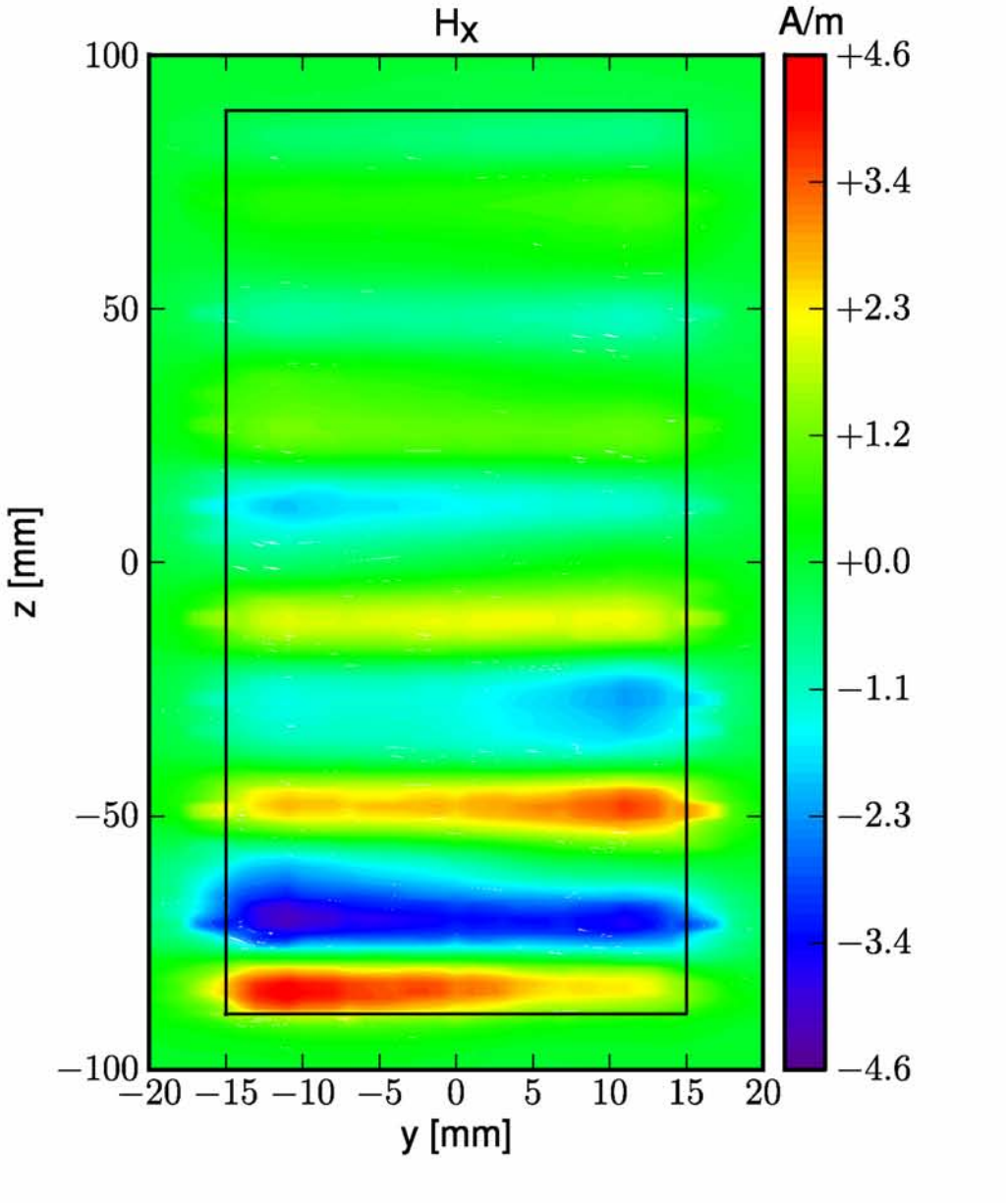

Figure B.10: H_x component of antenna field in the presence of plasma. The field shown is 2 mm in front of the antenna. The rectangle is the extent of the aperture on the antenna face.

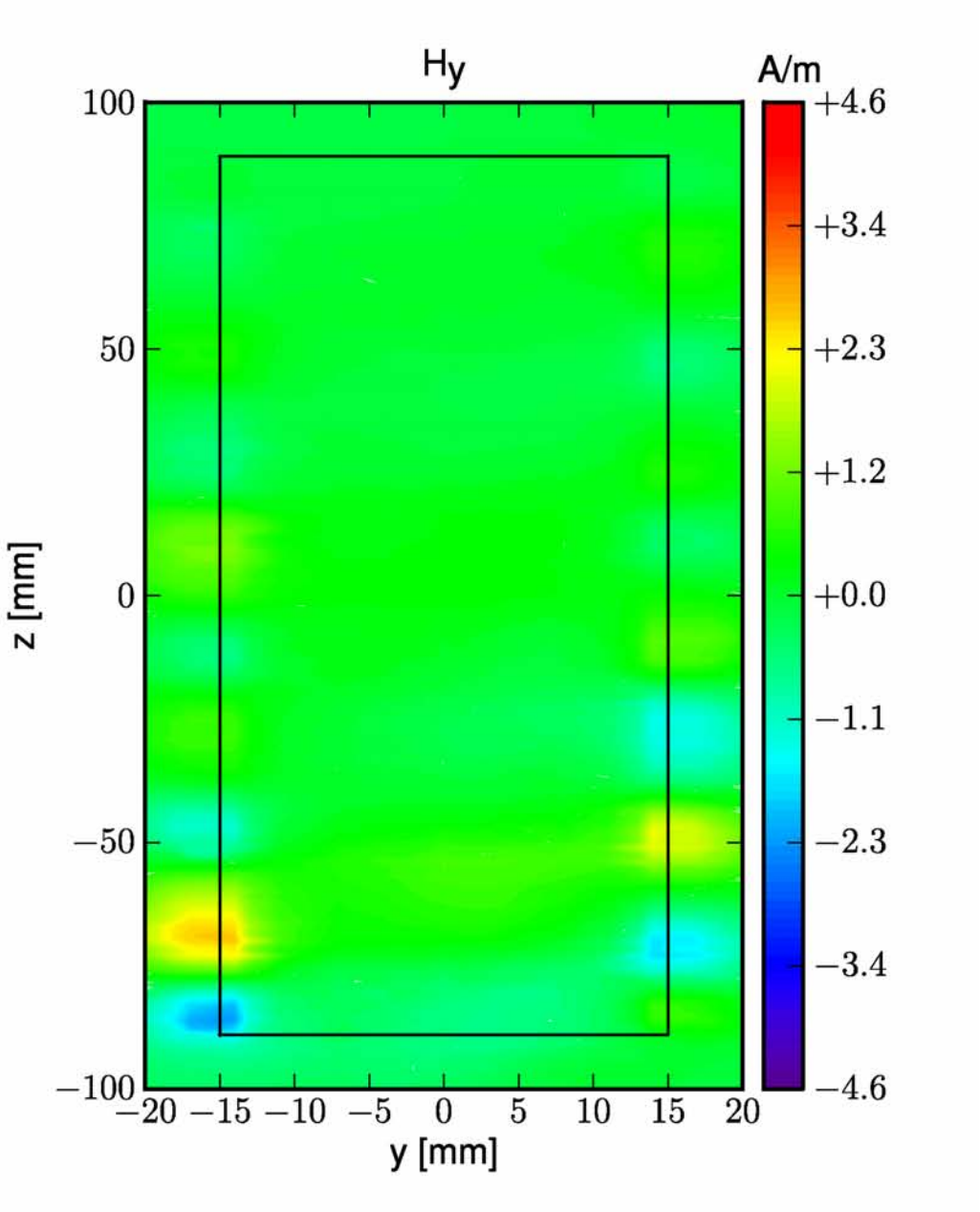

Figure B.11: H_y component of antenna field in the presence of plasma. The field shown is 2 mm in front of the antenna. The rectangle is the extent of the aperture on the antenna face.

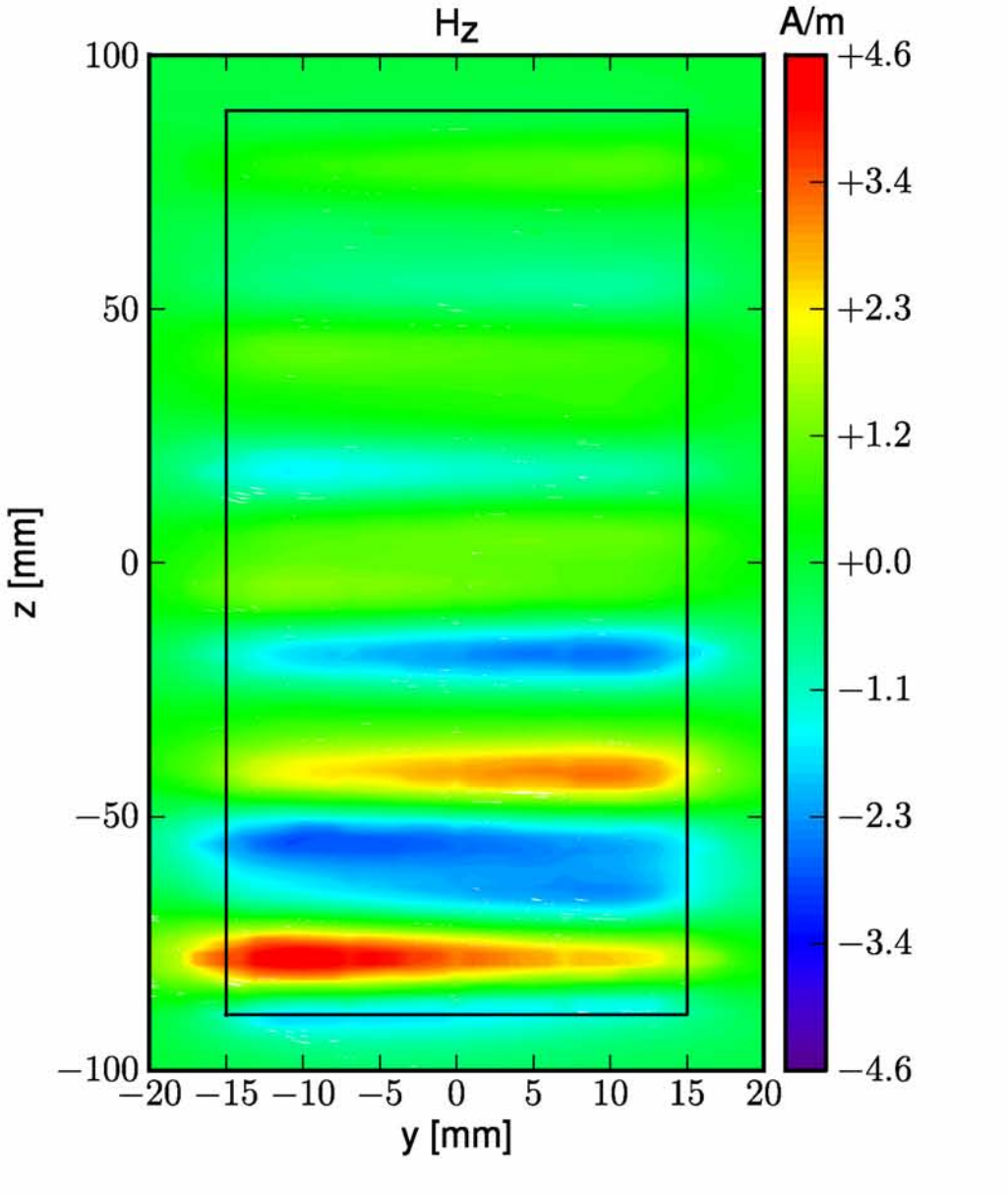

Figure B.12: H_z component of antenna field in the presence of plasma. The field shown is 2 mm in front of the antenna. The rectangle is the extent of the aperture on the antenna face.

Appendix C

Calibration of Power Couplers

C.1 Calibration of Coaxial Directional Couplers

Unlike low-power directional couplers, the Jampro™ RCID-302-F dual directional couplers attached to the transmission line can be adjusted for directionality and desired attenuation. A diagram of the device is shown in Figure C.1. A diagram of a directional coupler is shown in Figure C.2. The coupler is a slug with a loop inserted into a stub on the transmission line. The slug on each stub has a pair of ports attached to either end of the loop. These are the coupled and isolated ports for the coupler. One of the two couplers on the Jampro will be used for the forward power measurement and the other for the reflected power measurement.

To calibrate, the coupler section is removed from the rest of the transmission line. For the forward power calibration, choose one of the two couplers (arbitrary). The reflection (stimulus) port of a network analyzer is attached to the input port of the

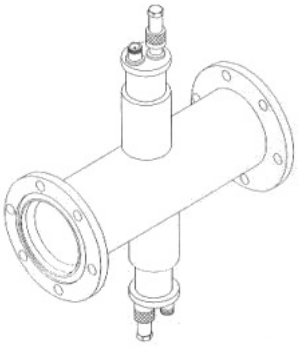

Figure C.1: Dual directional couplers attached to $3^1/_8$" transmission line section.

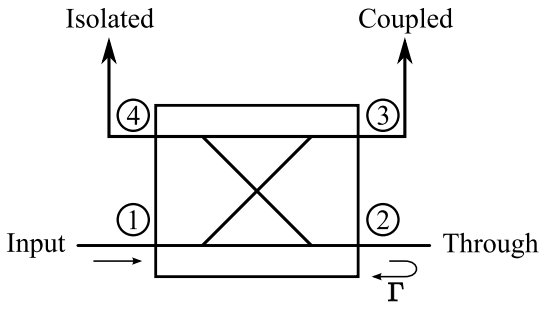

Figure C.2: Block diagram of a directional coupler.

coupler. The transmission port of the analyzer if attached to the coupled port on the stub of the transmission line. The through port of the coupler (the output of the transmission line) is attached to a signal generator. The ports of the network analyzer and the output of the signal generator should be impedance-matched to the transmission line, 50Ω. The isolated port is terminated as well. To sum up, the ports of the couplers are connected to:

Port 1: Input The reflection (stimulus) port of the network analyzer.

Port 2: Through The output port of the signal generator.

Port 3: Coupled The transmission port of the network analyzer.

Port 4: Isolated Terminated with matched (50Ω) load.

The setup is shown in Figure C.3.

The signal generator and the network analyzer stimulus are set to CW at the frequency of interest—in our case 800 MHz; network analyzer's stimulus acts as the

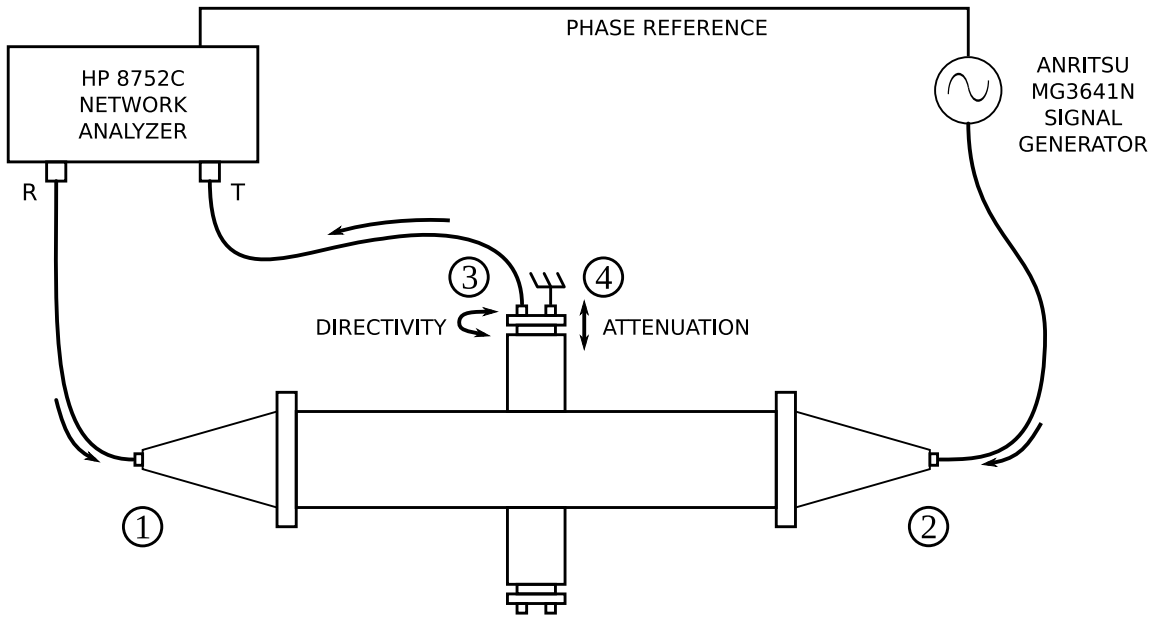

Figure C.3: The setup for calibrating Jampro dual directional couplers. The R port on the network analyzer is the stimulus port.

forward-traveling wave, the signal generator acts as the reflected wave. (Note: this procedure requires the output port of the signal generator to be able to handle the output power of the network analyzer and also to act as a matched load.)

To set the attenuation, first zero the signal generator power. Then the slug holding the coupler is slid in or out of its housing while noting the power received at the transmission port of the network analyzer. The Jampro couplers have a usable range of $35 - 70$dB attenuation.

With a target attenuation, the object now is to increase the directivity and isolation. On a practical level, we would like the coupled power to be entirely insensitive to power reflected from port 2, the through port. The directivity is tuned by rotating the

coupler's slug to sample more or less of the reflected wave in the transmission line. As it is difficult to minimize the power sampled from the reflected wave by rotating the slug without inadvertently changing the insertion depth of the slug as well, a couple of tricks can be used. A signal generator with the capability of performing a power sweep can be used to sweep from low reflected power up to 100% of the forward power. (This sweep time should be faster than the sweep time of the network analyzer.) The response of the coupled port from the reflected power sweep should be minimized.

Unfortunately, this is not enough as the swept reflected power will be at a particular phase relative to the forward power. Since reflections farther down the line will in general be at arbitrary phases, we need to sweep the phase of the reflected power and minimize the amplitude of the coupled response. Take the signal generator out of sweep mode and set the power output equal to the forward power for 100% reflection (the worst case). The signal generator and the network analyzer should be phase locked, and the signal generator's frequency should be offset from the analyzer's stimulus by a Hertz or two. This acts as a phase oscillation between the forward and reflected waves in the transmission line. If the coupler is not absolutely directive, then when the forward and reflected waves constructively interfere, the power received at the coupler will increase. Better directivity is achieved by minimizing the beat amplitude while maintaining the overall desired attenuation level. Figure C.4 shows sample output while performing the calibration for a target attenuation of -60 dB. The power and phase sweeps can be iterated to provide the best isolation.

As an optional first step, a spectrum analyzer can be attached to the isolated port with the through port terminated, and the power output at the CW frequency can be

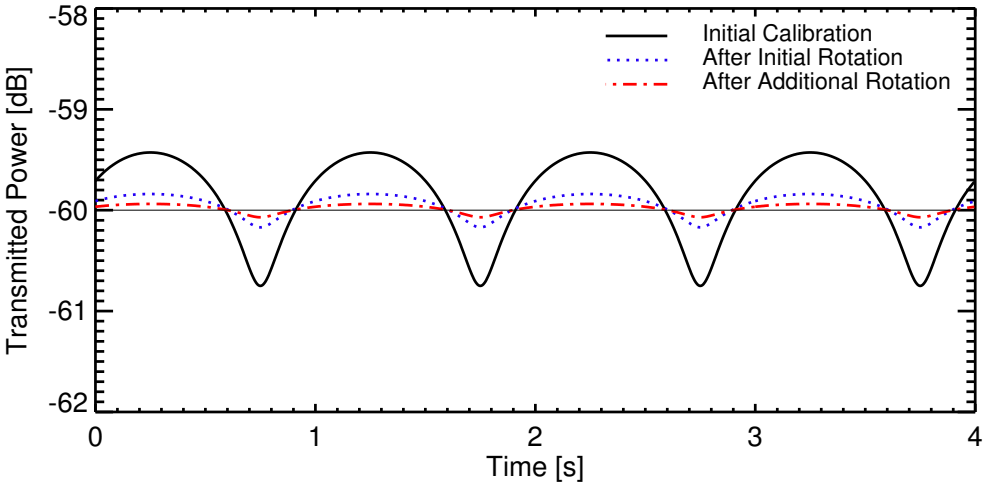

Figure C.4: Sample output for calibration of dual directional couplers. Reflected power is beating with the forward power by virtue of a small frequency offset. Successive rotations of the coupling slug will minimize the coupling of the reflected wave.

minimized by rotating the slug. This will result in the slug being more or less in the correct position before fine tuning.

Lastly, it should be noted that with the use of an electrostatic shield over the loop on the slug, one may be able to increase the directivity.

Appendix D

Derivation of Index of Refraction

D.1 Derivation of Equation 3.18

We start with the equation for E_z in the vacuum region from §3.1:

$$E_z(u) = C\, e^{\sqrt{n_z^2-1}u} + D\, e^{-\sqrt{n_z^2-1}u} \tag{3.16}$$

with the characteristic impedance,

$$Z = i\frac{E_z}{H_y} = \sqrt{n_z^2-1}\,\frac{De^{-2\sqrt{n_z^2-1}u} + C}{De^{-2\sqrt{n_z^2-1}u} - C}. \tag{3.17}$$

where C and D are to be determined by the boundary conditions. Let $\xi \equiv \sqrt{n_z^2-1}$, then multiplying by the right-side denominator, we have

$$\xi\left(De^{-2\xi u} - C\right) = Z\left(De^{-2\xi u} + C\right). \tag{D.1}$$

Collecting constants,

$$De^{-2\xi u}\left(\xi - Z\right) = -C\left(Z + \xi\right), \tag{D.2}$$

and applying the first boundary condition $Z = Z_p$ at $u = 0$:

$$D = -C\left(\xi + Z_p\right)\left(\xi - Z_p\right)^{-1}. \tag{D.3}$$

With the presumption that Z_p is small and that $Z_p/\xi \ll 1$, we keep only the terms linear in Z_p:

$$D \simeq -C\left(1 + 2Z_p/\xi\right) \tag{D.4}$$

to eliminate one constant. Applying the second boundary condition $Z = Z_s$ at $u = -u_s$,

$$Z_s = \xi\frac{D + Ce^{-2\xi u_s}}{D - Ce^{-2\xi u_s}}. \tag{D.5}$$

Substituting (D.4),

$$Z_s = \xi\frac{-C\left(1 + 2Z_p/\xi\right) + Ce^{-2\xi u_s}}{-C\left(1 + 2Z_p/\xi\right) - Ce^{-2\xi u_s}}. \tag{D.6}$$

Dividing out the $-C$'s and rearranging terms,

$$Z_s = \xi\,\frac{\left(1 - e^{-2\xi u_s}\right) + 2Z_p/\xi}{\left(1 + e^{-2\xi u_s}\right) + 2Z_p/\xi}. \tag{D.7}$$

Now we have defined $w \equiv \xi u_s$, so substituting where appropriate and bringing w to the left side, we have

$$w = Z_s u_s\frac{\left(1 + e^{-2w}\right) + 2Z_p u_s/w}{\left(1 - e^{-2w}\right) + 2Z_p u_s/w}. \tag{D.8}$$

Pulling out the terms in paratheses,

$$w = Z_s u_s \frac{1+e^{-2w}}{1-e^{-2w}} \left[1 + \frac{2Z_p u_s/w}{1+e^{-2w}}\right] \left[1 + \frac{2Z_p u_s/w}{1-e^{-2w}}\right]^{-1}. \tag{D.9}$$

If $Z \ll \xi$, then $Z \ll \xi\,(1-e^{-2w})$, so we can again approximate:

$$w \simeq Z_s u_s \frac{1+e^{-2w}}{1-e^{-2w}} \left[1 + \frac{2Z_p u_s/w}{1+e^{-2w}}\right] \left[1 - \frac{2Z_p u_s/w}{1-e^{-2w}}\right] \tag{D.10}$$

$$w \simeq Z_s u_s \frac{1+e^{-2w}}{1-e^{-2w}} \left[1 + \frac{2Z_p u_s/w}{1+e^{-2w}} - \frac{2Z_p u_s/w}{1-e^{-2w}} + \cancel{\frac{4Z_p^2 u_s^2/w^2}{(1+e^{-2w})\,(1-e^{-2w})}}\right] \tag{D.11}$$

where we neglect the product of two small terms. Collecting the second and third terms in (D.11),

$$w \simeq Z_s u_s \frac{1+e^{-2w}}{1-e^{-2w}} \left[1 + \frac{2Z_p u_s/w\,(1-e^{-2w}) - 2Z_p u_s/w\,(1+e^{-2w})}{(1+e^{-2w})\,(1-e^{-2w})}\right] \tag{D.12}$$

and finally cancelling terms and rearranging,

$$\boxed{w = Z_s u_s \frac{1+e^{-2w}}{1-e^{-2w}} \left[1 - Z_p \frac{4u_s e^{-2w}}{w\,(1-e^{-4w})}\right]} \tag{3.18}$$

which is the transcendental equation from §3.1.2.

D.2 Derivation of Equation 3.21

We can apply the perturbation $n_z = n_{z_0} + n_{z_1}$ to our variable w,

$$w = \sqrt{n_z^2 - 1}\, u_s = \sqrt{(n_{z_0} + n_{z_1})^2 - 1}\, u_s \tag{D.13}$$

$$= \sqrt{n_{z_0}^2 - 1}\left[1 + \frac{2n_{z_0}}{\sqrt{n_{z_0}^2 - 1}} n_{z_1} + \cancel{\frac{n_{z_1}^2}{\sqrt{n_{z_0}^2 - 1}}}\right]^{1/2} u_s \tag{D.14}$$

$$\simeq \underbrace{\sqrt{n_{z_0}^2 - 1}\, u_s}_{w_0} + \underbrace{\frac{n_{z_0}}{\sqrt{n_{z_0}^2 - 1}}\, n_{z_1} u_s}_{w_1} \tag{D.15}$$

Given the exact solution, n_{z_0}, we now rewrite (3.18) as

$$w = K_1(w) + Z_p K_2(w)\,. \tag{D.16}$$

We let $w = w_0 + w_1$ where w_1 is determined from (D.15). Expanding, we have:

$$w_0 + w_1 = K_1(w_0) + \left.\frac{\partial K_1}{\partial w}\right|_{w_0} w_1 + Z_p K_2(w_0) + \cancel{Z_p \left.\frac{\partial K_2}{\partial w}\right|_{w_0} w_1} \tag{D.17}$$

where the last term is neglected as the product of two small parameters. The non-perturbed solution has $w_1 = Z_p = 0$, so we have

$$w_0 = K_1(w_0) = Z_s u_s \frac{1 + e^{-2w}}{1 - e^{-2w}}. \tag{D.18}$$

The perturbation is then

$$w_1 = \left.\frac{\partial K_1}{\partial w}\right|_{w_0} w_1 + Z_p K_2(w_0)\,. \tag{D.19}$$

Collecting terms and dividing,

$$w_1 = Z_p \frac{K_2(w_0)}{1 - \left.\frac{\partial K_1}{\partial w}\right|_{w_0}} \tag{D.20}$$

Working with the denominator,

$$1 - \left.\frac{\partial K_1}{\partial w}\right|_{w_0} = 1 - \frac{\partial}{\partial w}\left[Z_s u_s \frac{1+e^{-2w}}{1-e^{-2w}}\right]_{w_0} \tag{D.21}$$

$$= 1 + \left[\frac{2e^{-2w} Z_s u_s}{1-e^{-2w}} + \frac{2e^{-2w}\left(1+e^{-2w}\right) Z_s u_s}{\left(1-e^{-2w}\right)^2} - \frac{1+e^{-2w}}{1-e^{-2w}} u_s \frac{\partial Z_s}{\partial w}\right]_{w_0} \tag{D.22}$$

and then inverting (D.18), substituting for $u_s Z_s$, and canceling terms, the denominator is

$$1 - \left.\frac{\partial K_1}{\partial w}\right|_{w_0} = 1 + \frac{2w_0 e^{-2w_0}}{1+e^{-2w_0}} + \frac{2w_0 e^{-2w_0}}{1-e^{-2w_0}} - w_0 \frac{1}{Z_s}\frac{\partial Z_s}{\partial w} \tag{D.23}$$

and collecting the second and third terms,

$$1 - \left.\frac{\partial K_1}{\partial w}\right|_{w_0} = 1 + \frac{4w_0 e^{-2w_0}}{1-e^{-4w_0}} - w_0 \frac{1}{Z_s}\frac{\partial Z_s}{\partial w}. \tag{D.24}$$

Plugging this term and $K_2(w_0)$ back into (D.20), we have

$$w_1 = \cancel{Z_s u_s \frac{1+e^{-2w_0}}{1-e^{-2w_0}}} \left[\frac{-Z_p 4u_s e^{-2w_0}}{\cancel{w_0}(1-e^{-4w_0})}\right] \frac{1}{1+\frac{4w_0 e^{-2w_0}}{1-e^{-4w_0}} - w_0 \frac{1}{Z_s}\frac{\partial Z_s}{\partial w}} \tag{D.25}$$

$$w_1 = -Z_p \frac{4u_s e^{-2w_0}}{1-e^{-4w_0}} \frac{1}{1+\frac{4w_0 e^{-2w_0}}{1-e^{-4w_0}} - w_0 \frac{1}{Z_s}\frac{\partial Z_s}{\partial w}} \tag{D.26}$$

$$\frac{n_{z_0}}{\sqrt{n_{z_0}^2-1}} n_{z_1} u_s = -4Z_p u_s \frac{e^{-2w_0}}{(1-e^{-4w_0})\left(1-w_0\frac{1}{Z_s}\frac{\partial Z_s}{\partial w}\right) + 4w_0 e^{-2w_0}}, \tag{D.27}$$

where we have used the substitution from (D.18) and replaced w_1 by the expansion from (D.15). Finally, we recast the term with derivative in the previous equation by applying the chain rule:

$$w_0 \frac{1}{Z_s}\frac{\partial Z_s}{\partial w} = w_0 \frac{1}{Z_s}\frac{\partial Z_s}{\partial n_z}\left[\frac{\partial w}{\partial n_z}\right]^{-1} = w_0 \frac{1}{Z_s}\frac{\partial Z_s}{\partial n_z}\left[\frac{n_{z_0}}{\sqrt{n_{z_0}^2-1}}\, u_s\right]^{-1} \tag{D.28}$$

and using the definition $w_0 \equiv \sqrt{n_{z_0}^2-1}\, u_s$, we have

$$\nu \equiv w_0 \frac{1}{Z_s}\frac{\partial Z_s}{\partial w} = \frac{n_{z_0}^2-1}{n_{z_0}^2}\frac{1}{Z_s}\frac{\partial Z_s}{\partial n_z}. \tag{D.29}$$

Plugging (D.29) into (D.27) and rearranging we arrive at

$$\boxed{n_{z_1} = -\frac{4\left(n_{z_0}^2-1\right)^{1/2}}{n_{z_0}} Z_p\, F(w_0), \quad F = \frac{e^{-2w_0}}{(1-e^{-4w_0})(1-\nu)+4w_0\, e^{-2w_0}}} \tag{3.21}$$

which is Golant's Equation 43.

Appendix E

Calculation of Etendue

To calculate an absolute x-ray flux, we need to know the the etendue $G = A\Omega$ where A is the projected area of the detector. Fig. E.1 shows the typical geometry of a detector and plasma volume element with a small "pinhole" aperture. Assuming the area of the

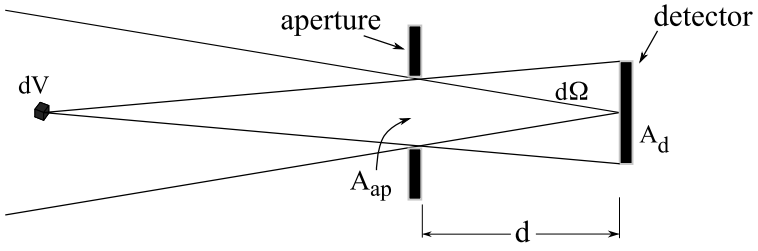

Figure E.1: Geometry for basic etendue calculation with pinhole aperture.

aperture area A_{ap} is small relative to d, then

$$\Omega = \frac{A_{ap}}{d^2} \tag{E.1}$$

and

$$G = \frac{A_{ap} A_d}{d^2} \tag{E.2}$$

This assumes that the aperture is small enough so that the projected area of the detector changes little with respect to the position of dV . In many instances this approximation is good enough. For the case of the HXR detectors on MST, we cannot make this assumption. We must use a more rigorous definition of etendue.

Fig. E.2 shows the more general situation where we have two surfaces, and we choose one to be the detector and the other to be the radiator. Then,

Given: a, b: 2 surfaces.

dS_a, dS_b: infinitesimal surfaces elements on a, b

$\vec{r}$: a chord connecting the centroids of dS_a, dS_b ($d \equiv |\vec{r}|$)

$\hat{n}_a$, $\hat{n}_b$: normals of dS_a, dS_b

α_a, α_b: the angles between $\vec{r}$ and $\hat{n}_a$, $\hat{n}_b$ respectively

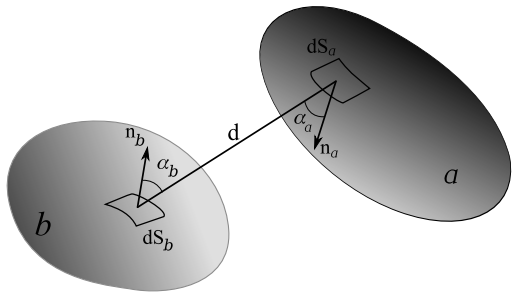

Figure E.2: Sketch of two surfaces a and b for which we calculate the etendue.

then the infinitesimal solid angles of dS_b as seen from dS_a and vice versa are:

$$d\Omega_a = \frac{dS_b \cos\alpha_b}{d^2}, \qquad d\Omega_b = \frac{dS_a \cos\alpha_a}{d^2} \tag{E.3}$$

and the differential etendue is:

$$d^2G = dS_a \cos\alpha_a d\Omega_a = dS_b \cos\alpha_b d\Omega_b = \frac{dS_a dS_b \cos\alpha_a \cos\alpha_b}{d^2}. \tag{E.4}$$

and finally,

$$G = \int d^2G. \tag{E.5}$$

By the principle of conservation of throughput (etendue) [3], the actual receiving surface need not be used in the calculation. Any intermediate surface — of any shape — can be picked. Since our detector surfaces are flat, without loss of generality, we will pick a flat surface in the plasma that is parallel to the detector surface. Also without loss of generality, we can rotate the coordinate system so that $\hat{n}_a, \hat{n}_b \,||\, \hat{z}$.

Then let a and b be in the planes $z = z_a$, $z = z_b$ respectively, then we have $z_0 = z_a - z_b$ so,

$$\cos\alpha_a = \frac{z_0}{d}, \qquad \cos\alpha_b = \frac{z_0}{d} \tag{E.6}$$

and the differential etendue is

$$d^2G = \frac{dS_a dS_b z_0^2}{d^4} \tag{E.7}$$

This is not the end of the story because surfaces a and b are not in free space. Instead there are one or more apertures in the intervening space which can occlude

part (or all) of the other surface.

When this is the case, we can only add parts of the integral where the ray between dS_a and dS_b intersects an aperture, otherwise radiation from one differential area patch could not reach the other. Specifically after approximating the integral as a sum:

$$G \simeq \sum_i \sum_j \frac{z_0^2}{d_{ij}^4} \Delta S_{a_i} \Delta S_{b_j} \prod_k^{\text{apertures}} \delta_{vis}^k \left(\vec{x}_i, \vec{x}_j \right) \tag{E.8}$$

where $\delta_{vis}^k \left(\vec{x}_i, \vec{x}_j \right)$ is 1 if a ray $\vec{r}$ between dS_a and dS_b, at $\vec{x}_i$, $\vec{x}_j$ respectively, $\vec{r} = \vec{x}_i - \vec{x}_j$, is within the boundary of the k'th aperture and 0 otherwise.

A small program was written to solve E.8 with an arbitrary set of rectangular and circular apertures. Error in the location and dimensions of the detector and apertures can be taken into account using Monte Carlo methods. A pair of examples are shown in Figure E.3.

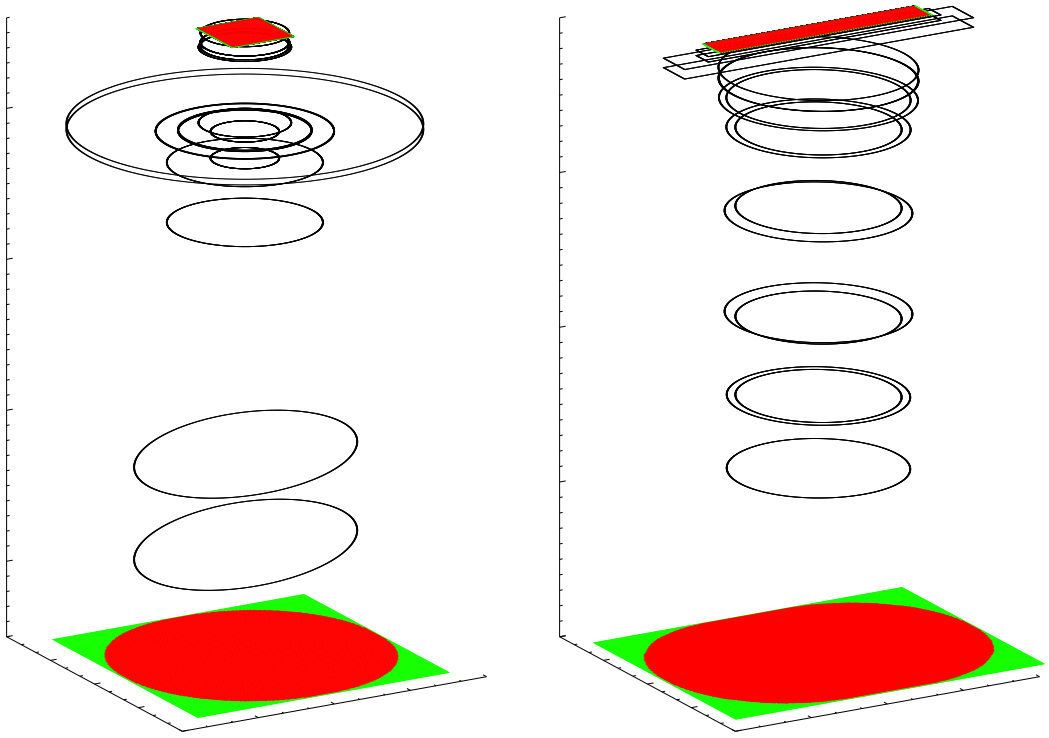

Figure E.3: Models of boxport x-ray detector mount with porthole and multichannel detector mount on standard porthole for etendue calculation. The apertures of the mounts are shown as the black circles. The red portions of one mesh are visible from some part of the other mesh.

Appendix F

Relativistic Particle Mover

The leap-frog method as outlined by Birdsall and Langdon [4] is:

$$\frac{\mathbf{u}^{n+1/2} - \mathbf{u}^{n-1/2}}{\Delta t} = \frac{q}{m}\left(\mathbf{E}^n + \frac{\mathbf{u}^{n+1/2} - \mathbf{u}^{n-1/2}}{2\gamma^n} \times \mathbf{B}^n\right) \tag{4.47}$$

$$\frac{\mathbf{x}^{n+1} - \mathbf{x}^n}{\Delta t} = \mathbf{v}^{n+1/2} = \frac{\mathbf{u}^{n+1/2}}{\gamma^{n+1/2}} \tag{4.48}$$

where $\mathbf{u} \equiv \gamma\mathbf{v}$, $\gamma^2 = 1 + u^2/c^2$, and $t^n = n\Delta t$.

To solve (4.47) we use the method by Boris [5] and separate the $\mathbf{E}$ and $\mathbf{B}$ fields completely by letting

$$\mathbf{u}^{n\pm1/2} = \mathbf{u}^{\pm} \pm \frac{q\mathbf{E}\Delta t}{2m} \tag{4.49}$$

with

$$\frac{\mathbf{u}^{+} - \mathbf{u}^{-}}{\Delta t} = \frac{q}{2\gamma^n m}\left(\mathbf{u}^{+} - \mathbf{u}^{-}\right) \times \mathbf{B}^n. \tag{4.50}$$

The procedure is thus: given $\mathbf{u}^{n-1/2}$ as the starting velocity, we use (4.49) to get $\mathbf{u}^{-}$.

We then need to solve (4.50) for $\mathbf{u}^+$. For this we use a trick, define $\mathbf{u}'$ perpendicular to $\mathbf{u}^+ - \mathbf{u}^-$ *and* $\mathbf{B}^n$:

$$\mathbf{u}' = \mathbf{u}^- + \mathbf{u}^- \times \mathbf{t} \tag{F.1}$$

where

$$\mathbf{t} = \frac{q\,\Delta t}{2\gamma^n m}\mathbf{B}^n \tag{F.2}$$

Then

$$\mathbf{u}^+ = \mathbf{u}^- + \mathbf{u}' \times \mathbf{s} \tag{F.3}$$

where $\mathbf{s} = 2\mathbf{t}/(1+t^2)$. Once we have $\mathbf{u}^+$, use (4.49) to get $\mathbf{u}^{n+1/2}$ and then (4.48) to get the position and velocity at the next timestep, $\mathbf{x}^{n+1}$, $\mathbf{v}^{n+1/2}$.

One thing to note is the fact that the starting velocity is $\mathbf{u}^{n-1/2}$ with the starting fields $\mathbf{E}^n$ and $\mathbf{B}^n$. In our case, the particle starts outside the force-field so $\mathbf{u}^{n-1/2} = \mathbf{u}^n$. If this is not the case, then another method must be used to take the first step.

The C function below does the heavy lifting for the particle mover by advancing an electron under the influence of electric and magnetic fields one timestep:

```
/*****************************************************************
 Copyright (C) 2008 - M.C. Kaufman

 Permission is hereby granted, free of charge, to any person obtaining a
 copy of this software and associated documentation files (the
 "Software"), to deal in the Software without restriction, including
 without limitation the rights to use, copy, modify, merge, publish,
 distribute, sublicense, and/or sell copies of the Software, and to
 permit persons to whom the Software is furnished to do so, subject to
 the following conditions:

 The above copyright notice and this permission notice shall be included
```

```
 in all copies or substantial portions of the Software.

 THE SOFTWARE IS PROVIDED "AS IS", WITHOUT WARRANTY OF ANY KIND, EXPRESS
 OR IMPLIED, INCLUDING BUT NOT LIMITED TO THE WARRANTIES OF
 MERCHANTABILITY, FITNESS FOR A PARTICULAR PURPOSE AND NONINFRINGEMENT.
 IN NO EVENT SHALL THE AUTHORS OR COPYRIGHT HOLDERS BE LIABLE FOR ANY
 CLAIM, DAMAGES OR OTHER LIABILITY, WHETHER IN AN ACTION OF CONTRACT,
 TORT OR OTHERWISE, ARISING FROM, OUT OF OR IN CONNECTION WITH THE
 SOFTWARE OR THE USE OR OTHER DEALINGS IN THE SOFTWARE.
*****************************************************************/

/*****************************************************************
  Boris' method to separate B and E fields. Relativistic formulation.
  Implementation uses an intermediate vector to perform the rotation.
  Accomplishes one timestep.

  inputs:
    particle's current position and time: x[3], t
    fields at x[3], t: E[3], B[3] (volts/meter and telsa respectively)
    timestep: timestep
    relatistic velocity: u[3] ( = gamma * v)

  outputs:
    new position: x[3]
    new velocity: v[3]
    new relatistic velocity: u[3]
    new time: t
*****************************************************************/
static void step_boris_rel(double timestep, double E[3], double B[3],
                           double x[3], double u[3], double v[3],
                           double *t)
{
  const double c2 = 9e16;              /* speed of light squared */
  const double q2m = -1.75884e11;      /* charge to mass ratio */

  double up[3], um[3];                 /* u+ and u- */
  double tt, T[3], s[3], uprime[3];    /* for the v x B rotation */
  double gammainv;                     /* inverse of gamma factor */
  double u2;                           /* intermediate variable */
  double alpha = 0.5 * q2m * timestep; /* scale factor */
```

```
/* step 0: scale fields appropriately */
E[0] *= alpha;
E[1] *= alpha;
E[2] *= alpha;
B[0] *= alpha;
B[1] *= alpha;
B[2] *= alpha;

/* step 1: get u- from u(t-delta t/2) which is the u from last step
 *         by adding half the electric field contribution */
um[0] = u[0] + E[0];
um[1] = u[1] + E[1];
um[2] = u[2] + E[2];

/* step 2: calculate u+ using uprime, T and s */
u2 = um[0] * um[0] + um[1] * um[1] + um[2] * um[2];
gammainv = sqrt(c2 / (c2 + u2));

T[0] = B[0] * gammainv;
T[1] = B[1] * gammainv;
T[2] = B[2] * gammainv;
tt = 2.0 / (T[0] * T[0] + T[1] * T[1] + T[2] * T[2] + 1.0);
s[0] = T[0] * tt;
s[1] = T[1] * tt;
s[2] = T[2] * tt;

uprime[0] = um[0] + um[1] * T[2] - um[2] * T[1];
uprime[1] = um[1] + um[2] * T[0] - um[0] * T[2];
uprime[2] = um[2] + um[0] * T[1] - um[1] * T[0];

up[0] = um[0] + uprime[1] * s[2] - uprime[2] * s[1];
up[1] = um[1] + uprime[2] * s[0] - uprime[0] * s[2];
up[2] = um[2] + uprime[0] * s[1] - uprime[1] * s[0];

/* step 3: get u(t + delta t/2) by adding the other half of the E-field */
u[0] = up[0] + E[0];
u[1] = up[1] + E[1];
u[2] = up[2] + E[2];
```

```
  /* step 4: get v(t + delta t) */
  u2 = u[0]*u[0] + u[1]*u[1] + u[2]*u[2];
  gammainv = sqrt(c2 / (c2 + u2));
  v[0] = u[0] * gammainv;
  v[1] = u[1] * gammainv;
  v[2] = u[2] * gammainv;

  /* step 5: get x(t + delta t) */
  x[0] += v[0] * timestep;
  x[1] += v[1] * timestep;
  x[2] += v[2] * timestep;

  *t += timestep;
}
```

Bibliography

[1] Hecht, F. *FreeFem++*, 3rd edition, 2009.
http://www.freefem.org/ff++/ftp/freefem++doc.pdf.

[2] Cristal, E. Coupled circular cylindrical rods between parallel ground planes. *Microwave Theory and Techniques, IEEE Transactions on*, **12**(4):428–439, 1964.

[3] A. Thorne, S. J., U. Litzén. *Spectrophysics Principles and Applications.* Springer-Verlag, 1999.

[4] Birdsall, C. and Langdon, A. *Plasma Physics via Computer Simulation.* Bristol : Institute of Physics Pub., 2005.

[5] Boris, J. Relativistic plasma simulation—optimization of a hybrid code. In *Proceedings from the Fourth Conference of Numerical Simulation of Plasmas*, pp. 3–67. Naval Research Laboratory, 1970.